

**TOPOLOGY OPTIMIZATION OF HIERARCHICAL HONEYCOMB
STRUCTURES TO REDUCE STRESS CONCENTRATION, DEFORMATION,
AND DEFLECTION**

By

Munashe Ignatius Chibinyani

A dissertation submitted in fulfilment of the requirements for the degree

Master of Engineering in Mechanical Engineering

in the

Department of Mechanical and Mechatronics Engineering

Faculty of Engineering, Built Environment, and Information Technology

at

Central University of Technology, Free State

Supervisor: Dr Thywill C. Dzogbewu, D.Eng.

Co-supervisor: Prof. Maina Maringa, Ph.D.

Co-supervisor: Dr Amos Mũirũrĩ, D.Eng.

BLOEMFONTEIN, FREE STATE, SOUTH AFRICA

DATE: November 2024

DECLARATION OF INDEPENDENT WORK

DECLARATION WITH REGARD TO INDEPENDENT WORK

I, **MUNASHE IGNATIUS CHIBINYANI**, Passport number ##### and student registration number #####, do hereby declare that this research project submitted to Central University of Technology, Free State, for the degree **MASTER OF ENGINEERING IN MECHANICAL ENGINEERING**, is my own independent work; and complies with the Code of Academic Integrity, as well as other relevant policies, procedures, rules and regulations of Central University of Technology, Free State; and has not been submitted before to any institution by myself or any other person in fulfilment (or partial fulfilment) of the requirements for the attainment of any qualification.

SIGNATURE OF STUDENT

01 November 2024

DATE

ACKNOWLEDGMENTS

First, I would like to express my deep gratitude to my supervisor, Dr Thywill Dzogbewu, for his invaluable support, guidance, and encouragement throughout my studies. I am also profoundly grateful to my co-supervisors, Prof. Maina Maringa and Dr Amos Muiruri, for their unwavering support, commitment, and constant availability for technical discussions related to my research. I extend my sincere thanks to the Centre of Rapid Prototyping and Manufacturing (CRPM) at Central University of Technology, Free State, for granting me access to the additive manufacturing facilities essential for producing the test specimens used in this study. I am deeply appreciative of Mr Hellmut Bowles from Dassault Systèmes for his dedication and technical assistance in modelling and simulations using ABAQUS software. I also wish to acknowledge the Research Center for Mechanical Engineering at Central University of Technology, particularly Dr Dean Koupryanoff and Mr Karabo Moore, for their support in providing equipment and assistance for compression testing of the additively manufactured parts. I am equally grateful to Mr Emmanuel Zungu at CUT Library and Information Services for his continuous support in accessing research materials and articles. I would like to acknowledge the financial support provided by the South African Department of Science and Innovation (DSI) through the Council for Scientific and Industrial Research (CSIR) under the Collaborative Program in Additive Manufacturing (Contract No.: CSIR-NLC-CPAM-18-MOA-CUT-03). My thanks also go to the Directorate of Research and Development & Postgraduate Studies (RD & PGS) at CUT for their financial assistance. More than anything else, I am grateful to God for His steadfast mercy and safeguarding grace all through my master's studies.



DEDICATIONS

This master's thesis is dedicated to the memory of my late father, Duncan Chibinyani, my mother, and my siblings, as well as to the committed researchers in the field of design for additive manufacturing, complex structure mechanics, modelling, and simulation.

TABLE OF CONTENTS

DECLARATION OF INDEPENDENT WORK	i
ACKNOWLEDGMENTS	ii
DEDICATIONS	iii
TABLE OF CONTENTS	iv
LIST OF FIGURES	ix
LIST OF TABLES	xv
LIST OF SYMBOLS, ABBREVIATIONS AND ACRONYMS	xvi
LIST OF PUBLICATIONS	xix
ABSTRACT	xx
CHAPTER ONE: INTRODUCTION	1
1.1. Summary	1
1.2. Cellular structures.....	1
1.3. Lattice structures	2
1.3.1 Hierarchical lattice structures	3
1.4. Topology optimization	4
1.5. Shape optimization	4
1.6. Additive manufacturing.....	4
1.7. Problem statement	5
1.8. Motivation of the research.....	6
1.9. Research aim	6
1.11. Dissertation outline.....	6
1.12. Benefits of this research.....	7
1.13. Delimitations of the study.....	8
1.14. Summary	8
References	8
CHAPTER TWO: LITERATURE REVIEW ON CELLULAR AND LATTICE STRUCTURES	11

2.1. Summary	11
2.2. Introduction	11
2.3. Cellular structures.....	12
2.3.1 Types of cellular structures in nature.....	12
2.3.2 Occurrence of cellular designs in nature	13
2.4. Lattice structures.....	16
2.4.1 Types of lattice structures	16
2.4.2 Evaluation of tessellation in lattice structures	17
2.4.3 Hierarchical lattice structures	22
2.5. Applications of lattice structures in engineering.....	24
2.6. Mechanical properties of cellular and lattice structures	27
2.7. Analytical modelling of the deformation behaviour of cellular and lattice structures	39
2.7.1 Stress-strain curves for cellular and lattice structures	39
2.7.2 A novel deformation mechanism added to the two-stage behaviour of cellular designs	40
2.7.3 Deformation behaviour models for cellular structures	42
2.7.4 Proposed model combining direct, buckling and bending deformation behaviour of lattice designs	48
2.7.5 Suggestions on the application of Tresca and von Mises failure criteria to the deformation behaviour of lattice designs	50
2.7.6 Analytical models of lattice structures built with polygon hollow shapes.....	52
2.8. Efficacy and limitations in designing lattice structures	59
2.8.1 Evaluation of lattice structures in mimicking natural cellular structures.....	59
2.8.2 Constraints in determining the order of hierarchy attainable for hierarchical lattice honeycombs (HCs)	63
2.9. Scope and opportunities for future work	65
2.9.1 Next-generation structural optimization and design guide for lattice structures	65
2.9.2 Challenges and future prospects in design for additive manufacturing of lattice structures.....	67
References	69
CHAPTER THREE: MATERIALS AND RESEARCH METHODS	81
3.1. Introduction	81
3.2. Literature review on cellular and lattice structures.....	81
3.3. Analytical modelling of lattice structures.....	81

3.3.1 Extending the reviewed deformation behaviour with analytical modelling	81
3.3.2 Analytical modelling of selected polygon structures	81
3.3.3 Analytical modelling of first-order hierarchical HC structures	82
3.4. Numerical modelling and crushing of lattice structures	84
3.4.1 Numerical modelling of polygon structures	84
3.4.2 Numerical modelling of first-order hierarchical HC structures	87
3.4.3 Numerical crushing hierarchical HC structures	87
3.5. Topology and shape optimization (TO and SO) of planar honeycomb (HC) structures	88
3.5.1 HC part design	88
3.5.2 Mesh convergence testing.....	88
3.5.3 The preliminary finite element (FE) hexagonal unit cell and HC model	89
3.5.4 The TO of hexagonal unit cell and HC model	90
3.5.5 The topology-optimized FE unit cell and HC model.....	90
3.5.6 The shape-optimized FE unit cell and HC model	91
3.6. Quasi-static crushing experiments of hierarchical HC structures.....	91
3.6.1 Design configurations of hierarchical parts	91
3.6.2 Additively-produced hierarchical HC parts	94
3.6.3 Heat-treatment protocol used on as-built Ti6Al4V hierarchical HC parts	95
3.6.4 Removal of supports from the hierarchical HC parts	96
3.6.5 Surface roughness testing for hierarchical HC parts	98
3.6.6 Quasi-static crushing analysis of hierarchical HC builds.....	99
3.7. Summary	100
References	100
CHAPTER FOUR: NUMERICAL MODELLING OF POLYGON STRUCTURES UNDER QUASI-STATIC LOADING.....	103
4.1. Summary	103
4.2. Comparative analysis of planar and extruded FE models	103
4.3. Preliminary FE findings for polygon structures	105
4.4. Deformation behaviour of HC models.....	109
4.4.1 Bending and axial behaviour	109
4.4.2. Primary buckling behaviour	114
4.5. Effects of the t/L ratio on the effective stiffness of HC structures.....	120
4.6. Comparison of implemented simulation/modelling in the current work and experimental findings in the literature	122

4.7. Scope and opportunities for future work	123
4.7.1 Extending the simulation and modelling implemented in this study to other metallics and their various applications	123
References	125
CHAPTER FIVE: NUMERICAL MODELLING OF FIRST-ORDER HIERARCHICAL STRUCTURES UNDER QUASI-STATIC LOADING.....	130
5.1. Summary	130
5.2. Numerical findings of stress levels and stress concentration	130
5.3. Numerical results of deflection	137
5.4. Comparison of experimental studies in literature and modelling implemented here	140
5.5. Scope and opportunities for future work	143
5.5.1 Extending the application of the modelling implemented in this study to design for additive manufacturing.....	143
References	144
CHAPTER SIX: NUMERICAL CRUSHING OF HIERARCHICAL STRUCTURES UNDER QUASI-STATIC LOADING.....	148
6.1. Summary	148
6.2. Preliminary results on numerical crushing hierarchical HCs	148
6.2.1. Deformation response modes	148
6.2.2. Energy absorption characteristics.....	150
References	151
CHAPTER SEVEN: TOPOLOGY AND SHAPE OPTIMIZATION OF POLYGON STRUCTURES.....	152
7.1. Summary	152
7.2. Introduction	152
7.2.1 TO of 3D HC parts	153
7.3. Results and discussion.....	154
7.3.1 Mesh convergence analysis	154
7.3.2 Preliminary FEA (numerical analysis before TO)	157
7.3.3 TO analysis	160
7.3.4 Numerical analysis of TO model	162

7.3.5 Numerical analysis of SO model	164
7.4. Scope and opportunities for future work	166
7.4.1 Extending the current topology-optimized low-fidelity HC models to high-fidelity ones	166
References	166
CHAPTER EIGHT: EXPERIMENTATION: QUASI-STATIC CRUSHING OF HIERARCHICAL LATTICE STRUCTURES	169
8.1. Summary	169
8.2. Introduction	169
8.3. Results and discussion.....	171
8.3.1 Surface roughness	171
8.3.2 Mechanical behaviour	173
8.4. Scope and opportunities for future work	182
8.4.1 Challenges and the way forward in updating design concepts and experimental tests for additively-produced hierarchical lattice parts	182
References	183
CHAPTER NINE: CONCLUSIONS AND RECOMMENDATIONS.....	188
9.1. Introduction	188
9.2. Conclusions emerging from the various chapters	188
9.2.1. Review of cellular and lattice structures (Chapter 2).....	188
9.2.2. Quasi-static numerical modelling of polygon structures (Chapter 4)	189
9.2.3 Quasi-static numerical modelling of first-order hierarchical structures (Chapter 5)	190
9.2.4. Quasi-static numerical crushing of hierarchical structures (Chapter 6).....	190
9.2.5 TO and SO for planar HCs (Chapter 7).....	191
9.2.6. Quasi-static crushing experiments of hierarchical structures (Chapter 8)	191
9.3. Recommendations for further research.....	191

LIST OF FIGURES

Figure 1-1. (a) Open cell structures; (b) closed cell structures [3]	1
Figure 1-2. The beehive prismatic configuration of an HC design [2].....	2
Figure 1-3. Bioinspired hierarchical HC designs for energy absorption applications [5]	3
Figure 1-4. Research flow diagram	7
Figure 2-1. Different types of cellular designs in nature	12
Figure 2-2. Groups of cellular designs, namely, (a) an open cellular structure used to build a glass sponge skeleton, (b) a closed cellular structure used to build a tibia bone, and (c) a polygon cell-based structure used to build honeycomb cell walls in wood [4, 14-15]	13
Figure 2-3. A skeletal composite of spicules in siliceous sponges built using cylindrical lattice cage-like structures, represented as (a) an organic and non-periodic form and (b) a systematically modelled and periodic form [14]	14
Figure 2-4. Numerous morphologies of bone tissue depending on their application [3].....	14
Figure 2-5. Different hierarchical orders of structuring material for numerous scales of a bone structure [18]	15
Figure 2-6. Numerous hierarchical levels of structuring material for a variety of scales of a wood structure [14]	15
Figure 2-7. Four types of lattice structures in engineering applications [11, 21]	16
Figure 2-8. Schematics of a planar-based method for creating hexagonal polygon unit cells [21]	17
Figure 2-9. Designing unit cells using a primitive-based method [26]	18
Figure 2-10. A skeletal TPMS-based unit cell type created by an implicit surface-based method [26]	18
Figure 2-11. Diagrams for direct patterning in both (a) two- and (b) three dimensions [26]	19
Figure 2-12. The (a) direct structuring method as opposed to the (b) conforming structuring method [35]	19
Figure 2-13. A strut-based lattice structure generated from density data [38]	20
Figure 2-14. The relationship between four different cell polygons within the same design space [51]	21
Figure 2-15. Planar tessellated structures with (a) triangular, (b) squared, (c) circular, and (d) hexagonal cells [51]	21
Figure 2-16. (a-b) vertex-based hierarchical polygonal structures, (c) vertex-based hierarchical re-entrant HCs, (d) cell-wall-based hierarchical triangle honeycomb (HC), (e) cell-wall-based hierarchical using tetra-chiral and hexa-chiral HCs, (f) cell-wall-based hierarchical re-entrant HCs, (g) fractal-based hierarchical hexa-chiral HC, (h) fractal-based hierarchical circular polygon structures, and (i-j) spiderweb-based hierarchical hexa-chiral HCs [58].....	23
Figure 2-17. Current applications of bioinspired cellular designs in the (a) aerospace [27, 75], (b) automotive [13, 27], and (c) biomedical industries [13, 27].....	26
Figure 2-18. Curve plot showing stress-strain dependence on the direction of loading [95].....	29
Figure 2-19. Curve plot showing stress-strain dependence on loading rate [95]	30

Figure 2-20. Experimental and numerical findings of built hierarchical lattice parts formed by replacing the cell walls with small-scaled triangular hollow structures of different wall thicknesses [114].....33

Figure 2-21. (a) Numerical findings showing the graphic progressive diamond mode of failure mechanism; and (b) the generated load-displacement curve based on experimental crush tests describing the gradual diamond deformation mechanism of a non-self-similar nested HC under dynamic extruded shell in-plane crushing loads [115]34

Figure 2-22. Load-displacement curve for numerical out-of-plane crushing of vertex-based hierarchical HCs built using aluminium [116].....35

Figure 2-23. Experimental and numerical findings for out-of-plane crushing of vertex-based hierarchical HCs with triangular substructures built using aluminium material [117].....36

Figure 2-24. From top to bottom, the graphics represent the deformation histories generated for in-plane crushing of a line beam vertex-based hierarchical HC with triangular substructures along the width and ribbon directions, respectively [117]37

Figure 2-25. Mechanical characteristics of regular HCs and hierarchical HC builds are contrasted with regard to performance ratio [58].....38

Figure 2-26. A typical two-stage stress-strain curve for cellular designs [124].....40

Figure 2-27. A four-stage behaviour stress-strain curve for cellular designs.....41

Figure 2-28. Open unit cell shape that has (a) no deformation, (b) buckling deformation, and (c) bending deformation [130]43

Figure 2-29. A mid-span concentrated transverse loading of a beam fixed at both ends, similar to one used in building cellular structures [132]43

Figure 2-30. Cross-section of rectangular beam and corresponding parameters adopted.....43

Figure 2-31. A strut fixed at the ends under direct axial loading [143]46

Figure 2-32. A hexagonal closed cellular structure, (a) the geometry before deformation, and (b) the stretching deformation in the x- and y-directions [130].....47

Figure 2-33. A 2D representation of a thin plate under x- and y-directional bending moments [139].....47

Figure 2-34. Combined direct, buckling and bending deformation of ribs used to build open lattice structures48

Figure 2-35. Typical polygon hollow shapes built using (a) struts [14] and (b) plates/beams [145]52

Figure 2-36. (a) Natural beehive honeycomb and (b) regular hexagonal geometry of a honeycomb [145]53

Figure 2-37. (a) in-plane and out-of-plane loading of a plate, (b) out-of-plane bending on the left and in-plane bending on the right, and (c) planes of walls before and after bending54

Figure 2-38. A typical hexagonal hollow structure showing all three mutually orthogonal directions in which the behaviour of polygonal hollow structures is analysed55

Figure 2-39. A planar unit hexagonal cell showing two mutually orthogonal planar in-plane directions of loading55

Figure 2-40. A planar unit triangular hollow cell showing two mutually orthogonal planar in-plane directions for loading56

<i>Figure 2-41. A planar unit square hollow cell showing two mutually orthogonal planar in-plane directions of loading</i>	57
<i>Figure 2-42. A planar circular unit hollow cell showing two mutually orthogonal planar in-plane directions of loading</i>	57
<i>Figure 2-43. A hexagonal structure under planar in-plane loading [166]</i>	58
<i>Figure 2-44. Other types of polygonal shapes that could potentially be used in generating hollow lattice designs for different engineering applications</i>	59
<i>Figure 2-45. Cellular structures in nature (a-b) barnacle, (c) microstructure of wood material, and (d) structure of the human trabecular bone [168]</i>	60
<i>Figure 2-46. Micro-CT scan white contours depicting powder that is stuck inside certain parts of an additively manufactured lattice bracket [20]</i>	63
<i>Figure 3-1. (a) Hexagonal substructures, (b) circular substructures, (c) triangular substructures and (d) a diagram illustrating the relationship between these three different substructures [5]</i>	83
<i>Figure 3-2. Typical (a) planar HC shell (b) extruded HC shell structure</i>	84
<i>Figure 3-3. Typical planar (a) triangular, (b) squared, and (c) circular polygon shell structures</i>	84
<i>Figure 3-4. Models of (a) planar hexagonal shell walls and (b) extruded hexagonal shell walls, generated using different element sizes</i>	85
<i>Figure 3-5. Typical (a) planar hexagonal shell and (b) extruded hexagonal shell models with boundary conditions</i>	86
<i>Figure 3-6. Loading fixed and pinned boundary conditions used, respectively, in the (a) y-direction and (b) z-direction of an extruded HC shell structure</i>	87
<i>Figure 3-7. The built planar geometry of the (a) HCR, (b, c and d) HCH, HCC and HCT, respectively</i>	87
<i>Figure 3-8. Graphical representation revealing energy-absorbing characteristics and damage zones [23]</i>	88
<i>Figure 3-9. Planar models for (a) the unit hexagonal cell and (b) the HC</i>	88
<i>Figure 3-10. The planar boundary conditions for (a) a unit hexagonal cell and (b) an HC model, where F denotes the force</i>	89
<i>Figure 3-11. The planar TO HC model (a) with a solid property defined for some of the members that are perpendicular to applied loads, and (b) without a solid property defined for these same members</i>	90
<i>Figure 3-12. The relation derived between the basic HC structure and its corresponding self-similar hierarchical configurations [35]</i>	91
<i>Figure 3-13. Hierarchical CAD designs and dimensions, (a) regular HC, (b) first-order hierarchical HC, and (c) second-order hierarchical HC</i>	93
<i>Figure 3-14. Additively-produced parts, (a) regular HC parts before being cut off from the build plate, and (b) from left to right are images of the regular HC, first-order hierarchical HC, and second-order hierarchical HC after being cut off from the build plate, respectively</i>	95
<i>Figure 3-15. A two-stage high-temperature annealing curve for Ti6Al4V(ELI) hollow parts</i>	96
<i>Figure 3-16. The setup used for pressing out supports in hierarchical HC parts</i>	97

Figure 3-17. The regular HC and its hierarchical parts produced via DMLS technology	98
Figure 3-18. Ti6Al4V(ELI) scrap resulting from removing supports of DMLS-produced hierarchical HC parts.....	98
Figure 3-19. Compression experimental setup using MTS Criterion TM , Model 43 universal tester for (a) a regular HC loaded in the x-direction, and (b) a regular HC loaded in the y-direction	99
Figure 4-1. Typical contour plot of stress obtained on (a) planar hexagonal and (b) extruded hexagonal shell models	104
Figure 4-2. Typical visual problem of unshared topology at the (a) outer and (b) inner vertices after extruding a thickness from the extruded shell model	104
Figure 4-3. The distribution of von Mises stresses in four different models of polygons for an applied load of 2000 N in the x-direction, highlighting (i-iii) members that transmit loads applied in the x-direction and (iv) areas of stress concentration	105
Figure 4-4. The distribution of von Mises stresses in four different models of polygons for an applied load of 2000 N in the y-direction	106
Figure 4-5. Distribution of deflections for the four different models of polygons for an applied load of 2000 N in the x-direction	107
Figure 4-6. Distribution of deflections for the four different models of polygons for an applied load of 2000 N in the y-direction	108
Figure 4-7. Typical elastic deformations of (a) the current numerical model and (b) schematic of a theoretical model in literature [4, 18] for an HC structure loaded along the x-direction	109
Figure 4-8. The deformation mechanics for the (a) current numerical model and (b) theoretical models [4, 18], for loading in the x-direction	109
Figure 4-9. Typical elastic deformations of (a) the hexagonal HC numerical model and (b) image of a theoretical model in literature [4, 18] of a HC structure loaded along the y-direction.....	110
Figure 4-10. The deformation mechanism obtained for the (a) current numerical mode and (b) theoretical models [4, 18] loaded in the y-direction.....	110
Figure 4-11. Numerical results of deflection for HC structures of different wall thicknesses loaded in the x-direction	111
Figure 4-12. Numerical results of deflection for HC structures of different wall thicknesses loaded in the y-direction.....	112
Figure 4-13. Curves with (a) maximum applied loads and (b) maximum deflections experienced in the x- and y-directions of the HC model at different values of thickness (t) of its members	113
Figure 4-14. Curves of the (a) x- and (b) y-direction maximum applied loads versus maximum corresponding deflections	113
Figure 4-15. Distribution of von Mises stresses at the buckling stresses of the HC model for different shell thicknesses	115
Figure 4-16. Critical buckling loads and stresses versus the wall thickness of the numerical HC model loaded in the z-direction.....	116

<i>Figure 4-17. Current numerical and existing theoretical elastic buckling first mode shapes on an HC structure with uniaxial loading acting in the z-direction</i>	<i>117</i>
<i>Figure 4-18. A buckled unit hexagonal cell and plates with and without vertical fixed sides from the left to the right, respectively, showing (a) von Mises stress and (b) deflection contours</i>	<i>118</i>
<i>Figure 4-19. von Mises stress contours of shell models of wall thickness 1 mm, including (a) the HC, (b) the unit hexagonal cell, (c) the plate with restrained vertical sides, and (d) the plate without restrained vertical sides</i>	<i>119</i>
<i>Figure 4-20. Plastic strain contours for the shell models of wall thickness 1 mm, including (a) the HC, (b) the unit hexagonal cell, and (c) the plate with restrained vertical sides</i>	<i>120</i>
<i>Figure 4-21. Numerical results for elastic strains against the ratio (a) t/L and (b) $(t/L)^3$ for the HC model.....</i>	<i>120</i>
<i>Figure 4-22. The effective stiffness of the regular hexagonal honeycomb, with out-of-plane load: Comparison between current FE predictions and analytical model predictions by Gibson and Ashby [4]</i>	<i>122</i>
<i>Figure 5-1. The von Mises stress distribution for (a) HCR structure and (b), (c) and (d) HCH, HCC, and HCT structures, respectively, for the case of a load applied in the x-direction.....</i>	<i>130</i>
<i>Figure 5-2. The von Mises stress distribution for (a) HCR structure and (b), (c) and (d) HCH, HCC, and HCT structures, respectively, for the case of a load applied in the y-direction.....</i>	<i>131</i>
<i>Figure 5-3. Stress distribution in (a) HCR model, and (b) HCH model, when loaded in the x-direction</i>	<i>133</i>
<i>Figure 5-4. Stress distribution in (a) HCC model and (b) HCT model, when loaded in the x-direction</i>	<i>134</i>
<i>Figure 5-5. Stress distribution in (a) HCR model and (b) HCH model, when loaded in the y-direction</i>	<i>135</i>
<i>Figure 5-6. Stress distribution in (a) HCC model and (b) HCT model, when loaded in the y-direction.....</i>	<i>136</i>
<i>Figure 5-7. Numerical results of deflection of the (a) HCR model, (b), (c) and (d) HCH, HCC and HCT models, respectively, when loaded in the x-direction.....</i>	<i>139</i>
<i>Figure 5-8. Numerical results of deflection of the (a) HCR model, (b), (c) and (d) HCH, HCC, and HCT models, respectively, when loaded in the y-direction.....</i>	<i>139</i>
<i>Figure 6-1. Deformation and failure mechanism of regular HC under x-directional load</i>	<i>149</i>
<i>Figure 6-2. Deformation and failure mechanism of regular HC under y-directional load</i>	<i>150</i>
<i>Figure 6-3. Deformation and failure mechanism of first-order hierarchical HC under x-directional load</i>	<i>150</i>
<i>Figure 6-4. Load-displacement curve for a regular HC under x-directional force.....</i>	<i>151</i>
<i>Figure 7-1. An HC part mimicked from a beehive and manufactured by the LPBF method [4].....</i>	<i>152</i>
<i>Figure 7-2. Convergence behaviour of the SIMP and ESO methods of TO [17].....</i>	<i>153</i>
<i>Figure 7-3. Von Mises stress distribution in the members of a planar hexagonal unit cell for different mesh sizes and the same applied load of 3188 N.....</i>	<i>155</i>
<i>Figure 7-4. Von Mises stress versus mesh size for a planar unit hexagonal cell model.....</i>	<i>156</i>
<i>Figure 7-5. Plot of axial deformation versus mesh size for a planar unit hexagonal cell model</i>	<i>157</i>
<i>Figure 7-6. The numerical results before TO for (a) a planar unit hexagonal cell model and (b) a planar HC model</i>	<i>158</i>

Figure 7-7. FEA showing the deflection of unit hexagon cell (left) and HC (right) along the (a) x-direction and (b) y-direction159

Figure 7-8. FEA results showing deflection contour plots of a (a) hexagonal unit cell and (b) HC original geometry superimposed on the deformed geometry159

Figure 7-9. FEA results: (a) a unit hexagonal cell model, (b) an HC model after TO yielding maximum reductions of material, (c) the TO unit hexagonal model without a minimum penalty score constraint, and (d) the TO HC model with no minimum penalty score constraint161

Figure 7-10. Areas on a unit hexagonal cell where the original material densities were preserved or experienced small changes162

Figure 7-11. The numerical results for a TO unit hexagonal cell model with different penalty scores for the fictitious densities reduced from the solid.....163

Figure 7-12. The numerical results for a TO HC model with different penalty scores (0.15 and 0.18) for the fictitious densities reduced from the solid.....164

Figure 7-13. The numerical results of SO unit hexagonal cell model with penalty scores for intermediate densities of (a) 0.05 reduced from solid, and (b) 0.3 reduced from solid.....165

Figure 7-14. The numerical results of the SO HC model with a penalty score of intermediate densities of (a) 0.15 reduced from solid, and (b) 0.18 reduced from solid165

Figure 8-1. The mean surface roughness (R_a) of the surfaces of the top flat faces of the various levels of hierarchy for HCs172

Figure 8-2. The mean surface roughness (R_a) of the surfaces of the side inclined faces of the various levels of hierarchy for HCs172

Figure 8-3. Grouped values of mean surface roughness for the top flat and side inclined faces173

Figure 8-4. Evolution of deformation, fracture and bulk sliding in the three levels of hierarchical HCs under x-directional loading.....174

Figure 8-5. Evolution of deformation, fracture and bulk sliding in the three levels of hierarchical HCs under y-directional loading.....175

Figure 8-6. The deformation trends and levels of crushing till densification of the material for the zero-order HC loaded in the (a) x-direction and (b) y-direction177

Figure 8-7. The deformation trends and levels of crushing before densification of the material for the first-order hierarchical HC loaded in the (a) x-direction and (b) y-direction178

Figure 8-8. The deformation trends and levels of crushing before densification of the material for the second-order hierarchical HC loaded in the (a) x-direction and (b) y-direction179

Figure 8-9. Load-displacement curves for crushing three levels of hierarchical HCs along the two x- and y-in-plane directions180

Figure 8-10. Specimen failure as a function of the manufacturing flaws in the cell walls182

LIST OF TABLES

Table 3-1. Ratios of effective elastic modulus to the elastic modulus of the solid material	82
Table 3-2. Material properties of Ti6Al4V(ELI) used in FE modelling of polygonal structures [22]	85
Table 4-1. Ranking of different polygon structures by stress levels for loading in the x- and y-directions, from the lowest to the highest	107
Table 4-2. Ranking of different polygon structures by deflection levels for loading in the x- and y-directions, from the lowest to the highest	108
Table 4-3. Values of load applied to an HC structure in the x- and y-directions and the corresponding values of deflection	112
Table 4-4. Calculated values of critical buckling loads and buckling stresses for the hexagonal extruded shell model with different wall thicknesses	114
Table 4-5. Numerical values of critical buckling loads and the corresponding stresses at these loads for the hexagonal extruded shell model with different wall thicknesses	114
Table 4-6. Set of J-C model parameters [28]	119

LIST OF SYMBOLS, ABBREVIATIONS AND ACRONYMS

I	Second moment of area
y_{max}	Maximum bending deflection
F	Crushing load
M_{max}	Maximum bending moment
L	Length of a beam or rib wall of a cellular structure
t	Thickness of the cell wall
τ_{xy}	Shear stress
V	Transverse shear force
A	Cross-sectional area
σ_x	Direct stress
δ	Direct deformation
L_E	Effective length
P_{cr}	Critical buckling load
σ_c	Crucial buckling stress
D	Flexural stiffness
ν	Poisson's ratio
h	Thickness of the unit cell
R	Radii of curvature of the loaded thin plate
w	Out-of-plane deflection of the loaded thin plate
τ_Y	Failure shear stress
ρ^*	Density of the polygon hollow structure
ρ_s	Density of the solid material of the polygon cell wall
E^*	Elastic modulus of the polygon hollow structure
E_s	Elastic modulus of the solid material of the polygon walls
$d\delta$	Crushing displacement
M	Overall mass of the structural part
θ	Angle between two connected walls
ϵ	Direct strains
A	Yield stress
B	Strain hardening factor
C	Dimensionless strain rate hardening coefficient
n	Strain hardening exponent
m	Thermal softening exponent
a	Base hexagonal edge length
$b \& c$	Edge lengths of the substructures
γ	Function of the ratio b or c and a
σ_v	Von Mises stresses

p	Penalization parameter used to allocate penalty scores for element densities
AFM	Atomic Force Microscopy
AI	Artificial Intelligence
AM	Additive Manufacturing
AMHH	Anisotropic Multifunctional Hierarchical Honeycomb
BC	Boundary Condition
CAD	Computer-Aided Design
CFD	Computational Fluid Dynamics
CFE	Crushing Force Efficiency
CRPM	Centre for Rapid Prototyping and Manufacturing
CT	Computed Tomography
DLP	Digital Light Processing
DMLS	Direct Metal Laser Sintering
EA	Energy Absorbed
ELI	Extra-Low Interstitial
EM	Electron Microscopy
EV	Electric Vehicle
FBR	Fly-by-Weight Ratio
FDM	Fused Deposition Modelling
FE	Finite Element
FEA	Finite Element Analysis
GHz	Giga-Hertz
GPa	Giga-Pascal
GPU	Graphics Processing Unit
HC	Honeycomb
HCC	Hierarchical Honeycomb with Circular Substructures
HCH	Hierarchical Honeycomb with Hexagonal Substructures
HCR	Regular Honeycomb
HCT	Hierarchical Honeycomb with Triangular Substructures
HPC	High-Performance Computing
HVAC	Heating, Ventilation, and Air Conditioning
ISO	International Organization for Standardization
KN	Kilo-Newton
LPBF	Laser Powder Bed Fusion
MCF	Average Crushing Force
MFCS	Multiple Cellular Tubed Structure with Customized Face-Centered Cubic Cross-sections
MJ	Mega-Joules
MN	Mega-Newton
MPa	Mega-Pascal
MRI	Magnetic Resonance Imaging
MTS	Metre-Tonne-Second

OAH	Basic Anisotropic Honeycomb
PCF	Peak Crushing Force
PGM	Platinum Group Metals
PLA	Poly lactides
PMMA	Polymethyl Methacrylate
PVA	Polyvinyl Alcohol
RCW	Re-entrant Combined-Wall
RE	Standard Re-entrant
SEA	Specific Energy Absorption
SEM	Scanning Electron Microscopy
SIMP	Solid Isotropic Material with Penalization
SLM	Selective Laser Melting
SLS	Selective Laser Sintering
SMA	Shape Memory Alloy
SO	Shape Optimization
TEM	Transmission Electron Microscopy
TO	Topology Optimization
TPMS	Triply Periodic Minimal Surface
UAV	Unmanned Aerial Vehicles
3D	Three-Dimensional
2D	Two-Dimensional

LIST OF PUBLICATIONS

Peer-Reviewed Journal Articles

1. **Chibinyani, M. I.,** Dzogbewu, T. C., Maringa, M., & Muiruri, A. M. (2022). Reduced order topology optimization of a planar honeycomb defined by a linear elastic Ti6Al4V(ELI) material model. *South African Journal of Industrial Engineering*, 33(3), 299-317. doi.org/10.7166/33-3-2808
2. **Chibinyani, M. I.,** Dzogbewu, T. C., Maringa, M., & Muiruri, A. M. (2023). Numerical modelling of DMLS Ti6Al4V (ELI) polygon structures. *Results in Materials*, 20, 100456. doi.org/10.1016/j.rinma.2023.100456
3. **Chibinyani, M. I.,** Dzogbewu, T. C., Maringa, M., & Muiruri, A. M. (2024). Lattice structures built with different polygon hollow shapes: A review on their analytical modelling and engineering applications. *Applied Sciences*, 14(4), 1582. doi.org/10.3390/app14041582
4. **Chibinyani, M. I.,** Dzogbewu, T. C., Maringa, M., & Muiruri, A. M. (2024). Numerical modelling of Ti6Al4V(ELI) hierarchical honeycomb structures of order one at the vertices. *Results in Engineering*, 21, 102024. doi.org/10.1016/j.rineng.2024.102024
5. **Chibinyani, M. I.,** Dzogbewu, T. C., Maringa, M., & Muiruri, A. M., Natural cellular structures in engineering designs built via additive manufacturing. *Materials Technology: Advanced Performance Materials* (Submitted).
6. **Chibinyani, M. I.,** Dzogbewu, T. C., Maringa, M., & Muiruri, A. M., Deformation behaviour, limitations in design, applications, and additive manufacturing of hierarchical honeycombs. *Manufacturing Review* (Submitted).

Peer-Reviewed Conference Proceeding Articles

1. **Chibinyani, M.,** Dzogbewu, T. C., Maringa, M., & Muiruri, A. M. (2023). A review of the types and tessellation of lattice structures, their effectiveness and limitations in mimicking natural cellular structures. In *MATEC Web of Conferences*, 388, 06008). EDP Sciences. doi.org/10.1051/mateconf/202338806008

Abstracts Read at Conferences

1. **Chibinyani, M. I.,** Dzogbewu, T. C., Maringa, M., & Muiruri, A. M., Natural cellular structures in engineering designs built via additive manufacturing. 2023, *Sustainable Research & Innovation Conference*, Nairobi, Kenya.
2. **Chibinyani, M. I.,** Dzogbewu, T. C., Maringa, M., & Muiruri, A. M., Deformation behaviour, limitations in design, applications, and additive manufacturing of hierarchical honeycombs. 2024, *AfriComp 6 Conference*, Cape Town, South Africa.

Book Chapters

1. Chibinyani, M. I., Dzogbewu, T. C., Maringa, M., & Muiruri, A. M. (2024). Numerical Modelling of DMLS Ti6Al4V(ELI) Polygon Structures. *Chemical and Materials Sciences - Developments and Innovations*(4), 1-53. doi.org/10.9734/bpi/cmsdil/v4/8584E

ABSTRACT

The fast growth of additive manufacturing (AM) has aided the design and manufacturing process of complex structures with customized mechanical properties for use in various engineering sectors. Design for additive manufacturing (DfAM) is a top priority research topic, particularly for lattice-structured shapes such as honeycombs (HCs). Adding hierarchical structures can enhance the mechanical properties of HCs but complicate the design, needing advanced AM technologies for production. In this study, optimal Ti6Al4V(ELI) hierarchical honeycomb (HC) lattice designs were numerically modelled, numerically crushed, and additively manufactured and were then investigated with regard to their mechanical properties for each method. At the onset of the study, a stress-strain curve was developed to better represent cellular and lattice design deformation mechanisms and analytical models were also developed to characterize natural cellular structures and lattice design behaviour.

The study reviewed open-access literature on analytical models for polygon-based lattice structures, grading them based on mechanical properties such as strength, stiffness, and deformation. Four polygonal hollow cells were graded in decreasing transverse stiffness order: circular, hexagonal, triangular, and square. These cells were configured into Ti6Al4V(ELI) lattice designs and numerically modelled in compression scenarios for planar in-plane uniaxial loading in the ABAQUS package. The hexagonal polygon was subjected to out-of-plane and in-plane uniaxial compression loads to compare the bending and buckling behaviour of finite element (FE) models to analytical models. The triangular polygon had the greatest load-bearing capacity and stiffness of all polygons modelled. The hexagonal model generated deformations due to compression, similar to those reported in literature. The critical buckling loads for analytical HC models were found to be below the yield stress for (1-, 1.125-, and 1.25-mm wall thicknesses) and above the yield stress for all FE HC models. The effective stiffness of HC models increased with increasing (t/L) ratio.

Ti6Al4V(ELI) hierarchical HC models with hexagonal, circular, and triangular polygons at their vertices were also analyzed in this work through ABAQUS software. The models were compared to regular HC models for out-of-plane loads in uniaxial compression tests. The hierarchical HC model with hexagonal substructures ranked higher in terms of load-bearing capacity and stiffness for loads applied in the in-plane x -direction. For loading in the in-plane y -direction, the model with circular substructures ranked highest. The highest load-bearing capacity and stiffness were observed for in-plane loading in the x -direction. Deflections were smaller for loading in the two in-plane directions than in the out-of-plane direction. In-plane loading at the vertices led to high stress concentrations at the loading points. Loading the models directly at the apex regions led to the highest stress and deflection magnitudes. Hierarchical HCs with lower sharp geometric changes minimized stress concentrations.

Quasi-static numerically crushed hierarchical HCs were investigated regarding the impact of their topologies on deformation response modes and energy absorption characteristics in ABAQUS. The findings showed that bending deformation dominated under x -directional load while bending and buckling loads influenced deformation response modes under y -directional load. The material at the vertices of these structures failed first for both loading directions. The buckling of the vertically positioned cell walls caused instability under the y -directional load, causing the structure to rotate along the z -axis instead of being crushed along the y -axis. Some deformed cells showed the Poisson's ratio phenomenon, and the load-displacement curve for loading the regular HC in the x -axis showed a low oscillatory response.

The study also presented an alternative method for generating effective iterations at the vertices and edges in planar HCs of Ti6Al4V(ELI) through the Altair-Optistruct modelling package. Mesh convergence tests were conducted on planar unit hexagonal cells, followed by topology and shape optimization and numerical analysis. The findings were compared with the numerical analysis before topology optimization. Acceptable predictions were obtained for the planar numerical models, with

material reductions of 30% and 8% for the planar unit hexagon cell and HC model, respectively. The maximum stresses in these numerical models after shape optimization were reduced by 58% and 4%, respectively.

Previous works have investigated HC structures, but the hierarchical design presented here offers significant improvements in load-bearing capacity and energy-absorption, as demonstrated through quasi-static crushing tests. Vertex-based hierarchical HCs were created and tested for surface quality and crushing behaviour in quasi-static scenarios. At the onset, zero-, first-, and second-order hierarchical Ti6Al4V(ELI) HCs were designed and produced using direct metal laser sintering (DMLS) technology. These Ti6Al4V(ELI) specimens were then quasi-statically crushed with an MTS CriterionTM, Model 43 universal testing machine to assess the mechanical behaviour regarding the HC topologies with various levels of hierarchy. The experimental results were compared with finite element predictions from ABAQUS, showing strong correlation in the mechanisms of deformation, stress distribution, and modes of failure, thereby validating the numerical models. This validation confirmed the accuracy of the topology and shape optimisation numerical models used thus, ensuring that the optimised designs are both mechanically robust and manufacturable. Surface roughness in hierarchical HCs increased with the hierarchy level of the structure. Hierarchical HCs exhibited primary deformation through beam bending, with pronounced buckling under y -direction loading. Post-peak load drops, observed in an oscillatory manner, were attributed to vertex fractures following initial bending or buckling deformation. The collapse under compressive loads followed a progression from bending and/or buckling to Poisson's ratio-driven lateral expansion, concluding with sliding along inclined and horizontal lines for x - and y -direction loading, respectively. Crushing occurred sequentially, beginning with the lowest hierarchy order and progressing upwards. Zero-order HCs demonstrated the lowest failure loads, with first-order HCs showing an increase and second-order HCs exhibiting the highest failure loads. The mechanical performance of the hierarchical honeycomb (HC) structures was assessed through quasi-static compression testing along multiple orientations. Zero-, first-, and second-order hierarchical HCs exhibited progressively increasing peak failure loads, indicating enhanced load-bearing capacity with the introduction of multiscale geometry. Specifically, zero-order HCs showed an average peak failure load of approximately **19.75 kN** and **21.25 kN** for x - and y -direction, respectively. While first-order HCs reached **23.25 kN** and **25.25 kN** for x - and y -direction, respectively. Second-order HCs reached **25.50 kN** and **27.50 kN** for x - and y -direction, respectively. These values were derived from load-displacement curves obtained in both the x - and y -directions. The improvement in failure loads with increasing hierarchy highlighted the mechanical benefits of hierarchical structuring, particularly the role of vertex-based geometry in distributing stress and delaying collapse-mechanisms. As the level of hierarchy increased, the variation in failure loads between the x and y loading directions decreased. This reduction made it difficult to rank the first- and second-order hierarchical HCs based on their response to loads applied along these two different loading directions. However, the overall trend observed in this work, confirmed that higher-order hierarchical designs contributed positively to structural integrity. Notable differences in load peaks were observed in zero-order specimens, particularly between x_1 and x_2 , with the latter showing lower peaks, likely due to failure along an inclined line, possibly caused by flaws or poor sintering at cell wall separation points. This study introduces novel mechanisms of deformation in hierarchical HC designs and provides critical insights into their mechanical behaviour under various loading conditions. These findings reveal how hierarchical structuring not only improves peak failure loads but also introduces controlled, progressive collapse mechanisms that enhance energy dissipation and structural resilience under multi-directional loading. Therefore, the optimised hierarchical HCs are anticipated to enhance the performance of structural components across the biomedical, automotive, and aerospace industries by significantly improving their load-bearing capacity, and strength-to-weight ratio.

CHAPTER ONE: INTRODUCTION

1.1. Summary

In this chapter, research work on cellular materials, providing a clear association between naturally and synthetically built cellular structures, is presented systematically. This is achieved by first introducing material on organic cellular parts, then lattice parts, and lastly, the primary focus of this research project, which is hierarchical lattice parts. Throughout the chapter, the manner in which organic cellular structures mimic natural structures is underscored. In addition, modelling techniques and manufacturing technologies utilized to enhance the mechanical properties of hierarchical lattice systems are also examined.

1.2. Cellular structures

Biomimicry of cellular structures is a perpetually evolving concept in the fields of science and technology. Such structures are built through an interconnected network of porous structures with solid struts that form ribs or cell walls [1]. There is a broader group of biological tissues that comprise cellular designs, including bone, wood, and glass sponge skeletons. These tissues are predominantly found in animals, plants, and the water kingdom and are often grouped into open, closed, and honeycomb (HC) cellular designs [2]. Open cellular designs are built using solid edges comprising voids in between, shown in Figure 1-1(a) [3]. Conversely, closed cellular designs are replicas of open cellular designs with added solid faces that render the cells enclosed, as illustrated in Figure 1-1(b) [3]. For the past three decades, significant research has been directed at cellular designs. This is because of their broad applicability in engineering, in addition to outstanding mechanical characteristics of stiffness, fracture toughness, strength, and low density that promise good load-bearing capacities with low weights [4-5].

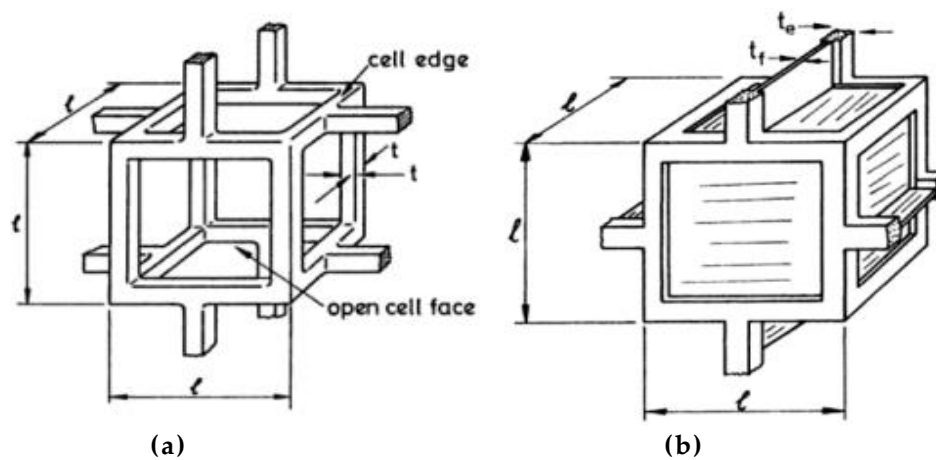


Figure 1-1. (a) Open cell structures; (b) closed cell structures [3]

Honeycomb cellular designs are described for both two-dimensional (2D or planar) and three-dimensional (3D) geometries [6]. Cellular designs also occur as foams, a group of cellular designs built from polyhedral cells. Polyhedral cells are packed to fill a space, and these cells are differentiated by interconnected pathways of controlled hollow-like or enclosed cell structures. Additionally, polyhedral cells exhibit perforated holes with anisotropic cell walls in nature [1]. Numerous studies [1-9] have shown HC designs to be accepted as the most efficient in terms of load-bearing capacity. This is because HC designs

absorb high-strain energies while maintaining acceptable flexural stiffness when high-stress loads are applied to them. The 3D HC configuration results from packing polygon cells in a continuous pattern, that fills a plane without gaps or overlapping at the walls. A good example of a HC design that normally occurs in nature, is the beehive, whose approximate design is that of hexagonal cells, illustrated in Figure 1-2 [2-3]. The HC configuration could, however, be applied to all designs that have a prismatic property, including structures with circular, rectangular, triangular another types of polygon cells [1, 10].



Figure 1-2. The beehive prismatic configuration of an HC design [2]

1.3. Lattice structures

Mimicking the physical characteristics of organic cellular designs gives rise to synthetic structures with good mechanical properties [2, 4-5], which are generally referred to as lattice structures. Lattice structures are porous, topologically arranged materials of one or more periodic cells. These periodic cells are defined by the dimensions and the connectivity of their rigidly joined struts [2, 11-12]. Lattice structures have gained broad interest due to their use to develop lightweight structures with good mechanical properties. Their mechanical properties, such as stiffness, energy absorption, fracture toughness, strength, thermal insulation, and more, are a marvel that researchers continue to explore for use in biomedical, aerospace, automotive, defence and infrastructural applications [2, 4] [5, 11-12].

In biomedical and engineering fields, two groups of polygon lattice designs are often used for structural applications. The HC design is just one example of prismatic structures, and the dodecahedral platonic solid design is also just one instance of polyhedral structures that are commonly adopted [2, 13]. The dodecahedral structure is formed when platonic solids are made of twelve regular pentagon faces that are all congruent and have vertices meeting the same number of edges as every other vertex and are packed together to fill a domain [3].

A good number of studies [1-2, 4-6, 8-9, 11-14] have successfully demonstrated that the mechanical properties of lattice designs are heightened through analysis and optimization of their geometrical parameters, including the shape of cells (size and internal matrices), aspect ratio of struts, connectivity of cell edges, relative density of the whole structure, and rates of loading.

1.3.1 Hierarchical lattice structures

Lattice structures mimic good mechanical properties observed in natural designs by drawing inspiration from cellular structures, which are hierarchically structured [2, 15]. Nature has succeeded in hierarchical structuring at macro, micro, and nano scales with ease. This is due to a dynamic process of growth present in growing organisms. The phenomenon has inspired mimicking of cellular designs in nature, using synthetic materials to build novel structures in automotive, aerospace, defence, biomedical, and infrastructural industries [2, 15-19]. This process is termed biomimicry, which involves the emulation of natural cellular designs to develop bioinspired lattice structures with similar macroscopic geometries, illustrated in Figure 1-3 [5]. However, most experimental studies [1-2, 4-5, 11-13] mimic macroscopic geometry but do not consider their micro and nanoscale complexities.

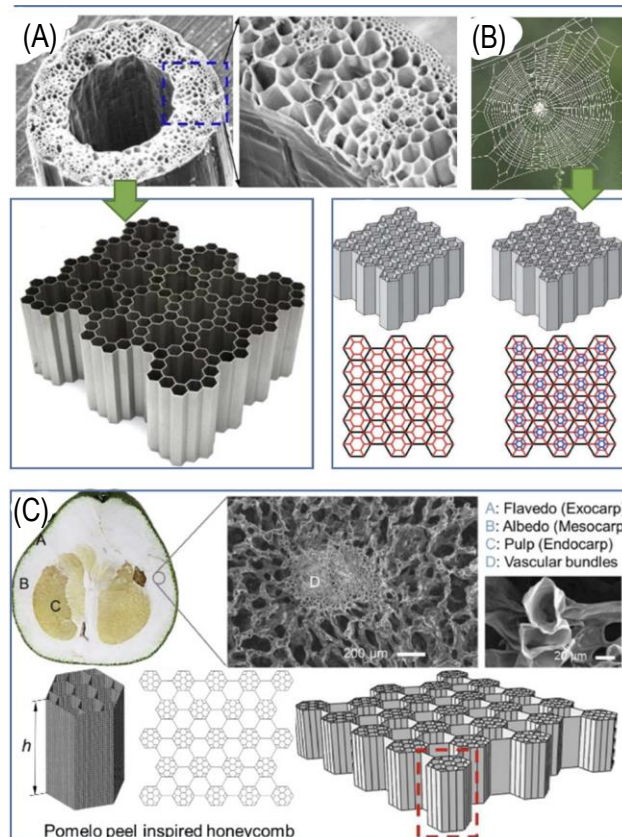


Figure 1-3. Bioinspired hierarchical HC designs for energy absorption applications [5]

Advanced technologies such as AM have been used effectively to fabricate parts at the macro and micro scales but suffer a shortcoming in mimicking cellular designs at nanoscale [2, 5, 9, 12]. Though fabricated cellular structures have achieved various continuous size levels of hierarchy, only a limited number of levels of hierarchy can be achieved, depending on the cell topology (connectivity) and geometries (sizes of cells and dimensions). At present, the achievable hierarchical levels include the zero-order, a continuous solid; first-order of hierarchy, whereby substructuring is introduced on a regular cellular structure; and the second order of hierarchy [1-2, 15, 20]. Lattice structures are extended to hierarchical lattice structures by mimicking the macroscopic geometry of structures. This,

however, disregards the microscopic complexities of the structures. Numerous studies [1-2, 4-5, 11-12, 20-22] have illustrated extensive use of cellular designs, particularly hierarchical HCs in aerospace and automotive industries. This research project focuses on HC designs with hierarchical structuring at the vertices.

1.4. Topology optimization

Topology optimization (TO) is described as a material model solution through which the optimal connectivity of structural members can be determined, in chorus, with the removal of ineffective elements and resizing the cross-section for optimal designs [23], [24]. In the case of natural cellular designs, the optimization strategy is more successive and is controlled by evolutionary mechanisms as opposed to the synthetic process of removing ineffective elements. Successive optimization is carried out strategically through modelling and re-modelling the structure, all together achieving smooth geometries at termination points. The specific structural optimization depends on the application of a specific cellular design [1]. Similarly, cutting-edge technologies which rely on TO software algorithms have become the face of innovation for improving hierarchical lattice designs [24]. Through optimization of regular lattice designs, extending the process to hierarchical designs by introducing substructures that develop new connectivity, cell size and shape, and dimensions has become easier. Furthermore, the TO strategy reduces redundant fabrication material and geometrical imperfections when producing lightweight lattice designs with enhanced mechanical properties [25].

Validation techniques such as analytical and numerical modelling are interposed with TO strategies, whereby discretisation of the optimal lattice designs occurs in the latter one of the first two processes [26]. Mathematical models whose analytical solutions are time-consuming and tedious are often built into available commercial numerical modelling packages to speed up computation by reducing complexities in simulations [2]. The development of adequate and accurately calibrated numerical models for validating findings against pre-existing data and analytical and experimental results aid this process [27].

1.5. Shape optimization

A shape optimization (SO) strategy is often used in conjunction with TO on designs such as cellular parts. Though TO is good for lightweighting, it does result in a decrease in the stiffness of structures [28-30]. This is because the boundaries of the shapes that are obtained after TO are typically rough and have sharp changes in geometry [31]. SO allows a structure's shape to be further optimized after TO by controlling the boundaries of its geometry [29, 31]. These changes of shape are applied to a structure's boundary to reduce stresses in high-stress areas. In chorus with the implementation of SO, an automated numerical analysis is conducted to confirm the changes in stress and strain after the structure is optimized [31]. When generating iterations for topologies, combined TO and SO can be more effective in structural optimization as they contribute to lightweighting and improved stiffness of cellular parts at the same time [31], [32].

1.6. Additive manufacturing

Conventional manufacturing techniques, such as casting, milling, and forging, are tedious, time-consuming, and challenging in fabricating periodic lattice structures with complex geometrical configurations and are typically used to produce a limited number of geometries [2, 4, 11]. On the contrary, AM technologies for fabricating lattice structures are ideal for complex geometries and higher orders of hierarchy [11, 22]. A common AM

fabrication method for metals and metal alloys known as direct metal laser sintering (DMLS) or selective laser melting (SLM), a subset of laser powder bed fusion (LPBF), is often used to fabricate lattice structures with intricate shapes [33]. The DMLS method is a layer-wise manufacturing technique [34].

The advancement of AM technologies also depends on the availability of suitable materials. Considerable research on the production of parts by way of DMLS or SLM has been carried out on the Ti6Al4V alloy [11, 33-34]. The Ti6Al4V material is an alpha-beta-type alloy with four basic microstructures. These include the lamellar, equiaxed, martensite and bimodal microstructures. The microstructures of the Ti6Al4V alloy can be changed from one phase to the other depending on composition, thermomechanical and heat-treatment processes used to achieve preferred mechanical properties. The Ti6Al4V material's adaptability to mechanical stress, advanced manufacturing methods, dynamic and corrosive environments, and high-temperature applications renders it beneficial for broader applications in engineering and biomedical industries [35]. Some of the keyways Ti6Al4V is adaptable include its biocompatibility, good mechanical characteristics, corrosion resistance, customization with AM, heat treatability, and resistance to fatigue. Mechanical applications that require physically lightweighted hierarchical lattice designs include load-bearing implants and prostheses, parts and prototypes for the automotive and aerospace industry, marine components and structures, gas turbines, firearm silencers and more. These structures prioritize the good mechanical properties of the alloy, which include stiffness, energy absorption, strength, fracture toughness and corrosion resilience [35-36].

1.7. Problem statement

Lattice designs are widely used for lightweight load-bearing structures with minimal material usage in engineering and biomedical applications. Currently, their geometries impose limitations on the order of hierarchy that can be introduced at the joints of these structures. The geometries of lattice designs are characterized by sharp angles at the intersections of the cell walls and ribs, also referred to as joints. These sharp geometrical angles subject the vertices to high-stress concentrations during loading.

Moreover, lattice structures are known to be compliant and weak in the out-of-plane direction. The highest deformations of these structures are expected to occur away from the joints of the ribs because of bending and/or combined loading. Therefore, the highest bending and/or direct stresses due to out-of-plane and in-plane loads will occur on the outer surfaces of ribs and at the joints of these structures, respectively. The increase of direct compressive loads beyond a critical value leads to buckling and collapse of ribs away from the vertices. The challenge in the design of lattice designs is thus to determine, for different cell geometries, the limiting loads with respect to stress concentrations and deflections.

The topologies of cells and the size of lattice cells and ribs limit the order of hierarchy that can be introduced at the vertices. Neglecting the first constraint leads to disjointed connectivity of the ribs at the vertices and imperfect tessellation. Such lattice designs will thus have even more points of stress concentration at which failure may initiate. This calls for careful selection of the topology cells and dimensioning of the cells. The increasing complexity and size of lattice structures demand the use of TO software to optimize the dimensions and shape of their members. Furthermore, the computational requirements to determine the magnitude and distribution of stresses and deformations for a multiplicity of load types become indomitable and require the use of numerical modelling software.

1.8. Motivation of the research

Hierarchical HCs, defined by nested geometries across multiple length scales, would be expected to exhibit superior mechanical behaviour compared to monolithic or single-scale cellular architectures. Their distinct advantages, such as high specific strength, enhanced energy dissipation, and tailorable stiffness, make them highly attractive for advanced engineering applications where weight-constraints and mechanical robustness must be balanced. Leveraging AM, particularly DMLS, enables the realisation of these complex multiscale geometries with a high degree of precision and functional customisation. This investigation focuses on understanding how geometric hierarchy, enabled by AM, influences the mechanical behaviour of HCs, particularly in terms of strength-optimisation, energy-absorption, and weight-efficiency. Such insights are critical for engineering systems operating under extreme loading conditions, including those in biomedical, aerospace, and automotive contexts. In biomedical applications, hierarchical HCs present a promising pathway for developing bone scaffolds and adaptive implants that require both structural integrity and biomechanical compatibility. In aerospace and automotive sectors, their integration can lead to next-generation lightweight panels and energy-absorbing components, contributing to improved performance and safety without sacrificing structural resilience. Recent progress in AM has removed previous constraints on design and fabrication, making it possible to explore new frontiers in material-structure-process-integration. By systematically analysing the mechanisms of deformation, modes of failure, and topological influences on performance, this study contributes to the formulation of design principles that link bioinspired concepts with practical implementations in multifunctional, lightweight, and load-bearing systems.

1.9. Research aim

The aim of the present study is to develop an optimal hierarchical HC lattice design with the highest possible order of hierarchy.

1.10. Research objectives

- To study different polygon types for lattice designs and grade them in terms of efficiency with reference to the mechanical properties of strength, stiffness, toughness, and deformation.
- To determine amongst several shapes the ones with the most efficient joint hierarchy.
- To investigate the limiting order of hierarchy that can be introduced at the joints and clearly identify the parameters that cause these limitations.
- To develop, using topology- and shape-optimization software, optimal design lattice cell shapes and sizes of selected lattice structures.
- To carry out FE analysis of the topologically optimized, identified most efficient lattice designs using available commercial numerical modelling packages.
- To validate the results of numerical modelling using DMLS Ti6Al4V(ELI) hierarchical HC structures based on their mechanical properties of strength, stiffness, toughness, and deformation.
- To identify the mechanisms of failure predominant in the modelled hierarchical HC designs.

1.11. Dissertation outline

The flow of the study presented in this dissertation is illustrated in Figure 1-4.

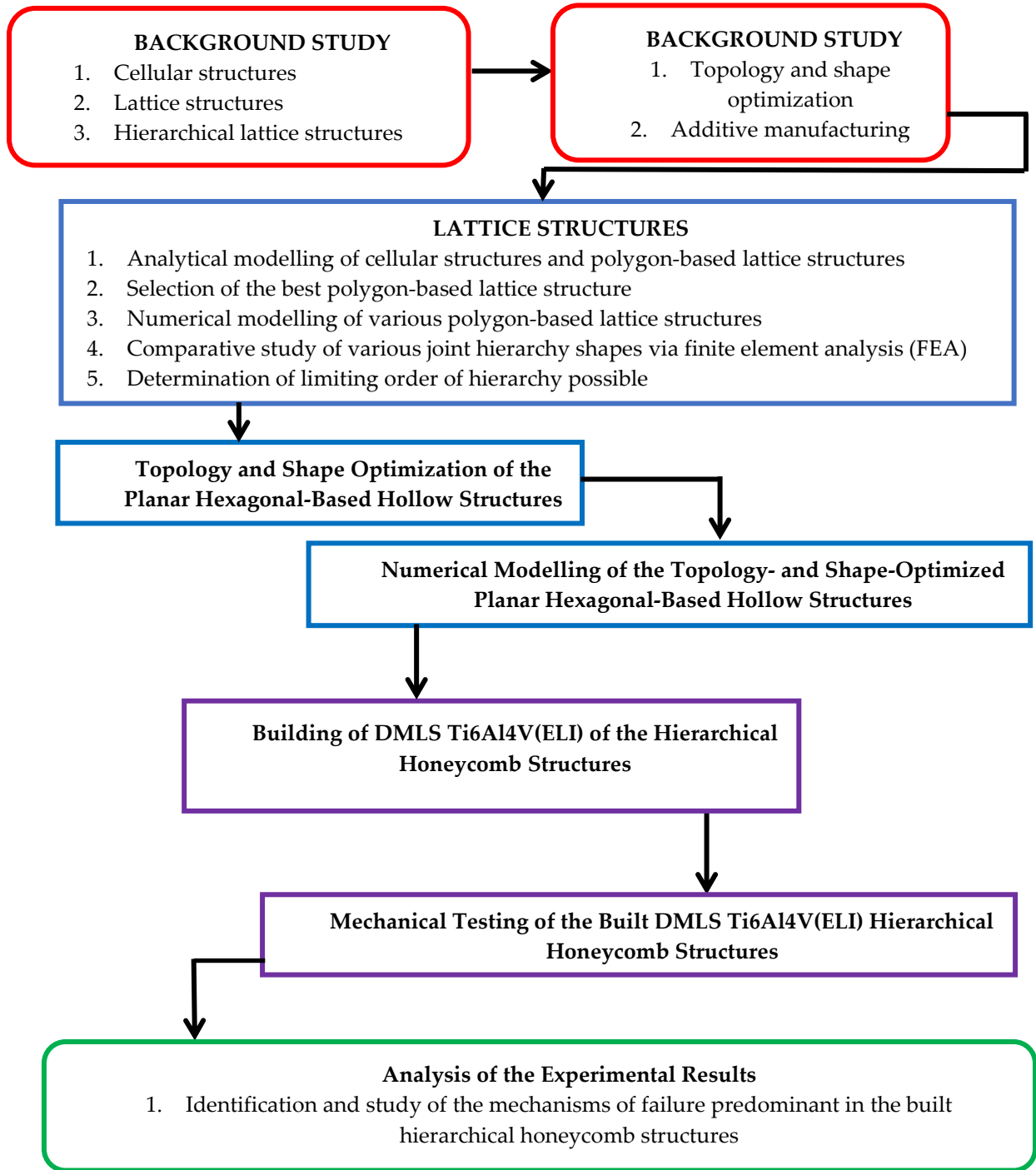


Figure 1-4. Research flow diagram

1.12. Benefits of this research

The outcomes of this study are expected to provide researchers in manufacturing industries with readily available solutions of optimized Ti6Al4V(ELI) hierarchical lattice designs with the most efficient load-bearing capacity and minimal usage of material. The low usage of material compared to the case for solid structures is expected to reduce the cost of manufacturing and, by this, release funds for investment elsewhere. Additionally,

the study specifies limits of the orders of hierarchies that can be achieved for hierarchical lattice designs and, with this, the limiting efficiency of the lattices in carrying the imposed load.

1.13. Delimitations of the study

The research will only focus on topology and shape optimization of a planar unit hexagonal cell and HC structure. The topology and shape optimizations will be limited to the edges and vertices of the ribs of a planar unit hexagonal cell and HC structure, as well as the determination of the maximum possible order of hierarchy for the lattice structures.

1.14. Summary

Hierarchical HC designs have gained traction in most mechanical applications in the aerospace and automotive industries. Many of the industries in these two sectors use ultra-lightweight hierarchical lattice designs with good mechanical properties. The challenge presently is how the hierarchical order in lattice designs can be extended and to what degree this can be done.

References

1. Alqassim, G. (2011). *Mechanical properties of hierarchical honeycomb structures*. Master's thesis, Northeastern University.
2. Zhang, Q., Yang, X., Li, P., Huang, G., Feng, S., Shen, C., ... & Lu, T. J. (2015). Bioinspired engineering of honeycomb structure—Using nature to inspire human innovation. *Progress in Materials Science*, 74, 332-400.
3. Ashby, M. F., and Gibson, L. J. (1997). Cellular solids: structure and properties. *Press Syndicate of the University of Cambridge, Cambridge, UK*, 175-231.
4. Wang, P., Yang, F., Zheng, B., Li, P., Wang, R., Li, Y., ... & Li, X. (2023). Breaking the tradeoffs between different mechanical properties in bioinspired hierarchical lattice metamaterials. *Advanced Functional Materials*, 2305978.
5. San Ha, N., and Lu, G. (2020). A review of recent research on bio-inspired structures and materials for energy absorption applications. *Composites Part B: Engineering*, 181, 107496.
6. Sun, Y., and Pugno, N. M. (2013). In-plane stiffness of multifunctional hierarchical honeycombs with negative Poisson's ratio sub-structures. *Composite Structures*, 106, 681-689.
7. Li, J., Wang, H., Kong, X., Jiao, Z., & Yang, W. (2024). Additively manufactured bionic corrugated lightweight honeycomb structures with controlled deformation load-bearing properties. *Materials*, 17(10), 2274.
8. Zou, Q., Zhou, X., Wang, R., Ning, Y., Chen, Z., Kong, F., & Liu, Y. (2022). Load-carrying and energy-absorbing performance of honeycombs with different cross sections under cyclic loading. *Materials Today Communications*, 33, 104582.
9. Chen, Q., Pugno, N., Zhao, K., & Li, Z. (2014). Mechanical properties of a hollow-cylindrical-joint honeycomb. *Composite Structures*, 109, 68-74.
10. Lakes, R. (1993). Materials with structural hierarchy. *Nature*, 361(6412), 511-515.
11. Kladovasilakis, N., Tsongas, K., Karalekas, D., & Tzetzis, D. (2022). Architected materials for additive manufacturing: A comprehensive review. *Materials*, 15(17), 5919.
12. Whenish, R., Arivazhagan, S., Velu, R., & Kumar, S. A. (2023). Bio-inspired advancements in additive manufacturing. In *Advances in Additive Manufacturing*, 313-324. Elsevier.
13. Azman, A. H. (2017). *Method for integration of lattice structures in design for additive manufacturing*. Doctoral dissertation, Université Grenoble Alpes.
14. Forés-Garriga, A., Gómez-Gras, G., & Pérez, M. A. (2023). Additively manufactured three-dimensional lightweight cellular solids: Experimental and numerical analysis. *Materials & Design*, 226, 111641.

15. Qiao, J., and Chen, C. (2016). In-plane crushing of a hierarchical honeycomb. *International Journal of Solids and Structures*, 85, 57-66.
16. Wu, Z., Xia, L., Wang, S., & Shi, T. (2019). Topology optimization of hierarchical lattice structures with substructuring. *Computer Methods in Applied Mechanics and Engineering*, 345, 602-617.
17. Sun, F., Lai, C., Fan, H., & Fang, D. (2016). Crushing mechanism of hierarchical lattice structure. *Mechanics of Materials*, 97, 164-183.
18. Sun, F., Lai, C., & Fan, H. (2016). In-plane compression behavior and energy absorption of hierarchical triangular lattice structures. *Materials & Design*, 100, 280-290.
19. Liu, R., Yao, G., Gao, K., Xu, Z., Yang, Y., Guo, X., ... & Han, C. (2023). Study on mechanical properties of lattice structures strengthened by synergistic hierarchical arrangement. *Composite Structures*, 304, 116304.
20. Ajdari, A., Jahromi, B. H., Papadopoulos, J., Nayeb-Hashemi, H., & Vaziri, A. (2012). Hierarchical honeycombs with tailorable properties. *International Journal of Solids and Structures*, 49(11-12), 1413-1419.
21. Kumar, S., Ubaid, J., Abishera, R., Schiffer, A., & Deshpande, V. S. (2019). Tunable energy absorption characteristics of architected honeycombs enabled via additive manufacturing. *ACS Applied Materials & Interfaces*, 11(45), 42549-42560.
22. Qi, C., Jiang, F., & Yang, S. (2021). Advanced honeycomb designs for improving mechanical properties: A review. *Composites Part B: Engineering*, 227, 109393.
23. Perez, C. H. V. (2016). *Topology Optimization Using the Level Set and Extended Finite Element Methods: Theory and Applications*. Doctoral dissertation, University of Colorado at Boulder.
24. Wu, Z., and Xiao, R. (2022). A topology optimization approach to structure design with self-supporting constraints in additive manufacturing. *Journal of Computational Design and Engineering*, 9(2), 364-379.
25. Chuang, W. A. N. G., Jihong, Z. H. U., Manqiao, W. U., Jie, H. O. U., Han, Z. H. O. U., Lu, M. E. N. G., ... & Zhang, W. (2021). Multi-scale design and optimization for solid-lattice hybrid structures and their application to aerospace vehicle components. *Chinese Journal of Aeronautics*, 34(5), 386-398.
26. Ali, M. A., and Shimoda, M. (2022). Toward multiphysics multiscale concurrent topology optimization for lightweight structures with high heat conductivity and high stiffness using MATLAB. *Structural and Multidisciplinary Optimization*, 65(7), 207.
27. Hussain, S., Nazir, A., Waqar, S., Ali, U., & Gokcekaya, O. (2023). Effect of additively manufactured hybrid and functionally graded novel designed cellular lattice structures on mechanical and failure properties. *The International Journal of Advanced Manufacturing Technology*, 128(11-12), 4873-4891.
28. Munk, D. J., Vio, G. A., & Steven, G. P. (2015). Topology and shape optimization methods using evolutionary algorithms: a review. *Structural and Multidisciplinary Optimization*, 52, 613-631.
29. Plocher, J., and Panesar, A. (2019). Review on design and structural optimisation in additive manufacturing: Towards next-generation lightweight structures. *Materials & Design*, 183, 108164.
30. Tyflopoulos, E., and Steinert, M. (2022). A comparative study of the application of different commercial software for topology optimization. *Applied Sciences*, 12(2), 611.
31. Allaire, G., Dapogny, C., & Jouve, F. (2021). Shape and topology optimization. *Handbook of Numerical Analysis* (22) 1-132. Elsevier.
32. Chibinyani, M. I., Dzogbewu, T. C., Maringa, M., & Muiruri, A. M. (2022). Reduced order topology optimisation of a planar honeycomb defined by a linear elastic Ti6al4V (ELI) material model. *South African Journal of Industrial Engineering*, 33(3), 299-317.
33. Patterson, A. E., Messimer, S. L., & Farrington, P. A. (2017). Overhanging features and the SLM/DMLS residual stresses problem: Review and future research need. *Technologies*, 5(2), 15.
34. Ahmed, N. (2019). Direct metal fabrication in rapid prototyping: A review. *Journal of Manufacturing Processes*, 42, 167-191.

35. Tamayo, J. A., Riascos, M., Vargas, C. A., & Baena, L. M. (2021). Additive manufacturing of Ti6Al4V alloy via electron beam melting for the development of implants for the biomedical industry. *Heliyon*, 7(5).
36. Parthasarathy, J., Starly, B., & Raman, S. (2011). A design for the additive manufacture of functionally graded porous structures with tailored mechanical properties for biomedical applications. *Journal of Manufacturing Processes*, 13(2), 160-170.

CHAPTER TWO: LITERATURE REVIEW ON CELLULAR AND LATTICE STRUCTURES

Part of the contents of this chapter has been submitted for publication or has been published in peer-reviewed journals, as follows:

1. **Chibinyani, M.I.**, Dzogbewu, T. C., Maringa, M., & Muiruri, A. M. (2023). A review of the types and tessellation of lattice structures, their effectiveness and limitations in mimicking natural cellular structures. *MATEC Web of Conferences* 388, 06008. *EDP Sciences*. doi.org/10.1051/mateconf/202338806008
2. **Chibinyani, M. I.**, Dzogbewu, T. C., Maringa, M., & Muiruri, A. M. (2024). Lattice structures built with different polygon hollow shapes: A review on their analytical modelling and engineering applications. *Applied Sciences*, 14(4), 1582. doi.org/10.3390/app14041582
3. **Chibinyani, M. I.**, Dzogbewu, T. C., Maringa, M., & Muiruri, A. M. *Natural cellular structures in engineering designs built via additive manufacturing*, Submitted to *Materials Technology: Advanced Performance Materials*.
4. **Chibinyani, M. I.**, Dzogbewu, T. C., Maringa, M., & Muiruri, A. M. Deformation behaviour, limitations in design, applications, and additive manufacturing of hierarchical honeycombs, Submitted to *Manufacturing Review*

2.1. Summary

This chapter begins by evaluating various types of natural cellular structures, exploring their occurrence and physical characteristics. It then transitions to an examination of modern lattice structures, focusing on their tessellation patterns, area/volume coverage, and material usage. The applications of lattice structures are highlighted, along with an analysis of the mechanical properties of cellular, lattice, and hierarchical structures to identify the predominant deformation mechanisms. Analytical models describing the deformation behaviour of these structures are reviewed and further refined to enhance understanding. Additionally, the chapter investigates the effectiveness and limitations of lattice structures in replicating organic cellular structures, as well as the challenges of incorporating hierarchical configurations into lattice designs. The discussion concludes by outlining future directions for advancing lattice design in the context of AM.

2.2. Introduction

Cellular structures have garnered significant interest in the engineering and manufacturing fields because of their unique capability of combining lightweight design while maintaining good load-bearing capacity [1]. This property renders cellular structures useful for a wide range of engineering applications in the aerospace, automotive and biomedical industries [1, 2]. Cellular structures present in numerous examples of biological materials such as bone, wood, and glass sponge skeletons are hierarchically structured, which means they have configurations or arrangements at multiple scales, including macro, micro, and nano [3]. This hierarchical arrangement results in their good mechanical properties, lightweight designs, and overall effectiveness in their applications [3-5]. The strength, stiffness, and fracture toughness of cellular structures are the result of built networks of solid struts that form ribs and cell walls [1, 3, 5]. These cells may occur in open, closed, or polygon cell-based designs, which have a significant effect on the structure's overall mechanical behaviour [3].

Lattice structures and their hierarchical structures are bioinspired, as they are designed by mimicking cellular structures found in nature [6]. Unfortunately, due to constraints in capturing the exact intricacies of the natural structural design, lattice structures are incapable of entirely reproducing the complexities of naturally growing cellular structures [7]. Furthermore, modern manufacturing tools like AM have limitations in terms of the minimum printable size of parts and part resolution that AM machines can effectively

produce [8]. Further research is required to establish the effectiveness and limitations of lattice structures in mimicking natural cellular architecture.

Lattice structures are generated via tessellation. Based on how efficiently their material is arranged over a design space, these structures can have a high load-bearing capability [9]. The mechanical properties of such structures are determined by relating their configuration to the connecting edges and vertices of the unit cells. Lattice structures generated from different types of configurations do not have the same mechanical properties [10]. The lattice structures currently available in the literature include polygon-based, strut-based, skeletal and sheet triply periodic minimal surface (TPMS)-based structures [11]. Advanced manufacturing technologies such as AM are coupled with tessellation to fabricate lattice structures with good mechanical properties and low usage of material [12]. Presently, the different types of lattice structures with good load-bearing capacities have not been ranked clearly in terms of area/volume coverage and material usage [11, 13]. Volume coverage here refers to the total volume within which polygons are fitted, whereas material usage refers to the actual material of the polygon struts in the fitted space. Therefore, it is necessary to undertake studies to relate the mechanical properties of lattice structures to their greater area/volume coverage and usage of material. Additionally, hierarchical structuring is often adopted to improve the mechanical properties of lattice parts such as HCs [6, 12]. This approach calls for embedding smaller unit cell shapes into larger structures, resulting in a multiscale structure. There are, however, gaps in the literature regarding the highest order of hierarchy that is physically attainable for hierarchical HCs built, irrespective of the different polygons used that need attention. Addressing these gaps is crucial for advancing the design and application of lattice structures.

2.3. Cellular structures

2.3.1 Types of cellular structures in nature

Three types of cellular structures are often observed in the designs of organic materials: open, closed, and polygonal cellular structures. Figure 2-1 shows a schematic classifying the three types of cellular structures typically observed in biological tissues.

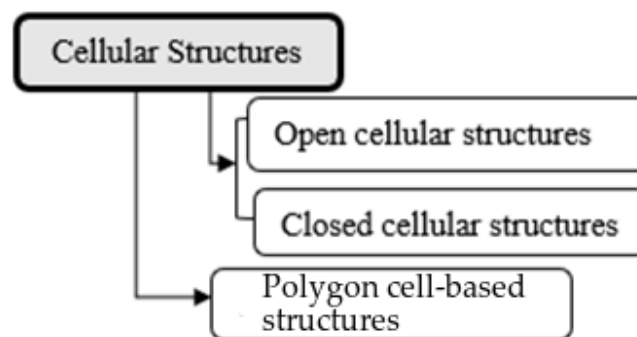


Figure 2-1. Different types of cellular designs in nature

Open cellular structures are built using solid edges with voids in between, whereas closed cellular structures have solid faces that enclose the cells. The third type of cellular structure comprises polygon cells arranged in both two- and three-dimensional geometric designs to fill a design space. Cellular structures, in nature, are characterized by coherent pathways of hollow-like or enclosed cell structures with perforated pores and anisotropic

cell walls. Figure 2-2 shows a few biological tissues with the aforementioned types of cellular structures [4, 14-15].

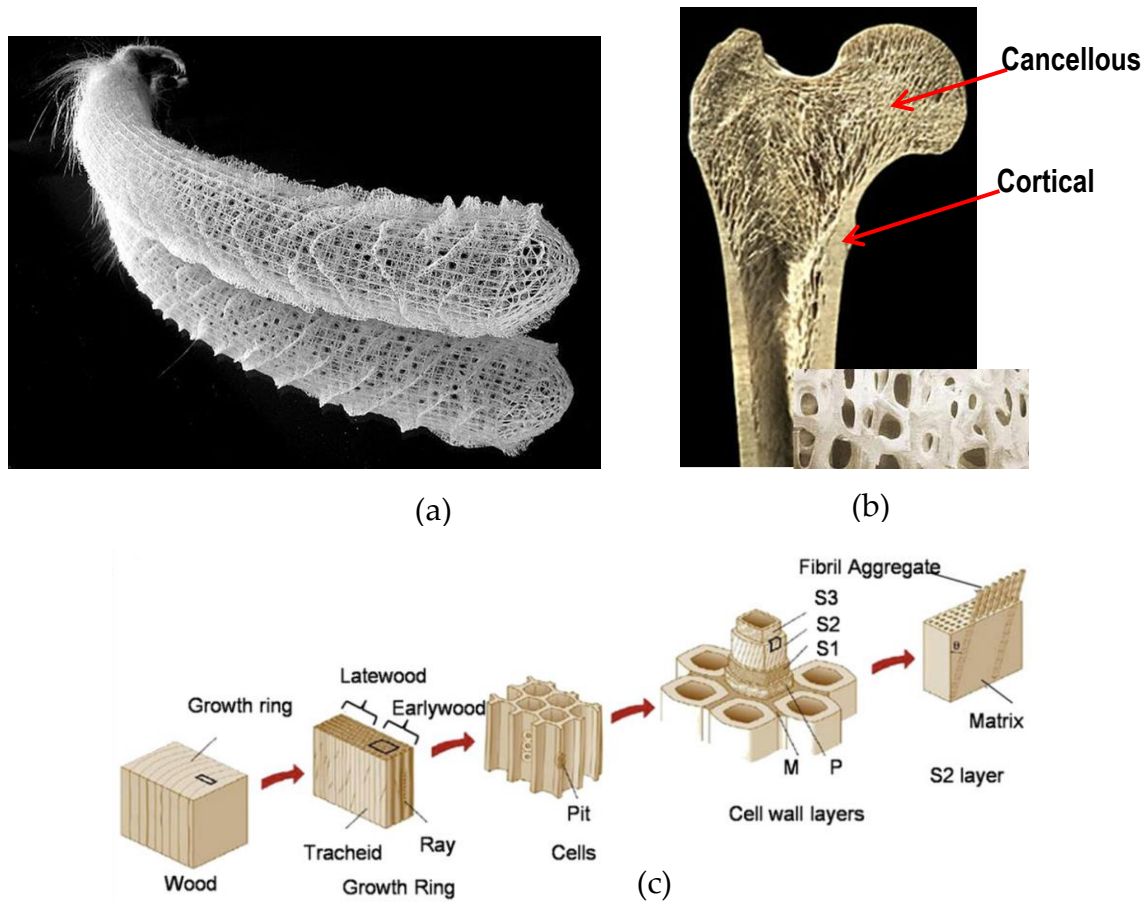


Figure 2-2. Groups of cellular designs, namely, (a) an open cellular structure used to build a glass sponge skeleton, (b) a closed cellular structure used to build a tibia bone, and (c) a polygon cell-based structure used to build honeycomb cell walls in wood [4, 14-15]

2.3.2 Occurrence of cellular designs in nature

In nature, the geometries of cellular structures are hierarchically structured. The hierarchical arrangement of biological tissues such as the glass sponge skeleton, bone, and wood is structured at the macro, micro, and nano scales [3, 14]. The hierarchically structured tissues have superior mechanical properties as a result of the organism's subsequent structural optimization [15]. This is a growth strategy that ensures that the structure has responsive load-bearing capacities to changing stimuli, which in turn allows biological tissues to adapt [16].

Glass sponge skeleton tissues have seven hierarchical levels that range in size from nanometres to centimetres, namely (a) laminated spicules (micrometres to centimetres), (b) axial filaments (nanometres to micrometres), and (c) silica particles and protein interlayers (nanometres to micrometres) [3, 14, 17]. The various levels of hierarchy all contribute to the structure of skeletal composites in nature. Figure 2-3 shows the skeletal composite of spicules in siliceous sponges comprised of cylindrical lattice cage-like structures with lateral openings [14].

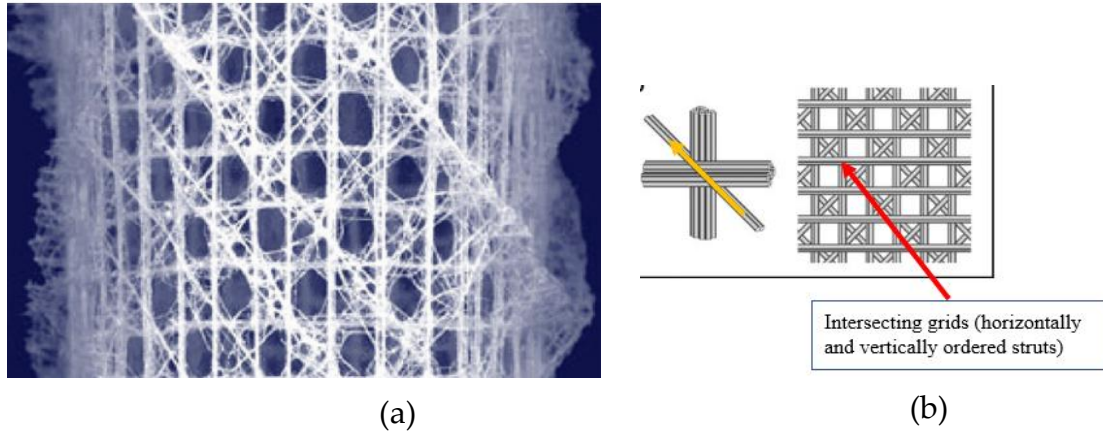


Figure 2-3. A skeletal composite of spicules in siliceous sponges built using cylindrical lattice cage-like structures, represented as (a) an organic and non-periodic form and (b) a systematically modelled and periodic form [14]

The cylindrical lattice-like cage structure is supported by grids built from vertically, horizontally, and diagonally ordered struts, which function as bonded spicules, as represented in Figure 2-3 [14]. Figure 2-3(b) shows a red arrow indicating the intersecting grid for vertically and horizontally structured struts. The yellow arrow indicates the direction of a diagonally structured strut.

Bone tissues are typically grouped together into three categories: plate-like bones (such as the skull), short bones (such as the vertebra), and long bones (such as the femur) [14, 18]. The tissue in question adopts different morphologies depending on the application, as seen in the final forms presented in Figure 2-4 [3].

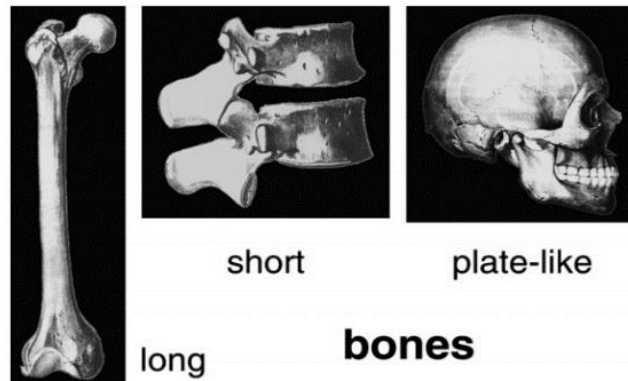


Figure 2-4. Numerous morphologies of bone tissue depending on their application [3]

Bone tissues are hierarchically structured at the macro, micro, and nano scales. Depending on the application, two sub-scales at the micro and nano levels can also be present [3]. Figure 2-5 shows the relationship drawn between connecting component phases of hierarchically configured bone structures at different scales [18].

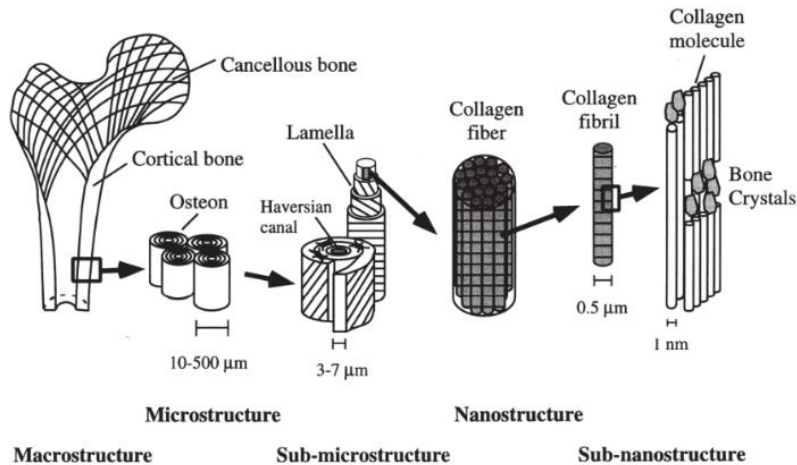


Figure 2-5. Different hierarchical orders of structuring material for numerous scales of a bone structure [18]

Wood tissues have four hierarchical levels, ranging from the greatest to the smallest scale. These levels comprise the macroscopic structure, cellular structure, fibrillary structure, and molecular structure, as depicted in Figure 2-6 [14].

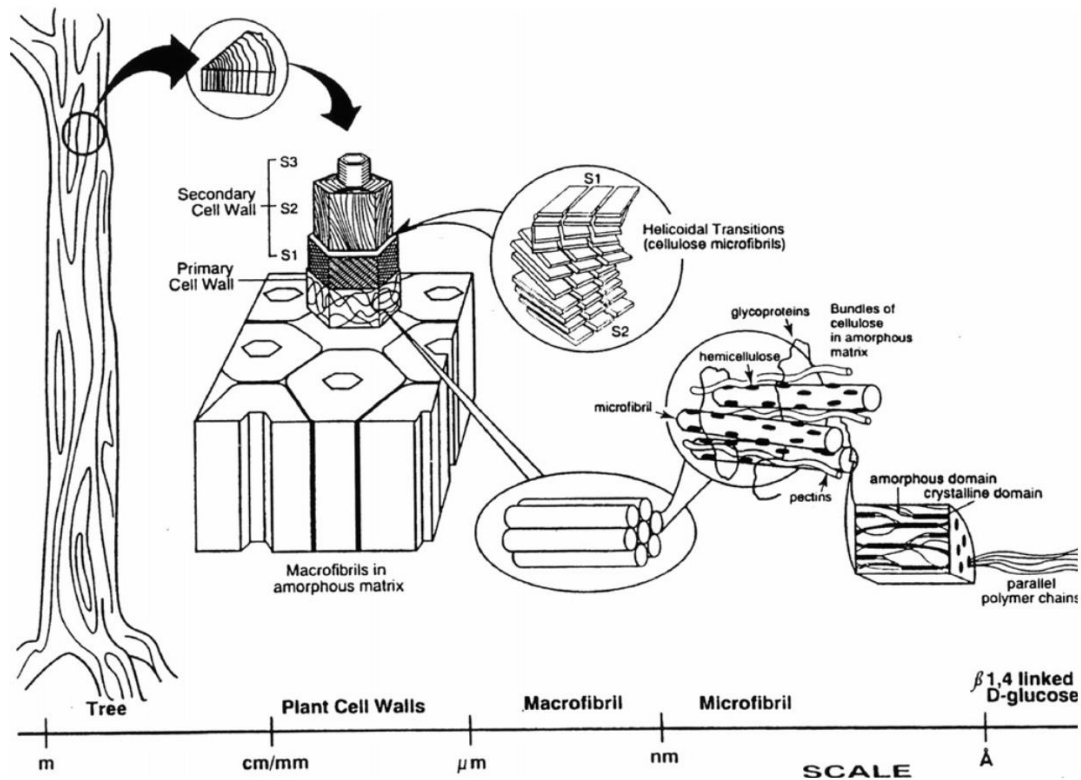


Figure 2-6. Numerous hierarchical levels of structuring material for a variety of scales of a wood structure [14]

The occurrence of cellular structures highlights the concept of function-driven design, in which the structure and arrangement of material correspond to its application. Different biological tissues and materials have a variety of cellular architectures that are optimized for specific functions, including load bearing, flexibility, or filtration. Additionally, biological materials can adapt to changes in external stimuli as a result of the dynamic process of evolution and hierarchical structuring of cellular structures. This adaptability is crucial for the longevity and growth of various organisms. In a comparable manner in

engineering, having the ability to produce materials that can adapt to changing conditions, such as lattice structures, can be advantageous in numerous types of applications.

2.4. Lattice structures

2.4.1 Types of lattice structures

Lattice structures are bioinspired designs (built by mimicking natural cellular structures), 3D structures built up of a series of interconnecting beams, struts, or triply periodic minimal surfaces (TPMSs) [19]. They are typically used to build lightweight [20] and robust structures [19-20] in engineering applications. Figure 2-7 depicts four types of lattice structures that are typically studied in engineering fields, including polygon-based, strut-based, skeleton-based, and sheet TPMS-based structures [11, 21].

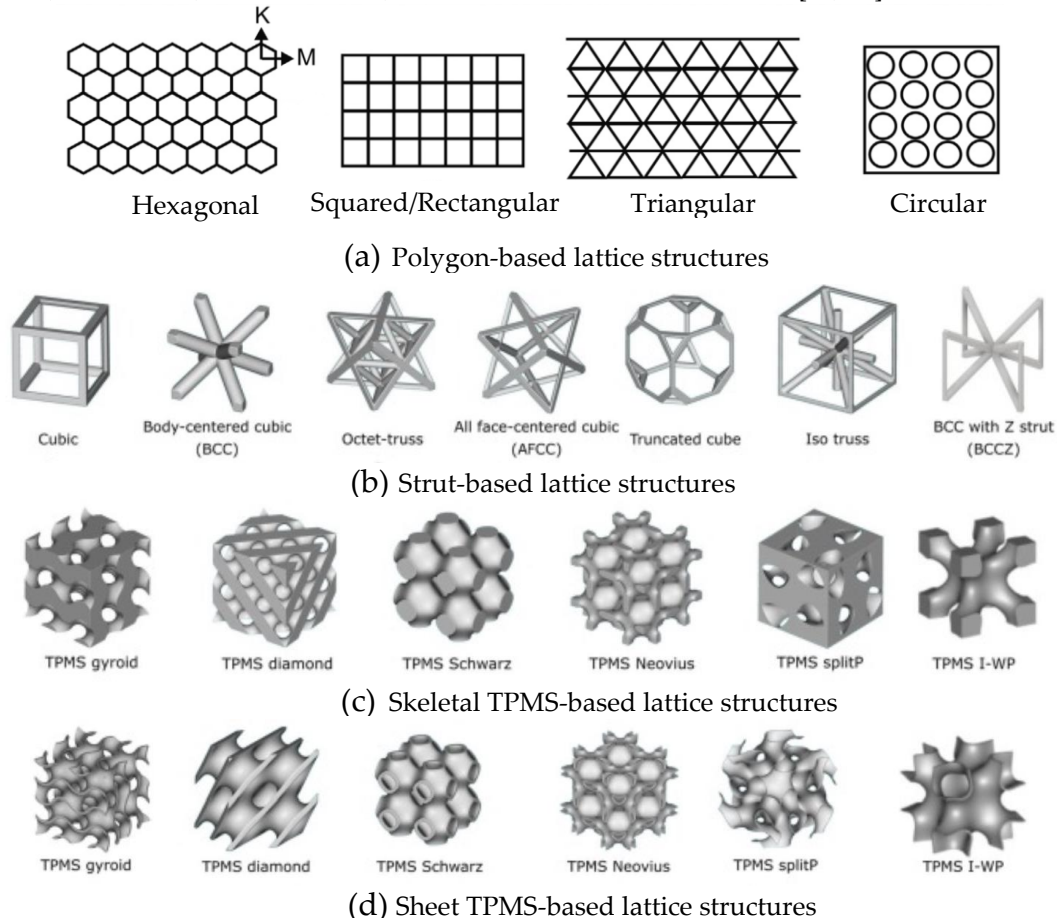


Figure 2-7. Four types of lattice structures in engineering applications [11, 21]

Polygon-based lattice structures are generated by arranging unit polygon cells in a design space. Polygon cells are the basic building blocks of this type of lattice structure. These polygons can be triangles, squares, hexagons, or any other regular polygon shape [21]. Strut-based lattice structures are built using struts to generate 3D structures [14]. Strut-based lattice structures include the body-centred cubic, rhombic dodecahedron and truncated cuboctahedron [11, 22]. Skeletal TPMS-based lattice structures are another particular type of lattice structure that is built via the geometry of TPMS. They are 3D minimal surfaces that have translational symmetry, which means their pattern can be repeated in all three directions indefinitely. The minimal surfaces have physical properties of minimal area or curvature [11, 22-23]. These lattice structures are composed of a network of joined surfaces that adhere to mathematical descriptions of the geometries of TPMSs. The surfaces in these structures connect with one another at nodes or joints to create a design that is repeated throughout the structure [24]. The TPMS-gyroid, diamond, Schwarz

primitive, and neovious models are some of the commonly used lightweight skeletal TPMS-based lattice structures in design. The same procedure for building skeletal TPMS-based lattice structures is used for sheet TPMS-based lattice structures, with the sole difference being that sheets or panels are used instead of surfaces similar to struts or beams [25].

2.4.2 Evaluation of tessellation in lattice structures

Lattice structures are designed and created primarily using tessellation techniques. The design process for lattice structures begins with determining the best unit cell and method for tessellation [20, 26]. Lattice structures used in numerous engineering applications, which have larger area/volume coverage, adopt different geometries than those of smaller area/volume coverage to generate parts with particular mechanical and lightweight properties [11, 13, 20, 26-27]. The lattice structures are generated by repeating a unit cell in a specific geometric pattern. The design of lattice structures, therefore, includes both the design of unit cells and configurations [26].

Methods for designing unit cells. The smallest part, which builds up and describes the entire lattice structure, is referred to as a unit cell [26]. Currently, there are three established methods for designing unit cells, including (1) a planar-based approach, where a unit cell is built up as a 2D polygon shape by reducing the third dimension to almost zero [21]; (2) a primitive-based approach, where the unit cell is made up of particular geometric primitives [28]; and (3) an implicit surface-based approach, where the surface of the unit cell is defined by mathematical equations [20, 26]. When combined with the method of latticing or TO, these methods for designing unit cells are advantageous in terms of the efficiency of designing structures built using unit cells [9]. The terms tessellation, repeating unit cell, and configuration are used interchangeably to refer to the process of joining small, regular unit cell shapes together without gaps or overlaps to entirely fill the design space.

A planar-based technique is an easy one that uses planar geometry (2D Euclidean geometry) to determine the internal and external geometry of a polygonal unit cell. As shown in Figure 2-8, for a hexagon, the unit hexagonal cell is created by identifying the straight lines that connect the corners of a hexagon in a 2D space [21].

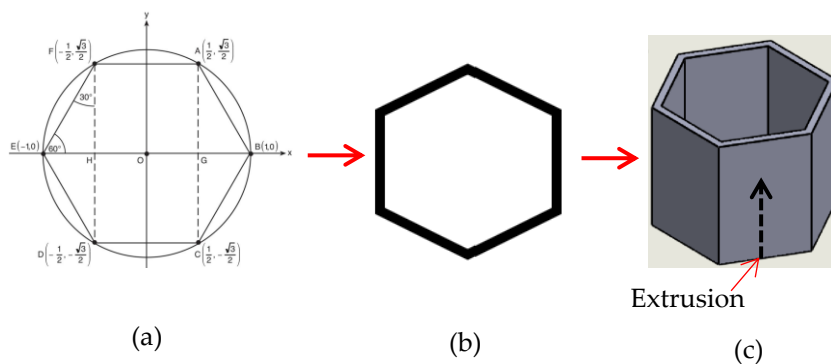


Figure 2-8. Schematics of a planar-based method for creating hexagonal polygon unit cells [21]

First, the procedure in Figure 2-8(a) is followed for both the outer and inner hexagons to produce the planar unit hexagonal cell in Figure 2-8(b). The planar unit hexagonal cell is then extruded in the third dimension to achieve the solid geometry shown in Figure 2-8(c). This approach is most preferable for generating polygon-based unit cells [6, 21, 26].

The primitive-based method works on Boolean operations of basic shapes, as shown in Figure 2-9 [26].

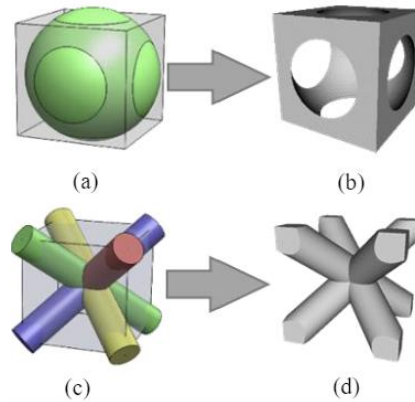


Figure 2-9. Designing unit cells using a primitive-based method [26]

The unit cubic cell in Figure 2-9(b) is generated by the procedure of Boolean subtraction shown in Figure 2-9(a). This method makes use of a cube as the base geometry and a concentric sphere as the subtractor. The unit truss-like cell shown in Figure 2-9(d) is generated by first performing a Boolean union of four diagonally structured cylinders before performing a Boolean intersection with a cube, as shown in Figure 2-9(c). This method is most preferred for generating strut-based unit cells [26].

In the design of unit cells, the implicit surface-based method is also a successful strategy. This technique represents the surface of a unit cell in three dimensions using implicit equations. Equations in the form $F(x, y, z) = 0$ are used to define an array of points that are positioned on the surface as a function of three coordinates with an origin at point zero. For instance, Figure 2-10 shows a unit cell geometry and the equation which works with it. This approach is most useful for generating skeletal or sheet TPMS-based unit cells [20, 26, 28].

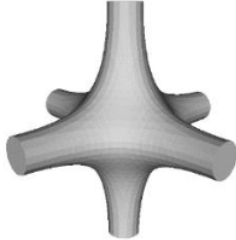
$$\begin{aligned}
 F(x, y, z) &= \cos(2\pi x) + \cos(2\pi y) + \cos(2\pi z) \\
 &+ a(\cos(2\pi x)\cos(2\pi y) \\
 &+ \cos(2\pi y)\cos(2\pi z) \\
 &+ \cos(2\pi z)\cos(2\pi x)) + b = 0
 \end{aligned}$$


Figure 2-10. A skeletal TPMS-based unit cell type created by an implicit surface-based method [26]

Elsewhere, algorithms based on mathematical equations are used in TO to determine the most efficient distribution of material. This approach often uses lattice unit cells to introduce pores into a solid to determine the best usage of material. TO methods are currently considered the most efficient for restructuring material on already generated unit cell structures. This is because the approach takes account of the load paths, thus ensuring that the unit cell has good mechanical properties [9-10, 29].

Design configuration (tessellation) methods. The procedure of repeating unit cells in two or three dimensions is known as design configuring or tessellation. Numerous reviews [26, 28, 30] have so far highlighted the following methods for tessellating lattice structures from a design and structural perspective: (1) regular or direct tessellation, in which the unit cells are translated repeatedly [30], and (2) conformal tessellation, in which the cell units are repeatedly packed in a way conforming to a specific surface geometry [26]. The configuration of designs is often complemented by structural optimizations to optimize the distribution of material. Latticing and TO are two methods that are used to optimise not only the distribution of material within a unit cell but also the materials within a spatial replication of the unit

cell across the entire design space [31]. These methods have been used extensively in the fields of engineering for building lightweight parts with good mechanical properties [9, 20].

In most studies [6, 19, 21, 32-34], unit cells are built as rectangular/square and cubic geometric models for ease of use. Then, by periodically repeating the unit cells in two or three dimensions (along the x , y , and z -axis), lattice structures can be created directly. In Figure 2-11(a, b), lattice structures made of 2×2 (2D), and $2 \times 2 \times 2$ (3D) unit cells [26], respectively, are depicted using this approach by translating the unit cell twice along each of the coordinate axes.

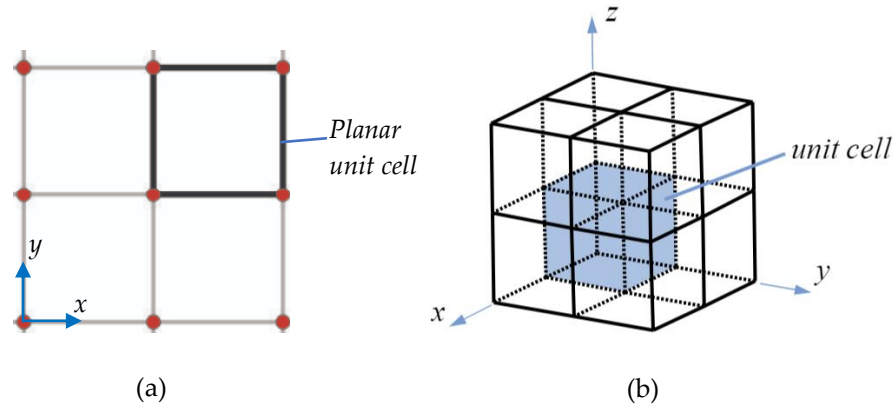


Figure 2-11. Diagrams for direct patterning in both (a) two- and (b) three dimensions [26]

Conformal structuring directs the total number of unit cells to conform to the shape of a design space, such as the dome-like lattice structures shown in Figure 2-12(a, b) [35].

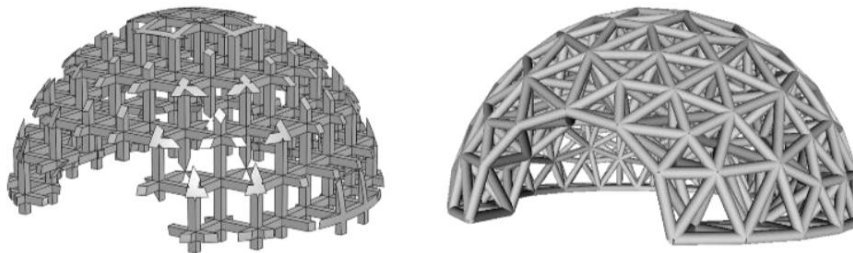


Figure 2-12. The (a) direct structuring method as opposed to the (b) conforming structuring method [35]

Direct structuring uses extra Boolean operations, as opposed to conformal structuring, which preserves the structural integrity of the unit cell and is considered a better approach to stiffening or strengthening structures [20, 26]. This is because it allows for the uniform distribution of loads throughout the entire structure. Nguyen et al. [35] developed a two-step procedure for creating a conformal lattice structure from a given surface of a part. In this procedure, a 3D conformal hexahedral mesh must first be computed to fit the unit cell. In the second step, the unit cells are populated to fill the hexahedral space occupied by the mesh elements from the previous step.

Latticing and TO are two independent methodologies used in engineering and design to optimize the structure of a component for specified performance. Latticing involves creating a lattice structure from an existing solid geometry to reduce weight. In contrast, TO begins with an empty design space and redistributes material to optimize a component's performance depending on specific constraints [33-38]. Latticing and TO methods can be applied to the already designed configurations of unit cells for best efficiency in the use of material, as has been done by several researchers [26, 36-38]. A lattice structure was developed by Alzahrani et al. [39], using information on the density derived from TO performed using ABAQUS FEA software, as shown in Figure 2-13.

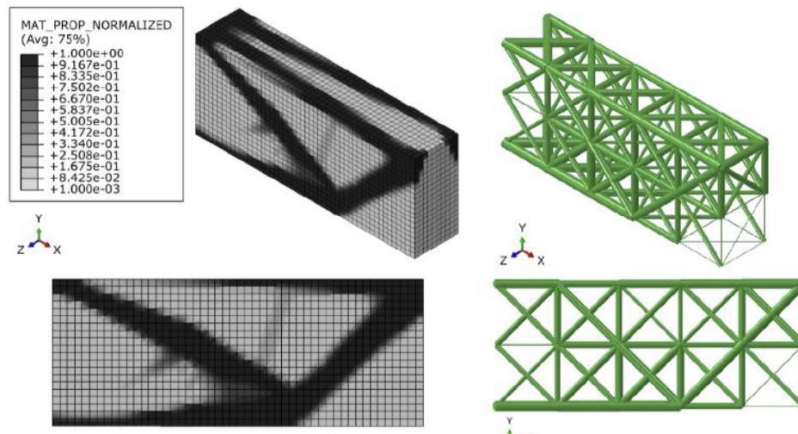


Figure 2-13. A strut-based lattice structure generated from density data [38]

The configurations arrived at through direct structuring are most preferred for the tessellation of lattice structures, as the approach preserves the structural stability of parts made of unit cells. Additionally, methods of combined latticing and TO offer the advantage of determining how to distribute the material in a design space in the most efficient way. This is because the latter tool, TO, can determine the load path of a structure before assigning an objective to reduce strain energies and response to where material should be lowered [30, 33, 35]. A combination of these methods should, therefore, be considered when designing lattice structures in order to improve the building procedure and achieve better mechanical properties.

Generative design approaches such as TO are advantageous, particularly when they apply to lattice structures. These tools can improve the manufacturability of such lightweight structures whilst accounting for the manufacturing constraints imposed by the complexities of designed shapes of lattice structures. They also help generate material-efficient designs that can be tailored according to particular performance-driven requirements [9, 37]. When integrated with advanced manufacturing approaches, generative designs are driving innovation in numerous types of industries, from aerospace and automotive to architecture and biomedical [9]. In addition, the use of generative design with TO can significantly reduce the time and costs that are typically related to conventional experimentation design methods [9, 37].

Design considerations for lattice structures. The mechanical properties of lattice structures generated via tessellation are affected by the design that arranges how the material is distributed, the degree of porosity inherent in the structures and the material used. To create parts with good mechanical properties that are unique to the chosen engineering application, careful consideration of these factors is necessary.

Existing literature [10-11, 21, 20, 26, 28, 38-50] shows that only explanations regarding the mechanical behaviour of specific types of lattice structures have been given separately based on their edges and the connectivity of their vertices and the chosen unit cell. It is recommended that the size, shape, and connectivity of the polygons be customized to tailor the mechanical properties of their related lattice structure to different applications.

Tessellation allows for the creation of numerous cell topologies of structures. However, differences in the area covered and how much material is used within a specific design space influence the mechanical properties of such structures with different cell topologies. Figure 2-14 shows the area covered by four different polygon-based lattice structures, including the triangular, squared, hexagonal, and circular, within the same design space [51].

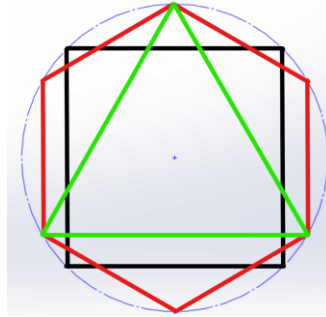


Figure 2-14. The relationship between four different cell polygons within the same design space [51]

The mechanical properties of the structures built with the polygons shown in this figure can be determined via tessellation in reference to the deduced relationships between the connecting edges and vertices of cells, similar to what was done in references [10, 44, 52-53]. As a result, structures built from different types of polygonal arrangements will have different mechanical properties. Figure 2-15 shows how different planar polygons tessellated on the same design space create different numbers of polygons, area coverage, and use of materials for a given wall thickness [51].

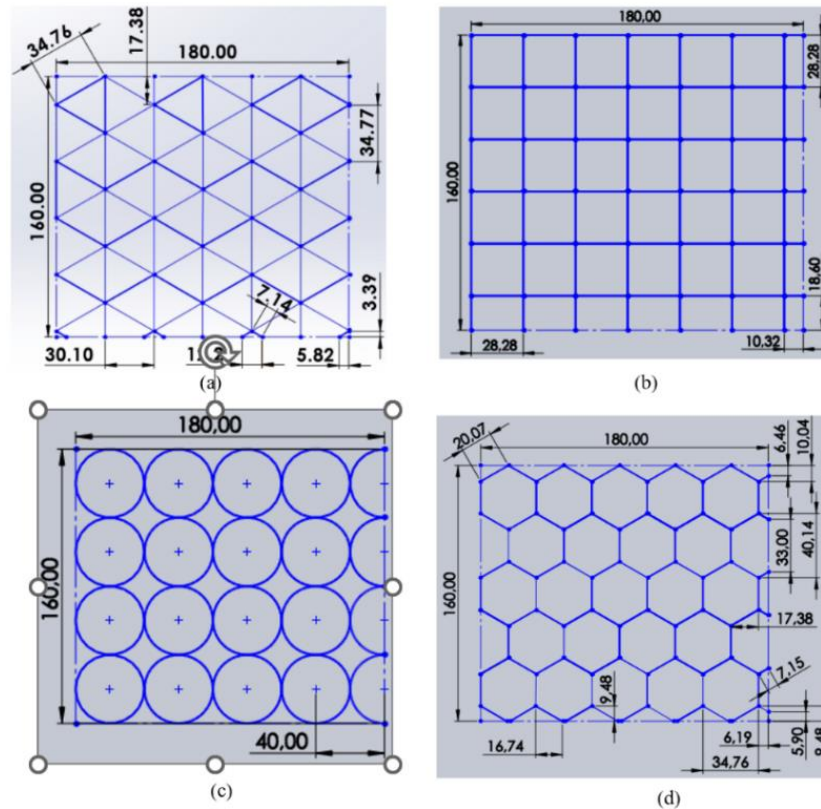


Figure 2-15. Planar tessellated structures with (a) triangular, (b) squared, (c) circular, and (d) hexagonal cells [51]

From Figure 2-15, it is deduced that the squares, triangular, hexagonal, and circular polygons have area coverages of 100%, 99.78%, 93.93%, and 78.54%, respectively, ignoring the very small incomplete polygon forms in Figures (2-15a and 2-15d). The incomplete polygons in Figures (2-15b and 2-15c), on the contrary, are considered because they cover a significantly observable fraction of the design space. As noted earlier in this chapter, area coverage here refers to the area within which polygons are fitted. The percentage figures for material used relative to the area of the whole design space for the same polygons, in the same order,

are 15.28%, 20.81%, 10.32%, and 7.85%, respectively. The amount of material used for each polygon type was calculated using a wall thickness of the polygon structures of 1 mm.

It is clear from the foregoing figures that the square polygon is undoubtedly the preferred shape in terms of area coverage when tessellated in a design space. This is because structures with greater area coverage tend to have better mechanical properties compared to those with smaller area coverage [13]. This demands care when designing structures with porosity so that they cover large enough areas to ensure good mechanical responses. Due to its minimal material requirements, the circular polygon will likely be the one with the lowest production costs. However, the hexagonal polygon is the most preferable when compared to the other polygons since it has a material requirement that is substantially lower than the square polygon while covering a slightly smaller area.

When the results obtained from determining the area covered and how much material is used are combined, they facilitate the ranking of different types of lattice structures in terms of mechanical properties and manufacturing costs. The following recommendation is made to determine the efficient design of lattice structures with the lowest production costs. In addition to the methodology for ranking the four types of lattice structures based on their different sizes, shapes, and connectivity of the polygons, the effect of area coverage and usage of material on the mechanical properties and production costs of lattice structures should be taken into consideration.

Though the auxetic type of lattice structures are outside the envisaged scope of this chapter, it is noted that their design principles are particularly important to comprehend because these structures exhibit a unique and counterintuitive mechanical property known as a negative Poisson's ratio. The design concepts for auxetic lattice structures involve altering the arrangement of unit cells to attain negative Poisson's ratios [54-56]. Therefore, the design of auxetic lattice structures requires a thorough review of unit cell shape, stretching mechanisms, orientation, scaling, material properties, boundary conditions, manufacturing methods, and validation procedures [56]. The negative Poisson's ratio of auxetic lattice structures distinguishes them from other structures, resulting in them being useful in several engineering applications, as outlined in references [55, 57].

2.4.3 Hierarchical lattice structures

Hierarchical structuring is often adopted to improve the mechanical properties of lattice parts such as HCs. This approach calls for embedding smaller unit cell shapes into larger structures, resulting in a multiscale structure, as shown in Figure 2-16 [58].

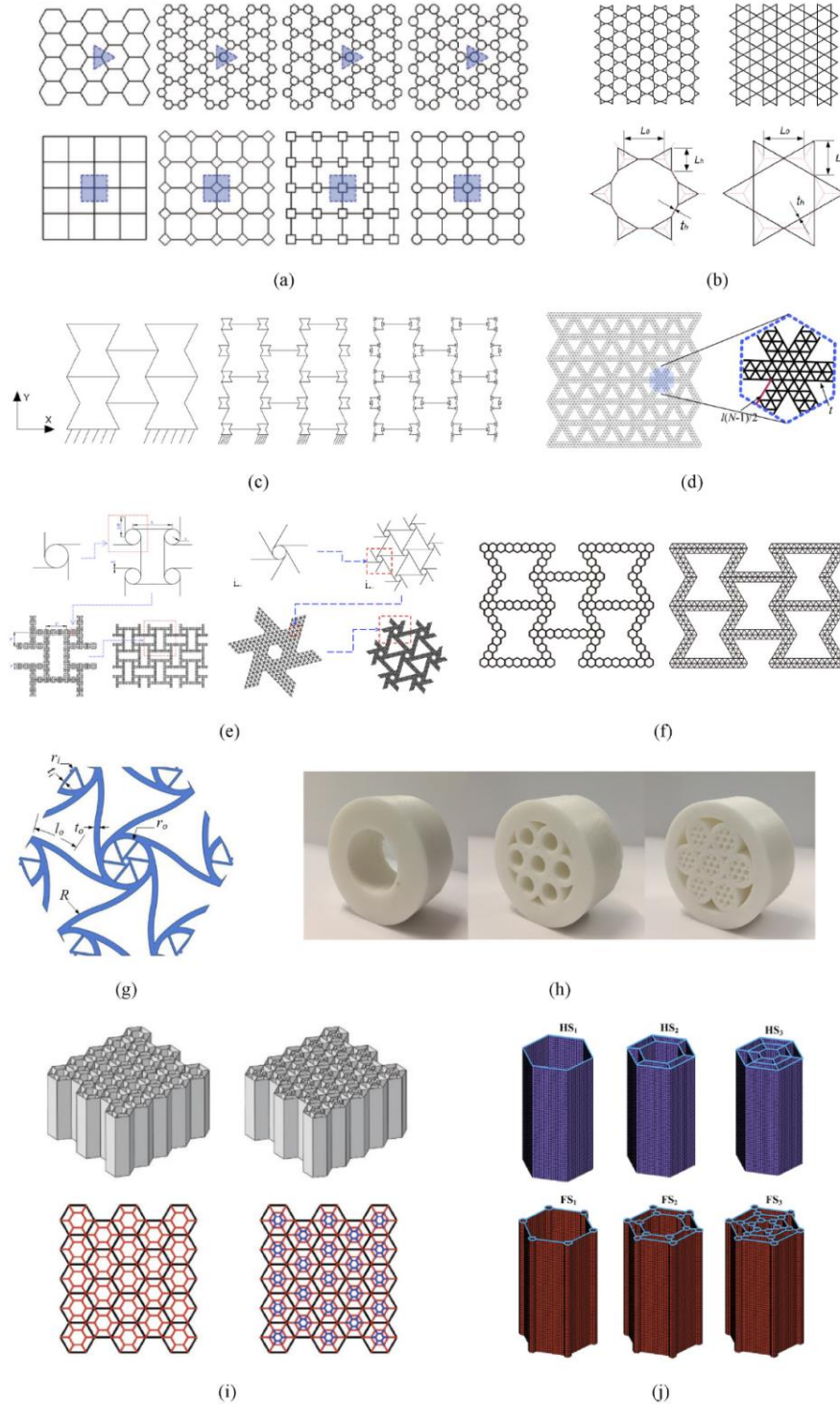


Figure 2-16. (a-b) vertex-based hierarchical polygonal structures, (c) vertex-based hierarchical re-entrant HCs, (d) cell-wall-based hierarchical triangle honeycomb (HC), (e) cell-wall-based hierarchical using tetra-chiral and hexa-chiral HCs, (f) cell-wall-based hierarchical re-entrant HCs, (g) fractal-based hierarchical hexa-chiral HC, (h) fractal-based hierarchical circular polygon structures, and (i-j) spiderweb-based hierarchical hexa-chiral HCs [58]

The four hierarchical design approaches mentioned in the previous figure, namely the vertex-based, cell-wall-based, fractal-based, and spiderweb-based observed are inspired by nature, where hierarchical structures are prevalent in numerous biological materials, as previously shown in Figure 2-2 of this chapter. Hierarchical HC designs can be enhanced with regard to their mechanical properties, such as strength, stiffness, and toughness, by incorporating different sizes of hollow structures. This is achieved by efficiently designing to distribute loads across different levels of the structures [21, 59-63]. Hierarchical HCs can achieve high strength with minimal material usage via optimization of their configuration at multiple levels, resulting in them being ideal for lightweight yet robust applications. This is crucial in applications requiring impact resistance, such as the development of crashworthy materials for automotive and/or aerospace applications [21, 62]. Material properties could be engineered with different levels of hierarchical structuring as well. The external surface of the macrostructures, for instance, could be engineered to provide overall strength, whilst the meso-structures and microstructures could be designed to improve flexural ability or energy absorption [62]. Hierarchical structures also aid in the reduction of sensitivity to bend-dominated deformation. Different levels within a hierarchical structure add to bending force resistance, resulting in the entire structure being more resistant to such deformation [21, 59, 61-62]. The choice of polygonal unit cell shape introduced at the vertices or walls of the parent structure influences the effectiveness of the entire structure under imposed loads. There are gaps in the literature with regard to the highest order of hierarchy that is physically attainable for hierarchical HCs built, irrespective of the different polygons used.

2.5. Applications of lattice structures in engineering

Incorporating biological cellular designs in engineering applications is an innovative and interesting method that has been inspired by the complexities as well as the efficiency of biological structures [5, 13]. Nature has evolved over billions of years, resulting in intricate cellular structures that optimize a variety of behaviours, including stiffness, strength, toughness, and flexibility, as well as self-repair and adaptability [7, 27, 36]. Engineers can create more sustainable, efficient, and adaptive structures by mimicking cellular designs in nature [22-23].

Additive manufacturing of bioinspired cellular designs. Conventional manufacturing methods, including casting, forging, and milling are challenging to use on complex designs for bioinspired cellular structures. This is due to the intricacies of the internal structures and geometrical arrangements exhibited in bioinspired designs being difficult to mimic using these methods of manufacturing [55-57]. This is so except for a special group of alloys known as "gasars," particularly lotos-like gasars [64]. Gasars exhibit distinctive characteristics that allow for more accurate replication of intricate structures, potentially overcoming some of the limits imposed by current manufacturing techniques in developing bioinspired designs. High precision casting, low viscosity, thermal stability, fine grain structure, customizable characteristics, compatibility with additives, and corrosion resistance are some of their distinguishing characteristics [71]. Alternative manufacturing technologies that are more suited to bioinspired cellular parts have been investigated to solve these limitations. Among these advanced procedures is AM, often known as 3D printing, which is advantageous for its ability to build complex designs of bioinspired cellular structures with high precision and customization [31, 35, 55-57]. This method builds structures layer by layer and, in doing so, aids in fabricating complicated designs which mimic natural cellular structures [55]. The combination of AM and bioinspired designs has enormous potential in industries such as automotive, aerospace, and biomedical [31].

With optimal control over design parameters, highly customized structures are attainable via AM. Functional cellular parts in specific applications are obtained by mimicking complex cellular geometries observed in nature, such as vascular networks, honeycombs, and trabecular bone structures [13, 31]. These bioinspired cellular architectures often have a good strength-to-weight ratio, resulting in them being ideal

for building robust yet lightweight parts [13]. With the implementation of AM, lightweight materials with complex internal structures could be built, thus improving their mechanical properties [31]. Typical hierarchical structuring and multiple-scale repetitive structures observed in natural cellular structures can be replicated through AM. In turn, this improves the effectiveness and usefulness of engineered cellular materials [5, 13, 31, 55]. AM enables the rapid manufacture of prototypes of cellular parts. This ensures that mechanical tests can be carried out for multiple bioinspired designs before finalizing the product. This enables the acceleration of the development process and improvement of the overall efficiency of design iterations [31, 35, 66-67].

Application of bioinspired cellular designs in aerospace industries. Bioinspired cellular parts, including honeycombs and foams, have high strength-to-weight ratios [13]. In the aerospace sector, these structures are used to build lightweight structural parts, including wing panels, fuselage parts, and fairings. Their reduced weight improves fuel efficiency and the overall performance of aircraft and spacecraft [68]. Natural cellular designs are useful for parts with high absorption of strain energies to maintain the safety of passengers and crew during emergencies [5, 7, 13, 36]. Aerospace engineers and scientists are also improving crashworthiness and impact resistance by incorporating bioinspired cellular materials in critical regions, such as landing gear and cabin parts [69-70]. Natural cellular structures, including those observed in the leaves of plants, can alter the shape or respond to external stimuli [33]. Implementing similar principles to aircraft wings or other surfaces could result in adaptive and morphing structures that improve aerodynamics and control under different flying conditions [59]. In the case of spacecraft and re-entry vehicles, bioinspired cellular structures capable of resisting high temperatures are expected to be used as thermal protection materials, ensuring the safe entry of spacecraft into the Earth's atmosphere [31, 53]. Inspired by the principles used by natural flyers such as insects and birds, engineers are looking into bioinspired propulsion systems. For some aeronautical applications, biomimetic propellers and flapping wing designs could result in improved efficiency and manoeuvrability [33].

Application of bioinspired cellular designs in automotive industries. Automobile manufacturers lower the overall weight of vehicles by integrating lightweight materials into automobile parts such as body panels, chassis, and interior parts, thus, in turn, improving fuel efficiency and lowering emissions [33]. Natural cellular architectures tend to be preferable regarding energy absorption applications [13]. Vehicles are engineered to better withstand the energies generated by impacts during crashes by incorporating bioinspired materials in critical regions such as bumpers and crumple zones [69-70]. Moreover, bioinspired cellular architectures with optimized thermal conductivity are used to improve overall thermal management and vehicle performance in automotive cooling systems, battery packs, and engine components [33]. Researchers are investigating bioinspired tyre tread designs inspired by natural surface patterns. These designs seek to improve traction, reduce rolling resistance, and improve overall tyre performance, all of which contribute to improved fuel efficiency [13, 33]. The ability to mimic the flow patterns inherent in nature, such as fish scales or bird feathers, results in more aerodynamically efficient vehicle designs [33]. More streamlined shapes reduce drag while improving fuel efficiency [72-73]. Bioinspired self-healing cellular materials are being researched for automotive applications. These materials are capable of self-repairing small cracks or damage, thus extending the life of automotive parts and lowering maintenance costs [73].

Application of bioinspired cellular designs in biomedical industries. Bioinspired cellular parts such as scaffolds can be used as structural supports during tissue regeneration of damaged or wounded biological organs. These scaffolds mimic the natural extracellular matrix of biological materials, allowing cells to proliferate and differentiate into functional tissues [74]. Additionally, bioinspired structures could be used for vascularization, which allows nutrients and oxygen to reach developing tissue [31, 36]. These structures are also used as carriers for targeted drug delivery. They are capable of encapsulating drugs while controlling their release, replicating the behaviour of cells within the body that carry and release chemical substances as required [31]. Bioinspired materials, which mimic the cellular architecture found in

biological tissues, can be used for building biocompatible implants. These implants have the capability to integrate seamlessly with the tissues that surround them, thus lowering the possibility of rejection while improving patients' prospects for recovery [5, 13, 36].

Figure 2-17 shows some current instances of bioinspired cellular designs used in numerous engineering industries [13, 27, 75].

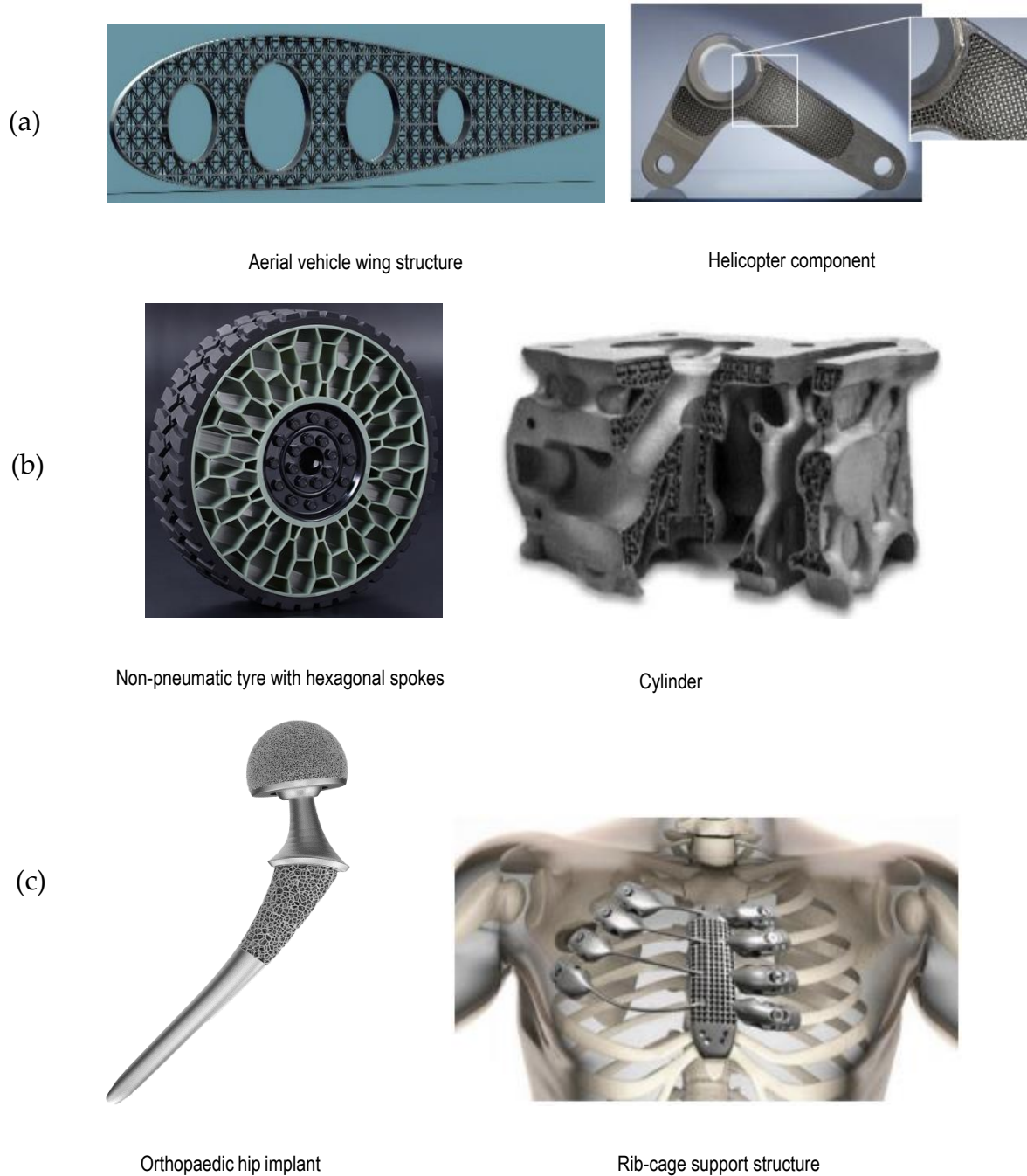


Figure 2-17. Current applications of bioinspired cellular designs in the (a) aerospace [27, 75], (b) automotive [13, 27], and (c) biomedical industries [13, 27]

Incorporating bioinspired cellular structures into engineering applications covers numerous industries, driving innovation, efficiency, and sustainability in several fields. This multidisciplinary strategy uses nature's design concepts to tackle complicated technological problems and develop advanced and advantageous technologies.

2.6. Mechanical properties of cellular and lattice structures

Glass sponge skeletons, nacre, keratin, bone, and wood have all been carefully studied to mimic their remarkable mechanical properties in nature [15]. Numerous studies have focused on the most important factors of loading structures, including direction of loading, rate of loading, degree of mineralization, porosity, and hierarchical structuring for macro, micro, and nanoscales. To some extent, researchers have attained novelty and advances in fabricating energy absorption structures [15, 76-79].

A bionic lattice structure mimicking the double slope-like reinforced structuring of a deep-sea sponge skeleton was suggested by Zhang et al. [80]. A bionic lattice built using a wall thickness value of $t = 1.2$ mm was observed to have better energy absorption capabilities compared to one with a value of $t = 0.45$ mm. Their specific absorption of energies (*SEA*), energy absorption (*EA*) and crushing mean force (P_m) increased by 216.5%, 745.0%, and 744.3%, respectively, with this increase in wall thickness. It is worth noting that the skeletons of glass sponges have hierarchical configurations that span various length scales, from nanometres to centimetres. Though the double-diagonal reinforced configuration is macroscopically replicated by the bionic lattice structure, as observed in references [79-80], the addition of hierarchical features is recommended here at even smaller scales to enhance the performance of the lattice design further. To achieve this, prospective research must focus on the use of biomimicry and advanced manufacturing technologies such as AM to design and manufacture multiscale hierarchical structures mimicking the skeleton of a deep-sea sponge. Yao et al. [81] constructed a hierarchical foamy multiple-cellular square structure, modelled after the gradient distribution of various sizes of unit cells in organic structures, including bamboo and bone tissue. Their findings showed that the third-order biologically inspired hierarchical multiple cellular tube structure absorbs 173.7% more energy than the conventional square tube cellular structure. The hierarchical foamy multiple cellular square structure improves energy absorption, as determined by the findings of their research [81] and as reviewed by [79]. However, these studies do not fully comprehend the specific mechanisms underlying this enhancement. Therefore, further studies are required in terms of physical experiments and numerical modelling to develop a full comprehension of deformation behaviour, stress distribution, and energy dissipation mechanisms within the hierarchical structure, none of which have been discussed in their work.

Wang et al. [82] developed a novel thin-walled multiple cellular tubed structure comprising customized face-centred cubic (MFCS) cross-sections, which were mimicked based on the physical properties of deep-sea sponge's skeleton. Through FE simulation and physical experiments, the compression response and the capacity to absorb the energies of the suggested structure were compared with those of the conventional multiple-celled tube structure. Their findings regarding the energy absorption characteristics of the suggested multiple-celled tube structure outperformed those of the strut-lattices and plate-lattices that were used for comparison. The suggested MFCS multiple-celled tube design exhibited a specific energy absorption that is 37.13% greater than that of the third-order bioinspired hierarchical multiple cellular tube structure. This indicates that their suggested MFCS multiple cellular tube design enhances the prospect for energy absorption of multiple cellular tube structures, as was also reviewed in reference [79]. The parts were fabricated via AM technology, which allows for the direct integration of functional features and parts into the overall structure during printing. Further research work should focus on incorporating sensors, actuators, or various functional parts into the MFCS multiple cellular tube structure to allow adaptive or controllable behaviour in response to the changing external stimulus.

Natural cellular structures are hierarchically structured, with solid struts and unit cells building larger units. These units merge to produce even larger structures [20, 79]. The hierarchical design results in the repetition of unit cells and, in turn, provides multiple load paths. These multiple load paths ensure efficient distribution of stress in biological tissues, improving their overall mechanical strength. The unit cells of these structures are built using solid struts and walls, which in turn add to their load-bearing capacity [3, 7, 13, 20, 83-84]. The material properties of these struts, such as their strength and stiffness, are crucial factors in determining the corresponding mechanical strength of the cellular material [13]. Moreover, the connectivity of the cells also assists in how the load is distributed effectively across the structure [13, 20]. When subjected to external loads, the load is distributed among multiple cells and struts, minimizing stress concentration and increasing the overall structural strength of the tissue [85]. Cellular structures in biological materials can adapt and grow in response to mechanical loads. This dynamic growth mechanism allows tissues to change their cellular arrangement to optimize mechanical strength according to specific requirements for functionality [1, 3, 14, 16]. Their geometric configuration influences the mechanical stiffness of cellular structures. The geometric configuration has factors such as shape, size, and connectivity of cells that affect the stiffness of these structures [86]. Structures with larger cells or struts, for example, may have higher stiffness [1,3, 14]. Furthermore, the choice of material used for cellular structures has a significant effect on their mechanical stiffness as well [20]. In most studies [1, 3, 14, 18, 20, 77-78], the stiffness of biological tissues is normally determined based on the modulus of elasticity of the solid struts and walls. To fully comprehend tissue stiffness and mechanical behaviour, other material characteristics such as density, viscoelasticity, and anisotropy can be accounted for. The interconnected cellular network of cellular structures ensures effective distribution of load and causes the structure to become rigid and stiff. This load-bearing capability is crucial for the structural integrity of tissue [1].

Higher values of mechanical strength have been reported [79, 87-89] in biological nacles and seashells, which are typically plastic, with intrinsic deformation occurring at the nanoscale and extrinsic behaviour of deformation occurring at the micrometre level. By mimicking the robust and durable nacre design, bioinspired materials, comprised of hard micro-scaled layers of mica as well as soft polyimide have been built to achieve more effective mechanical strength for prospective aerospace materials, particularly those used in the lower Earth orbit [79, 90]. For this lattice design, the nano-scaled mica functions like a brick that substantially improves mechanical properties to achieve values as high as tensile strength of 125 MPa, surface hardness of 0.37 GPa, and elastic modulus of 2.2 GPa for nanocomposites, as well as the enhanced temperature and ultraviolet resistance, as reported by Soucek [90], and later reviewed by [79]. Though the foregoing work found improved mechanical characteristics in bioinspired materials that mimic nacre structures, there are gaps in comprehending the specific mechanisms that support the reported strength and durability. Prospective research must, therefore, concentrate on addressing nanoscale and microscale deformation mechanisms within materials, particularly the function of interfaces, defects, and stress distribution.

The gradient-like feature that characterizes organic plants highlighted in [79, 91] has been adopted and mimicked in the design of bioinspired materials experiencing gradient microstructures, resulting in good mechanical properties or responsive behaviour. Frey et al. [92] generated smart response materials by incorporating biologically inspired chemical, structural, and mechanical gradients into delignified wood, mimicking the gradient-like structure and mechanical strength of natural wood. The value of stiffness for the delignified wood that these authors attained was 35 GPa and a high value of 270MPa for the strength compared to typical values of wood falling within the range 7-24 GPa and 7.2-48 MPa, respectively, as a result of the close connection between the hydrogen bonding and the mechanically interlocked fibres for good transfer of loads. Their work was centred around the enhancement of smart responding materials with bioinspired gradients, though there are possibilities to improve mechanical effectiveness and adaptability by optimizing design and manufacturing parameters. New studies should

include comprehensive studies into the influence of different gradient profiles, transitions, and interfaces on mechanical properties such as stiffness, strength, and other relevant parameters.

Audibert et al. [93] generated the size, shape, and configurations of porosities from either avian or terrestrial mammal bone structures and used them for TO and bioinspired structural design. A 3D metal printing process was used for fabricating steel structures with a density of approximately 65%, which were inspired by organic bone designs. The terrestrial mammalian-inspired beam improved the failure load and stiffness to reduce flexure by 7.5% and 17%, respectively, as compared to the topologically optimized beam-like design due to reduced pore size and stress field homogenization. Their study suggests that biological inspiration is relevant and applicable not just for material advancements but also for 3D printing, and it opens up new avenues for developing tough and strong mechanical lightweight structures. Given that the work employed 3D metal printing for building bone-inspired steel structures, scaling up production and manufacturing procedures for engineering applications could also pose challenges in consistency and quality control of parts, as well as requiring extensive use of post-processing and finishing. Extension of this work ought to investigate scalable manufacturing procedures, process optimization, and cost-effective methods of production to enable large-scale deployment of bioinspired structures across engineering fields.

In its entirety, it is deduced that the mechanical strength and stiffness of organic cellular structures are influenced by their hierarchical configuration, solid struts, material properties, and adaptability to changing environments or physiological changes. These properties assist organic tissues in withstanding external loads, maintaining structural integrity, and efficiently undertaking their particular applications. The comprehension and mimicking of physical characteristics like the solid struts and hierarchical structuring in cellular structures hold significant promise for developing new materials and structures with improved mechanical characteristics as well as improving flexibility in design. Researchers can pave new routes for novel strategies aimed at improving strength, durability, and functionality across a wide range of engineering and medical uses by drawing on concepts from biological tissues.

According to Gibson and Ashby [1], cellular structures have greater load-bearing capacity when they are loaded in the longitudinal direction than transverse directional loading. Cellular structures fail with ease in the transverse direction due to shearing and bending critical loads. This is because the highest mineralization rate of material in cellular structures is observed in the longitudinal direction [14, 16, 94]. Gibson and Ashby [1] observed that the axial direction has the highest yield stress compared to the radial and tangential directions for wood tissue. Figure 2-18 shows longitudinal and transverse stress vs strain curves of loaded structures [95].

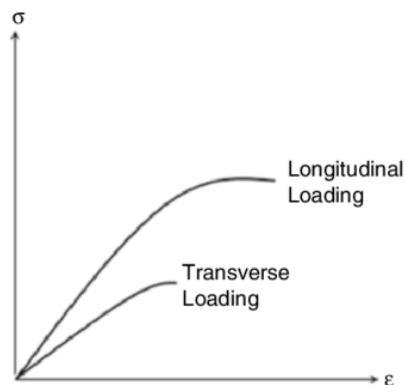


Figure 2-18. Curve plot showing stress-strain dependence on the direction of loading [95]

The mechanical behaviour of cellular structures is also influenced by the rate at which loads are applied [1, 94-95]. Cellular structures withstand rapidly applied loads far better than slowly applied loads. In this way, cellular structures stiffen and strengthen with increasing strain rates, as seen in Figure 2-19 [95].

The increasing strain rate is represented by the red arrow in the figure.

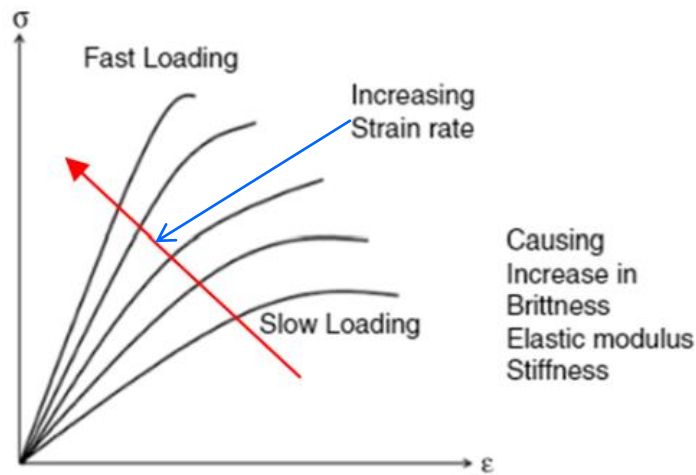


Figure 2-19. Curve plot showing stress-strain dependence on loading rate [95]

Adharapurapu et al. [96] presented evidence that the strain rate is highest on the cortical bone because it has the densest material or lowest porosity compared to other bone parts and, as a result, has the greatest load-bearing capability. It was established in this work that cortical bone possesses structural material that enhances stiffness by 150 MPa compared to the trabecular bone with stiffness of 8 GPa but with lower strains (2%) to failure. When compared to cortical bone, the trabecular bone structure deflected from its original position without fracturing. The latter type of bone was shown to withstand lower loads (50 MPa) and lower strains (50% lower than the strains in the cortical bone) to failure. Simkin and Robin [97] studied the mechanical behaviour of all forms of bones under bending loads. It was found in this study that increasing bone formation improves load-bearing capacity. Ascenzi and Bonucci [98] studied the compressive behaviour of single osteons in a human femur. They observed that the mechanical properties of bones are stronger and stiffer in compression than in tension. It was further noted that the more mineralized the osteons in the bone became, the more rigid and more brittle they became. The cell walls were observed to contract and contact those of neighbouring cells, thus reducing the pore gaps and increasing the bone's compressive resistance. Tensile-loaded bone structures, on the contrary, were observed to exhibit lower values of stiffness than compression-loaded bone structures. The strained cell walls separated at the maximum tensile strains and, therefore, allowed cracks to form, thus leading to bone fracture. However, for the stresses prevailing at the initial stages of plastic deformation, the bone developed some tensile toughness [14]. This property allows organic structures such as the bone, keratin, and nacre to withstand numerous types of loads without immediately cracking and, in turn, aids in supporting and protecting tissues of the body [1, 3, 14, 18, 94]. Jeronimidis [99] proposed that the fibre pull-out process is primarily responsible for good fracture toughness as a result of the energy absorbed in the process for both bone and wood. The mechanics of fibre pull-out and fracture toughness in biological materials such as bone and wood are not well understood. Although energy absorbed during fibre pull-out is thought to contribute to fracture resistance, accurately quantifying and modelling this process at multiple levels is challenging due to variations in fibre orientation, bonding strength, and the complicated anisotropic structure of these materials. The next advances in fibre pull-out technologies can include the development of multiscale computer models and advanced imaging techniques, such as in-situ micro-CT or atomic force microscopy, which can visualize and quantify fibre pull-out processes in real time under various loading scenarios. These models can be combined with algorithms that use machine learning to predict fracture toughness based on material microstructure. This could result in the development of ultra-tough,

lightweight, and fracture-resistant materials for engineering and medical applications. Niebel et al. [100] used Al_2O_3 and polymethyl methacrylate (PMMA) parts that mimic brick-and-mortar lamellar structures observed in nacre, which were effectively improved to generate a synthetic ceramic composite by freeze casting. The toughness of the manufactured parts reached 300 times that of its conventional structures, indicating the effectiveness of the toughening mechanisms found in naturally occurring biological composites. As a result of such studies [79, 100], there has been a significant rise in interest in using natural cellular structure's toughening mechanisms in manufactured parts that are resistant to damage. The combined use of Al_2O_3 and PMMA in freeze casting to mimic the nacre structure could, however, be constrained by the compatibility and processing of the materials. The next generation of work to be conducted in this area must, therefore, investigate alternative materials or processing techniques that provide better compatibility, homogeneity, and control over microstructure, resulting in better mechanical properties and performance.

Libonati et al. [101] experimented with a structure inspired by organic bone in composites with fibre reinforcements to improve toughness and thus reduce fracture while maintaining a balance of stiffness and strength. Carbon fibres, an epoxy matrix, and glass fibres were used to replicate the lamellar, osteons, interstitial tissues and cement sheaths occurring in the osteonal, which is located in the secondary bone structure. Compared to laminated composites, the design that was inspired by organic bone demonstrated substantially improved mechanical characteristics with reference to tensile strength, modulus of elasticity, and fracture toughness, with tensile strength and fracture toughness improving by 26% and 86%, respectively, when contrasted against a previous structural design and other selected conventional laminated composites. The distinctive mechanical characteristics observed in organic bone structures have spurred the generation of polymer and polypeptide-based biomaterials [79]. Fibre-reinforced composites can pose challenges in terms of design complexity, manufacturing, and microstructure control when attempting to mimic the complex hierarchical structure of bone, including cement sheaths, interstitial tissues, lamellar, and osteons. To optimize the biomimetic design and comprehend the effect of various structural characteristics on mechanical properties, further work must include advanced computational modelling and simulation strategies.

Cracks begin and spread longitudinally as a result of shear stresses, contributing to the pulling apart of each cell wall without them experiencing transverse loads through fracture. Crack propagation along the grains of cells is much easier compared to propagation perpendicular to the grains, and thus, there is higher resilience in the latter case. This is particularly so because weak interfaces slow cracks in the perpendicular direction. The anisotropic toughening property of wood is similar to that of organic bone structures and has similarities to that of nacre [4, 14]. This contributes to the cellular structures' high load-bearing capacity [1, 4, 14]. Amini et al. [102] developed a strong glass with enhanced mechanical characteristics by mimicking the organic nacre structure. The glass comprised of SiO_2 and modified PMMA with identical refractive indexes. The bioinspired design of the glass allowed for progressive fracture rather than catastrophic failure, increasing the work done to fracture and the toughness level in reducing fracture by 30% and 55%, respectively. The toughness level in reducing fracture of the biologically inspired glass was observed to be twice that predicted by the SiO_2 tablet alignment. During the fracture phase, deformation and delamination followed the toughening mechanism observed for extrinsic deformation, in which the polymer material bound and bridged the tablets until full debonding or the development of microscopic voids [79, 102]. There are, however, limitations in the current understanding of the exact toughening mechanisms in effect associated with nacre-inspired glass. To clarify the contributions of delamination, deformation, and polymer bridging to overall toughness, future studies should entail comprehensive characterization using cutting-edge imaging and analytical methods.

The foregoing material describes nature's remarkable ability in building efficient and functional cellular structures. Understanding the concepts behind these natural designs could provide valuable insights to engineers and material scientists to develop novel structures and materials with improved

mechanical properties.

This study focuses particularly on the deformation behaviour of hierarchical lattice HCs, which deform as a function of complicated interactions of numerous aspects in their internal structures that are influenced by their distinct nature. Understanding how hierarchical HCs deform under different loading conditions is crucial for maximizing their performance in a variety of engineering applications.

Hierarchical HCs are referred to as multiscale structures, which implies that they are built up of nested unit cells that come in different sizes [21, 58]. Their hierarchical structuring allows them to distribute loads while resisting deformation [64] efficiently. During deformation, smaller unit cells within larger ones often fail or deform first, whereas larger unit cells remain relatively intact. Such a deformation mechanism allows hierarchical HCs to redistribute loads that are imposed on them. The external forces applied to such structures are typically transferred from collapsed or deformed unit cells to neighbouring unit cells that are still intact [11, 13, 58, 63, 103-111]. This load redistribution strategy serves the primary objective of safeguarding against localized failure and preserving the structural integrity of the entire hollow structure [11, 13, 107-111].

Ajdari et al. [112] created a hierarchical HC by substituting all three-edge joints of the regular hexagonal hollow build with smaller hexagons. Their work demonstrated that hierarchical HCs with one or two levels have a stiffer modulus of elasticity than regular HCs with the same relative density. The effects of thermal expansion, changes in temperature, and environmental factors such as humidity and corrosion on hierarchical HCs, however, are not examined in their work. The limitations identified in Ajdari and co-authors' work, as now reviewed in this chapter, suggest that, though hierarchical HCs show promise in terms of stiffness and effectiveness in the use of materials, their practical use warrants further research. Comprehending the effects of thermal expansion, temperature variations, and external factors such as humidity and corrosion is significant for ensuring the accuracy and strength of these structures in different mechanical loading scenarios. To fully grasp the bounds of hierarchical HCs, extensive experimental testing, materials advancement, and the development of new manufacturing technologies are required. Sun et al. [113] built the anisotropic multifunctional hierarchical HC (AMHH) by substituting the solid cell walls of the basic anisotropic HC (OAH) with the same-weight isotropic substructures referred to as triangular or Kagome HCs. This structuring approach yields two types of AMHH structures. The study showed that triangular HC substructures can enhance the in-plane stiffness of AMHH by 1.5 to 100 times, depending on the thickness-to-length ratio (t/l) of the oblique cell wall and the relative density of the OAH. However, the influence of boundary conditions and edge or vertex effects on the mechanical characteristics of these hierarchical structures has not been thoroughly reviewed not only in their study but also in the open literature. These considerations could result in significant effects on performance, particularly for engineering applications with edge or vertex constraints. The absence of extensive analysis of edge and vertex effects could affect the dependability and safety of AMHH structures in engineering applications. Unexpected failures or performance drops tend to occur close to the edges or vertices, wherein high-stress concentrations typically occur. Conducting thorough studies on the effect of edge and vertex behaviour on the general structural strength and stiffness of AMHH structures should prove useful. This includes predicting the patterns related to the distribution of stresses and determining possible failure regions. In addition, strategies for lowering high-stress concentrations close to edges and vertices should be devised. This may entail tailoring the configuration of the substructures or adding new support parts.

Chen et al. [114] investigated the in-plane compressive behaviour of a novel hierarchical lattice structure formed by substituting cell walls in regular HCs with triangular lattice topologies. The research conducted revealed that hierarchical HCs have high energy dissipation and shape integrity at strains of up to 60% during cyclic loading. Their experimental and numerical findings also suggest that the peculiar mechanical behaviour is accounted for by a hierarchical structure controlled by the triangular lattice's slenderness and the shape memory effect caused by thermal and mechanical compression. Figure 2-20

shows hierarchical lattice structures of different wall thicknesses formed by replacing cell walls in regular HCs with triangular lattice shapes [114].

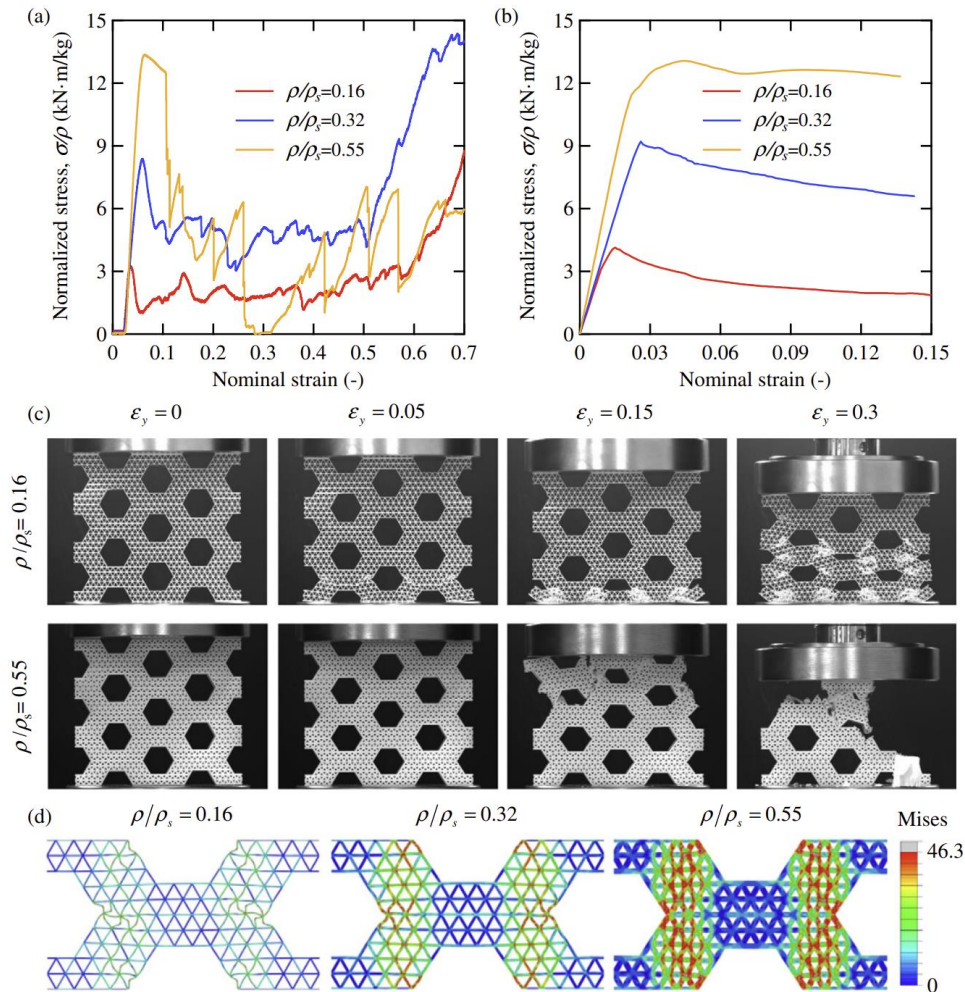


Figure 2-20. Experimental and numerical findings of built hierarchical lattice parts formed by replacing the cell walls with small-scaled triangular hollow structures of different wall thicknesses [114]

Song et al. [63] built bioinspired hierarchical polygon hollow metastructures with good mechanical characteristics. The hierarchical squared hollow structure with circular holes reduced stiffness by 0.84%, strength by 19.38%, and improved energy absorption by 199.67%. When compared to the regular parent hollow structures, the hierarchical HC with circular holes improved stiffness by 1.06%, reduced strength by 5.55%, and improved energy absorption by 345.24%. As a result, though the hierarchical design provides significant energy absorption benefits, its lowered strength and stiffness must be carefully addressed when examining possible applications, especially for load-bearing and high-strength conditions. Further studies should focus on tailoring these structures for a more balanced enhancement in all mechanical properties.

The walls of individual unit cells in hierarchical HCs typically experience buckling or collapse during deformation [58, 107]. This behaviour allows the honeycomb to absorb energy by converting mechanical energy into deformation of the unit cell walls [21, 58, 108-109]. The hierarchical structuring of unit cells often determines the order and extent of cell wall buckling and collapse, which in turn influences the structure's overall deformation behaviour [58, 103]. The hierarchical structuring of HCs not only allows for efficient energy absorption via phenomena such as cell wall buckling and unit cell collapse but also through

plastic deformation [58]. This is the primary reason why hierarchical HCs are typically adopted in engineering applications that require impact protection, such as automotive crash structures and protective gear [21, 58, 68, 103]. Hu et al. [115] reported a novel non-self-similar nested HC constructed using an aluminium alloy inspired by bamboo's vascular bundles. This structure consisted of one centred circular tube and six encircling circular tubes. The drop-weight test for impact pointed out that this nested HC's failure mechanism is a gradual diamond mode, exhibiting the highest specific energy absorption of 29.3 J/g. Their gradual diamond deformation mechanism or failure mode, shown in Figure 2-21 [115], suggests a controlled deformation pattern, which is ideal in structural parts wherein progressive energy dissipation is crucial to avoid catastrophic failure.

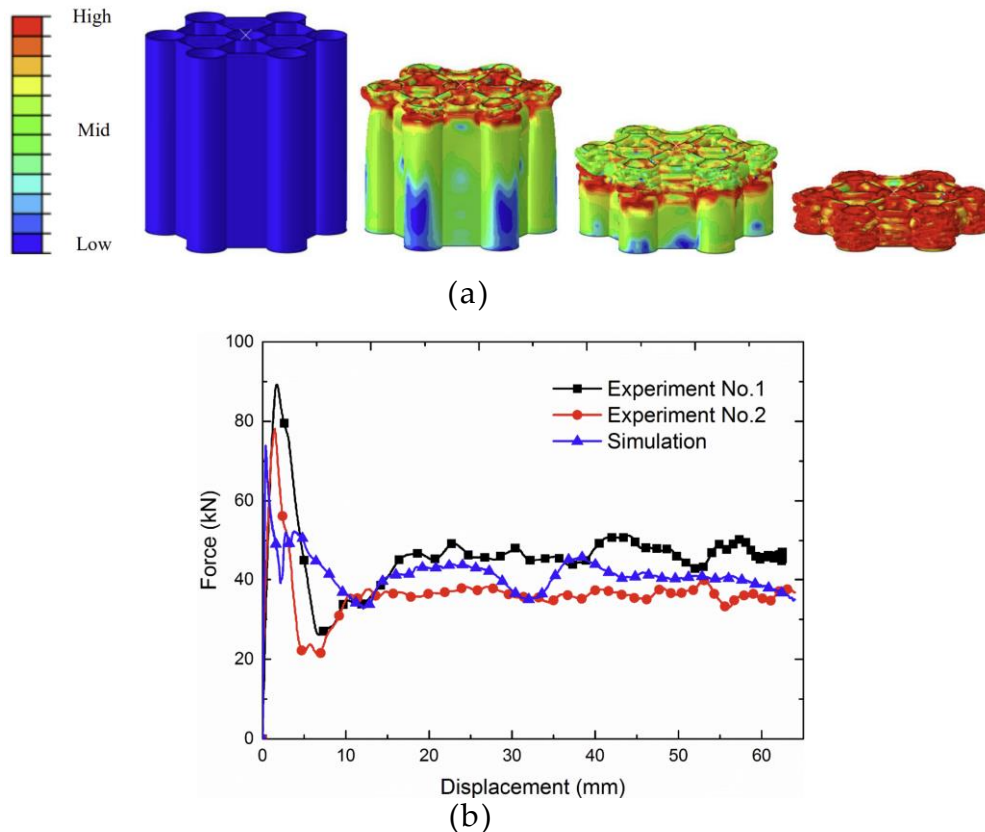


Figure 2-21. (a) Numerical findings showing the graphic progressive diamond mode of failure mechanism; and (b) the generated load-displacement curve based on experimental crush tests describing the gradual diamond deformation mechanism of a non-self-similar nested HC under dynamic extruded shell in-plane crushing loads [115]

The drop-weight impact test is a singular form of dynamic loading condition. The structure's behaviour under other loading conditions, such as cyclic loading and high-strain-rate impacts, was not examined and could result in different findings. Further analysis under numerous types of loading conditions, including cyclic loading, high-strain-rate impacts, and multi-axial loads, could provide a broader understanding of the structure's behaviour. Sun et al. [116] investigated HCs with first- and second-order hierarchical configurations under out-of-plane loading. They observed that both hierarchical structures enhanced the specific energy absorption by over 80% and 180%, respectively. Figure 2-22 shows their corresponding load-displacement curves describing the crushing behaviour of the preceding mentioned vertex-based hierarchical HCs [116].

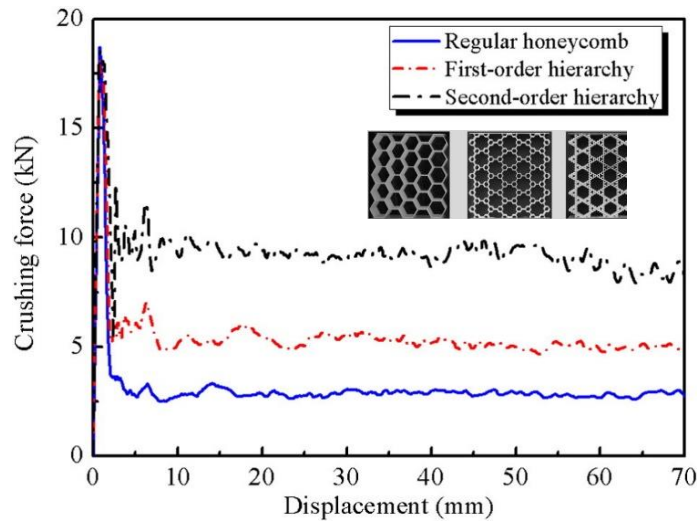
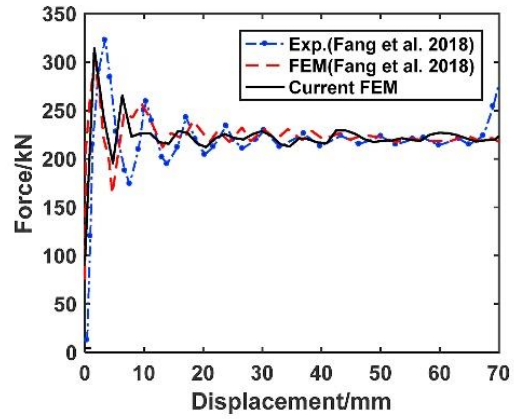
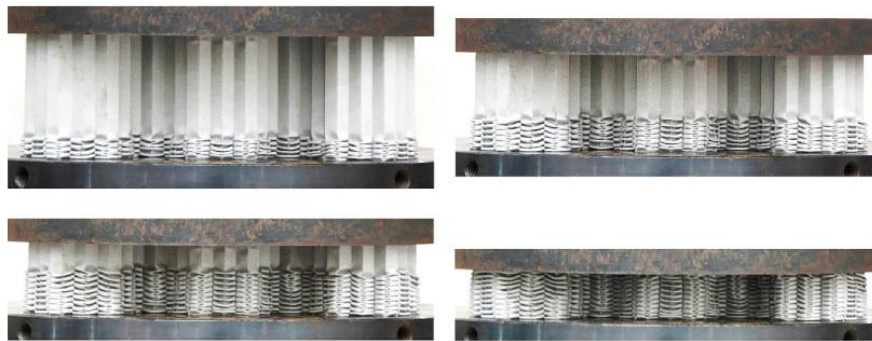


Figure 2-22. Load-displacement curve for numerical out-of-plane crushing of vertex-based hierarchical HCs built using aluminium [116]

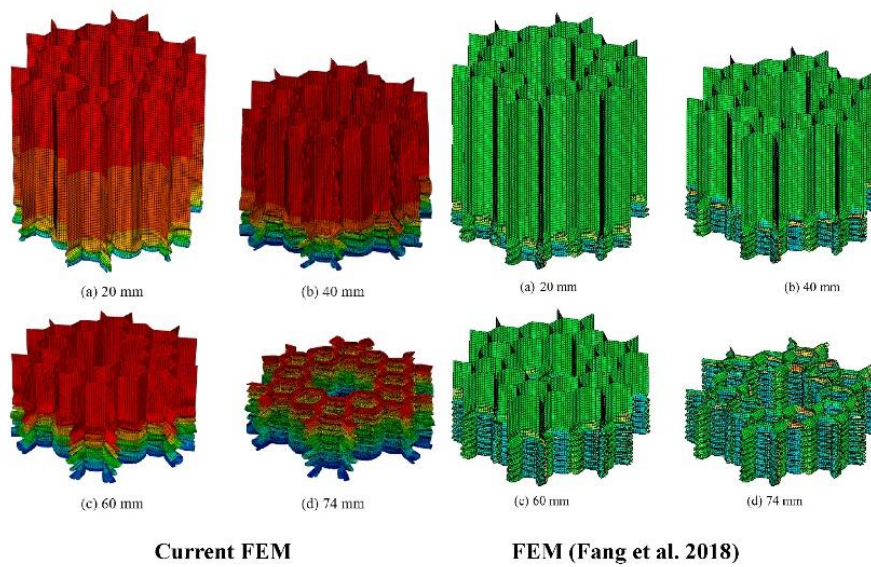
The significant rise in specific energy absorption by a value of 80% and 180% for first- and second-order hierarchical HCs, respectively, suggests that these structures could prove useful in applications that require high energy absorption, such as protective materials and crashworthy structures. Their study, however, fails to include an analysis of the surface roughness of the manufactured parts. Surface roughness in additively produced hierarchical HCs, particularly metallic parts, often increases as the grade of hierarchy increases, which could result in a substantial impact on their energy absorption behaviour. Extending work must focus on surface roughness analysis of these complicated builds to better comprehend its effects on the energy absorption property. Zhang et al. [117] added a triangular structure into a regular HC via a vertex substitution strategy. They reported that the plateau stress and specific energy absorption were improved by 127% and 109%, respectively, in the in-plane ribbon direction. For the identical characteristics highlighted in the preceding sentence, an improvement of 122% and 108% was found along the in-plane width direction, respectively, whereas improvements of 30% and 34% were obtained under out-of-plane loading conditions. Figure 2-23 and 2-24 shows their work on crushing behaviour, with reference to out-of-plane and planar in-plane loading conditions, respectively [117].



(a)



(b)



(c)

Figure 2-23. Experimental and numerical findings for out-of-plane crushing of vertex-based hierarchical HCs with triangular substructures built using aluminium material [117]

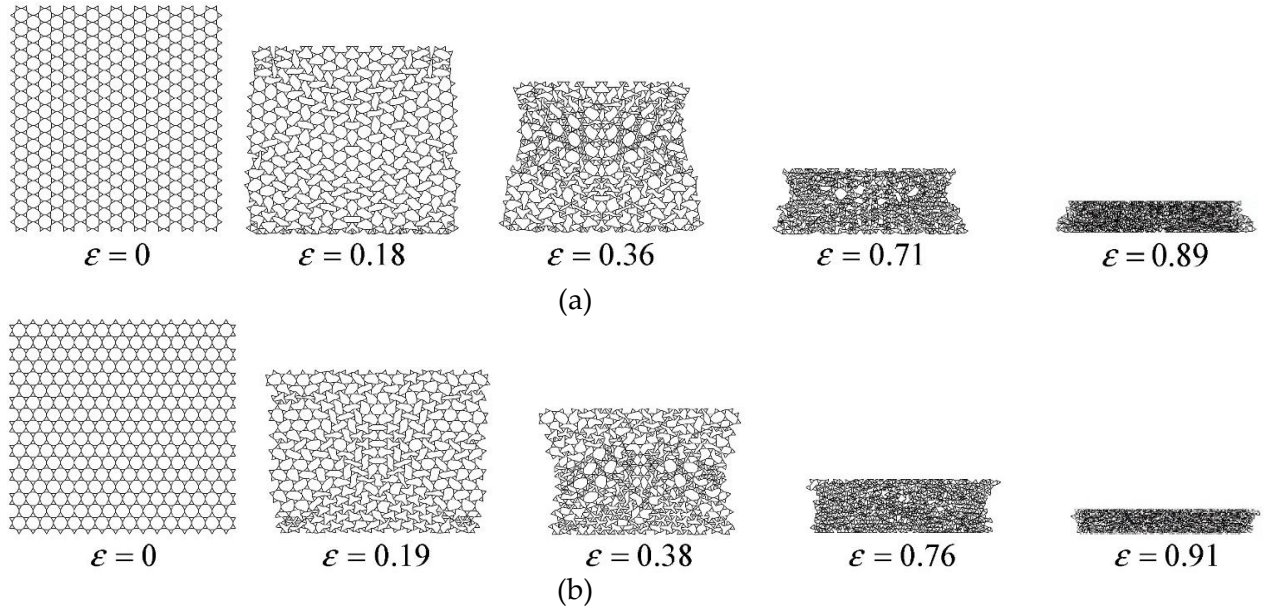


Figure 2-24. From top to bottom, the graphics represent the deformation histories generated for in-plane crushing of a line beam vertex-based hierarchical HC with triangular substructures along the width and ribbon directions, respectively [117]

The analytical models adopted in the work conducted by Zhang et al. [117] describe the crushing behaviour of the produced intricate structures based on general mathematical representations of the absorbed energy EA and specific absorbed energy SEA . The analytical models often adopted during the crushing process of the discussed structural parts are expressed in equations 2.1 and 2.2, respectively.

$$EA = \int_0^{\delta} F d\delta \quad (2.1)$$

$$SEA = \frac{EA}{M} \quad (2.2)$$

The symbols F , $d\delta$, M represent the crushing load, crushing displacement and overall mass of the structural part, respectively. Given the way various parts of the structural frame are connected via the nodes, these models could fail to predict the complicated behaviour that is often observed at the vertices of such systems. It is imperative to extend work into building advanced analytical models that account for the complex interactions between structural parts at the vertices. Effective application of advanced behaviour models could provide fresh insights into how the complex connectivity at the vertices influences the behaviour of hierarchical HCs. He et al. [118] designed a spiderweb-based hierarchical HC by incorporating a smaller hexagon structure into the centre of the parent structure, emerging in a hexagonal network design. Their numerical findings indicated that the specific energy absorption of first- and second-order hierarchical HC increased by 62.1% and 82.4%, respectively. The numerical models, however, are generic and fail to account for particular engineering conditions such as dynamic impacts, changing temperatures, and lasting strength, all of which have significant effects on the effectiveness of hierarchical structures in engineering applications in aerospace, automotive, offshore, and medical fields. Extending studies must focus on integrating the numerical models to specific engineering uses such as scaffolding in bones and crash behaviour of automobile bumpers. For the latter case, crash behaviour models tailored to automotive uses could lead to the development of lighter, more effective automobiles that meet safety criteria while reducing fuel consumption and emissions, particularly sports racing cars. For the expected prospect, modern algorithms are used to develop new surgical techniques and materials, extending past the boundaries of what is currently attainable in regenerative medicine and orthopaedics. Tan et al. [119] generated a new hierarchical re-entrant HC design by substituting the cell wall of auxetic HC with regular

hexagonal and triangular polygon shapes. Their numerical findings suggested that, as contrasted with regular re-entrant HC, hierarchical HC improved specific energy absorption and crushing force by approximately 292% and 298%, respectively, under a quasi-static loading condition. Qi et al. [58] compared and categorized mechanical parameters of normal classical HCs and their related hierarchical configurations. They made available bar graphs to describe mechanical performance ratios. As reported in their findings, the specific absorbed energy, modulus of elasticity, and compressive strength increased by 590% with ID 24, 1230% with ID 28, and 316% with ID 23, respectively, as envisaged in Figure 2-25 [58].

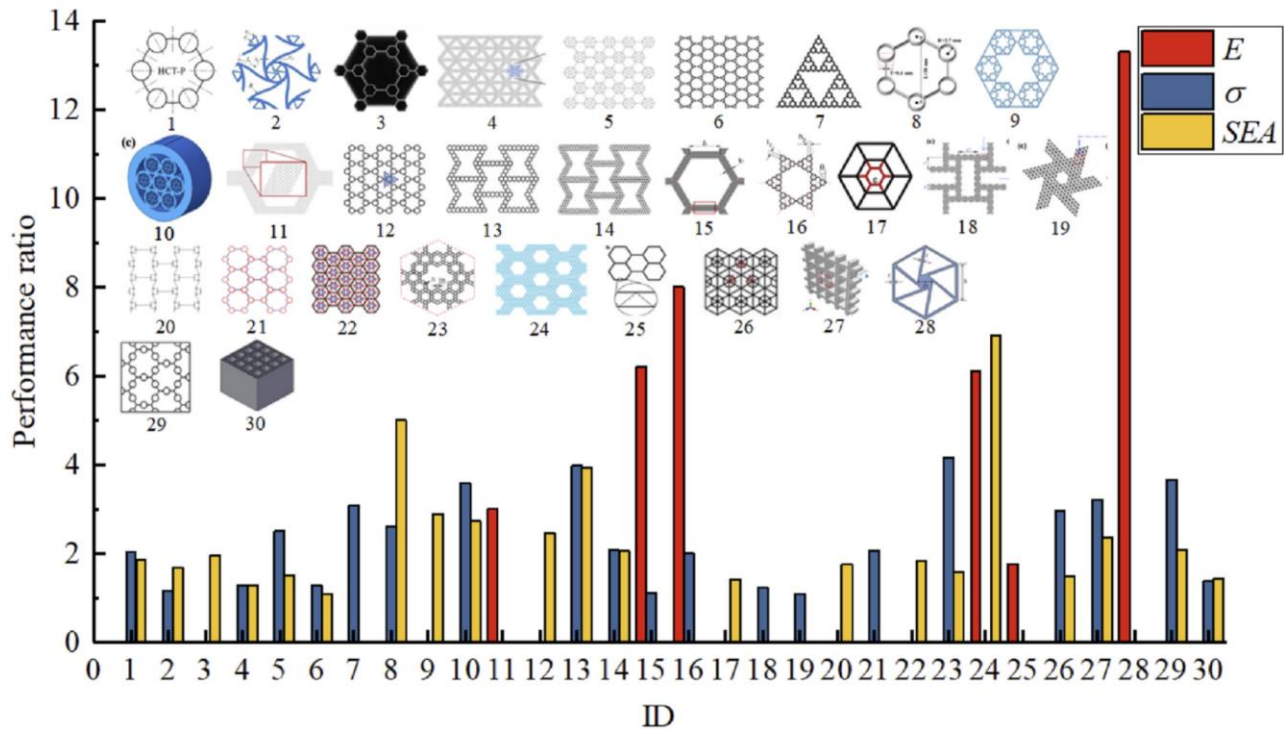


Figure 2-25. Mechanical characteristics of regular HCs and hierarchical HC builds are contrasted with regard to performance ratio [58]

The hierarchical configuration of unit cells often results in anisotropic deformation behaviour, which implies that the mechanical behaviour of the hierarchical honeycomb differs based on the chosen direction of loading [11, 13, 58, 108-111]. Anisotropic properties result from asymmetry in unit cell configurations and sizes within the overall structure [58, 107-109]. Therefore, understanding and characterizing this heterogeneity is often crucial when predicting and optimizing the structural performance of hierarchical HCs in engineering applications. The deformation behaviour of hierarchical HCs is also dependent on the size and configuration of the unit cells built at different length scales [58, 107]. Deformation mechanisms at smaller scales differ from those at higher scales, causing the hierarchical HC's overall mechanical behaviour to change [11, 13, 58, 107, 120]. It is important to account for scale dependency as it is critical for accurate modelling and prediction of the behaviour of hierarchical HCs subjected to different loading conditions. Chen et al. [121] developed numerical models that describe better thermal resistance in hierarchical HC lattice metamaterials. Their heat transfer analysis suggested that hierarchical HCs are capable of thermal anisotropy while also enhancing thermal resistance because of their hierarchical structuring and topologies. Their findings are primarily theoretical and are based on numerical models only for support. Validation by experiment is required to confirm the predicted thermal resistance and anisotropy in engineering applications of such hierarchical HC lattice metamaterials. Through successful experimental validation of the findings, Chen and colleagues [121] suggested that through numerical modelling

strategies, the hierarchical HC lattice metamaterials could be used to design cutting-edge thermal management systems in electronics, lowering areas of concern and improving overall device effectiveness via tailored thermal resistance and anisotropy.

Despite their hierarchical structure and inherent toughness, hierarchical HCs are prone to fracture and do fail under extreme load conditions [11, 13, 58, 105-106, 111]. Comprehending the fracture and failure mechanisms of these structures is crucial when designing engineering structures required to withstand specific loading conditions while guaranteeing safety and reliability in structural applications. Techniques such as finite element analysis (FEA) and multiscale modelling are crucial and popular for providing quick understanding and prediction of the deformation behaviour of hierarchical HCs, compared to experimentation [58, 107-110]. FEA models can represent the complex interactions between unit cells across different length scales, thus providing insight into deformation mechanisms and failure possibilities [107]. Experimental validation of these computational predictions is, however, critical in guaranteeing the fidelity of models and expanding the comprehension of hierarchical HC deformation behaviour in structural applications [11, 13, 58, 111]. Ryvkin and Shraga [122] used numerical modelling approaches to examine the effect of self-similar hierarchical structuring on the brittle fracture behaviour of a 2D HC. Their work revealed that an HC with a higher level of hierarchy has greater fracture toughness than one with a lower level. They also suggested that hierarchical architecture has a more advantageous effect on HCs with lower relative densities. A comparison of Mode I fracture toughness between second-order hierarchical HCs and regular HCs revealed a 5.4% increase for $\rho = 0.115$ and 39% for $\rho = 0.0289$, respectively. Their work is limited to Mode I and II fracture toughness, therefore ignoring the implications of additional fracture modes such as Mode III, also referred to as out-of-plane shear mode or tearing mode, which can occur in engineering applications. The emphasis on Mode I and II fracture toughness limits our comprehension of how hierarchical configuration influences overall fracture toughness under different loading conditions; therefore, extended studies are required to investigate its effects on other fracture modes. Ajdari et al. [112] investigated the mechanical properties of hierarchical HCs with self-similar microstructures using theoretical, experimental, and numerical modelling methods. Their analysis showed that the primary and secondary HC structures were 2.0 and 3.5 times harder than regular HCs, respectively. The capacity of the modelling and experimental methods could limit the degree of abstraction and resolution of the investigated hierarchical microstructures. A limited resolution could result in a lack of comprehension of how microstructural details at various scales influence overall mechanical properties, which can result in missing crucial insights. To overcome scale and resolution constraints, prospective studies should use advanced methodologies that are capable of better resolution and multiscale analysis. This allows for an extensive understanding of how microstructural characteristics affect overall mechanical performance.

The review in this section of the chapter clearly shows that the deformation behaviour of hierarchical HCs is typically influenced by their multiscale design, load transfer mechanisms, anisotropic characteristics, scale dependency, energy absorption capacities, and fracture behaviour. By fully comprehending and characterizing these aspects, engineers could benefit more from developing hierarchical HCs with specific mechanical properties for a variety of engineering applications, such as lightweight parts, impact-resistant materials, and energy-absorbing structures.

2.7. Analytical modelling of the deformation behaviour of cellular and lattice structures

2.7.1 Stress-strain curves for cellular and lattice structures

This subsection gives an overview of the known two-stage stress-strain curve for cellular and lattice structures. It then proceeds to compare it with a newly suggested curve in the next subsection, aiming to extend our comprehension of deformation mechanisms.

Two-stage stress-strain curve for cellular designs. During the first stage of deformation observed in the typical two-stage stress-strain curve, cellular structures are represented as acting elastically, with a linear relationship between stress and strain. During this stage, the structure's cells are assumed to stretch

or compress while remaining structurally intact. The slope of the stress-strain curve in this region is taken to represent the material's stiffness, also known as Young's modulus [123-124]. Following the first deformation, cellular structures often go into a plateau state with a relatively constant stress level despite rising strain. The plateau phase is caused by different kinds of mechanisms, including buckling, bending, and collapse of cell walls, which allow the material to withstand more deformation without significantly increasing stress. During this stage, the material could undergo significant plastic deformation while remaining under relatively constant stress, exhibiting a high level of energy absorption and structural resilience [124-126]. Figure 2-26 shows a typically adopted two-stage stress-strain curve for cellular structures in engineering uses [124].

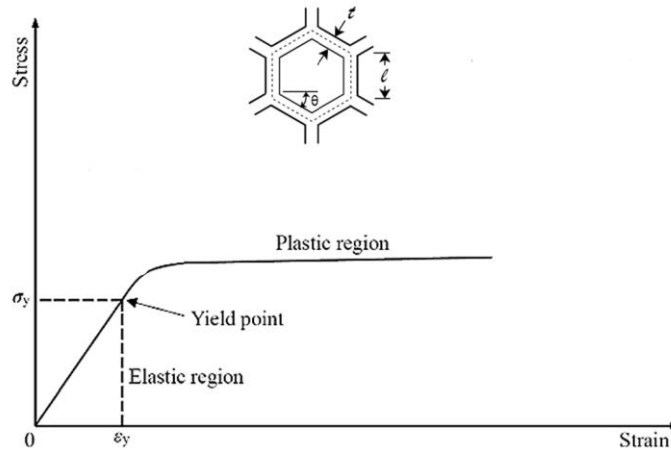


Figure 2-26. A typical two-stage stress-strain curve for cellular designs [124]

In its entirety, the open literature only discusses a two-stage deformation curve for cellular structures, which ranges from elastic behaviour characterized by a linear stress-strain response to the plateau phase, in which the material undergoes plastic deformation while maintaining close to constant stress. Comprehending these behaviours has implications when building and optimizing cellular designs that meet particular performance standards such as mechanical strength and energy absorption.

2.7.2 A novel deformation mechanism added to the two-stage behaviour of cellular designs

Cellular structures, such as foams, honeycombs, and numerous types of lattice structures, have different mechanical properties due to their intricate internal designs. Though the stress-strain curve for cellular structures generally follows standard trends, such as elastic deformation followed by plastic deformation of the cellular materials [124], additional mechanisms unique to these structures are here.

In a typical stress-strain curve, the elastic region depicts the range of elastic deformation, which means that the material returns to its original shape after the stress is removed. However, in certain cases, particularly with cellular designs or porous structures, there could be two separate stages of elastic deformation that have not been reported in the available literature. A new stress-strain curve for cellular parts, which has a four-stage deformation mechanism before the structure undergoes densification, is proposed, as shown in Figure 2-27.

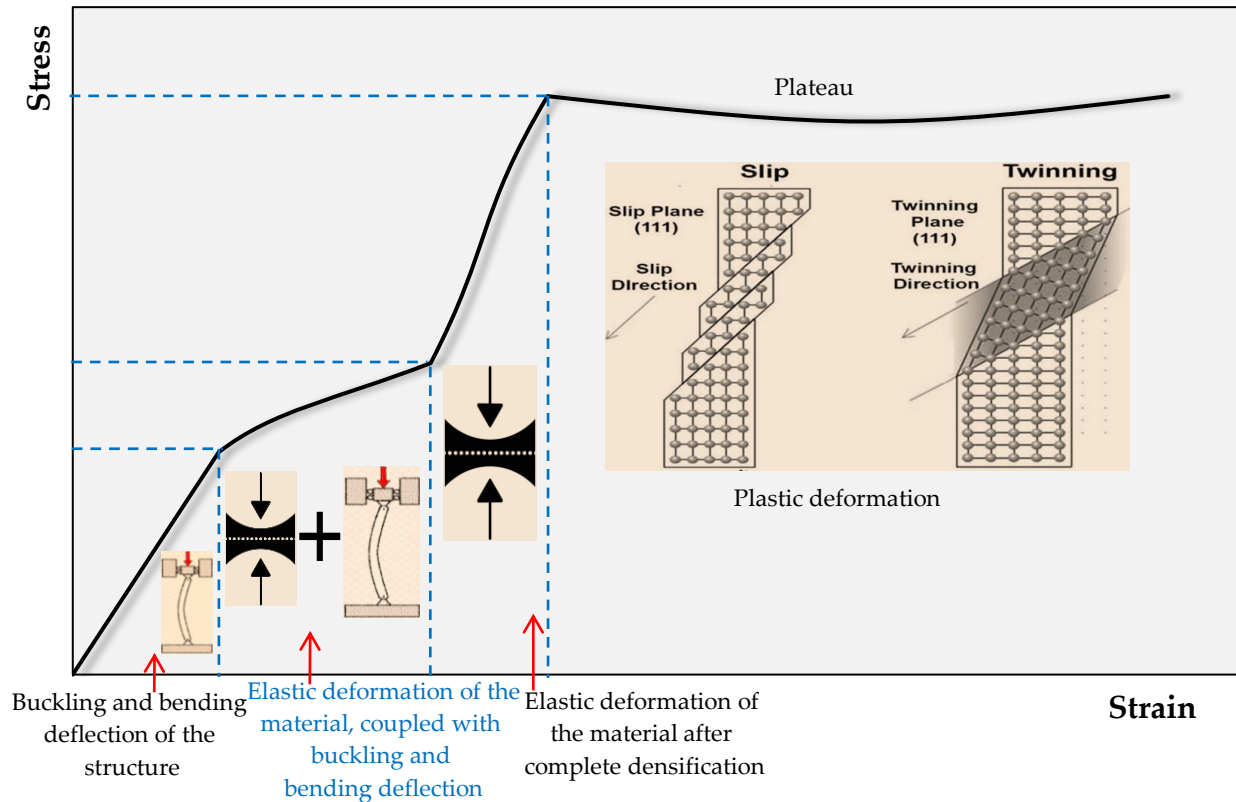


Figure 2-27. A four-stage behaviour stress-strain curve for cellular designs

The first stage, identified here, represents the buckling and bending deflection of the structure. The second stage, densification, causes elastic deformation of the material, combined with buckling and bending deflection of the structure. The third stage is the elastic deformation of the material after full densification. Stage four is plastic deformation, leading to the formation of a plateau. Researchers and engineers can better comprehend and analyse the behaviour of complicated structures and materials by splitting the elastic region into two phases. This allows for more advanced characterization of elasticity and aids in the design of structures that incorporate specific performance criteria.

Though the two-stage stress-strain curve provides useful insights into the deformation behaviour of cellular structures, recent research by the author [127] recommends a more advanced comprehension that considers other deformation mechanisms. The recommended curve in the last three paragraphs of the discussion aims to expand our understanding of cellular structural behaviour, and by including the following features in the list of future work to be tackled, information on the mechanisms of deformation for cellular structure is expected to become more detailed. As a result of this, the modelling approach to predicting the mechanical behaviour of cellular structures is expected to improve.

In addition to the two elastic stages suggested and the typical plateau stage, the author highlights that the curve also includes an intermediate transition area between the elastic structural deformation and elastic material deformation phases. This transition phase indicates a progressive shift from elastic structure to elastic material deformation, during which the material's deformation mechanisms change, such as cell wall bending, localised buckling, or cellular architecture reconfiguration. By recognizing this intermediate step, the curve provides a more thorough representation of the deformation process, allowing for a better understanding of the underlying mechanisms that govern the material and structural behaviour

in the elastic region. The authors also mention that the suggested curve is significant for improving energy absorption mechanisms beyond the typical plateau phase. By extending the deformation mechanism beyond the plateau region, the curve could highlight the prospect of additional energy dissipation mechanisms, such as strain hardening, strain rate sensitivity, or material reconfiguration, which are not often reported in the available literature. This expanded understanding allows for the development of cellular structures with higher energy absorption capacity, mechanical robustness, and resilience under dynamic loading conditions.

2.7.3 Deformation behaviour models for cellular structures

Cellular designs, typically built up of repeated unit cells, exhibit complex deformation behaviour due to their peculiar architecture. Different models have been developed that describe this behaviour according to various cellular structures and uses [128-129]. This section of the paper particularly examines the Gibson and Ashby models, which are used for different investigations on the deformation behaviour of cellular structures found in the literature. The first model, put forth by Ashby and Gibson [124, 130], relates the mechanical properties of foams to their relative densities. It is based on the concept of scaling principles as well as on empirical studies of numerous types of foams. Fundamental mechanical properties as functions of relative density, elastic modulus, yield strength, and energy absorption, are captured by the model. The first Gibson and Ashby model has been improved on and updated over the years to improve its accuracy and usefulness. These improvements take account of aspects such as size, shape, or thickness of the cell wall. The Gibson and Ashby model has been extensively adopted in the design and optimization of cellular materials for a wide range of engineering applications, including impact absorption, thermal insulation, lightweight structures, and biomedical implants [124-130]. The model aids engineers and materials scientists in choosing or designing foams with characteristics matched to their intended application by predicting the mechanical behaviour of foams based on their relative densities.

The Gibson and Ashby models provide a framework for analysing the mechanical behaviour of cellular structures centred on their geometry and material properties. Their models for predicting the behaviour of cellular structures are typically built based on two geometries, namely the open and closed cellular shapes, previously presented in Figure 1-1, in Section 1.2 of Chapter 1 [130].

Both open and closed cellular structures have advantages and drawbacks, and the choice between the two is often influenced by the application's specific requirements, including mechanical performance, weight considerations, fluid permeability, and manufacturing constraints [124-127, 129]. The behaviour models of these two types of cellular structures are limited to elastic deformation.

Open cellular designs at first exhibit linear elastic behaviour when loaded with small deformations, primarily governed by stretching and bending of the cell walls and struts. The structures return to their original shape once the applied load is removed if the deformation remains within the elastic limit of the material. However, open cellular structures are also liable to buckling under compressive loads, particularly for slender struts or cells [124, 130]. Figure 2-28 shows Gibson and Ashby's models built to describe the bending and buckling behaviour of open cellular structures [130].

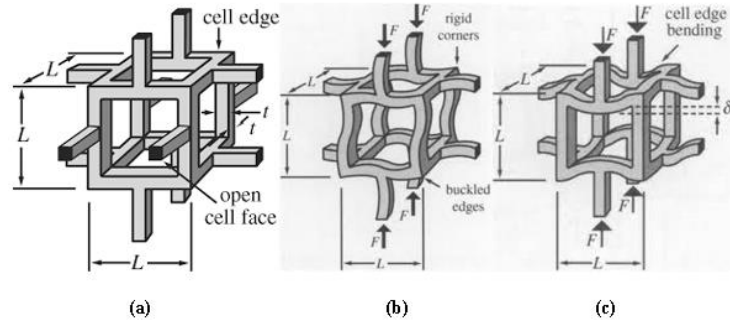


Figure 2-28. Open unit cell shape that has (a) no deformation, (b) buckling deformation, and (c) bending deformation [130]

Designing for critical loading conditions is a paramount concept in the field of engineering that must be considered for safety, reliability, and optimal performance in a wide range of applications, including civil infrastructure, automotive, aeronautical, and medical engineering [131]. Presently, only critical loading conditions in the transverse and axial directions are considered in the deformation behaviour models for cellular structures discussed here. The geometries for cellular designs are normally built up of beams or ribs. Therefore, theories of beams are often adopted to develop their corresponding behaviour models [124, 127-130]. Figure 2-29 shows the transverse loading of an open cellular structure, represented by the mid-span concentrated transverse loading of a beam fixed at both ends. This load case is often thought of as the critical transverse loading scenario for a cellular structure [132].

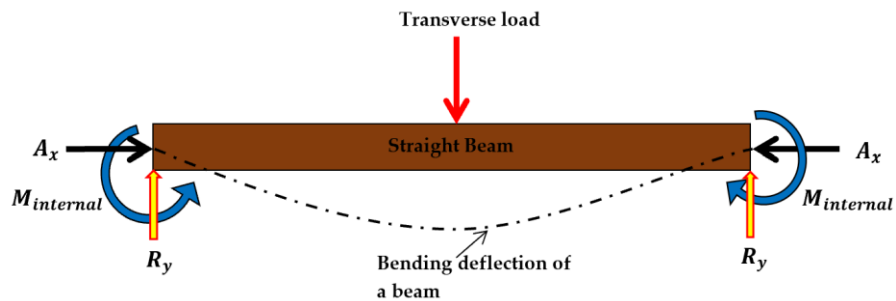


Figure 2-29. A mid-span concentrated transverse loading of a beam fixed at both ends, similar to one used in building cellular structures [132]

For simplicity, the ensuing analysis is based on a beam with a rectangular cross-section with sides of breadth b and depth h , both of which are equal and may be represented by symbol t . Figure 2-30 shows the cross-section and the associated parameters used.

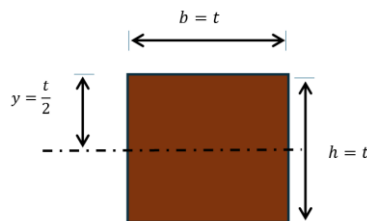


Figure 2-30. Cross-section of rectangular beam and corresponding parameters adopted

The cross-sectional parameters of a rectangular beam that are observed in Figure 2-30 are used to derive the second moment of area I presented in Equation 2.3.

$$I = \frac{bh^3}{12} = \frac{t^4}{12} \quad (2.3)$$

Following the determination of the second moment of area, Equation 2.4 shows the maximum bending deflection, y_{max} , due to transverse loading of the beam structure at midspan with both ends fixed, as determined by beam theory.

$$y_{max} = \frac{\epsilon}{R} = \frac{FL^3}{192EI} = \frac{FL^3}{16Et^4} \quad (2.4)$$

The symbols ϵ , R , F , L , and E represent the normal strain, radius of curvature, applied load, beam length, and elastic modulus of the material, respectively. The expression in Equation 2.4 highlights the fact that the maximum transverse deflection, y_{max} of ribs/beams for a cellular structure is inversely proportional to both the modulus of elasticity E of the chosen material of the structure and inversely proportional to the t raised to power 4. These relationships are from the equation seen to be linear and non-linear, respectively. This implies that the cellular structure with a greater value of parameter t will be able to withstand higher transverse loads than one with a smaller value. This is consistent with the observations in reference [132].

The maximum bending stress $\sigma_{b_{max}}$ generated in the cell walls or ribs of a transversely loaded cellular structure is determined using the following general equation for bending [124, 130, 132].

$$\sigma_{b_{max}} = \frac{M_{max}}{I} y \quad (2.5)$$

The symbol M_{max} represents the maximum bending moment experienced under transverse load F on the ribs building up the cellular structure. For mid-span concentrated loading, the M_{max} is typically described by Equation 2.6.

$$M_{max} = \frac{F}{2} x = \frac{FL}{4} \quad \text{for } x = \frac{L}{2} \quad (2.6)$$

The symbol L represents the length of the transversely loaded beam or rib of the cellular structure. Substituting Equation 2.3 and 2.6, with expressions for I and M_{max} , respectively into Equation 2.7 gives rise to the following expression for $\sigma_{b_{max}}$:

$$\sigma_{b_{max}} = \frac{3FL}{t^4} y \quad (2.7)$$

From the numerous studies conducted on the behaviour of loaded beam structures [124-130, 132], it is known that $\sigma_{b_{max}}$ occurs on the outermost fibres of the ribs or beams building up the cellular design. Therefore, Equation 2.7 can be simplified to:

$$\sigma_{b_{max}} = \frac{3FL}{2t^3} \quad (2.8)$$

Clearly, from Equation 2.8, $\sigma_{b_{max}}$ is inversely proportional to parameter t raised to power 3. The relationship is non-linear, which is consistent with the observations made in references [126-130]. The maximum bending stress, $\sigma_{b_{max}}$ is also seen from the equation to increase with increasing L/t^3 ratio. In addition to the bending stresses, shear stresses also play a significant part in the structural stability of lattice structures. Understanding how shear stresses are distributed within the connecting members assists in ensuring that they remain within the elastic limit of the material to prevent premature failure. The shear stress induced in the rectangular cross-section ribs for a transverse concentrated load F is described by Equation 2.9 as follows [132].

$$\tau_{xy} = V \frac{A\bar{y}}{bI} = \frac{3F}{t^4} \left[\left(\frac{t}{2} \right)^2 - y_1^2 \right] \quad (2.9)$$

The symbol V in Equation 2.9 represents the transverse shear force induced in each rib of the chosen lattice design. Parameter V for the centrally loaded, simply supported beam is known from standard engineering texts to be equal to $F/2$. The maximum transverse shear stress is known to occur at the centroidal axis where the parameter y_1 is equated to zero, thus reducing Equation 2.9 to [132]:

$$\tau_{xy}|_{max} = \frac{3F}{4t^2} \quad (2.10)$$

The maximum transverse shear stress is seen from Equation 2.8 to be inversely related to the parameter t raised to the power 2. As with Equations 2.2 and 2.6, this relationship is non-linear. Thus, small changes in the parameter t could result in significant differences in the maximum transverse shear stress. From the expressions presented in Equation 2.7 and 2.9, the ratio between the maximum bending stress and the maximum transverse shear stress is derived as:

$$\frac{\sigma_{bmax}}{\tau_{xy}|_{max}} = 2 \left(\frac{L}{t} \right) \quad (2.11)$$

Since the ratio L/t for cellular structures is always greater than unity, the ratio $\sigma_{bmax}/\tau_{xy}|_{max}$ will always be greater than one. This, combined with the knowledge that shear yield stress is known to be equal to half the direct yield stress [132], suggests that failure for such cellular structures is L/t more times probable to occur due to induced bending stresses than from induced shear stresses, for a concentrated load applied at midspan. This is similar to what has been reported in references [124, 132]. The L/t ratio for cellular structures typically equals at least 5, which ensures sufficient structural stability. This ratio helps maintain the material's ability to resist bending deformation under loads [124, 130].

Gibson and Ashby [130] reported that either direct or buckling deformation is likely to occur in the case of longitudinal loading of the rib or beam structures used to build cellular parts. In its simplest form, the direct deformation of a unit rib or beam used to build cellular designs can be represented by the expression for direct stress given here as Equation 2.12.

$$\sigma_{x(a)} = -\frac{F}{A} = -\frac{F}{t^2} \quad (2.12)$$

The symbol A represents the cross-sectional area $bh = t^2$, whereas the minus (-) sign represents compression loading. The longitudinal stresses are caused by the internal opposition to the externally imposed axial load F , causing compressive or tensile behaviour in the beam [132]. Therefore, the direct deformation δ caused by direct axial loading of the beam can be represented as shown in equation 2.13.

$$\delta = \frac{PL}{EA} = \frac{PL}{Et^2} \quad (2.13)$$

The symbol E represents the modulus of elasticity of the chosen material. Buckling deformation can also occur in these structurally thin members, also referred to as struts, under direct axial loads. This deformation behaviour is determined by the stiffness, boundary constraints, and the value of the load that is imposed on the struts. Figure 2-31 shows the buckling behaviour of a strut in an open cellular configuration with fixed ends. Their critical load results in buckling along the effective length L_e , as highlighted in the figure [132].

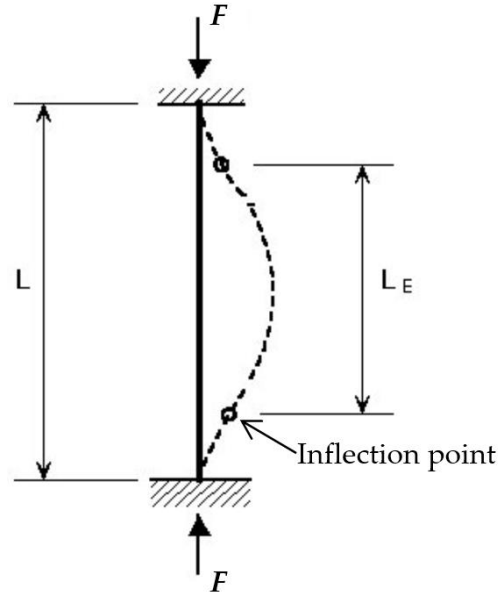


Figure 2-31. A strut fixed at the ends under direct axial loading [143]

Based on the general Euler buckling theory, Gibson and Ashby [124, 130] derived the critical buckling load P_{cr} as presented in Equation 2.14.

$$P_{cr} = \frac{\pi^2 EI}{L_e^2} = \frac{\pi^2 Ehb^3}{12L_e^2} = \frac{\pi^2 Et^4}{12L_e^2} \quad (2.14)$$

The critical buckling stress σ_e of a strut is determined from Equation 2.14 as:

$$\sigma_e = \frac{P_{cr}}{A} = \frac{\pi^2 Et^2}{12L_e^2} \quad (2.15)$$

The following section compares the critical buckling stress, maximum bending stress, and maximum transverse shear stress under the same applied point load F . This comparison is essential to assessing the relative significance of each stress type and serves as the core conclusion of all the theories presented in this section.

The elastic deformation behaviour of closed cellular structures is arguably more complicated compared to that of open cellular structures. For closed cellular structures, cases of internal pressure combined with the transverse as well as direct loads in the vertices must be considered [124, 127-128]. The deformation of closed cellular structures involves not only the effects of these last two types of loads but also the stretching of cell wall membranes under internal pressure. The pressure generated inside closed cellular structures is caused by the compression of fluids enclosed in cavities found in the cellular cells and the corresponding shortening and lengthening of the cell walls [130-131]. Figure 2-32 shows a hexagonal closed cellular structure, in addition to the two orientations in which the cellular structure extends under applied internal or external pressure [130].

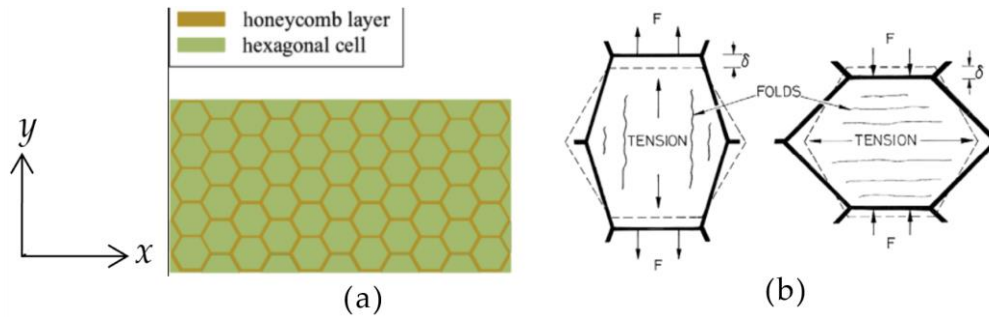


Figure 2-32. A hexagonal closed cellular structure, (a) the geometry before deformation, and (b) the stretching deformation in the x - and y -directions [130]

Given that pressure loads act over finite areas, the load is considered to be uniformly distributed across the span, and therefore, the effects of stress concentration are often disregarded. Depending on the magnitude of the ratio L/t , a loaded cell wall could be regarded as a thick or thin plate with fixed-end constraints on all four edges [124, 130-134]. Cellular structures typically occur as thin plates, which effectively minimizes the usage of material usage, while interconnection of the walls provides additional restraint of each wall, thus maintaining the structures' overall load-bearing capacity [13, 124, 130, 135-137, 138].

The classical theory of plates, specifically the Love Kirchhoff's theory with its eight assumptions [139], can be used to determine the deflection and stresses induced in them by any applied loads.

The case of bending moments (M_x and M_y) acting on the edges of a plate is represented as shown in Figure 2-33, which for a thin plate leads to the generation of a 2D stress state [139].

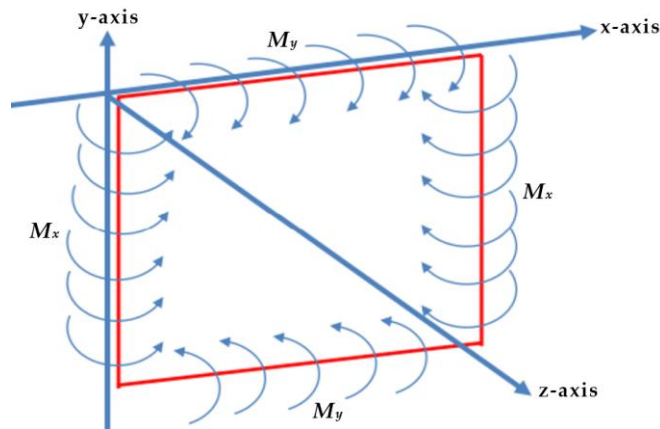


Figure 2-33. A 2D representation of a thin plate under x - and y -directional bending moments [139]

It is clear from Figure 2-33 that the induced bending moments due to externally applied loads cause out-of-plane bending deflections of the thin plates in cellular structures. Such bending deflections are counteracted by opposing bending moments induced by pressure generated inside closed cellular structures, which is caused by the compression of fluids contained in the cavities found in them. Consequently, closed cellular architecture deforms not just at the vertices connecting unit cells but also because of in-plane stretching of the thin walls used to encapsulate the fluids inside their cavities. Equations 2.16 and 2.17 determine the bending moments generated by a thin plate in the x - and y -direction, respectively, as a function of the in-plane mutually orthogonal radii of curvature and parameter D , which is defined as shown in Equation 2.18 [140].

$$M_x = D \left[\frac{1}{R_x} + \frac{\nu}{R_y} \right] \quad (2.16)$$

$$M_y = D \left[\frac{1}{R_y} + \frac{\nu}{R_x} \right] \quad (2.17)$$

$$D = \frac{Et^3}{12(1-\nu^2)} \quad (2.18)$$

The symbols D , ν , t , and R represent the flexural stiffness, Poisson's ratio, the thickness of the unit cell, and radii of curvature of the loaded thin plate, respectively. The direct stresses in a thin plate are inversely related to the radii of curvature and directly proportional to the distance from the neutral plane, through the thickness of the plate [139, 141]. It has been shown in standard engineering textbooks that with some manipulation, the foregoing equations reduce to Equations 2.19 and 2.20 for the direct in plane-stresses induced in such plates [139]

$$\sigma_x = \frac{12M_x t}{h^3} \quad (2.19)$$

$$\sigma_y = \frac{12M_y t}{h^3} \quad (2.20)$$

2.7.4 Proposed model combining direct, buckling and bending deformation behaviour of lattice designs

Integrating direct, buckling and bending deformation behaviours in a new model proposed here for lattice structures is expected to result in better predictions of their mechanical deformation behaviour. The proposed model is based on the free body diagram shown in Figure 2-34, showing two connected ribs of an open lattice structure under combined direct and bending loads.

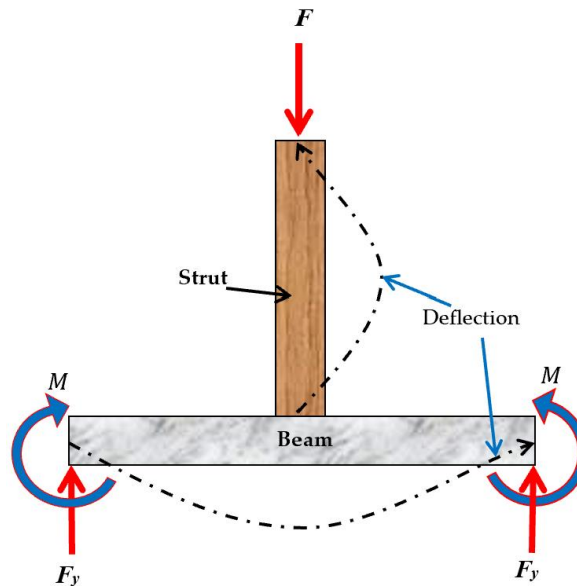


Figure 2-34. Combined direct, buckling and bending deformation of ribs used to build open lattice structures

To determine which one of the direct, buckling and bending deformations arising from the load shown in Figure 2-34 is critical, the direct and shear yield stresses of the material must be combined in a single function together with the direct, shear and bending loads arising from the applied load in the structure. This approach provides a better means of accessing the failure of lattice structures as opposed to the prevalent approach that carries out the analysis load by load and member by member [1, 124, 126]. It is

known that the maximum bending moment and bending stress at yield in the horizontal member in Figure 2-34 will occur at midspan and are given by the following respective expressions [132, 139]:

$$M_{max} = \frac{FL}{4} \quad (2.21)$$

$$\sigma_y = \frac{FL}{8t^3} \quad (2.22)$$

where the terms F , L , σ_y , and t in these two equations stand for applied load, length of the beam or strut, bending stress at yield, and thickness of the walls of the beam or strut, respectively. To determine the maximum allowed bending load $F_{b_{max}}$ at yield, the th applied load (F) is made the subject in Equation 2.22 at this maximum allowed value, thus:

$$F_{b_{max}} = \frac{8\sigma_y t^3}{L} \quad (2.23)$$

In the case of buckling of the vertical rib in Figure 2-34, the critical load presented here as $F_{e|_{max}}$ is equated to the term for the first mode of buckling in the Euler equation thus [139]:

$$F_{e|_{max}} = \frac{\pi^2 EI}{L_e^2} = \frac{4\pi^2 EI}{L^2} = \frac{\pi^2 Et^4}{3L^2} \quad (2.24)$$

The buckling stress $\sigma_{e|_{max}}$ (not yield stress) at this critical buckling load is obtained from the ratio of this critical load and the cross-sectional area of the strut $A = (t^2)$ thus giving rise to the relationship:

$$F_{e|_{max}} = \sigma_{e|_{max}} A = \sigma_{e|_{max}} t^2 \quad (2.25)$$

Substituting this expression into Equation 2.28 and making the direct stress at this critical load the subject leads to the equation:

$$\sigma_{e|_{max}} = \frac{\pi^2 Et^2}{3L^2} \quad (2.26)$$

The compressive maximum allowed direct stress σ_y is determined as follows:

$$\sigma_{y|_{max}} = \frac{F}{A} = \frac{F}{t^2} \quad (2.27)$$

Therefore, the critical direct load is equal to:

$$F_{d|_{max}} = \sigma_y t^2 \quad (2.28)$$

The applied loads for critical direct and buckling as well as bending stresses induced in the vertical strut as well as the horizontal strut of the lattice structure are given by the ratio of Equations 2.28 and 2.24, as well as 2.23, respectively, thus:

$$F_{d_{max}} : F_{e|_{max}} : F_{b_{max}} = \sigma_y t^2 : \frac{\pi^2 Et^4}{3L^2} : \frac{16\sigma_y t^3}{L} \quad (2.29)$$

This relationship may be simplified to:

$$F_{d_{max}} : F_{e|_{max}} : F_{b_{max}} = 1 : \frac{\pi^2 Et^2}{3L^2 \sigma_y} : \frac{16}{L} \quad (2.30)$$

Substituting typical values of the parameters E , t and L for materials used to produce lattice structures of thin walls shows that the largest, second largest and lowest values of these loads are for buckling, bending and direct loads, respectively. Based on the foregoing analysis, the most critical mode of failure for the applied load shown in Figure 2-34 is direct, followed by bending and, lastly, buckling. However,

this analysis is limited, as it considers each of these modes of failure separately. Direct, bending, transverse shear and possible buckling should be considered together, as is done in the next section.

2.7.5 Suggestions on the application of Tresca and von Mises failure criteria to the deformation behaviour of lattice designs

The Tresca and von Mises failure criteria find application in engineering for predicting the failure of materials under complex stress conditions [141]. Though these criteria are generally used to predict the failure of components made of homogenous materials [141-143], they can also be applied to lattice structures. To the best knowledge of the author, there are no analytical models available in the literature describing the use of these failure criteria on lattice structures. The Tresca criterion, also referred to as the maximum shear stress theory, suggests that a material fails when its maximum shear stress exceeds a critical threshold [141]. The Tresca criterion can be used for lattice structures by considering the stress condition at critical points within the structure, such as interfaces of cells or locations with high-stress concentrations. The criterion can be used to determine the start of yielding or plastic deformation in lattice parts, particularly in areas where shear loads are predominant. The von Mises criterion, referred to as the equivalent stress or distortion energy criterion, contends that a material fails when its equivalent von Mises stress exceeds a critical value [142-144]. This criterion is commonly employed for ductile materials and is particularly useful in predicting failure under combined loading conditions [141-144]. For lattice structure both the Tresca and von Mises criteria can be used to determine the equivalent failure stress based on the prevailing principal stresses at specific spots on the structures. Both criteria can be used in cases where tensile, compressive, and shear stresses occur simultaneously.

To provide proof of the value of the two suggested failure standards, the author analyses a beam structure similar to that used as a building block for lattice parts under loads in order to determine the limiting loads. The present work examines the failure of a beam structure under the already discussed transverse and direct loads using a 2D principal stress example. This is the case because beam structures used for building cellular designs are often viewed as plane stress problems. Plane stress occurs in cases where the out-of-plane direction is very thin to carry no stress in that direction. Combining the equation for principal stresses and the Tresca criterion for a plane gives rise to Equation 2.31.

$$\tau_y \frac{\sigma_1 - \sigma_2}{2} = \frac{\sqrt{(\sigma_x - \sigma_y)^2 + 4\tau_{xy}^2}}{2} \quad (2.31)$$

For the type of loading shown in Figure 2-34, the direct stress σ_y is zero, which transforms Equation 2.31 to one seen in Equation 2.32. From the Tresca failure criterion, the failure shear stress τ_y is equivalent to the largest difference of the principal stress divided by two, as shown in equation 2.34. By substituting the imposed bending, direct, and shear maximum stresses into Equation 2.32 yields Equation 2.33.

$$\tau_y = \frac{\sigma_1 - \sigma_2}{2} = \frac{\sqrt{\sigma_x^2 + 4\tau_{xy}^2}}{2} \quad (2.32)$$

Substituting the expressions for the direct, bending and transverse shear stresses for the load case shown in Figure 2-34 into Equation 2.32 in terms of the applied load F gives rise to the following equation for the stress at which shear failure occurs:

$$\tau_y = \sqrt{\left(-\frac{\pi^2 Et^2}{3L^2} - \frac{FL}{8t^3}\right)^2 + 4\left(\frac{3F}{4t^2}\right)^2} \quad (2.33)$$

This expression explains the relationship between direct, bending, and transverse shear stress. Buckling stress is accounted for in this study by assuming that direct and buckling deformation occur concurrently, the latter being the most critical load case. For the titanium alloy referenced in this work, the shear yield stress is obtained from the known value of yield stress of 790 MPa [13], based on the known ratio of shear yield stress to direct yield stress of 2 [139]. Substituting this value of shear yield stress into Equation 2.33 and making the applied load, F . The subject of the resulting expression transforms the equation to

$$F = \frac{-8t^3(\pi^2 ELt^2 + 12\sqrt{-\pi^4 E^2 t^6 + 3.693 \times 10^{39} L^6 + 5.318 \times 10^{44} L^4 t^2})}{3L^2(L^2 + 144t^2)} \quad (2.34)$$

As was earlier pointed out in Figure 2-34, the beam structure acting as the building block for cellular designs is subjected to compression axial reaction loads on both sides. The region above the neutral axis is expected to be under tension, whereas the part below the neutral axis is predicted to be in compression. The derived shear yield strength indicates that the combined effect of bending and axial loading will result in greater magnitudes of compression stresses in certain regions of the material. This implies that the structure is likely to fail under compression first as compared to tension, which supports the supposition made earlier for using the highest numerical value of axial stresses.

Following a similar procedure for the von Mises failure criterion applied to a case of planar stresses in which the stress, σ_y , is equal to zero, the following expressions for the shear yield stress and applied load arise:

$$\tau_{xy} = \sqrt{\frac{\sigma_y^2 - \sigma_x^2}{3}} \quad (2.35)$$

$$\frac{3F}{4t^2} = \sqrt{\frac{(790 \times 10)^6 - F/t^2}{3}} \quad (2.36)$$

$$F = \frac{-16t^2 + \sqrt{(16t^2)^2 - 28 \times (-790 \times 10^6) \times 16t^4}}{54} \quad (2.37)$$

An expression for the ratio of the calculated load F in both situations is developed and compared to determine their relationship, as illustrated in the expression below.

$$Ratio = \frac{F_{Von\ Mises\ failure\ criterion}}{F_{Tresca\ Mises\ failure\ criterion}} = \frac{-(16 + \sqrt{354560 \times 10^6}) \times (L^2 + 144t^2)}{144t(\pi^2 ELt^2 + 12\sqrt{-\pi^4 E^2 t^6 + 3.693 \times 10^{39} L^6 + 5.318 \times 10^{44} L^4 t^2})} \quad (2.38)$$

In this ratio, the geometrical parameters L and t appear in nonlinear terms, indicating that larger dimensions (reflected by L^2) and thicker structures (through t^2) influence the distribution of stresses and, consequently, the failure loads predicted by each failure criterion. The ratio offers insights into how sensitive the structure's failure response is to variations in geometry. For example, if $L^2 + 144t^2$ dominates, this signifies a considerable geometric impact on structural integrity. Additionally, the presence of t in the denominator underscores the role thickness plays in either amplifying or mitigating the ratio, which in turn affects whether the von Mises or Tresca failure criterion governs the response. The complex square root term in the denominator, $\sqrt{-\pi^4 E^2 t^6 + 3.693 \times 10^{39} L^6 + 5.318 \times 10^{44} L^4 t^2}$, suggests that the ratio accounts for nonlinear interactions between material and geometric factors. This indicates that structural behaviour, especially under high loads, may exhibit nonlinear characteristics. The balance between material elasticity (represented by E) and geometric contributions from L and t can lead to critical thresholds, where the dominant failure mode transitions between the von Mises and Tresca criteria.

2.7.6 Analytical models of lattice structures built with polygon hollow shapes

This section briefly reviews lattice architectures built with different polygon hollow shapes. Its purpose is to draw attention to the often-used polygon hollow shapes in the design of lattice structures.

Lattice structures that incorporate polygonal hollow shapes do so by building a configuration of interconnecting beams or struts structured in a grid-like pattern. These polygonal hollow shapes, which may comprise triangles, hexagons, rectangles/squares, circles or other types of polygons, are used as the basic building blocks of lattice structures. The strut-and-node structures differ from the polygonal hollow cells that are the subject of this chapter in that the latter have walls, while the others do not. Figure 2-35 shows polygon hollow shapes typically used in engineering applications [11, 145].

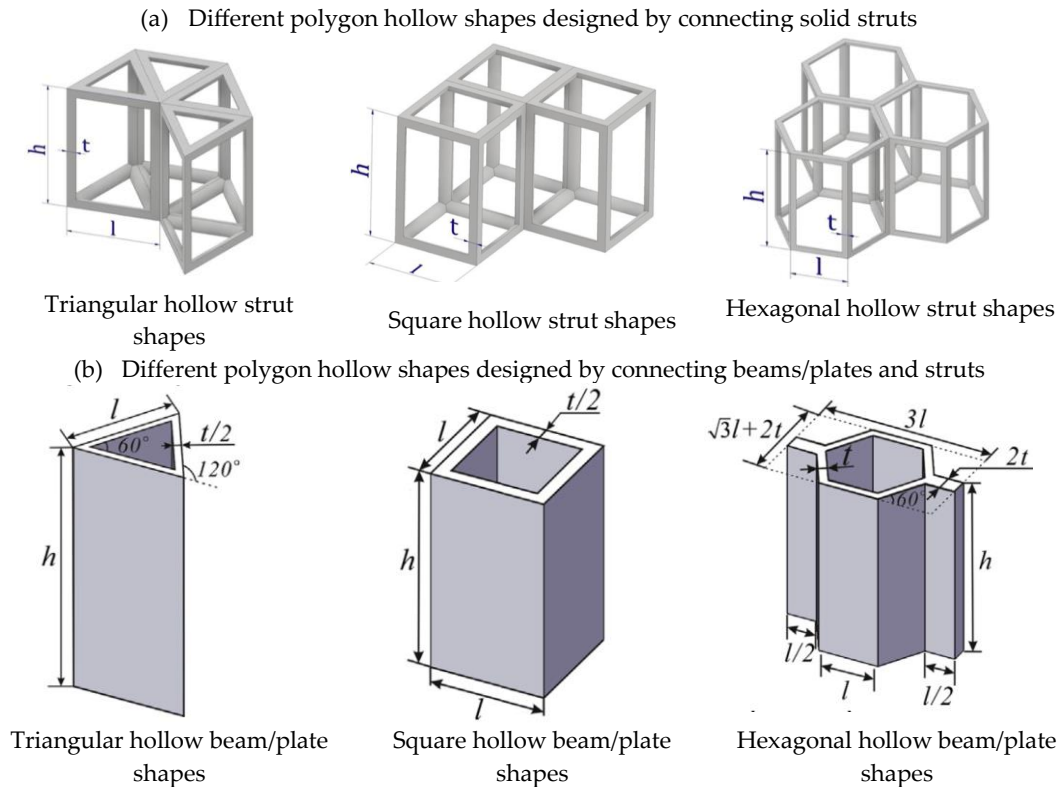


Figure 2-35. Typical polygon hollow shapes built using (a) struts [14] and (b) plates/beams [145]

Figure 2-35(a) shows struts being used as the basic building blocks for polygonal hollow structures, whereas Figure 2-35(b) displays beams or plates as the alternative basic building blocks. Given that such polygon hollow structures can be built with either one of the two types of basic building blocks, it is imperative to make an informed decision on the best choice using analytical models that describe their respective behaviour [135, 145]. As a result, it is crucial to conduct a comparative examination of the behaviour of polygon hollow shapes built using the two building blocks to rank them regarding their mechanical efficiency. Additionally, for lattice structures with the same dimensions, it is important to determine the difference in the amount of material used to design these structures based on the two types of building blocks [135]. Polygon hollow structures built with struts are predicted to use less material than the ones built with beams or plates [11, 135]. This is because the latter type of building blocks requires the use of more material than adopting struts [145].

In its entirety, selecting between struts and beams in the design and manufacturing of polygon-based lattice structures is determined by the engineering application's particular requirements [135]. When simple, straight-line load pathways are preferred and efficiency in the usage of materials and axial stiffness

are crucial, struts are typically used [11]. Beams, in contrast, provide a higher degree of flexibility in terms of how to apply loads and have the capacity to carry loads with more complex distributions [81]. However, their manufacturing could prove more challenging in terms of the selection of materials, speed of manufacturing, and scaling of parts, in addition to requiring more material [145]. The choice between struts or beams/plates must, therefore, be based on a careful analysis of the primary structural specifications, cost, and desired design outcomes of a project.

Analytical modelling of lattice structures constructed with polygonal hollow shapes requires the development of mathematical representations and equations to describe the geometrical and mechanical properties of these structures. This modelling approach is critical for predicting how these structures respond to different loads and assists engineers and designers in optimizing their structural designs. The next subsection contains a review of several pertinent analytical models available in the literature for polygon hollow structures built with plates as the basic building blocks.

Geometry representation models of selected polygon hollow structures. Geometrical representations of four polygon unit cell shapes, including the hexagon, triangle, square, and circle, are adopted to determine the relevant geometric parameters used to describe the various lattice designs. Figure 2-36 shows one of the most used polygonal shapes and its geometrical parameters, the hexagonal cell inspired by the honeycomb [145].

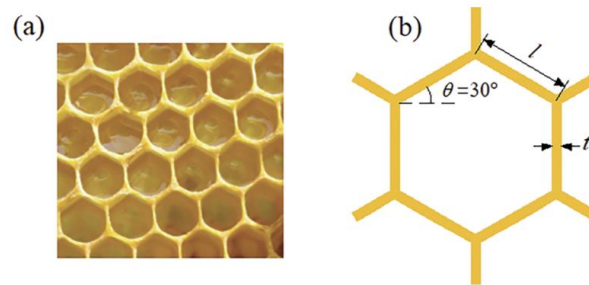


Figure 2-36. (a) Natural beehive honeycomb and (b) regular hexagonal geometry of a honeycomb [145]

These geometrical parameters are modelled and represented in the form of density equations for the four polygonal hollow shapes of the hexagon, triangle, square, and circle, as illustrated by the following equations [135].

$$\frac{\rho_h^*}{\rho_s} = \frac{2}{\sqrt{3}} \frac{t}{L} \quad (2.39)$$

$$\frac{\rho_t^*}{\rho_s} = 2\sqrt{3} \frac{t}{L} \quad (2.40)$$

$$\frac{\rho_s^*}{\rho_s} = 2 \frac{t}{L} \quad (2.41)$$

$$\frac{\rho_c^*}{\rho_s} = \frac{4}{\sqrt{3}} \frac{t}{L} \left[\frac{1}{2} + \left(\frac{2\pi}{3} - 1 \right) \frac{R}{L} \right] \quad (2.42)$$

where the symbols t and L , R , and ρ^* and ρ_s represent the wall thickness and length of the polygon hollow walls, radius of a unit circular cell, and density of the polygon hollow structure and the solid material for the cell wall, respectively. The parameters ρ_h^* , ρ_t^* , ρ_s^* , and ρ_c^* denote the densities of regular hexagonal, triangular, square, and circular structures, respectively. Equations 2.39-2.42 show that the relative densities of each of the four polygon hollow cells are related to their ratios of wall thickness t to wall length L . These ratios have a significant impact on the stiffness of polygonal hollow structures. When the thickness (t) is greater than the overall dimension (L), the structure is more resilient to deformation. The material is distributed over a larger cross-sectional area in this case, resulting in an improved stiffness. Structures are referred to as thin-walled when their thickness is ten times or less smaller than the overall

dimension L . Structures with thin walls are more prone to buckling deflection and are less resilient. Their stiffness is lower given the fact that buckling deflection will precede direct deformation for such thin cross-sections. In investigating all four polygon designs discussed in this review, consistency is guaranteed by considering t/L ratios lesser or equal to 0.1.

Numerous studies [135-136, 145-148] have, however, ignored analytical modelling of the effects of the connections at the nodes of polygonal hollow structures on their stiffness. This is a concern because numerous studies [145, 149-152] suggest that vertices are highly stressed regions, which, thus, are prone to failing first under applied loads. The authors are currently focusing on this challenge in their ongoing research.

Analytical models for predicting the behaviour of selected polygon hollow structures. Analytical models predicting the structural behaviour of lattice structures are available in the literature for in-plane and out-of-plane loads [135-136, 146–152]. The in-plane and out-of-plane loads for the analytical models derived for polygon hollow structures based on plates/beams are depicted in Figure 2-37.

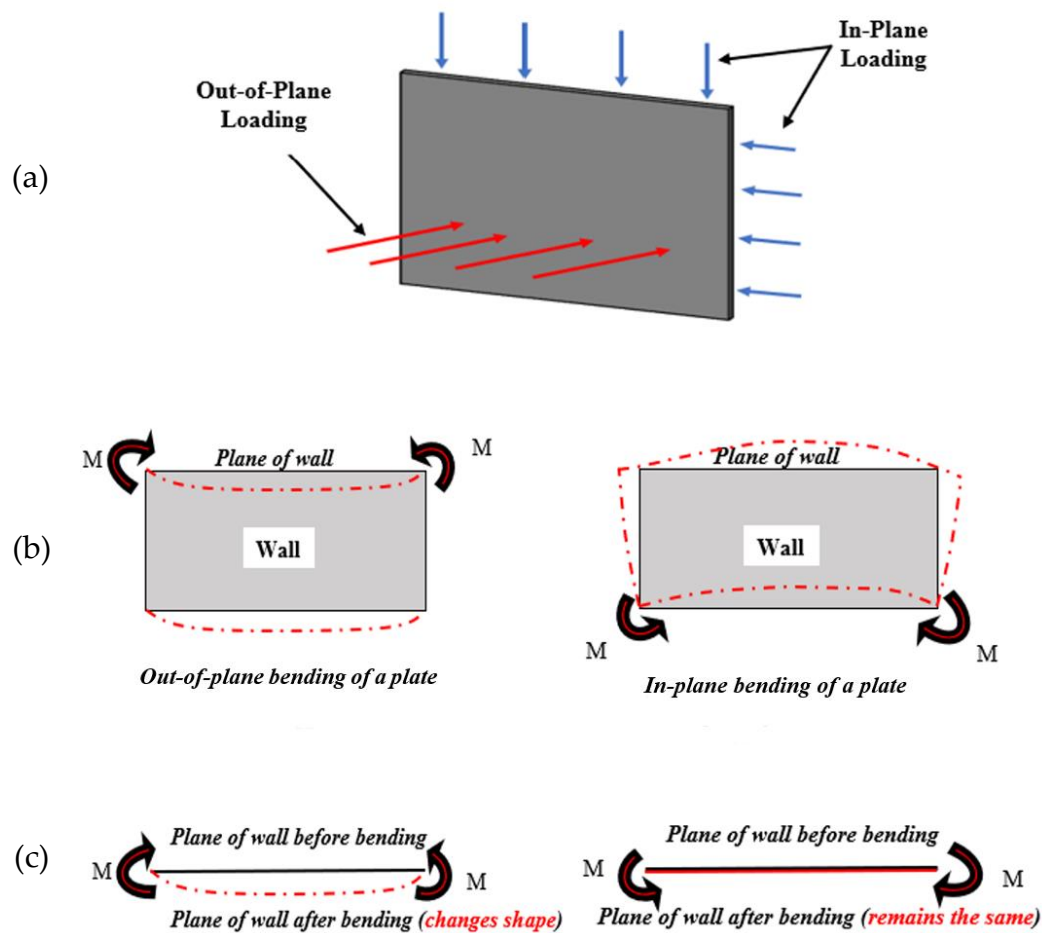


Figure 2-37. (a) in-plane and out-of-plane loading of a plate, (b) out-of-plane bending on the left and in-plane bending on the right, and (c) planes of walls before and after bending

Analytical models for polygon structures, such as hexagonal hollow shapes built with plates or beams, have been developed using tensile or compressive loads, which leads to respective tensile or compressive deformation behaviour [135-136]. Numerous studies have investigated these two deformation behaviours for three mutually orthogonal directions [135]. Figure 2-38 illustrates the three mutually

orthogonal directions used in studying the deformation behaviour of polygonal structures, in this case, a hexagonal hollow structure.

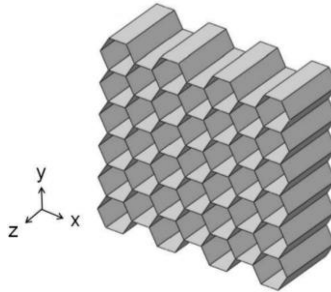


Figure 2-38. A typical hexagonal hollow structure showing all three mutually orthogonal directions in which the behaviour of polygonal hollow structures is analysed

Currently, the analytical models for the deformation behaviour of polygonal structures that are available in the literature only describe the bending stiffness of these hollow structures with respect to their elastic moduli [135, 145-146] and predict their load-bearing capacity with reference to the yield stress of their wall-material [62, 64]. Polygonal structures are particularly useful in applications for high-energy absorption [11, 13, 16, 20, 23, 145, 147-151, 153-155]. Given the fact that there are no specific models for the absorption mechanisms of energy for polygon hollow structures, this poses a challenge in accurately predicting their related behaviour. Presently, the analytical models that are available in the literature for use in predicting the absorption mechanisms of energy for polygon hollow structures are predicated on general mathematical equations that describe the strain energies caused by bending, tensile, and shear loading [23, 135-136, 145]. A supposition is being investigated by the authors in ongoing work, and the two-stage stress-strain curve typically used for predicting the behaviour of lattice structures is not accurate as it does not represent all the deformation mechanisms taking place in a lattice structure. This presents a clear limitation regarding having specific analytical models for describing the energy-absorption behaviour of polygon structures. Therefore, further investigation is required to address these gaps in knowledge with a view to building more accurate analytical models to describe the deformation behaviour of polygon hollow structures. For particularly porous materials such as polygon hollow structures, the Gibson–Ashby model is typically employed to relate their stiffness and yield strength to density [146].

The Gibson–Ashby model for a regular hexagonal hollow cell. Figure 2-39 shows a unit planar hexagonal hollow cell with two mutually orthogonal planar in-plane directions of loading indicated. Equation 2.45 represents the analytical model describing the behaviour of a planar hexagonal polygon structure when subjected to loads in the in-plane directions [135, 146].

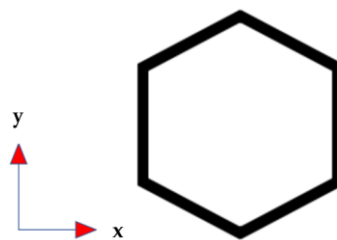


Figure 2-39. A planar unit hexagonal cell showing two mutually orthogonal planar in-plane directions of loading

The stiffness of the hexagonal hollow cell is seen from Equation 2.43 to be related directly to the third power of the ratio (t/L), which from Equation 2.39 implies a direct relationship to the third power of the relative density of the cell [135].

$$E_y^* = E_x^* = \frac{4}{\sqrt{3}} E_s \left(\frac{t}{L}\right)^3 \quad (2.43)$$

The symbols E^* and E_s in this equation represent the elastic modulus of the polygon hollow structure and that of the solid material of the polygon walls, respectively. Subscripts y and x in the parameter E^* represent the y - and x -directions, respectively. It is garnered from Equation 2.43 that the stiffness of the structure with respect to its elastic modulus grows with an exponential of order 3 of the ratio t/L for a hexagonal hollow structure loaded in the two planar in-plane directions, individually.

The Gibson–Ashby model of an equilateral triangular hollow cell.

Figure 2-40 shows a unit planar triangular cell highlighting the directions for the planar in-plane loading of an equilateral triangular hollow cell. Equation 2.44 represents the analytical model describing the behaviour of a planar triangular polygon structure when subjected to loads in the in-plane directions [135, 146].

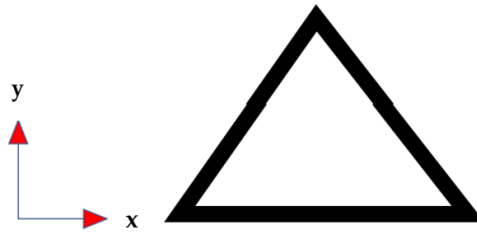


Figure 2-40. A planar unit triangular hollow cell showing two mutually orthogonal planar in-plane directions for loading

For this triangular hollow structure, Equation 2.44 represents stiffness in each of the two planar in-plane directions [135].

$$E_y^* = E_x^* = 1.15E_s \left(\frac{t}{L}\right) \quad (2.44)$$

It is observed that the stiffness of the triangular hollow cell is directly related to its relative density, which, from Equation 2.44, is known to be equal to the t/L ratio. This difference in the relationship of stiffness to the t/L ratio between a hexagonal hollow cell and a triangular hollow cell is because the triangular hollow cell deforms primarily through the axial deformation of the cell walls, as opposed to the hexagonal hollow cells, which deform predominantly through the bending of the cell walls [135, 145, 149]. Equations 2.43 and 2.44 show that the triangular hollow polygon cell is less stiff than the hexagonal hollow cell under planar in-plane loading by a factor of 2.

The Gibson–Ashby model of a square hollow cell. Gibson and Ashby [135] suggested that the stiffness behaviour of a square hollow structure was comparable to that of a triangular hollow structure built using the same relative density. In addition, square hollow structures are designed for particularly anisotropic structural applications [145]. Inherently, the square hollow structure consists of two mutually parallel stiff walls and another two mutually parallel walls that are perpendicular to the first set of walls, which are particularly prone to transverse bending deflections when subjected to planar in-plane loading [135]. A unit planar square cell showing the planar in-plane directions of loading for a square hollow cell is shown in Figure 2-41.

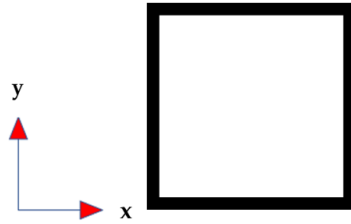


Figure 2-41. A planar unit square hollow cell showing two mutually orthogonal planar in-plane directions of loading

Equation 2.45 represents the stiffness behaviour in either of the two planar in-plane directions of the square hollow cell [135]:

$$E_y^* = E_x^* = E_s \left(\frac{t}{L} \right) \quad (2.45)$$

The ratio of the stiffnesses of the triangular and square hollow cells is seen from Equations 2.44 and 2.45 to be 1.15, with both stiffnesses being directly related to the relative density. Therefore, the triangular hollow cell ranks higher than that of the square hollow cell by a factor of this ratio of 1.15, with reference to transverse stiffness. However, longitudinal deformation was observed to be more prevalent in the triangular hollow cell than in the square hollow cell [135]. Gibson and Ashby [146] determined that the triangular hollow cell underwent less than 2% deformation due to bending loads and that more than 90% of its primary deformation was a result of longitudinal loads. They further found that the square hollow cell deformed by close to 13% due to bending loads and that approximately 80% of its deformation was caused by longitudinal loads. Stiffness was determined by these two authors to be critical for transverse loads.

The Gibson–Ashby model of a circular hollow cell. A circular unit cell illustrating the two mutually orthogonal planar in-plane directions of loading for a circular hollow cell is shown in Figure 2-42.

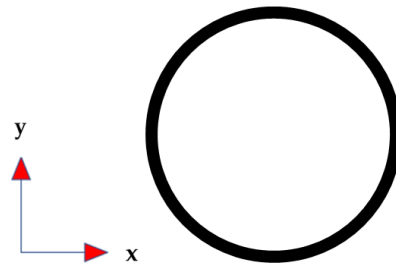


Figure 2-42. A planar circular unit hollow cell showing two mutually orthogonal planar in-plane directions of loading

Equation 2.46 represents stiffness in either of one of the two planar in-plane directions [135]:

$$E_y^* = E_x^* = \frac{8.329}{(1-\nu^2)} \left(\frac{t}{R} \right)^3 E_s \quad (2.46)$$

where symbol ν represents the Poisson's ratio of the walls of the hollow cell. The circular hollow cell under planar in-plane compression loads deforms due to the contraction of the circular unit cells in the direction of the applied load, as well as stretching in the perpendicular direction, the direction without an applied load [6, 11, 20, 135, 145]. Therefore, the loading and perpendicular directions of the circular hollow structure experience a reduction and increase in radius, respectively, upon the application of the load. This converts the circular cell into an ellipse [145]. From a comparison of Equations 2.43-2.46, it is evident that the circular hollow structure ranks first regarding its transverse stiffness for values of the radius (R) of the cell equal to the lengths (L) of the other types of polygon hollow cells considered here. This is because, compared to polygon structures with corners, circular shapes transfer stress more uniformly. Stress in a circular hollow design tends to be distributed uniformly along its circumference, resulting in an efficient load transfer [6, 20]. Stress concentrations are often observed at the vertices of polygonal structures with

non-circular unit cells, which in turn serve as weak points. Given that circular designs do not have corners, there is a reduced possibility of stress concentrations, leading to them being more resilient against localized deformation and deflection [20].

It is clear from the analytical models reviewed here that the order of the ranking of the four polygonal hollow cells goes from circular to hexagonal, triangular, and square cells, in decreasing order of transverse stiffness.

Analytical models describing the load-bearing capacity of three-dimensional (3D) polygon hollow structures loaded in the cell walls' in-plane directions are lacking in the available literature. Presently available analytical models only describe the load-bearing capability of 3D polygon hollow structures for loads applied in the cell wall out-of-plane direction [6, 11, 23, 135-136, 145, 149, 152, 156]. This is because all the identified studies [145, 157-165] investigating the crashworthiness of polygonal hollow structures are based on loading in the cell wall out-of-plane direction as a result of its high capacity to absorb strain energy compared to loading in the cell wall in-plane directions. Therefore, there is a need to develop analytical models that describe the load-bearing capability of polygon hollow structures loaded along the cell wall in-plane direction.

Gibson and Ashby [135] highlighted the fact that the cell wall in-plane loading of polygon structures discussed here could be simplified and represented by a rectangular plate or beam model subjected to either direct or buckling loads based on the t/L ratio that was used. They also highlighted the fact that the cell wall in-plane loading of polygon structures resulted in relatively smaller changes in the load-bearing capacity and stiffness, as the cell wall has insignificant in-plane anisotropy compared to the out-of-plane direction. Figure 2-43 shows a hexagonal structure subjected to a cell wall in-plane load [166].

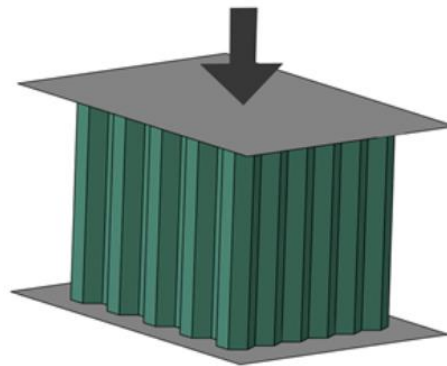


Figure 2-43. A hexagonal structure under planar in-plane loading [166]

Predicting the deformation behaviour of polygon structures subjected to cell wall in-plane loads accurately depends on the cell wall in-plane geometrical properties [145]. Compared to the cell wall out-of-plane loading of polygon structures, the cell walls of these structures exhibit a higher stiffness as well as a higher load-bearing capacity along the in-plane direction. The cell walls in in-plane loading predominantly deform due to stretching, compression, and buckling behaviour instead of the transverse bending deflections observed when the structures are loaded in the cell wall out-of-plane direction [135].

To determine the cell wall in-plane behaviour, the four polygonal hollow cells discussed here are extruded in the in-plane direction to generate 3D cells. To determine the compressive strength related to the elastic buckling behaviour, Gibson and Ashby [135] developed an analytical model representing the compression strength or crucial buckling stress $(\sigma_{el}^*)_3$ of a hexagonal unit cell subjected to cell wall in-plane compression loading given in Equation 2.47:

$$(\sigma_{el}^*)_3 = 5.2E_s \left(\frac{t}{L}\right)^3 \quad (2.47)$$

The resulting compressive strength was determined to be 20 times greater than the compressive strength calculated for cell wall out-of-plane loading [135]. This suggests a possibility of using hexagonal

hollow structures in crashworthy applications for cell wall in-plane loads instead of cell wall out-of-plane loads for materials with lower stiffnesses than those presently used for their out-of-plane crashworthiness.

Currently, available analytical models face the limitation of being based on unit cells rather than the overall structure [23, 135-136, 145, 149, 152]. This approach fails to consider the influence of connectivity of the unit cells in a structure and, therefore, cannot accurately predict how the final polygon structure responds to applied loads. For one, the unit cells are connected at the vertices, which are designated as high-stress concentration regions and are prone to failure under lower applied loads [135-136, 145, 149]. However, the vertices act to stiffen lattice structures [136, 145]. Therefore, there is a need to build analytical models that account for the whole structure's configuration and introduce the mechanics related to the connectivity of cells at the vertices. Furthermore, the analytical models for polygonal shapes under cell wall in-plane loading are only available in the literature for hexagon hollow structures. Therefore, analytical models should be developed for the other polygonal shapes to accurately predict their behaviour rather than having to estimate their response based solely on the available model for the hexagonal hollow structure.

The current analytical models of polygon hollow structures in the literature are typically based on the four basic polygon forms, namely the hexagonal, square, triangular, and circular cells presented here. Thus, this review of analytical modelling is limited to the foregoing four shapes. Other types of polygon hollow shapes that could be adopted in building lattice structures include pentagonal, octagonal, dodecagonal, irregular, mixed, kagome, and rhombic shapes, despite the lack of knowledge of their corresponding analytical models. Figure 2-44 shows these other types of polygonal shapes that could potentially be used for designing hollow lattice parts.

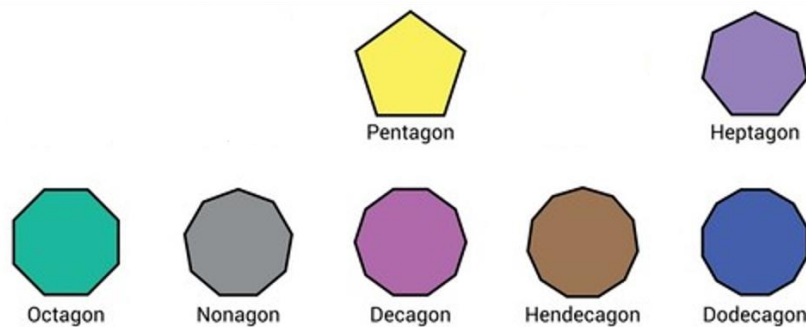


Figure 2-44. Other types of polygonal shapes that could potentially be used in generating hollow lattice designs for different engineering applications

However, numerous research [11, 13, 16, 23, 135-136, 145, 148, 167] have been conducted using other types of lattice shapes, excluding the polygonal ones, such as the strut-based, skeletal TPMS-based and sheet TPMS-based geometries. Examples of other types of hollow structures adopted in numerous studies [11, 13, 145] are shown in Figure 2-7.

2.8. Efficacy and limitations in designing lattice structures

2.8.1 Evaluation of lattice structures in mimicking natural cellular structures

Cellular structures typically occur in nature. These biological structures are created by an interconnected network of organic solid struts that form ribs and cell walls. Different examples of cellular structures in nature include bone, wood, glass sponge skeletons and honeycomb, which have been extensively studied [21, 20, 42-43, 53, 168]. A recent review article [169] on the use of cellular designs in engineering structures, focused on the biomimetic design of cellular materials. Figure 2-45 shows micro-computed tomography (micro-CT) scans of some naturally occurring cellular materials [168].

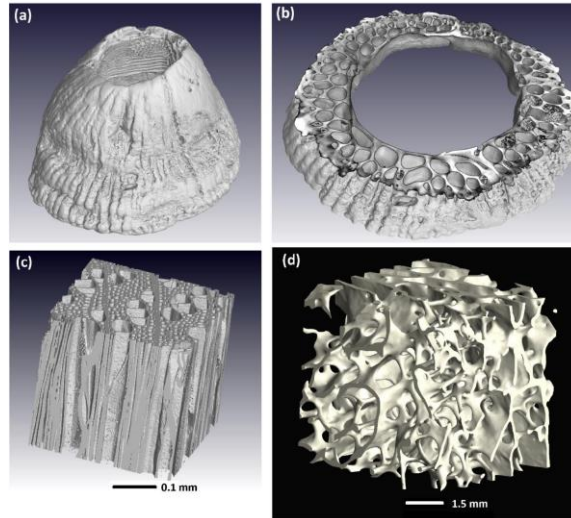


Figure 2-45. Cellular structures in nature (a-b) barnacle, (c) microstructure of wood material, and (d) structure of the human trabecular bone [168]

Cellular structures in nature have generated considerable interest, and this interest has worked a path into functional mechanical engineering via the latest developments in AM technologies [20]. This is because the design flexibility of AM technologies allows one to construct lattice structures by mimicking the complex cellular designs in nature. Biological cellular materials have been targeted for bioinspiration and biomimetic studies, particularly because of their superior mechanical properties, including high stiffness, strength, and fracture toughness. Researchers rely on this knowledge to develop structures that mimic the hierarchical configuration of biological tissues. In turn, designs of lattice structures that have specific geometry and mechanical properties can be attained via this process [13].

Several benefits of mimicking cellular structures in nature have been highlighted in reference [44]. Biological tissues typically show hierarchical structuring, with structures arranged at multiple length scales [170]. Lattice structures are designed to mimic natural cellular structures by hierarchically arranging unit cells of various degrees of complexity and size. In return, this mimics the structural configuration observed in structures of nature [20]. This approach is useful for improving the mechanical properties and functionality of lattice structures. In biology, cellular structures are well known for having superior mechanical characteristics such as lightweight, high strength-to-weight ratios, and energy absorption [21, 170]. By optimizing the geometry, unit cell shape, and material composition of lattice structures, mechanical characteristics comparable to requirements in various engineering applications are attained [13, 20, 26, 28]. This allows for the development of lightweight materials with increased strength and impact resistance, which can be used in a variety of applications ranging from biomedical, automotive, and aerospace to safety equipment.

The porosity and permeability of cellular structures allow for the efficient transport of fluids, nutrients, and waste products [170]. Lattice structures with controlled porosity are designed to mimic the transport properties of biological structures. This is particularly advantageous in tissue engineering, where the interrelated scaffolds with porosity allow for the exchange of nutrients and the growth of cells simultaneously [20]. Lattice structures can also be customized to mimic tailored biochemical and biological functions that occur in natural cellular structures.

Functional molecules or bioactive agents, for instance, can be integrated into the lattice design to promote the adhesion, proliferation, and differentiation of cells, thus making them useful for applications in tissue engineering and regenerative medicine [171]. The capacity for self-assembly and reproduction in some biological cellular structures permits growth and adaptation. Although artificial lattice structures lack

the same degree of complexity, researchers have investigated self-assembly methods to develop dynamic lattice structures that can alter their configuration in response to outside stimuli [26]. This mimics the evolution and growth of biological structures. However, even though lattice structures offer new possibilities for mimicking cellular structures in nature, there are several challenges and limitations to consider that are a result of the unique properties of biological tissues [21, 20, 42, 53].

Choosing the right materials for lattice structures is crucial in attaining the desired properties. However, it is often difficult to determine materials that mimic the mechanical and biochemical properties of biological tissues. Although progress has been made in developing biomimetic materials [21, 20, 42, 53], matching the full range of properties found in nature, it is still difficult [42, 170]. Wang et al. [172] generated four Ti6Al4V scaffolds based on honeycomb designs to repair human bone defects. The elastic modulus, strength, and permeability of the four scaffold designs were evaluated in comparison to human bones. Their findings showed that the elastic modulus of the four scaffolds was in the 1.6-3 GPa range. This is comparable to the range of human trabecular bone (0.1-4.5 GPa). The yield strength in the range, 88-146 MPa, was, however, significantly higher than that of the femoral neck (0.56-3.71 MPa). Except for the conventional uniform scaffold's excess permeability, the permeability of the other three scaffold designs (1.5×10^{-8} - 4.8×10^{-8} m²) were all within the range of cancellous bone permeability (0.5×10^{-8} - 5.0×10^{-8} m²). The same trend was observed in reference [173]. The authors found no relevant information in literature that provides a direct quantitative comparison of natural cellular structures and their biomimetic architectures in terms of coefficients of diffusivity and thermal conductivity. This is ongoing work by the researchers that is primarily focused on improving fluid transportation and heat management systems in industrial applications.

Numerous dynamic behaviour, including shape changes, growth, and responses to stimuli, are often observed in biological cellular structures [44, 168]. However, it is difficult to mimic this dynamic behaviour in lattice structures. Despite the development of some self-assembling and reconfigurable lattice structures [20], these structures typically lack the complexity and adaptability observed in biological structures.

The ability to integrate with biological structures is of the utmost importance when mimicking cellular structures for biomedical applications. Lattice structures must not only mimic the physical properties of biological tissues but also interact with surrounding tissues, such as allowing adhesion, cell migration, and tissue regeneration [13, 30, 33 174-175]. It continues to be difficult to attain seamless integration of lattice structures with biological structures [21, 30].

Fabrication of lattice structures is complicated via conventional methods. Traditional manufacturing techniques, such as subtractive machining or casting, are often inadequate for lattice structures because they require intricate internal geometries that are challenging to attain [13, 175]. Even though AM (3D printing) has emerged as a promising technique for fabricating lattice structures, it continues to face challenges regarding the selection of materials, speed of manufacturing, and scaling of parts [12, 27, 176-177].

The materials used to construct lattice structures have a bearing on their manufacturability. For optimum performance, some lattice geometries require materials with specific mechanical properties, such as high strength or stiffness [12]. However, not all materials are appropriate for all manufacturing methods [25]. Certain lattice structures designed for AM, for instance, could require materials with specific thermal properties to ensure efficient printing without deformation or delamination. Choosing materials for lattice structures is often difficult due to a lack of material options that are compatible with specific manufacturing processes [27, 177].

Support structures are often required when building lattice structures, to prevent them from failing or deforming during construction. The removal of support structures after manufacturing, however, is often time-consuming and could result in surface imperfections or call for extra post-processing steps to achieve the desired finish on the surfaces. The manufacturing process thus becomes more complex and costly as a result of this and their structural design. In the worst cases, lattice structures have permanent internal supports, which means they cannot be removed [12, 27, 175, 176-177]. Research has recommended the use

of improved designs for the lattice structure to ensure that no support is needed inside the lattice regions [20].

The fabrication of lattice structures, particularly through AM, can be time-consuming. Building intricate lattice geometries layer by layer can take a long time, especially for large structures. When there is a demand for rapid manufacturing or mass production, this extended production time becomes a drawback [44, 177]. Furthermore, because there are often large volumes of leftover powder in areas where the laser does not strike during printing, specific manufacturing equipment, and post-processing requirements, the cost of manufacturing lattice structures could be higher than that of solid structures [12, 20, 177].

The build size of 3D printers can limit the largest dimensions for lattice structures. This can be a limitation when attempting to create large-scale lattice components. Secondly, certain lattice geometries could prove challenging to produce accurately because of the limitations of resolution of respective AM machines or the behaviour of materials during the process of printing [12, 49, 177]. Rahmati [178] highlighted that the minimum resolution for a DMLS machine ranges between 10-45 μm . Dropping below the minimum resolution will, therefore, result in fewer details of the designed structures being obtained [177-178]. Furthermore, structures with thinner walls of less than 1 mm thickness could fail readily due to residual stresses generated by rapid cooling during manufacturing [12, 178]. To achieve the desired results, printing process parameters ought to be carefully tailored and considered.

Lattice structures typically have complex geometries with interconnected beams or struts, causing them to be highly prone to manufacturing defects. Manufacturing flaws such as cracks, voids, or inconsistencies in the lattice members result in stress concentration points. Stress concentrations occur in localized areas of high stresses, thus reducing the overall strength and load-bearing capacity of structures. The presence of defects causes cracks to form or propagate, resulting in premature failure under applied loads. Manufacturing defects also reduce the stiffness of lattice structures. Irregularities or variations in the size, shape, or thickness of lattice members cause irregular deformation and deflection under load. This results in reduced stiffness, which is undesirable in applications where rigidity and minimal deformation are required. Defects in lattice structures further act as stress raisers, speeding up the initiation and propagation of fatigue cracks. Cyclic loading, when combined with the presence of manufacturing defects, results in the formation and growth of cracks, thus reducing the fatigue life of structures [8, 12, 177]. This shortcoming is particularly crucial in applications where lattice structures are subjected to repeated loading or dynamic loads [25]. Furthermore, manufacturing defects have a bearing on the deformation properties of lattice structures. In AM procedures, for instance, voids or improper fusion occur in areas of reduced material density and irregular powder depths, respectively, thus resulting in differences in mechanical properties such as strength, stiffness, and toughness [20, 26, 28]. Such discrepancies could give rise to unpredictable behaviour and compromise the lattice structure's overall performance and reliability. Lattice structures with intricate internal designs are often challenging to inspect and control during the manufacturing process. Conventional non-destructive testing methods such as visual testing, penetrant testing, magnetic testing, ultrasonic testing, radiographic testing and eddy current testing often prove ineffective for detecting defects within the internal parts and surfaces of the members of lattice structures [12, 177]. Therefore, determining and correcting manufacturing defects during sampling becomes difficult and increases the risk of creating defective or substandard lattice structures. To overcome these constraints, manufacturers must employ stringent measures of quality control, as well as inspection techniques tailored to lattice structures. Internal defects and the quality of lattice structures can be detected using advanced imaging technologies such as X-ray computed tomography and ultrasound [20]. In addition, optimizing manufacturing processes, refining fabrication techniques, and implementing process monitoring can help reduce defects and improve the overall quality and reliability of lattice structures [8, 20].

The powder is also prone to get stuck in intricate regions, such as between sharp changing edges and vertices of lattice designs. This results in reduced density of lattice structures and is potentially

hazardous in cases of medical implants. Figure 2-46 shows a micro-CT image of a printed bracket with powder stuck inside certain parts of the lattice [20].

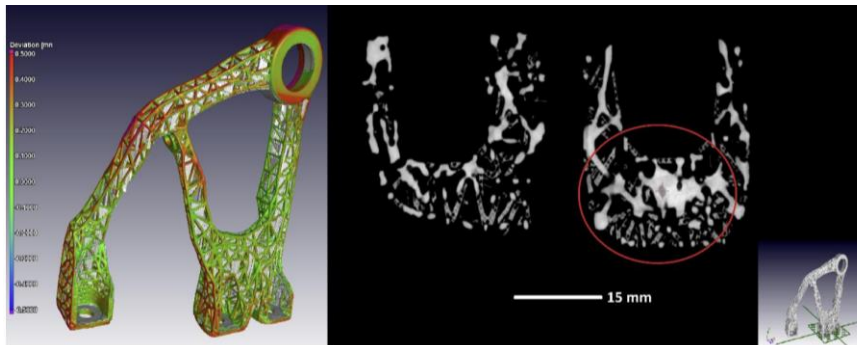


Figure 2-46. Micro-CT scan white contours depicting powder that is stuck inside certain parts of an additively manufactured lattice bracket [20]

After AM of parts, the removal of support structures and powder stuck to them is carried out. Powder and support removal methods and their efficacy differ based on the AM process and materials used [12]. The preferred methods and efficacy for powder and support removal include the following seven methods. (1) Manual removal, which involves manually breaking or cutting off support structures as well as removing surplus powder, typically using basic hand tools such as pliers, wire cutters, and brushes. Manual removal is efficient for parts with basic geometry and easily accessible support structures. However, complex or intricate designs could prove time-consuming and labour-intensive [8]. (2) Blowing with compressed air is a rapid and efficient approach to removing powder but is not efficient in removing all of the support structures, particularly in difficult-to-reach regions. As a result, the approach is often followed by manual removal of any residual support structures [8, 12]. (3) Parts are mechanically agitated in a tumbler or vibratory finishing machine using abrasive media such as plastic beads to remove stuck powder and support structures. This method works efficiently for parts with complicated geometries and difficult-to-reach areas. It additionally makes the surface smoother [177]. (4) High-pressure water jets are also highly efficient in removing excess powder and support structures, particularly when working with water-soluble supports and complex parts. However, the strategy might not be entirely suitable for all materials [8, 26]. (5) Soaking in a solvent bath such as acetone for some plastics dissolves support material. Ultrasonic agitation is typically used to speed up the process. Solvent baths are efficient in removing support structures and could result in high-quality outcomes. They might, however, require post-processing to remove any leftover solvent from parts. (6) The procedure of heat treatment, also referred to as thermal de-binding, involves exposing the part to high temperatures to burn off or evaporate support structures. Heat treatment is useful for removing support structures; however, it may require specially designed equipment and careful control of the temperature to prevent part deformation [13]. (7) Numerous AM technologies include built-in support removal features. To remove supports, these technologies employ automated processes such as cutting and milling. Automated processes, particularly for industrial-scale production, are typically highly efficient and accurate. They are, however, not available for all AM technologies [8, 12, 26, 175].

2.8.2 Constraints in determining the order of hierarchy attainable for hierarchical lattice honeycombs (HCs)

The order of hierarchy in relation to hierarchical HCs refers to the structuring of smaller polygonal cell sizes within HC structures [107]. This section points out the numerous factors that determine the level of hierarchy attainable in hierarchical HCs.

The properties of materials that are used to fabricate hierarchical HCs have a direct influence on the order of hierarchy attainable. Comprehending the mechanical, thermal, and electrical properties of the

selected materials at different hierarchical orders is crucial when undertaking thorough studies on their use in specific engineering applications. This is because the behaviour of the structures under external loading and environmental conditions is determined by the choice of materials [13, 21, 107]. Furthermore, the availability of ideal materials that can be efficiently processed while maintaining the desired levels of hierarchy could pose a challenge as well [13, 107, 109].

Limitations of imaging tools are typically pointed out in literature [58, 62-63, 103-110] and are often related to their limited capacities in observing and analysing structures at a scale that is desired. This is because HCs have complicated hierarchical features at different lengths and scales that can prove challenging to capture in detail [21, 58, 107]. Conventional ways of analysis and measurement can fail to include the entirety of the scale spectrum, resulting in its inability to accurately capture every level of the hierarchy, as well as the relationships between the differently scaled structures [58, 107]. The complex configurations observed within HCs tend to occur at micro and nanoscales [21, 58]. To accurately analyze these structural parts, high-resolution imaging methods are typically required. Thus, limitations in imaging methods can render it challenging for researchers to get comprehensive details regarding smaller-scale structures that are built-in [21, 107]. Given the broad range of the structures, understanding and determining the relationships and different hierarchical configurations across different scales is often challenging [21]. Numerous numerical values are reported in the open literature [179] that are comparable to the typical scales encountered and the level of detail of microscale and nanoscale imaging systems for analysing structures such as hierarchical HCs. For instance, the optical microscopy technique offers a resolution of 200 nm and is ideal for examining structures larger than 1 μm . The imaging approach is effective for analysing structures in the micrometre range but less so for greater levels of detail [180]. In contrast, a scanning electron microscopy (SEM) imaging system has a higher resolution (in the range of 1 nm) compared to optical microscopy, resulting in it being ideal for thorough microscale investigation [181-182]. Transmission electron microscopy (TEM) works well for nanoscale imaging. The TEM imaging technology has resolutions of up to 0.1 nm, facilitating the analysis of atomic-scale structures [181]. Atomic force microscopy (AFM) gives comprehensive surface topography with resolutions ranging from 1-10 nm, which is useful for analysing the characteristics of surfaces at the nanoscale [183]. Cryo-electron microscopy (Cryo-EM), on the contrary, allows for imaging with near-atomic resolution, generally around 0.2 nm. It is typically required for examining the accurate structures of proteins and other biological macromolecules [184]. Comprehending the constraints and capabilities of these imaging techniques is crucial for determining the best strategy for examining hierarchical HC structures at various scales. Blending different imaging strategies often yields a more comprehensive view of these complicated systems.

Numerical modelling of hierarchical HCs involves dealing with complex geometries and multiscale interactions. Accurate modelling requires advanced numerical methods such as FE methods, finite difference methods, finite volume methods, boundary element methods, multigrid methods, adaptive mesh refinement, mesh-free methods, level set methods, discontinuous Galerkin method, and optimization algorithms, as well as significant computational resources such as high-performance computing (HPC) systems, graphics processing units (GPUs), cloud computing resources, advanced software tools, large memory and high-speed networks, and algorithm optimization. It may prove challenging to generate feasible computer models for simulating and predicting the hierarchical levels of HCs [11, 13, 107-111]. This is because challenges with building accurate numerical models for hierarchical HCs emerge when they are required to describe complicated geometries and multiscale interactions accurately, retain high resolution, and use advanced numerical strategies. These characteristics, together with the need for significant processing resources and extensive algorithm optimization, render generating models complicated [185]. The complex nature of hierarchical HCs requires a delicate balance between computational efficiency and model fidelity, necessitating advanced methodologies and large computational capacity. This is because, for engineering applications, striking a balance between accuracy and processing efficiency is crucial [21].

Additionally, toward an in-depth comprehension of HC hierarchies, information gathered from experiments and numerical models must be integrated. However, challenges often arise when incorporating experimental and numerical data, such as data discrepancies, data processing and comprehension, uncertainty quantification, validation, boundary and first conditions, scale variations, complicated geometries, and material characteristics. As a result of this, assuring accuracy across different levels and validating the generated models can pose an additional challenge [21, 107].

The large amount of data generated by imaging and modelling techniques requires complicated processing and analysis approaches, even for simple lattice structures [58]. Developing algorithms that can control complex hierarchical data sets is presently an ongoing challenge. Furthermore, incorporating data from different sources, such as imaging, numerical modelling, and field research, requires advanced integration and analysis strategies [21, 58, 62, 104-106]. Thus, building comprehensive models that account for the intricacies of hierarchical HCs is even more difficult.

To achieve hierarchical structures in HCs, accurate manufacturing methods are required as well. Conventional methods, such as casting, extrusion, or moulding, have challenges duplicating complex hierarchical structures, particularly at lower scales [105-107]. Designing complex hierarchical structures throughout the manufacturing process requires a high level of precision and precise tolerances. A significant number of AM machines are used for building objects with dimensions in the range of centimetres or larger with accuracy that exceeds a few hundredths of a millimetre [186]. Maintaining these tolerances gets more challenging as the HC structure's complexity and scale increase [107]. Scalable manufacturing procedures for HCs with hierarchical features are crucial for engineering applications. Scaling can pose problems in terms of consistency, quality control, and cost-effectiveness. Ensuring the quality and consistency of HCs, particularly those with intricate hierarchies, presents quality control issues during the manufacturing process [120, 187-188]. Defects or differences from the original design tend to be challenging to detect. To achieve specified functionality, some HCs may call for the integration of different materials with different properties [127, 188-189]. It can be difficult to link or connect these materials whilst maintaining the intended hierarchy. Customizing hierarchical HCs for specific uses often requires a degree of tailoring and flexibility in design. Challenges can be encountered with manufacturing methods when tackling varying design requirements and hierarchical feature changes. Materials and manufacturing methods must be chosen based on objectives for sustainability and environmental requirements [120, 127, 187-189]. Developing eco-friendly ways of manufacturing while preserving the desired hierarchy adds a level of complexity to manufacturing [189].

2.9. Scope and opportunities for future work

2.9.1 Next-generation structural optimization and design guide for lattice structures

The next generation of structural optimization and design principles for lattice structures is expected to incorporate several breakthroughs and trends in response to changing technology, materials, and engineering requirements. Some prospective paths for the development of lattice structures are discussed in the following paragraphs.

Through the advancement of metamaterials and engineered composites, lattice structures are expected to be designed with materials that have specific properties, such as variable stiffness or properties that can dynamically change based on external influences, such as stress or temperature [188, 190-191]. Using auxetic metamaterials in lattice structures provides varying stiffnesses. Auxetic materials have a negative Poisson's ratio and expand in numerous directions when stretched. Engineers incorporate these materials to build lattice structures that dynamically vary their stiffness depending on the applied load. As an illustration, in the field of sports equipment, a tennis racket could potentially be designed with lattice structures that use auxetic materials. During a robust swing, the lattice structure customizes to the amount of load applied, optimizing the racket's stiffness for the maximum energy transfer. Additionally, new lattice designs could incorporate bioinspired materials with exceptional strength-to-weight ratios, mimicking the

efficiency seen in structures such as bone or spider silk [145]. Lattice parts could be manufactured using synthetic materials that mimic specific properties of spider silk, such as tensile strength and elasticity. Spider silk is recognised for its remarkable strength and elasticity. Mimicking the molecular structure of the proteins of spider silk in synthetic materials could yield lattices that are both strong and resilient. These structures potentially have uses in a variety of fields, including aerospace engineering as well as construction. Machine learning and artificial intelligence (AI) are being used to automate and optimize the design process, allowing for the rapid production and testing of multiple design alterations. The AI and machine learning techniques are expected to be implemented more often to optimize lattice structures by analyzing huge amounts of data and iteratively improving designs, resulting in more efficient designs [192-193]. AI algorithms can respond to real-time feedback during the manufacturing and testing processes by incorporating this knowledge into subsequent design iterations. As lattice structures are built and tested, AI systems can gather information about the designs' actual performance and behaviour. The algorithms use this feedback to iteratively improve future designs, learning via both successes and failures. This adaptive learning strategy speeds up the optimization of lattice designs by using real-world performance data. Furthermore, improving predictive capabilities by using digital twin technologies to simulate and analyze the functionality of lattice structures in real-world engineering conditions is anticipated as well [194]. Using contemporary 3D modelling and simulation software to generate digital replicas of actual lattice parts, digital twin technologies allow for the generation of computer-generated alternatives that mirror actual lattice designs, capturing their geometry, material properties, and behaviour under various loading conditions. Quantum computing is expected to come into play for use in highly complicated simulations and optimizations, thus allowing for the design of traditionally unattainable lattice structures [195]. Engineers must also interact with modern design software and AI to create novel and efficient lattice structure designs [193]. In addition, engineers will ultimately be allowed to enter more complicated and specific design constraints as well as performance goals into automated generative design procedures, and the modelling packages will suggest optimized lattice designs [196]. Lattice structures that are tailored to certain performance parameters, such as the maximum strength-to-weight ratio, can be created. Generative design techniques, which are driven by complex algorithms, would not only explore a wide range of design choices but additionally pick and recommend lattice structures that are optimized based on the provided constraints and goals. This optimization could involve the material usage, manufacturability, and overall performance, resulting in highly efficient lattice designs.

Multi-material AM technologies are emerging that enable the printing of lattice structures with graded materials and different properties within the same structure [20]. Techniques such as multi-material 3D printing and Digital Light Processing (DLP) with numerous resin vats can be used. These methods allow the simultaneous use of various materials during the printing process. Multi-material 3D printing, for example, allows for the layer-by-layer deposition of different materials, resulting in it being easier to build complex structures with multiple material compositions. Improved methods of AM, such as nanoscale printing, have the capacity to support the manufacture of complicated lattice structures at extremely small dimensional scales and thus serve to update industries such as microelectronics and the manufacture of medical devices [76]. Nanoscale 3D printing uses techniques such as two-photon polymerization and direct laser writing. Current 3D printing processes could be limited in their ability to produce high-resolution structures at the nanoscale. Improved methods, such as two-photon polymerization or direct laser writing, provide improved precision and resolution, allowing for the creation of complex lattice structures at levels that cannot be achieved with conventional manufacturing procedures.

Material advancements could also allow lattice structures to self-assemble or repair damage, providing greater resilience and life expectancy [197-198]. Materials with shape-memory capabilities are capable of self-assembling into lattice forms. Shape-memory materials can change their shape in response to external stimuli, such as temperature or stress. By incorporating these materials into lattice designs, they could self-assemble into predetermined configurations, improving the manufacturing effectiveness and facilitating the building of complicated structures without the need for external assembly procedures. Additionally, lattice parts that offer different functions, such as structural support and energy storage or sensing

capabilities, could become more prevalent. The integration of sensors into lattice structures is expected to allow for the real-time monitoring of stress and strain, allowing responses that adapt to changing conditions or loads. This will allow the growth of design principles that take account of dynamic loading conditions, which is particularly crucial for applications in aerospace, automotive, and civil engineering [6, 145, 153].

Methods of TO are changing as well to take advantage of more complex constraints and allow for the generation of lattice designs that are tailored to specific functions [196], considering thermal, acoustic, and multifunctional constraints in addition to structural requirements. TO has generally focused on structural challenges. However, emerging approaches now include a broader set of constraints, allowing engineers to optimize lattice designs for heat dissipation, sound absorption, and other particular functional requirements.

A focus on concepts of sustainable design should also result in the manufacturing of lattice structures constructed using eco-friendly and recyclable materials. Circular design principles, such as designing for disassembly and reusability, are expected to reduce waste and encourage a more sustainable lifecycle for these structures [136]. Bio-based polymers, recycled metals, or sustainable composites are used to produce lattice structures. Sustainable design strategies include using materials that have a lesser environmental impact. For lattice structures, this could include choosing materials produced from renewable sources, recycled content, or those with a lower environmental imprint. Bio-based polymers, for example, can be used to produce functional and eco-friendly lattice structures.

The next generation of the design and optimization of lattice structures is anticipated to be highly dynamic, driven by emerging technology and the growing demand for robust, lightweight, recyclable, and efficient structures in several industries. This will lead to more environmentally friendly and advanced cutting-edge methods and technology.

2.9.2 Challenges and future prospects in design for additive manufacturing of lattice structures

Design for additive manufacturing (DfAM) of lattice parts holds enormous promise for the aerospace, automotive, and medical engineering industries, but it is also facing several challenges as well, which raises prospects for the future to consider.

Challenges related to DfAM of lattice structures. Given the complexity of the geometry, designing intricate lattice parts can be challenging. This could result in manufacturing difficulties related to the support structure requirements, printability, and post-processing constraints. AM often results in rough surfaces that require post-processing to improve the surface design and mechanical properties. Post-processing methods for lattice parts tend to be challenging to optimize [6, 13, 19-20, 145, 153, 154, 199]. For instance, challenges associated with removing support structures without damaging delicate lattice features. After printing, lattice parts typically call for post-processing to remove support structures. The delicate nature of lattice features makes this process challenging, as excessive force or the use of improper techniques could damage the structure. Addressing these post-processing limitations may require careful study and manual labour. Furthermore, identifying and developing materials that are equally good for AM and with the capacity to attain the required mechanical properties of lattice designs is presently a significant challenge as well [13], for example, developing polymers or metal alloys that perform well during the layer-by-layer deposition process in 3D printing. Some materials might not be naturally compatible with specific AM procedures. Certain polymers or metal alloys, for example, can present challenges during the printing process due to their melting viscosity, cooling rates, or adhesion, compromising the overall quality and structural integrity of lattice structures. The current methods for optimizing lattice structures are not capable of taking advantage of AM's capacity. These methods fail to take full advantage of multiple objectives, as well as other aspects, such as support structure requirements, layer adhesion, and minimizing the manufacturing time while maximizing the structural performance. Adapting designs for different scales and resolutions in AM technologies, as well as guaranteeing the structure's integrity and performance over different sizes, is presently challenging [11, 16, 27, 200-203]. In a lattice design, weight reduction is balanced with mechanical strength and thermal conductivity. Traditional optimization methods could zero in on a

particular objective, such as minimizing the material usage in lightweight structures. However, in AM, where complex lattice geometries are feasible, it is possible to optimize multiple targets at the same time, such as obtaining lightweight designs with precise mechanical and thermal properties.

Maintaining consistency and quality control in AM is difficult, particularly for lattice parts requiring a specific degree of porosity inherent in the structure and geometrical accuracy [11, 27, 200, 202]. In addition, building advanced multi-material and multi-colour printing technologies to attain adaptable and useful lattice structures is also difficult. Advanced validation procedures are required to ensure that the planned lattice parts meet performance and safety requirements that could vary from typical solid structures. These methods are presently challenged when it comes to predicting the behaviour of resulting lattice designs accurately [11, 145, 200], for instance, constructing lattice parts with a specific degree of porosity for use in bone implants. Lattice parts, such as those used in medical implants, could require an accurate degree of porosity for biological integration. Maintaining consistency in attaining the correct porosity over multiple prints while adhering to quality control is often difficult due to differences in material characteristics, printing conditions, and post-processing steps.

Future prospects in DfAM of lattice structures. Ongoing developments in designing tools ideally suited to lattice structures could assist in making complex designs simpler and more accurate to generate. Engineers will be able to rapidly generate complex lattice parts tailored for AM because of the ongoing developments of contemporary design software packages. Additionally, the research and development of new materials designed for AM, with customized characteristics, lightweight properties, and structural integrity, is anticipated to improve the functionality of lattice parts [196, 200], for instance, the introduction of CAD (computer-aided design) plugins or specialized design algorithms that make it easier to create lattice geometries. Current advancements in design tools aim to develop capabilities and plugins for CAD software that cater specifically to lattice designs. These tools could produce complex lattice designs automatically, giving engineers efficient and user-friendly interfaces for exploring, modifying, and generating complex lattice geometries.

Further advances in methods of TO are expected to assist in the generation of lattice designs that fully use the design freedom offered by AM machines [20, 192-193, 200]. Future work consists of AI-driven design procedures that automate and optimize lattice structures for specific performance criteria while simultaneously taking multiple variables into account all at the same time [192-193]. The generation of lattice structures for medical implants that are optimized for biocompatibility and load-bearing capacity is one such example. Future advances in AI-driven design techniques could automate the building of lattice designs matched to specific performance requirements. For instance, in the medical industry, an AI-driven design strategy could generate lattice structures for implants with optimized properties for biocompatibility, load-bearing capacity, and additional characteristics relevant to the medical application. Moreover, digital twin technology, in conjunction with upgraded simulation, is expected to play a significant part in predicting the behaviour of lattice designs during and after AM and, in this way, assist in the performance analysis and quality control of the resulting parts [192]; for instance, the use digital twin technology to compare the virtual models of lattice structures to actual 3D scan data of manufactured products for the reason of quality control. Digital twins allow for a direct comparison of the virtual and physical representations of lattice structures. By integrating 3D scan data from the actual product into the digital twin, methods of quality control can detect differences between the intended design and the manufactured part, thereby ensuring quality and consistency.

Lattice designs are predicted to be used in structures that have different functions, such as embedded sensors for real-time monitoring, conduits, and advanced metamaterials [193-194]; for instance, designing lattice structures within aircraft parts that integrate functions such as fuel conduits or vibration dampening. Lattice designs are often used in aeronautical applications when a reduction in weight is critical. Beyond structural support, lattice structures can incorporate additional functions, such as conduits for fuel or hydraulic fluids, which improves the overall efficiency of aircraft. This multifunctional strategy expands the applications of lattice structures in aerospace engineering. Collaboration across the globe should prove crucial to facilitate the sharing of knowledge and best practices and in overcoming global challenges as the

field of AM lattice designs grows [145]. This can be achieved through the creation of online platforms or forums for researchers and engineers worldwide to communicate research papers, methodologies, and insights learned in AM lattice design. The setting up of websites for sharing knowledge will allow experts to share their experiences, successes, and challenges with AM lattice designs. This collective exchange of information will assist in identifying best practices, efficient design strategies, and insights gained, thus allowing a community-driven strategy for advancement. In addition, mimicking the design concepts observed in biological structures, such as trabecular bones or honeycombs, should provide new alternative designs for lattice parts [145]. This can be achieved using optimization algorithms inspired by natural phenomena, such as genetic algorithms or swarm intelligence, to improve lattice design. Nature-inspired optimization algorithms are designed to replicate natural problem-solving processes. Applying these methods to lattice design could result in novel geometries that are optimized according to performance criteria. For instance, evolutionary algorithms can iteratively evolve lattice structures to attain desired characteristics, resulting in alternative designs that are challenging to envision using traditional methods.

The use of DfAM for lattice structures offers a promising future, with the capacity to change industries such as aerospace, automotive, and medical engineering. Addressing the existing challenges and exploring prospects in this respect should pave the path for new and efficient designs that take full advantage of the capacities of AM.

References

1. Gibson, L. J., and Ashby, M. F. (2014). Cellular solids: structures and properties. *Cambridge University Press*, 2nd ed. Cambridge.
2. Zhang, Q., Yang, X., Li, P., Huang, G., Feng, S., Shen, C., Han, B., Zhang, X., Jin, F., Xu, F., & Lu, J. (2015). Bioinspired engineering of honeycomb structure-using nature to inspire human innovation. *Prog. Mater. Sci.*, vol 74, 332-400.
3. Fratzl, P., and Weinkamer, R. (2007). Nature's hierarchical materials, *Prog. Mater. Sci.*, vol 52, 1263-1334.
4. Chen, Q. and Pugno, N. M. (2013). Biomimetic mechanisms of natural hierarchical materials: a review. *J. Mech. Behav. Biomed. Mater.*, vol 19, 3-33.
5. Zhang, P. (2015). Bioinspired hierarchical materials and cellular structures: design, modelling, and 3D printing. Ph.D. dissertation, Dept. Mech. Eng. and Mater. Sci., Uni. Pittsburg., Pennsylvania.
6. San Ha, N., and Lu, G. (2020). A review of recent research on bio-inspired structures and materials for energy absorption applications. *Composite Part B: Engineering*, 181, 107496.
7. Wegst, U. G., Bai, H., Saiz, E., Tomsia, A. P., & Ritchie, R. O. (2015). Bioinspired structural materials. *Nature Materials*, 14(1), 23-36.
8. Attaran, M. (2017). The rise of 3D printing: the advantages of additive manufacturing over traditional manufacturing. *Business Horizons*, 60(5), 677-688.
9. Panesar, A., Abdi, M., Hickman, D., & Ashcroft, I. (2018). Strategies for functionally graded lattice structures derived using topology optimization for additive manufacturing. *Additive Manufacturing*, 19, 81-94.
10. Park, K. M., Min, K. S., & Roh, Y. S. (2022). Panimisation of lattice structures under compression: study of unit cell types and cell arrangements. *Materials*, 15(1), 97.
11. Benedetti, M., Du Plessis, A., Ritchie, R. O., Dallago, M., Razavi, S. M. J., & Berto, F. (2021). Architected cellular materials: A review on their mechanical properties towards fatigue-tolerant design and fabrication. *Materials Science and Engineering: R: Reports*, 144, 100606.
12. Tofail, S. A., Koumoulos, E. P., Bandyopadhyay, A., Bose, S., O'Donoghue, L., & Charitidis, C. (2018). Additive manufacturing: scientific and technological challenges, market uptake and opportunities. *Materials Today*, 21(1), 22-37.

13. Du Plessis, A., Razavi, N., Benedetti, M., Murchio, S., Leary, M., Watson, M., & Berto, F. (2022). Properties and applications of additively manufactured metallic cellular materials: A review. *Progress in Materials Science*, 125, 100918.
14. Meyers, M. A., Chen, P. Y., Lin, A. Y. M., & Seki, Y. (2008). Biological materials: structure and mechanical properties. *Prog. Mater. Sci.*, vol 53, 1-206.
15. <https://slideplayer.com/slides/10778066/>, accessed on 14th December 2023.
16. Maconachie, T., Leary, M., Lozanovski, B., Zhang, X., Qian, M., Faruque, O., & Brandt, M. (2019). SLM lattice structures: Properties, performance, applications and challenges. *Materials & Design*, 183, 108137.
17. Sundar, V. C., Yablon, A. D., Grazul, J. L., Ilan, M., & Aizenberg, J. (2003). Fibre -optical features of a glass sponge. *Nature.*, vol 424, 899-900.
18. Rho, J. Y., Kuhn-Spearing, L., & Zioupos, P. (1998). Mechanical properties and the hierarchical structure of bone. *Med. Eng. Phys.*, vol 20, 92-102.
19. Wang, Z. (2019). Recent advances in novel metallic honeycomb structure. *Composites Part B: Engineering*, 166, 731-741.
20. Du Plessis, A., Broeckhoven, C., Yadroitsava, I., Yadroitsev, I., Hands, C. H., Kunju, R., & Bhate, D. (2019). Beautiful and functional: A review of biomimetic design in additive manufacturing. *Addit. Manuf.*, 27, 408-427. <https://doi.org/10.1016/j.addma.2019.03.033>
21. Zhang, Q., Yang, X., Li, P., Huang, G., Feng, S., Shen, C., & Lu, T. J. (2015). Bioinspired engineering of honeycomb structure—Using nature to inspire human innovation. *Progress in Materials Science*, 74, 332-400.
22. Ren, X., Xiao, L., & Hao, Z. (2019). Multi-property cellular material design approach based on the mechanical behaviour analysis of the reinforced lattice structure. *Materials & Design*, 174, 107785.
23. Brøtan, V., Fergani, O., Sørby K., Welo, T., (2016). *Mechanical properties of biocompatible 316L steel rhombic dodecahedron lattice structure*. Proceedings of the International Solid Freeform Fabrication Symposium, SFF, University of Texas, Austin, USA.
24. Maskery, I., Sturm, L., Aremu, A. O., Panesar, A., Williams, C. B., Tuck, C. J., & Hague, R. J. (2018). Insights into the mechanical properties of several triply periodic minimal surface lattice structures made by polymer additive manufacturing. *Polymer*, 152, 62-71.
25. AlMahri, S., Santiago, R., Lee, D. W., Ramos, H., Alabdouli, H., Alteneiji, M., & Alves, M. (2021). Evaluation of the dynamic response of triply periodic minimal surfaces subjected to high strain-rate compression. *Additive Manufacturing*, 46, 102220.
26. Tao, W., and Leu, M. C. (2016). Design of lattice structure for additive manufacturing. 2016 International Symposium on Flexible Automation (ISFA), IEEE. 325-332.
27. Liu, G., Zhang, X., Chen, X., He, Y., Cheng, L., Huo, M., & Lu, J. (2021). Additive manufacturing of structural materials. *Materials Science and Engineering: R: Reports*, 145, 100596.
28. Elsayed, M. S., and Pasini, D. (2010). Analysis of the elastostatic specific stiffness of 2D stretching-dominated lattice materials. *Mechanics of Materials*, 42(7), 709-725.
29. Zhang, B., Pei, X., Zhou, C., Fan, Y., Jiang, Q., Ronca, A., & Zhang, X. (2018). The biomimetic design and 3D printing of customized mechanical properties porous Ti6Al4V scaffold for load-bearing bone reconstruction. *Materials & Design*, 152, 30-39.
30. Wang, C., Gu, X., Zhu, J., Zhou, H., Li, S., & Zhang, W. (2020). Concurrent design of hierarchical structures with three-dimensional parameterized lattice microstructures for additive manufacturing. *Structural and Multidisciplinary Optimization*, 61, 869-894.

31. Zhang, Y., Xu, X., Fang, J., Huang, W., & Wang, J. (2022). Load characteristics of triangular honeycomb structures with self-similar hierarchical features. *Engineering Structures*, 257, 114114.
32. Zhang, W., and Xu, J. (2022). Advanced lightweight materials for Automobiles: A review. *Materials & Design*, 221, 110994.
33. Egan, P. F., Gonella, V. C., Engensperger, M., Ferguson, S. J., & Shea, K. (2017). Computationally designed lattices with tuned properties for tissue engineering using 3D printing. *PloS one*, 12(8), e0182902.
34. Nguyen, J., Park, S. I., Rosen, D. W., Folgar, L., & Williams, J. (2012). *Conformal lattice structure design and fabrication*. 2012 International Solid Freeform Fabrication Symposium. University of Texas at Austin.
35. Zhang, H., Wang, Y., & Kang, Z. (2019). Topology optimization for concurrent design of layer-wise graded lattice materials and structures. *International Journal of Engineering Science*, 138, 26-49.
36. Chen, L. Y., Liang, S. X., Liu, Y., & Zhang, L. C. (2021). Additive manufacturing of metallic lattice structures: Unconstrained design, accurate fabrication, fascinated performances, and challenges. *Materials Science and Engineering: R: Reports*, 146, 100648.
37. Zhang, L., Song, B., Fu, J. J., Wei, S. S., Yang, L., Yan, C. Z., & Shi, Y. S. (2020). Topology-optimized lattice structures with simultaneously high stiffness and light weight fabricated by selective laser melting: Design, manufacturing and characterization. *Journal of Manufacturing Processes*, 56, 1166-1177.
38. Alzahrani, M., Choi, S. K., & Rosen, D. W. (2015). Design of truss-like cellular structures using relative density mapping method. *Materials & Design*, 85, 349-360.
39. Smith, M., Guan, Z., & Cantwell, W. J. (2013). Finite element modelling of the compressive response of lattice structures manufactured using the selective laser melting technique. *International Journal of Mechanical Sciences*, 67, 28-41.
40. Li, C., Lei, H., Zhang, Z., Zhang, X., Zhou, H., Wang, P., & Fang, D. (2020). Architecture design of periodic truss-lattice cells for additive manufacturing. *Additive Manufacturing*, 34, 101172.
41. Rashed, M. G., Ashraf, M., Mines, R. A. W., & Hazell, P. J. (2016). Metallic microlattice materials: A current state of the art on manufacturing, mechanical properties and applications. *Materials & Design*, 95, 518-533.
42. Ashby, M. F., & Gibson, L. J. (1997). Cellular solids: structure and properties. *Press Syndicate of the University of Cambridge, Cambridge, UK*, 175-231.
43. Ahmadi, S. M., Amin Yavari, S., Wauthle, R., Pouran, B., Schrooten, J., Weinans, H., & Zadpoor, A. A. (2015). Additively manufactured open-cell porous biomaterials made from six different space-filling unit cells: The mechanical and morphological properties. *Materials*, 8(4), 1871-1896.
44. Seharing, A., Azman, A. H., & Abdullah, S. (2020). A review on integration of lightweight gradient lattice structures in additive manufacturing parts. *Advances in Mechanical Engineering*, 12(6). 1687814020916951.
45. Catchpole-Smith, S., Sélo, R. R. J., Davis, A. W., Ashcroft, I. A., Tuck, C. J., & Clare, A. (2019). Thermal conductivity of TPMS lattice structures manufactured via laser powder bed fusion. *Additive Manufacturing*, 30. 100846.
46. Mohammed, M. I., and Gibson, I. (2018). Design of three-dimensional, triply periodic unit cell scaffold structures for additive manufacturing. *Journal of Mechanical Design*, 140(7).
47. Al-Ketan, O., and Abu Al-Rub, R. K. (2019). Multifunctional mechanical metamaterials based on triply periodic minimal surface lattices. *Advanced Engineering Materials*, 21(10), 1900524.

48. Al-Ketan, O., Rezgui, R., Rowshan, R., Du, H., Fang, N. X., & Abu Al-Rub, R. K. (2018). Microarchitected stretching-dominated mechanical metamaterials with minimal surface topologies. *Advanced Engineering Materials*, 20(9), 1800029.
49. Helou, M., and Kara, S. (2018). Design, analysis and manufacturing of lattice structures: an overview. *International Journal of Computer Integrated Manufacturing*, 31(3), 243-261.
50. Gebisa, A. W., and Lemu, H. G. (2018). Additive manufacturing for the manufacture of gas turbine engine components: literature review and future perspectives. *Turbo expo: Power for land, sea, and air*, 51128, V006T24A021.
51. Chibinyani, M. I., Dzogbewu, T. C., Maringa, M., & Muiruri, A. M. (2023). Numerical modelling of DMLS Ti6Al4V (ELI) polygon structures. *Results in Materials*, 20. 100456.
52. Distefano, F., Pasta, S., & Epasto, G. (2023). Titanium lattice structures produced via additive manufacturing for a bone scaffold: A review. *Journal of Functional Biomaterials*, 14(3), 125.
53. Bhate, D., Penick, C. A., Ferry, L. A., & Lee, C. (2019). Classification and selection of cellular materials in mechanical design: Engineering and biomimetic approaches. *Designs*, 3(1), 19.
54. Ai, L., and Gao, X. L. (2017). Metamaterials with negative Poisson's ratio and non-positive thermal expansion. *Composite Structures*, 162, 70-84.
55. Saxena, K. K., Das, R., & Calius, E. P. (2016). Three decades of auxetics research— materials with negative Poisson's ratio: a review. *Advanced Engineering Materials*, 18(11), 1847-1870.
56. Prawoto, Y. (2012). Seeing auxetic materials from the mechanics point of view: A structural review on the negative Poisson's ratio. *Computational Materials Science*, 58, 140-153.
57. Xue, X., Lin, C., Wu, F., Li, Z., & Liao, J. (2022). Lattice structures with negative Poisson's ratio: A review. *Materials Today Communications*. 105132.
58. Qi, C., Jiang, F., & Yang, S. (2021). Advanced honeycomb designs for improving mechanical properties: A review. *Composites Part B: Engineering*, 227. 109393.
59. Bührig-Polaczek, A., Fleck, C., Speck, T., Schüler, P., Fischer, S. F., Caliaro, M., & Thielen, M. (2016). Biomimetic cellular metals—using hierarchical structuring for energy absorption. *Bioinspiration & biomimetics*, 11(4). 045002.
60. Fratzl, P., Dunlop, J., & Weinkamer, R. (Eds.). (2015). *Materials design inspired by nature: function through inner architecture*. Royal Society of Chemistry.
61. Horstemeyer, M. F. (2012). *Integrated Computational Materials Engineering (ICME) for metals: using multiscale modelling to invigorate engineering design with science*. John Wiley & Sons.
62. Song, K., Li, D., Zhang, C., Liu, T., Tang, Y., Xie, Y. M., & Liao, W. (2023). Bio-inspired hierarchical honeycomb metastructures with superior mechanical properties. *Composite Structures*, 304. 116452.
63. Wang, Z. (2019). Recent advances in novel metallic honeycomb structure. *Composites Part B: Engineering*, 166, 731-741.
64. Bao, F., Liu, B., Liu, E., Guo, G., Li, Z., & Zhang, X. (2024). Fabrication of Gasar porous Mg Ag x (x= 0.5, 17.57) alloys via the Metal-H Eutectic Directional Solidification Process. *JOM*, 76(4), 1856-1869.
65. Zhang, X., Li, Y., Liu, Y., & Zhang, H. (2013). Fabrication of a bimodal micro/nanoporous metal by the Gasar and dealloying processes. *Materials letters*, 92, 448-451.
66. Verma, S., Kumar, A., Lin, S. C., & Jeng, J. Y. (2002). A bioinspired design strategy for easy powder removal in powder-bed based additive manufactured lattice structure. *Virtual Phys. Prototyp.*, vol 17, 46.
67. Vaneker, T., Benard, A., Moroni, G., Gibson, I., & Zhang, Y. (2020). Design for additive manufacturing: framework and methodology. *CIRP Annals*, vol 69, 578-59.

68. Zhu, L., Li, N., & Childs, P. R. N. (2018). Light weighting in aerospace component and system design. *Propuls. Power Res.*, vol 7, 103-119.
69. Lazarus, B. S., Velasco-Hogan, A., Gómez-del Río, T., Meyers, M. A., & Jasiuk, I. A. (2020). Review of impact resistant biological and bioinspired materials and structures. *J. Mater. Res. Tech.*, vol 9, 15705-15738.
70. Yang, X., Ma, J., We, D., & Yang, J. (2020). Crashworthy design and energy absorption mechanisms for helicopter structures: a systematic literature review. *Prog. Aerosp. Sci.*, vol 114, 100618.
71. Li, S., & Wang, K. W. (2016). Plant-inspired adaptive structures and materials for morphing and actuation: a review. *Bioinspiration & biomimetics*, 12(1), 011001.
72. Wijegunawardana, I. D., & De Mel, W. R. (2021). Biomimetic designs for automobile engineering: a review. *International Journal of Automotive and Mechanical Engineering*, 18(3), 9029-9041.
73. Abdulbari, H. A., Mahammed, H. D., & Hassan, Z. B. (2015). Bio-inspired passive drag reduction techniques: a review. *ChemBioEng Reviews*, 2(3), 185-203.
74. Hussey, G. S., Dziki, J. L., & Badylak, S. F. (2018). Extracellular matrix-based materials for regenerative medicine. *Nature Reviews Materials*, 3(7), 159-173.
75. Pan, C., Han, Y., & Lu, J. (2020). Design and optimization of lattice structures: A review. *Applied Sciences*, 10(18), 6374.
76. Libonati, F., & Buehler, M. J. (2017). Advanced structural materials by bioinspiration. *Advanced Engineering Materials*, 19(5), 1600787.
77. Chen, P. Y., Lin, A. Y. M., Lin, Y. S., Seki, Y., Stokes, A. G., Peyras, J., ... & McKittrick, J. (2008). Structure and mechanical properties of selected biological materials. *Journal of the mechanical behavior of biomedical materials*, 1(3), 208-226.
78. Zimmermann, E. A., & Ritchie, R. O. (2015). Bone as a structural material. *Advanced healthcare materials*, 4(9), 1287-1304.
79. Wijerathne, B., Liao, T., Ostrikov, K., & Sun, Z. (2022). Bioinspired robust mechanical properties for advanced materials. *Small Structures*, 3(9), 2100228.
80. Zhang, H., Hu, D., Peng, H., Yuan, W., & Yang, Z. (2024). In-plane crushing behavior and energy absorption of sponge-inspired lattice structures. *International Journal of Mechanical Sciences*, 274, 109328.
81. Yao, R., Pang, T., He, S., Li, Q., Zhang, B., & Sun, G. (2022). A bio-inspired foam-filled multi-cell structural configuration for energy absorption. *Composites Part B: Engineering*, 238, 109801.
82. Wang, P., Yang, F., Fan, H., & Lu, G. (2023). Bio-inspired multi-cell tubular structures approaching ideal energy absorption performance. *Materials & Design*, 225, 111495.
83. A. Bührig-Polaczek, C. Fleck, T. Speck, P. Schüler, S. F. Fischer, M. Caliaro and M. Thielen, "Biomimetic cellular metals-using hierarchical structuring for energy absorption," *Bioinspir. Biomim.*, vol 11, pp. 45002, 2016.
84. Plocher, J., & Panesar, A. (2019). Review on design and structural optimisation in additive manufacturing: Towards next-generation lightweight structures. *Materials & Design*, 183, 108164.
85. Chatzigeorgiou, C., Piotrowski, B., Chemisky, Y., Laheurte, P., & Meraghni, F. (2022). Numerical investigation of the effective mechanical properties and local stress distributions of TPMS-based and strut-based lattices for biomedical applications. *Journal of the mechanical behavior of biomedical materials*, 126, 105025.
86. Yu, X., Zhou, J., Liang, H., Jiang, Z., & Wu, L. (2018). Mechanical metamaterials associated with stiffness, rigidity and compressibility: A brief review. *Progress in Materials Science*, 94, 114-173.
87. Sun, J., and Bhushan, B. (2012). Hierarchical structure and mechanical properties of nacre: a review. *RSC Advances*, 2(20), 7617-7632.

88. Luz, G. M., and Mano, J. F. (2009). Biomimetic design of materials and biomaterials inspired by the structure of nacre. *Philosophical Transactions of the Royal Society A: Mathematical, Physical and Engineering Sciences*, 367(1893), 1587-1605.
89. Liang, S. M., Ji, H. M., & Li, X. W. (2021). A high-strength and high-toughness nacreous structure in a deep-sea Nautilus shell: Critical role of platelet geometry and organic matrix. *Journal of Materials Science & Technology*, 88, 189-202.
90. Soucek, M. D. (2007). Inorganic/organic hybrid coatings. *Hybrid Materials*. Weinheim, German: Wiley-VCH Verlag GmbH & Co. KGaA.
91. Wang, Y., Jiang, X., Li, X., Ding, K., Liu, X., Huang, B., ... & Xu, W. (2023). Bionic ordered structured hydrogels: structure types, design strategies, optimization mechanism of mechanical properties and applications. *Materials Horizons*, 10(10), 4033-4058.
92. Frey, M., Biffi, G., Adobes-Vidal, M., Zirkelbach, M., Wang, Y., Tu, K., ... & Keplinger, T. (2019). Tunable wood by reversible interlocking and bioinspired mechanical gradients. *Advanced Science*, 6(10), 1802190.
93. Audibert, C., Chaves-Jacob, J., Linares, J. M., & Lopez, Q. A. (2018). Bio-inspired method based on bone architecture to optimize the structure of mechanical workpieces. *Materials & Design*, 160, 708-717.
94. Gibson, L. J., Ashby, M. F., & Harley, B. A. (2010). *Cellular materials in nature and medicine*. Cambridge University Press.
95. Özkaya, N., Nordin, M., Goldsheyder, D., & Leger, D. (2012). Fundamentals of biomechanics, *Springer International Publishing*, 4th ed, Vol. 86.
96. Adharapurapu, R. R., Jiang, F., & Vecchio, K. S. (2006). Dynamic fracture of bovine bone. *Materials Science and Engineering: C*, 26(8), 1325-1332.
97. Simkin, A., & Robin, G. (1973). The mechanical testing of bone in bending. *Journal of biomechanics*, 6(1), 31-39.
98. Ascenzi, A., & Bonucci, E. (1968). The compressive properties of single osteons. *The Anatomical Record*, 161(3), 377-391.
99. Jeronimidis, G. (2000). Structure-property relationships in biological materials. In *Pergamon Materials Series: Pergamon*, Vol. 4, 3-16.
100. Niebel, T. P., Bouville, F., Kokkinis, D., & Studart, A. R. (2016). Role of the polymer phase in the mechanics of nacre-like composites. *Journal of the Mechanics and Physics of Solids*, 96, 133-146.[Correct the indentation and style.]
101. Libonati, F., Vellwock, A. E., Ielmini, F., Abliz, D., Ziegmann, G., & Vergani, L. (2019). Bone-inspired enhanced fracture toughness of de novo fiber reinforced composites. *Scientific reports*, 9(1), 3142.
102. Amini, S., Tadayon, M., Idapalapati, S., & Miserez, A. (2015). The role of quasi-plasticity in the extreme contact damage tolerance of the stomatopod dactyl club. *Nature Materials*, 14(9), 943-950.
103. Vogel, N., Retsch, M., Fustin, C. A., Del Campo, A., & Jonas, U. (2015). Advances in colloidal assembly: the design of structure and hierarchy in two and three dimensions. *Chemical Reviews*, 115(13), 6265-6311.
104. Chen, Y., Ma, Y., Yin, Q., Pan, F., Cui, C., Zhang, Z., & Liu, B. (2021). Advances in mechanics of hierarchical composite materials. *Composites Science and Technology*, 214, 108970.
105. Zhang, X. Y., Fang, G., & Zhou, J. (2017). Additively manufactured scaffolds for bone tissue engineering and the prediction of their mechanical behavior: A review. *Materials*, 10(1), 50.
106. McDowell, D. L., and Backman, D. (2011). Simulation-assisted design and accelerated insertion of materials. *Computational methods for microstructure-property relationships*, 617-647.

107. Ru, K., Swati, R. F., Zeng, H., Khan, Z., Chen, Z., Qian, A., & Hu, L. (2024). The whole bone mechanical properties and modeling study. *Bone Cell Biomechanics, Mechanobiology and Bone Diseases*, Academic Press, 53-94.
108. Colombo, P., and Bernardo, E. (2008). 10 Cellular Structures. *Ceramics Science and Technology, Volume 1: Structures*, 407.
109. Hoffmann, K. A., Chen, T. G., Cutkosky, M. R., & Lentink, D. (2023). Bird-inspired robotics principles as a framework for developing smart aerospace materials. *Journal of Composite Materials*, 57(4), 679-710.
110. Vazic, B., Abali, B. E., Yang, H., & Newell, P. (2021). Mechanical analysis of heterogeneous materials with higher-order parameters. *Engineering with Computers*, 1-17.
111. Arabnejad, S., and Pasini, D. (2013). Mechanical properties of lattice materials via asymptotic homogenization and comparison with alternative homogenization methods. *International Journal of Mechanical Sciences*, 77, 249-262.
112. Ajdari, A., Jahromi, B. H., Papadopoulos, J., Nayeb-Hashemi, H., & Vaziri, A. (2012). Hierarchical honeycombs with tailorable properties. *International Journal of Solids and Structures*, 49(11-12), 1413-1419.
113. Sun, Y., Wang, B., Pugno, N., Wang, B., & Ding, Q. (2015). In-plane stiffness of the anisotropic multifunctional hierarchical honeycombs. *Composite Structures*, 131, 616-624.
114. Chen, Y., Li, T., Jia, Z., Scarpa, F., Yao, C. W., & Wang, L. (2018). 3D-printed hierarchical honeycombs with shape integrity under large compressive deformations. *Materials & Design*, 137, 226-234.
115. Hu, D., Wang, Y., Song, B., Dang, L., & Zhang, Z. (2019). Energy-absorption characteristics of a bionic honeycomb tubular nested structure inspired by bamboo under axial crushing. *Composites Part B: Engineering*, 162, 21-32.
116. Sun, G., Jiang, H., Fang, J., Li, G., & Li, Q. (2016). Crashworthiness of vertex-based hierarchical honeycombs in out-of-plane impact. *Materials & Design*, 110, 705-719.
117. Zhang, D., Fei, Q., Liu, J., Jiang, D., & Li, Y. (2020). Crushing of vertex-based hierarchical honeycombs with triangular substructures. *Thin-Walled Structures*, 146. 106436.
118. He, Q., Feng, J., Chen, Y., & Zhou, H. (2020). Mechanical properties of spider-web hierarchical honeycombs subjected to out-of-plane impact loading. *Journal of Sandwich Structures & Materials*, 22(3), 771-796.
119. Tan, H. L., He, Z. C., Li, K. X., Li, E., Cheng, A. G., & Xu, B. (2019). In-plane crashworthiness of re-entrant hierarchical honeycombs with negative Poisson's ratio. *Composite Structures*, 229. 111415.
120. Fang, J., Sun, G., Qiu, N., Pang, T., Li, S., & Li, Q. (2018). On hierarchical honeycombs under out-of-plane crushing. *International Journal of Solids and Structures*, 135, 1-13.
121. Chen, Y., Jia, Z., & Wang, L. (2016). Hierarchical honeycomb lattice metamaterials with improved thermal resistance and mechanical properties. *Composite structures*, 152, 395-402.
122. Ryvkin, M., and Shraga, R. (2018). Fracture toughness of hierarchical self-similar honeycombs. *International Journal of Solids and Structures*, 152, 151-160.
123. Xiao, L., Xu, X., Feng, G., Li, S., Song, W., & Jiang, Z. (2022). Compressive performance and energy absorption of additively manufactured metallic hybrid lattice structures. *International Journal of Mechanical Sciences*, 219. 107093.
124. Gibson, L. J., Ashby, M. F., Schajer, G. S., & Robertson, C. I. (1982). The mechanics of two-dimensional cellular materials. *Proceedings of the Royal Society of London. A. Mathematical and Physical Sciences*, 382(1782), 25-42.
125. Zhong, H., Song, T., Li, C., Das, R., Gu, J., & Qian, M. (2023). The Gibson-Ashby model for additively manufactured metal lattice materials: Its theoretical basis, limitations and new insights from remedies. *Current Opinion in Solid State and Materials Science*, 27(3). 101081.
126. Ashby, M. F., Evans, A., Fleck, N. A., Gibson, L. J., Hutchinson, J. W., Wadley, H. N. G., & Delale, F. (2001). Metal foams: a design guide. *Applied Mechanics Reviews*, 54(6), B105-B106.

127. Chibinyani, M. I., Dzogbewu, T. C., Maringa, M., & Muiruri, A. M. (2024). Lattice structures built with different polygon hollow shapes: A review on their analytical modelling and engineering applications. *Applied Sciences*, 14(4), 1582.
128. Avalor, M., Belingardi, G., & Ibba, A. (2007). Mechanical models of cellular solids: Parameters identification from experimental tests. *International Journal of Impact Engineering*, 34(1), 3-27.
129. Kucewicz, M., Baranowski, P., Małachowski, J., Popławski, A., & Płatek, P. (2018). Modelling, and characterization of 3D printed cellular structures. *Materials & Design*, 142, 177-189.
130. Gibson, I. J., and Ashby, M. F. (1982). The mechanics of three-dimensional cellular materials. *Proceedings of the Royal Society of London. A. Mathematical and Physical Sciences*, 382(1782), 43-59.
131. Reda Taha, M., Ayyub, B. M., Soga, K., Daghash, S., Heras Murcia, D., Moreu, F., & Soliman, E. (2021). Emerging technologies for resilient infrastructure: Conspectus and roadmap. *ASCE-ASME Journal of Risk and Uncertainty in Engineering Systems, Part A: Civil Engineering*, 7(2). 03121002.
132. Case, J., and Chilver, A. H. (2013). *Strength of materials and structures: an introduction to the mechanics of solids and structures*. Elsevier.
133. Falzon, B. G., and Aliabadi, M. F. (2008). *Buckling and postbuckling structures: experimental, analytical and numerical studies 1*. World Scientific.
134. Wadee, M. A., and Bai, L. (2014). Cellular buckling in I-section struts. *Thin-Walled Structures*, 81, 89-100.
135. J. Pinski and D. Howard, From bioinspiration to computer generation: developments in autonomous soft robot design, *Adv. Intell. Syst.*, vol 41, 2100086, 2022. [Incorrect format]
136. Yeo, S. J., Oh, M. J., & Yoo, P. J. (2019). Structurally controlled cellular architectures for high-performance ultra-lightweight materials. *Advanced Materials*, 31(34). 1803670.
137. Nazir, A., Abate, K. M., Kumar, A., & Jeng, J. Y. (2019). A state-of-the-art review on types, design, optimization, and additive manufacturing of cellular structures. *The International Journal of Advanced Manufacturing Technology*, 104. 3489-3510.
138. Ren, R., Ma, X., Yue, H., Yang, F., & Lu, Y. (2024). Stiffness enhancement methods for thin-walled aircraft structures: A review. *Thin-Walled Structures*. 111995.
139. Armstrong, C. (1987). *Mechanics of engineering materials*. Prentice Hall.
140. Yu, H., Zhang, J., Zhang, S., & Han, Z. (2023). Bionic structures and materials inspired by plant leaves: A comprehensive review for innovative problem-solving. *Progress in Materials Science*. 101181.
141. Crawford, R. J., and Martin, P. J. (2020). *Plastics engineering*. Butterworth-Heinemann.
142. Bedford, A., Liechti, K. M., Bedford, A., & Liechti, K. M. (2020). Criteria for failure and fracture. *Mechanics of Materials*, 823-893.
143. Cunha, A., Yanik, Y., Olivieri, C., & da Silva, S. (2023). Tresca vs. von Mises: Which failure criterion is more conservative in a probabilistic context? *Journal of Applied Mechanics*, 1-8.
144. Barsanescu, P. D., and Comanici, A. M. (2017). von Mises hypothesis revised. *Acta Mechanica*, 228, 433-446.
145. Zhang, Q., Yang, X., Li, P., Huang, G., Feng, S., Shen, C., Han, B., Zhang, X., Jin, F., Xu, F., & Lu, T. J. (2015) Bioinspired engineering of honeycomb structure – Using nature to inspire human innovation. *Prog. Mater. Sci.*, 74, 332-400. <https://doi.org/10.1016/j.pmatsci.2015.05.001>
146. Benedetti, M., Klarin, J., Johansson, F., Fontanari, V., Luchin, V., Zappini, G., & Molinari, A. (2019) Study of the compression behaviour of Ti6Al4V trabecular structures produced by additive laser manufacturing. *Materials*, 12, 1471. <https://doi.org/10.3390/ma12091471>
147. Maconachie, T., Tino, R., Lozanovski, B., Watson, M., Jones, A., Pandelidi, C., Alghamdi, A., Almalki, A., Downing, D., Brandt, M., & Leary, M. (2020). The compressive behaviour of ABS gyroid lattice structures manufactured by fused deposition modelling. *Int. J. Adv. Manuf. Technol.* 107, 4449-4467. <https://doi.org/10.1007/s00170-020-05239-4>

148. Raghavendra, S., Molinari, A., Zappini, G., & Benedetti, M. (2021). Correlation between as-designed and as-built Young's modulus of cubic regular, cubic irregular, and trabecular cellular materials. *Mater. Des. Process. Commun.*, 3, e257.
149. Masters, I., and Evans, K. (1996). Models for the elastic deformation of honeycombs. *Compos. Struct.*, 35, 403-422. [https://doi.org/10.1016/s0263-8223\(96\)00054-2](https://doi.org/10.1016/s0263-8223(96)00054-2)
150. Wang, N., and Deng, Q. (2021). Effect of axial deformation on elastic properties of irregular honeycomb structure. *Chin. J. Mech. Eng.*, 34, 1-12. <https://doi.org/10.1186/s10033-021-00574-3>
151. Luo, H. C., Ren, X., Zhang, Y., Zhang, X. Y., Zhang, X. G., Luo, C., Cheng, X., & Xie, Y. M. Mechanical properties of foam-filled hexagonal and re-entrant honeycombs under uniaxial compression. *Compos. Struct.* 2022, 280, 114922. <https://doi.org/10.1016/j.compstruct.2021.114922>
152. Chen, D. H., and Ushijima, K. (2013). Deformation of honeycomb with finite boundary subjected to uniaxial compression. *Metals* 2013, 3, 343-360.
153. Wu, W., Xia, R., Qian, G., Liu, Z., Razavi, N., Berto, F., & Gao, H. (2023). Mechanostructures: Rational mechanical design, fabrication, performance evaluation, and industrial application of advanced structures. *Prog. Mater. Sci.*, 131, 101021. <https://doi.org/10.1016/j.pmatsci.2022.101021>
154. Kumar, M. B., and Sathiya, P. (2021). Methods and materials for additive manufacturing: A critical review on advancements and challenges. *Thin-Walled Struct.*, 159, 107228. <https://doi.org/10.1016/j.tws.2020.107228>
155. Borikar, G. P., Patil, A. R., & Kolekar, S. B. (2023). Additively manufactured lattice structures and materials: Present progress and future scope. *Int. J. Precis. Eng. Manuf.*, 24, 2133-2180. <https://doi.org/10.1007/s12541-023-00848-x>
156. Luo, C., Han, C. Z., Zhang, X. Y., Zhang, X. G., Ren, X., & Xie, Y. M. (2021). Design, manufacturing and applications of auxetic tubular structures: A review. *Thin-Walled Struct.*, 163, 107682. <https://doi.org/10.1016/j.tws.2021.107682>
157. Li, X., Lin, Y., & Lu, F. (2019) Numerical simulation on in-plane deformation characteristics of lightweight aluminum honeycomb under direct and indirect explosion. *Materials*, 12, 2222.
158. Lu, Q., Qi, D., Li, Y., Xiao, D., & Wu, W. (2019). Impact energy absorption performances of ordinary and hierarchical chiral structures. *Thin-Walled Struct.*, 140, 495-505. <https://doi.org/10.1016/j.tws.2019.04.008>
159. Zhang, Y., Xu, X., Wang, J., Chen, T., & Wang, C. H. (2018). Crushing analysis for novel bio-inspired hierarchical circular structures subjected to axial load. *Int. J. Mech. Sci.*, 140, 407-431. <https://doi.org/10.1016/j.ijmecsci.2018.03.015>
160. Santosa, S., and Wierzbicki, T. (1999). Effect of an ultralight metal filler on the bending collapse behavior of thin-walled prismatic columns. *Int. J. Mech. Sci.*, 41, 995-1019. [https://doi.org/10.1016/s0020-7403\(98\)00066-6](https://doi.org/10.1016/s0020-7403(98)00066-6)
161. Nian, Y. Wan, S., Zhou, P., Wang, X., Santiago, R., & Li, M. (2021). Energy absorption characteristics of functionally graded polymer-based lattice structures filled aluminum tubes under transverse impact loading. *Mater. Des.*, 209, 110011. <https://doi.org/10.1016/j.matdes.2021.110011>
162. Wang, Z., Yao, S., Lu, Z., Hui, D., & Feo, L. (2016). Matching effect of honeycomb-filled thin-walled square tube—Experiment and simulation. *Compos. Struct.*, 157, 494-505. <https://doi.org/10.1016/j.compstruct.2016.03.045>
163. Liu, J., Chen, W., Hao, H., & Wang, Z. (2019) Numerical study of low-speed impact response of sandwich panel with tube filled honeycomb core. *Compos. Struct.*, 220, 736-748. <https://doi.org/10.1016/j.compstruct.2019.04.023>

164. Yang, C., Xu, P., Yao, S., Xie, S., Li, Q., & Peng, Y. (2018). Optimization of honeycomb strength assignment for a composite energy-absorbing structure. *Thin-Walled Struct.*, 127, 741-755. <https://doi.org/10.1016/j.tws.2018.03.014>
165. Safaei, B., Onyibo, E. C., & Hurdoganoglu, D. (2022). Effect of static and harmonic loading on the honeycomb sandwich beam by using finite element method. *Facta Univ. Series: Mech. Eng.*, 20, 279-306. <https://doi.org/10.22190/fume220201009s>
166. Djemaoune, Y., Krstic, B., Rasic, S., Radulovic, D., & Dodic, M. (2021). Numerical investigation into in-plane crushing of tube-reinforced damaged 5052 aerospace grade aluminum alloy honeycomb panels. *Materials*, 14, 4992. <https://doi.org/10.3390/ma14174992>
167. Xiong, J., Mines, R., Ghosh, R., Vaziri, A., Ma, L., Ohrndorf, A., & Wu, L. (2015). Advanced micro-lattice materials. *Adv. Eng. Mater.*, 17, 1253-1264.
168. Du Plessis, A., Le Roux, S. G., & Guelpa, A. (2016). The CT Scanner Facility at Stellenbosch University: An open access X-ray computed tomography laboratory. *Nuclear Instruments and Methods in Physics Research Section B: Beam Interactions with Materials and Atoms*, 384, 42-49.
169. Donderwinkel, I., Van Hest, J. C., & Cameron, N. R. (2017). Bio-inks for 3D bioprinting: recent advances and future prospects. *Polymer Chemistry*, 8(31), 4451-4471.
170. Chen, P. Y., McKittrick, J., & Meyers, M. A. (2012). Biological materials: functional adaptations and bioinspired designs. *Progress in Materials Science*, 57(8), 1492-1704.
171. Chan, G., and Mooney, D. J. (2008). New materials for tissue engineering: towards greater control over the biological response. *Trends in Biotechnology*, 26(7), 382-392.
172. Wang, S., Liu, L., Huang, Z., Li, Z., Liu, J., & Hao, Y. (2021). Honeycomb structure is promising for the repair of human bone defects. *Materials & Design*, 207, 109832.
173. Kang, J. H., Sakthibirami, K., Jang, K. J., Jang, J. G., Oh, G. J., Park, C., ... & Park, S. W. (2022). Mechanical and biological evaluation of lattice structured hydroxyapatite scaffolds produced via stereolithography additive manufacturing. *Materials & Design*, 214, 110372.
174. Vijayavenkataraman, S., Zhang, L., Zhang, S., Hsi Fuh, J. Y., & Lu, W. F. (2018). Triply periodic minimal surfaces sheet scaffolds for tissue engineering applications: An optimization approach toward biomimetic scaffold design. *ACS Applied Biomaterials*, 1(2), 259-269.
175. Mahmoud, D., and Elbestawi, M. A. (2017). Lattice structures and functionally graded materials applications in additive manufacturing of orthopedic implants: a review. *Journal of Manufacturing and materials Processing*, 1(2), 13.
176. Najmon, J. C., Raesi, S., & Tovar, A. (2019). Review of additive manufacturing technologies and applications in the aerospace industry. *Additive Manufacturing for the Aerospace Industry*, 7-31.
177. Ngo, T. D., Kashani, A., Imbalzano, G., Nguyen, K. T., & Hui, D. (2018). Additive manufacturing (3D printing): A review of materials, methods, applications, and challenges. *Composites Part B: Engineering*, 143, 172-196.
178. Rahmati, S. (2014). 10.12-direct rapid tooling. *Comprehensive Materials Processing*, 10, 303-344.
179. Ghosh, S., Zollinger, J., Zaloznik, M., Banerjee, D., Newman, C. K., & Arroyave, R. (2023). Modeling of hierarchical solidification microstructures in metal additive manufacturing: Challenges and opportunities. *Additive Manufacturing*, 78, 103845.
180. Ntziachristos, V. (2010). Going deeper than microscopy: the optical imaging frontier in biology. *Nature Methods*, 7(8), 603-614.
181. Inkson, B. J. (2016). Scanning electron microscopy (SEM) and transmission electron microscopy (TEM) for materials characterization. *Materials characterization using nondestructive evaluation (NDE) methods*, 17-43. Woodhead Publishing.

182. Kammers, A. D., and Daly, S. (2011). Small-scale patterning methods for digital image correlation under scanning electron microscopy. *Measurement Science and Technology*, 22(12), 125501.
183. Johnson, D., and Hilal, N. (2015). Characterisation and quantification of membrane surface properties using atomic force microscopy: A comprehensive review. *Desalination*, 356, 149-164.
184. Chua, E. Y., Mendez, J. H., Rapp, M., Ilca, S. L., Tan, Y. Z., Maruthi, K., ... & Carragher, B. (2022). Better, faster, cheaper: recent advances in cryo-electron microscopy. *Annual Review of Biochemistry*, 91, 1-32.
185. Gill, S. S., Xu, M., Ottaviani, C., Patros, P., Bahsoon, R., Shaghghi, A., ... & Uhlig, S. (2022). AI for next generation computing: Emerging trends and future directions. *Internet of Things*, 19, 100514.
186. Paul, C. P., Jinoop, A. N., & Bindra, K. S. (2018). Metal additive manufacturing using lasers. *Additive manufacturing: applications and innovations*, 37-94.
187. Oftadeh, R., Haghpanah, B., Papadopoulos, J., Hamouda, A. M. S., Nayeb-Hashemi, H., & Vaziri, A. (2014). Mechanics of anisotropic hierarchical honeycombs. *International Journal of Mechanical Sciences*, 81, 126-136.
188. Oftadeh, R., Haghpanah, B., Vella, D., Boudaoud, A., & Vaziri, A. (2014). Optimal fractal-like hierarchical honeycombs. *Physical Review Letters*, 113(10), 104301.
189. Haghpanah, B., Oftadeh, R., Papadopoulos, J., & Vaziri, A. (2013). Self-similar hierarchical honeycombs. *Proceedings of the Royal Society A: Mathematical, Physical and Engineering Sciences*, 469(2156), 20130022.
190. Jia, Z., Liu, F., Jiang, X., & Wang, L. (2020). Engineering lattice metamaterials for extreme property, programmability, and multifunctionality. *J. Appl. Phys.*, 127, 150901. <https://doi.org/10.1063/5.0004724>
191. Lincoln, R. L., Scarpa, F., Ting, V. P., & Trask, R. S. (2019). Multifunctional composites: A metamaterial perspective. *Multifunct. Mater.*, 2, 043001.
192. Garland, A. P., White, B. C., Jensen, S. C., & Boyce, B. L. (2021). Pragmatic generative optimization of novel structural lattice metamaterials with machine learning. *Mater. Des.*, 203, 109632. <https://doi.org/10.1016/j.matdes.2021.109632>
193. Hanifi, M., Chibane, H., Houssin, R., Cavallucci, D., & Ghannad, N. (2022). Artificial intelligence methods for improving the inventive design process, application in lattice structure case study. *Artif. Intell. Eng. Des. Anal. Manuf.*, 36. <https://doi.org/10.1017/s0890060422000051>
194. Kantaros, A., Piromalis, D., Tsaramirsis, G., Papageorgas, P., & Tamimi, H. (2021). 3D printing and implementation of digital twins: Current trends and limitations. *Appl. Syst. Innov.*, 5, 7. <https://doi.org/10.3390/asi5010007>
195. Eskandarpour, R., Ghosh K. J., B., Khodaei, A., Paaso, A., & Zhang, L. (2020). Quantum-enhanced grid of the future: A primer. *IEEE Access*, 8, 188993-189002.
196. Plocher, J., and Panesar, A. (2019). Review on design and structural optimization in additive manufacturing: Towards next-generation lightweight structures. *Mater. Des.*, 183, 108164. <https://doi.org/10.1016/j.matdes.2019.108164>
197. Arisoy, E. B., Musuvathy, S., Mirabella, L., & Slavin, E, III. (2015). Design and topology optimization of lattice structures using deformable implicit surfaces for additive manufacturing. *Proceedings of the International Design Engineering Technical Conferences and Computers and Information in Engineering Conference*; American Society of Mechanical Engineers: New York, United States of America, 57113, V004T05A003.
198. Ngo, T. D., Kashani, A., Imbalzano, G., Nguyen, K. T. Q., & Hui, D. (2018). Additive manufacturing (3D printing): A review of materials, methods, applications and challenges. *Compos. Part B Eng.*, 143, 172-196. <https://doi.org/10.1016/j.compositesb.2018.02.012>

199. Yuan, S., Li, S., Zhu, J., & Tang, Y. (2021). Additive manufacturing of polymeric composites from material processing to structural design. *Compos. Part B: Eng.*, 219, 108903. <https://doi.org/10.1016/j.compositesb.2021.108903>
200. Sefene, E. M. (2022). State-of-the-art of selective laser melting process: A comprehensive review. *J. Manuf. Syst.*, 63, 250-274. <https://doi.org/10.1016/j.jmsy.2022.04.002>
201. Korkmaz, M. E., Gupta, M. K, Robak, G., Moj, K., Krolczyk, G. M., & Kuntoğlu, M. (2022). Development of lattice structure with selective laser melting process: A state of the art on properties, future trends and challenges. *J. Manuf. Process.*, 81, 1040-1063.
202. Kamal, M., Rizza, G., (2019). Design for metal additive manufacturing for aerospace applications. *Additive Manufacturing for the Aerospace Industry*; Elsevier: Amsterdam, Netherlands, 67-86.
203. Katz-Demyanetz, A., Popov, V. V., Kovalevsky, A., Safranchik, D., & Koptyug, A. (2019). Powder-bed additive manufacturing for aerospace application: Techniques, metallic and metal/ceramic composite materials and trends. *Manuf. Rev.*, 6, 5. <https://doi.org/10.1051/mfreview/2019003>

CHAPTER THREE: MATERIALS AND RESEARCH METHODS

3.1. Introduction

The development of an optimal hierarchical HC lattice design with the highest possible order of hierarchy was based on a comprehensive review of the literature on cellular and lattice structures. Analytical and numerical topology, shape optimization and experimental models were designed for lattice designs with improved mechanical properties. The research was organized into four main areas, which include:

- i. A comprehensive review of the physical and mechanical characteristics of cellular and lattice structures.
- ii. Development of analytical and numerical models to describe the deformation and crushing behaviour of polygonal structures.
- iii. Topology and shape optimization strategies were effectively used in the iteration of planar HC models.
- iv. Quasi-static crushing experiments were used to derive key insights on the behaviour of DMLS Ti6Al4V(ELI) hierarchical HC parts.

3.2. Literature review on cellular and lattice structures

This work extensively reviewed cellular and lattice designs with various cell topologies, focusing on their mechanical behaviour, including stiffness, toughness, strength, deflection, and deformation. Optimal cellular designs were identified for this research, laying the groundwork for bioinspired lattice designs. A comparative analysis was conducted between cellular and lattice structures, examining stress distribution, buckling, and deformation under different load types.

Additionally, hierarchical lattice designs were reviewed, with a focus on enhanced mechanical properties and material efficiency. The study also explored the limits of hierarchy in lattice structures, particularly the impact of joints and ribs. Numerical modelling was used to validate findings from this review and optimise joint shapes (hexagonal, circular, and triangular) in hierarchical lattices.

3.3. Analytical modelling of lattice structures

3.3.1 Extending the reviewed deformation behaviour with analytical modelling

Existing analytical models were reviewed, and new ones were proposed to describe the behaviour of lattice structures better. A novel model was developed using beam theories to capture the behaviour of lattice structures under combined buckling and bending deformation. Additionally, failure theorems, including Tresca and von Mises, were applied together in the form of analytical models to provide further insights into the failure mechanisms of lattice structures.

3.3.2 Analytical modelling of selected polygon structures

The effective density model used to predict the analytical behaviour of the selected polygon structures in this study was the same one used by Gibson and Ashby [1], and is expressed as shown in Equation 3.1:

$$\frac{\rho^*}{\rho_s} = \frac{2}{\sqrt{3}} \frac{t}{L} \quad (3.1)$$

where, ρ^* and ρ_s are the densities of the specific structure and solid material, respectively. Gibson and Ashby [1] modelled the stiffness of regular HC structures in compression tests regarding the effective stiffness E^{eff} . This effective stiffness is an estimated theoretical modulus of a homogeneous material that has the same stress-strain behaviour as the cellular structure. Their model estimated the bending and axial behaviour of HC structures according to the Euler-Bernoulli beam theory while neglecting the deformations occurring within the nodes [1-3]. Taking into consideration deflection due to compression,

bending and axial behaviour, the effective stiffness of the regular hexagonal structure was, therefore, estimated as follows:

$$\frac{E^{eff}}{E_s} = \frac{E_x^{eff}}{E_s} = \frac{E_y^{eff}}{E_s} = \frac{4}{\sqrt{3}} \left(\frac{t}{L}\right)^3 \quad (3.2)$$

where the symbols, $E_{x^{eff}}$ and $E_{y^{eff}}$ represent the effective stiffness in the x - and y -axis directions, respectively. The symbol E_s stands for the elastic modulus of the solid material. The Gibson and Ashby model presented in Equation (3.2) assumed stiffness can be varied by changing parameters such as the wall thickness, which is known to be related to the effective stiffness. Throughout this study, the t/L ratio was varied from 0.05 to 0.0875 at 0.00625 intervals, while the length of the cell wall's mid-plane was held constant. The resulting ratios of effective stiffness along the x - and y -axis to the elastic modulus of the solid material were calculated and recorded, as shown in Table 3-1.

Table 3-1. Ratios of effective elastic modulus to the elastic modulus of the solid material

t/L	E^{eff}/E_s
0.05	0.000289
0.05625	0.00041
0.0625	0.000564
0.06875	0.000753
0.075	0.000974
0.08125	0.00124
0.0875	0.00155

The analytical predictions in Table 3-1 were then compared to the numerical results obtained in the present work in the numerical modelling section. Another investigation was carried out regarding the elastic buckling behaviour of the selected polygon structures. The analytical model adopted for this investigation was the same one developed by Gibson and Ashby [1, 4]. A critical Euler buckling load was determined in this investigation for its first or primary buckling shape that occurs when the structure is loaded along the z -axes. Gibson and Ashby's work estimated the magnitudes of crucial buckling stress (the stress corresponding to the critical buckling load) for linear buckling to occur using the following equation [1]:

$$(\sigma_{el}^c)_z = 5.2 E_s \left(\frac{t}{L}\right)^3 \quad (3.3)$$

where, $(\sigma_{el}^c)_z$ is the crucial buckling stress that occurs for loading in the z -direction.

3.3.3 Analytical modelling of first-order hierarchical HC structures

Based on the regular planar HC structure, first-order vertex-based hierarchical structures were constructed. The HC structure has basic geometric parameters, such as the sloping angle $\theta = 30^\circ$, cell wall thickness t , and cell wall length l , as previously shown in Figure 2-36, in Section 2.7.6 of Chapter 2 [5].

The parameter t is designed to decrease in value when the same design parameters are assigned to the first-order planar vertex-based hierarchical HC configuration. The parent structure previously shown in Figure 2-36(b), in Section 2.7.6 of Chapter 2 and its hierarchical configurations are related based on the geometrical features shown in Figure 3-1(a), 3-1(b), and 3-1(c) [5]. The circular polygon substituted at the vertex was defined as the smallest circumscribed circle of the hexagonal and triangular substructures using a radius parameter r . This, in turn, yields the relationship seen in Figure 3-1(d) [5]. The lengths of the walls within the hexagonal substructure, therefore, are related as follows:

$$l_{12} = l_{23} = l_{34} = l_{45} = l_{56} = l_{61} = r \quad (3.4)$$

Similarly, the lengths of the cell walls within the triangular substructure are related as follows:

$$l_{13} = l_{35} = l_{51} = r\sqrt{3} \quad (3.5)$$

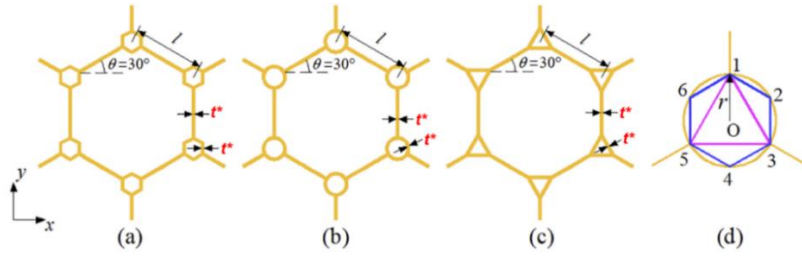


Figure 3-1. (a) Hexagonal substructures, (b) circular substructures, (c) triangular substructures and (d) a diagram illustrating the relationship between these three different substructures [5]

Planar regular and hierarchical HC structures were produced with the same relative density of $\bar{\rho} = 0.10$ and base hexagonal edge length of $l_o = 20 \text{ mm}$. This setting of the relative density was because structures with a relative density greater than 30% of the parent solid structure are no longer categorized as cellular structures but rather as solids with separated holes [6]. The thickness of the cell walls of the planar hierarchical HC structures was lowered to preserve overall relative density. This was accomplished by using a structural configuration parameter obtained from pre-existing analytical models that have been published [7-9]. From this, the corresponding configuration for the first-order planar vertex-based hierarchical HC configuration was predicted as follows:

$$\gamma_{(h,c,t)} = \frac{l_{(h,c,t)}}{l_o} \quad (3.6)$$

The symbols l , and l_o are the lengths of the substructure and base hexagon edges, respectively, and parameter γ denotes the function of the ratio of these two lengths. The hexagonal, circular, and triangular substructures are represented by the subscripts h , c , and t , respectively. Geometric constraints of $0 \leq \gamma_h \leq 0.5$, $0 \leq \gamma_c \leq 0.5$, and $0 \leq \gamma_t \leq \sqrt{3}/2$ were imposed on the first-order hierarchical HC structures comprising hexagonal, circular, and triangular substructures at the vertices, respectively. These constraints have been documented in numerous studies [10-19] as being advantageous for designing hierarchical HC structures with acceptable mechanical properties. In addition, hierarchical HC structures built with AM technology under the imposed constraints are predicted to be most accurate in their designs [5, 7-8, 12-13, 20]. As a result, the relative density for each of these hierarchical HC structures was determined using the formulae [5]:

$$\frac{\rho_h^*}{\rho_s} = \frac{2}{\sqrt{3}}(1 + 2\gamma_h) \frac{t_h^*}{l_o} \quad (3.7)$$

$$\frac{\rho_c^*}{\rho_s} = \frac{2}{3\sqrt{3}} \left[-3 \left(\frac{t_c^*}{l_o} \right) + 2\gamma_c(2\pi - 3\gamma_c) + 3 \right] \left(\frac{t_c^*}{l_o} \right) \quad (3.8)$$

$$\frac{\rho_t^*}{\rho_s} = \frac{1}{3}(2\sqrt{3} + 4\sqrt{3}\gamma_t - 4\gamma_t) \frac{t_t^*}{l_o} \quad (3.9)$$

To reduce the complexity of the models, the thicknesses of the cell walls of planar hierarchical HC structures were assumed to be uniform and, therefore, were assigned the same value ($t_h^* = t_c^* = t_t^*$) in this study. As a result, the constructed and numerically simulated planar regular HC model had a value of wall thickness $t = 1.75 \text{ mm}$. The first-order planar hierarchical HC models comprised of hexagonal, circular, and triangular structures at the

vertices had values of the parameter $\gamma_h = 0.3$ and $t_h^* = 1$ mm, $\gamma_c = 0.3$ and $t_c^* = 1$ mm, and $\gamma_t = 0.58$ and $t_t^* = 1$ mm, respectively. When predicting the behaviour of first-order hierarchical HC structures with good mechanical properties, the aforementioned values of the parameters are often used [8, 12-13, 20-21].

3.4. Numerical modelling and crushing of lattice structures

3.4.1 Numerical modelling of polygon structures

Two different geometry designs, a planar and an extruded hexagonal polygon shell generated in SolidWorks (2020), were used in this study. The geometries were generated using primary parameters such as the outer cell shape ($\theta = 240^\circ$) and length ($L = 20$ mm), as shown in Figure 3-2(a). The value of the parameter t that was allocated to the planar hexagonal shell was 1 mm, whereas the extruded hexagonal shell had t values ranging from (1, 1.125, 1.25, 1.375, 1.5, 1.625 and 1.75) mm. These geometries were then imported into ABAQUS/CAE (version 2020) for their analysis with applied loads.

SolidWorks was additionally used to develop planar structures based on three other geometries, including triangular, squared, and circular polygons, with $t = 1$ mm, as shown in Figure 3-3, which were also analysed numerically, in ABAQUS/CAE.

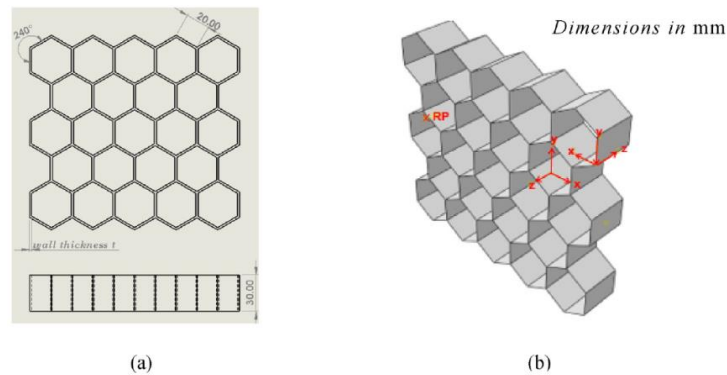


Figure 3-2. Typical (a) planar HC shell (b) extruded HC shell structure

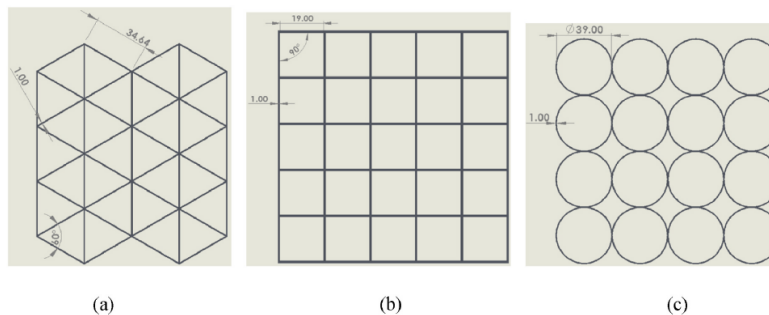


Figure 3-3. Typical planar (a) triangular, (b) squared, and (c) circular polygon shell structures

Numerical modelling of Ti6Al4V(ELI) polygon structures was carried out using ABAQUS/CAE (Version 2020). Regular polygon structures, which were generated using different cell types and wall thickness, were simulated, respectively. The values of the properties of the Ti6Al4V(ELI) material used in these polygon models are listed in Table 3-2 [22].

Table 3-2. Material properties of Ti6Al4V(ELI) used in FE modelling of polygonal structures [22]

Material property	Mass Density (ρ)	Young's Modulus (E)	Poisson's Ratio (ν)	Yield Stress (σ_{ys})
Magnitude	4430 kg/m ³	113.8 GPa	0.342	790 MPa

For simple and faster FEA, the stress distribution in the xy -plane and out-of-plane (z) direction of an HC structure was determined at the onset using planar and extruded hexagonal shell geometry, respectively. This was done to determine how representative the results of the planar model were of the HC structure, as the former is simpler and faster to run, for later use in comparing the behaviour of different polygon structures under load. In this analysis, a mesh with S8R type of shell elements was generated on a planar and extruded hexagonal shell geometry with 1 mm thick walls, shown in Figure 3-4. These second-order shell elements have a significant advantage in terms of computation speed and employ simplified methods of calculating strain and hourglass control. The mesh size on the two geometries was then varied within the range of 0.2-1 mm. This was done so that a large mesh size of 1 mm was located in the middle regions of the wall members and reduced movement towards the edges and vertices (0.2 mm), as shown in Figure 3-4. This was done to accurately capture results at the vertices and edges, which are known to be areas of high-stress concentration. This was followed by simulation under a simple uniaxial compression load of 2000 N applied to each one of the two model geometries, as shown in Figure 3-5.

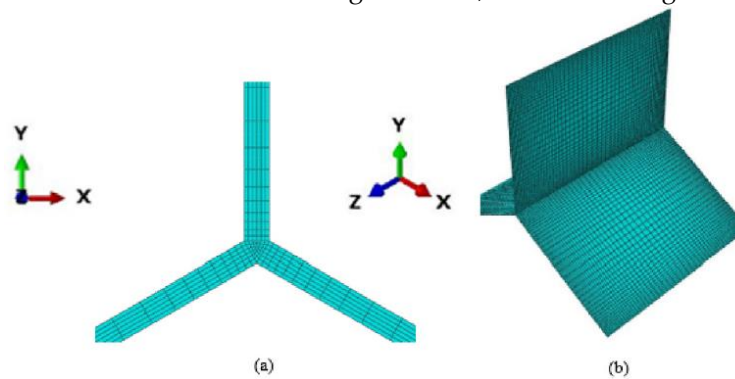


Figure 3-4. Models of (a) planar hexagonal shell walls and (b) extruded hexagonal shell walls, generated using different element sizes

The compression load was applied using rigid plates on opposing ends of the model. The interfaces between the two rigid plates and each one of the two models were assigned a frictionless contact, and the normal interaction property was modelled as a hard contact to prevent the model from penetrating the rigid surface. One rigid plate for the two models was assigned a fixed constraint, and a load was applied on the other, as shown in Figure 3-5. The latter rigid plate was constrained and only allowed to move in the direction of the load.

Simulation tests based on the boundary conditions shown in Figure 3-5(a and b) were used to determine the stress distributions in the xy and z -axis of the HC models, respectively. In these simulation tests, contour plots of stress results were obtained. Unit cells cut off from the central region of the planar and extruded hexagonal, or HC shell models were then used for analysis of the arising stresses, as shown in Figure 4-1, in Section 4.2 of Chapter 4.

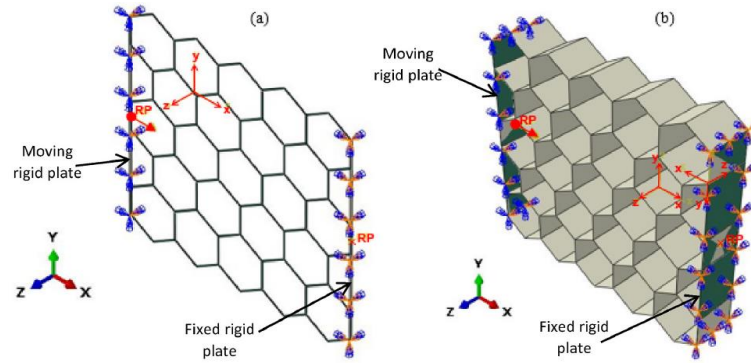


Figure 3-5. Typical (a) planar hexagonal shell and (b) extruded hexagonal shell models with boundary conditions

In the ensuing analysis, the planar hexagonal shell model was used to compare and rank triangular, rectangular, circular, and hexagonal planar models for the same load of 2000 N applied along the x - and y -directions. The numerical results obtained were also compared to the theoretical results. Because the hexagonal or HC model is the most extensively researched polygon cell type, it was used in all ensuing polygonal model investigations to allow for a more accurate comparison of results and literature. This cell type was simulated as an extruded HC shell model with different wall thicknesses for maximum elastic loads in the x - and y -direction, and the arising numerical results compared to the analytical results in the literature.

The HC geometrical models were generated using an extruded shell, which was then discretized into elements. The crushing behaviour of the analysed structure subjected to a simple uniaxial compression load for linear-elastic behaviour was then investigated. This was carried out to predict the elastic bending behaviour of the structure and compare its behaviour with the one predicted from analytical models. Thereafter, the effect of the ratio of thickness to length (t/L) on the effective stiffness for both analytical and numerical results was compared. Effective stiffness was obtained by first determining the maximum direct stresses and then calculating the corresponding strains using the magnitudes of deformation obtained in the FE analysis. The ratio of these two values gave rise to a calculated value of the effective stiffness, which was then divided by the stiffness of the material (E_s) to obtain the stiffness ratio. The value of effective stiffness (E^{eff}) was predicted in the x - or y -directions of the HC model for maximum elastic bending using the following expressions:

$$E_x^{eff} = \frac{\sigma_x}{\varepsilon_x}, E_y^{eff} = \frac{\sigma_y}{\varepsilon_y} \quad (3.10)$$

where, σ_x and σ_y are the maximum direct stresses in the x - and y -axes, respectively. The symbols ε_x and ε_y are the maximum direct strains in the x - and y -axes, respectively. Numerical analysis was also carried out in this study to predict linear elastic buckling for loading in the z -direction, and the results were compared to the theoretical behaviour of the HC structure. The bottom edges of the HC model were fixed in the x -, y -, and z -axes, with no rotations allowed. This meant that the structure could flex and bend along these edges but not leave the bottom's surface when loaded. The top edges and vertices were then assigned equivalent equations to determine the loading constraints of the HC model, which were allocated to specific parts of the structure in pre-defined sets. One set was assigned to the top-driven edges and the other to the top-driving vertex, as shown in Figure 3-6(b). A 1000 N load was then applied uniaxially to the top-driving vertices in order to simulate buckling; the same load was felt uniaxially by all of the top-driven edges in the z -direction. Figure 3-6 shows two additional loading and boundary conditions that were investigated for loading in the y - and z -direction of the extruded hexagonal shell model.

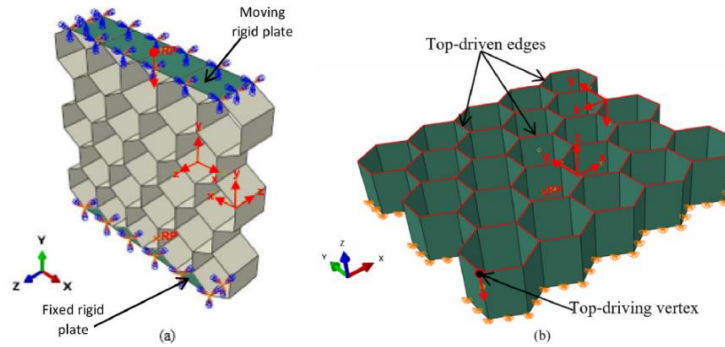


Figure 3-6. Loading fixed and pinned boundary conditions used, respectively, in the (a) y-direction and (b) z-direction of an extruded HC shell structure

3.4.2 Numerical modelling of first-order hierarchical HC structures

Figure 3-7 shows geometries created in SolidWorks software by employing the foregoing values of parameters for first-order hierarchical configurations of the regular HC geometry. In the ensuing work, the abbreviations HCR, HCH, HCT, and HCC are used to refer to the regular HC structure and hierarchical HC structures with hierarchical hexagonal, triangular, and circular substructures, respectively. The numerical modelling conducted for the first-order hierarchical honeycomb planar structures followed the same setup that was used in Section 3.4.1 of this chapter to model the behaviour of various polygon structures.

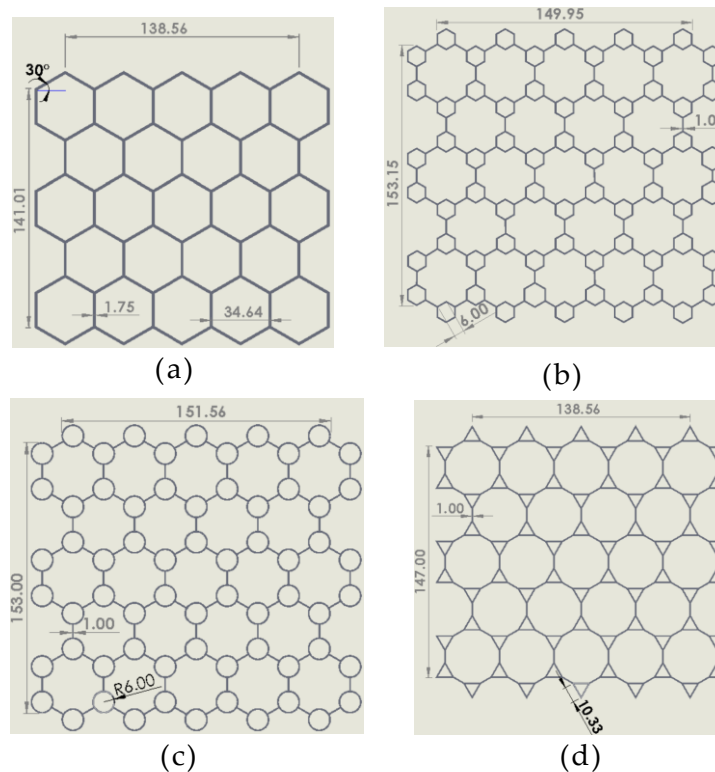


Figure 3-7. The built planar geometry of the (a) HCR, (b) HCH, (c) HCC and (d) HCT, respectively

3.4.3 Numerical crushing hierarchical HC structures

To examine the crushing behaviour of hierarchical HCs under axial compression, the nonlinear FE software ABAQUS (2020 version) was used to generate FE models of the structures established on the geometric models. The same setup for numerical modelling described in the last two Sections (Sections

3.4.1 and 3.4.2) was used in numerical crushing hierarchical HCs, in addition to the uniform load rate of 5 mm/min that was introduced.

The force-displacement curves generated by quasi-static compression experiments are useful in predicting the energy absorption capacity of hierarchical HCs. The general force-displacement curve is split into three sections: pre-damage, progressive damage, and densification [23]. Several factors are used for assessing the efficiency of energy-absorbing structures, including specific energy absorption (*SEA*), energy absorption (*EA*), peak crushing force (*PCF*), average crushing force (*MCF*), and crushing force efficiency (*CFE*). In Figure 3-8, $F(\delta)$ represents a crash force as a function of displacement δ , wherein δ_T is the displacement and m represents the mass. However, the numerical modelling study of crushing hierarchical HCs here only described deformation behaviour and does not account for damage-induced failure.

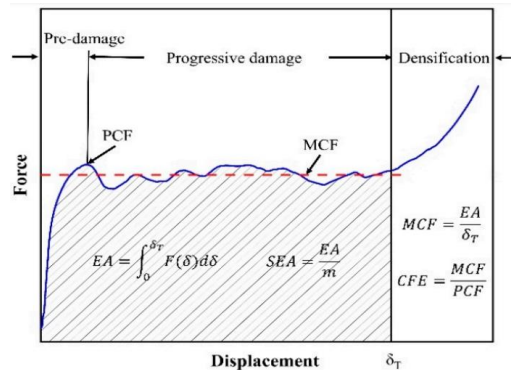


Figure 3-8. Graphical representation revealing energy-absorbing characteristics and damage zones [23]

3.5. Topology and shape optimization (TO and SO) of planar honeycomb (HC) structures

3.5.1 HC part design

The 3D unit hexagonal cell and the HC model were generated in SolidWorks design software (version 2021 SP5) with consistent wall thickness. The two models were then reduced to planar problems using Altair-Optistruct design software (HyperWorks 2021), as shown in Figure 3-9.

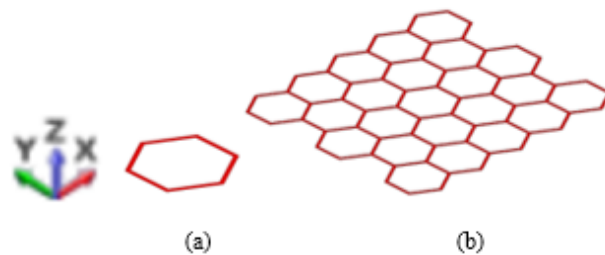


Figure 3-9. Planar models for (a) the unit hexagonal cell and (b) the HC

3.5.2 Mesh convergence testing

Using Altair-Optistruct software, mesh convergence tests were conducted on a planar unit hexagonal cell model with material properties of Ti6Al4V(ELI), which are presented in Section 3.4 of this chapter. The planar model was assigned a shell property with a depth of 2 mm and was used to predict the behaviour of the material. A second-order quadrilateral element type was used as the primary element to generate meshes on the geometry. This type of element was recommended for stress analysis, especially for finding stress concentrations near small features such as vertices and edges. The reason for their use is that it is easier to create streamlined meshes around vertices when quadrilateral elements are used [24]. This helps to capture the normal stress-strain relationships with more accuracy. Numerical tests were conducted using different mesh sizes in the range of 0.7 to 9 mm to test for mesh convergence. A descending

order of mesh sizes, from 9 mm, 8 mm, 7 mm, 6 mm, 5 mm, 4 mm, 3 mm, 2 mm, 1 mm, 0.9 mm, 0.8 mm, to 0.7 mm was used, and mesh convergence was considered to have been achieved when the result of stress obtained varied from the previous one by less than 5%. Convergence of the mesh size was first tested with reference to the von Mises stress at the mid-span of the loaded member for transverse deflection. This was because the maximum transverse deflection, and therefore, the von Mises stress, was expected to occur at mid-span. A similar test was conducted for axial and bending deformation for all types of members in the structure. These members all experienced differing values of axial and bending deformation for each different mesh size that was used.

The mesh size for convergence determined this way was then used in all ensuing numerical analyses and structural optimizations of the planar unit hexagonal cell and the HC model. It was observed in previous studies [25-30] that discontinuity of meshes occurred as a function of the size of the sharp angles formed at the edges and vertices, irrespective of the type of geometrical shape, such as the HC. With the increasing sharpness of the angles in a geometry, it was noted in the literature that it became increasingly difficult to find the best possible arrangement of elements for the various meshing algorithms in many numerical modelling packages [27-28]. As the elements generated in the corner regions of HC models have been observed to show low connectivity in literature, triangular elements were substituted for the quadrilateral elements at the vertices in the present work.

3.5.3 The preliminary finite element (FE) hexagonal unit cell and HC model

Preliminary FE modelling for the unit hexagonal cell and HC geometries was conducted using Optistruct software before implementing TO. The numerical models were based on the Gibson and Ashby models for the elastic behaviour of HCs [31]. The material parameters considered were the same ones used for the mesh convergence tests described in the previous section. The FE models were investigated based on a linear elastic behaviour for all loads used. A simple compressive mid-span uniaxial concentrated load was used, as shown in Figure 3-10. Furthermore, fixed constraints were assigned to the labelled region of the model, also shown in Figure 3-10. The fixed constraints were chosen because of their ability to restrain against both rotation and translation displacement of the walls so restrained [32]. The FE model for the unit hexagonal cell and HC was also simulated based on the following expression for the von Mises stresses σ_v :

$$\sigma_v = E\varepsilon \quad (3.11)$$

where the symbols E and ε represent the material elastic modulus and the strain of the model. It was assumed that the generated von Mises stresses were equal to the yield strength of the material ($\sigma_v = \sigma_y$) [31]. This implied that the material was modelled at yield to determine its mechanical behaviour at the maximum elastic load it could carry.

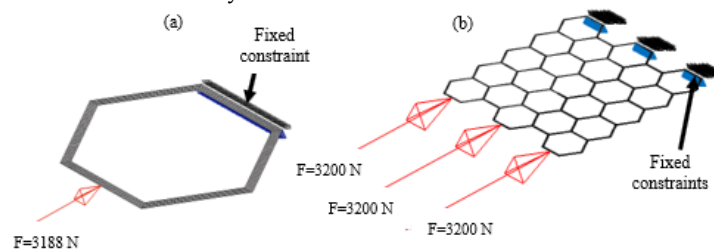


Figure 3-10. The planar boundary conditions for (a) a unit hexagonal cell and (b) an HC model, where F denotes the force

The results of this preliminary work served to define the load paths and stress distribution in the hexagonal unit cell and the HC model. This provided useful insights to assist in TO for the purposes of lightweighting.

3.5.4 The TO of hexagonal unit cell and HC model

TO of the hexagon unit cell and the HC model was implemented in a two-phase structural optimization process of lightweighting followed by stress reduction. The first phase was implemented based on the SIMP method developed by Bendsøe [29]. An Altair-Optistruct solver was used to carry out the TO of the unit hexagonal cell and HC structures. First, the solver automatically assigned a mathematical objective function to the discretized problem to describe a typical discrete result during the process of optimization. This result was based on the iteration of the design variables (x) of the geometry or material in the design space while following the objective function $f(x, y)$. In turn, state variables (y) were generated in terms of stresses and strains to describe the loading behaviour of the subsequent FE models. The TO model of the hexagon cell unit and HC structures obtained using Equation (3.12) were obtained as discrete element densities. Therefore, a second step of TO was automatically carried out to change the discrete structure into a continuous structure. This process involved adjusting the Young's modulus of the material to match the specific properties of individual components within the structure. Thus, effective values of stiffnesses E_s were assigned to the TO model for which the fictitious densities of the iterations carried out were given penalty scores according to the power law [33], expressed as follows:

$$E_s(\rho_e) = \rho_e^p E_0, p \geq 1, E_0 \neq 0 \text{ (Lower boundary)} \quad (3.12)$$

where p is the penalization parameter used to allocate penalty scores for element densities ($x = \rho_e$) between 0 and 1 values. The range of the parameter p lies between 1 and 3. The range is responsible for confirming the varying densities of the material at different points in the structure being modelled. A continuous structure is modelled with a value of the parameter $p = 3$ [34]. The higher the p -value, the more effective the penalty score is in controlling the TO algorithm using the continuous relaxation approach. For TO, the penalty scores were implemented by reducing the densities on the TO model until the possible minimum densities were left on the continuous structures. The initial TO of the planar HC structure deleted most of the members that were perpendicular to the applied loads because they were redundant, thus leading to the mechanism (not structure) shown in Figure 3-11(b). Therefore, these members were allocated a solid property, as shown in Figure 3-11(a).

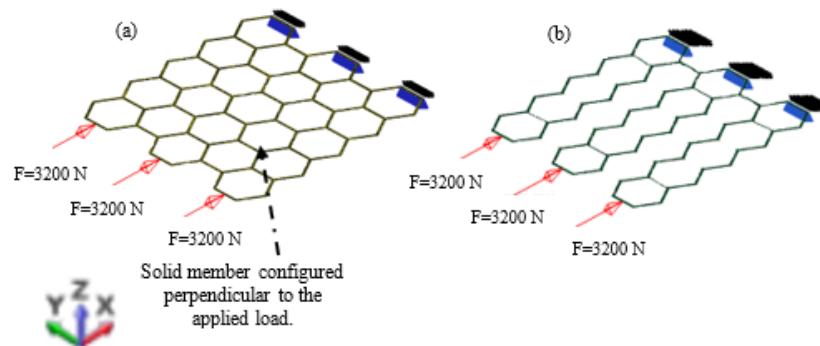


Figure 3-11. The planar TO HC model (a) with a solid property defined for some of the members that are perpendicular to applied loads, and (b) without a solid property defined for these same members

The topology-optimized models were subsequently analysed numerically, as described in the next subsection, and the results obtained were compared with those of preliminary numerical modelling done before carrying out TO.

3.5.5 The topology-optimized FE unit cell and HC model

The topology-optimized FE HC models were meshed with dominant second-order triangular elements of the size arrived at in the convergence tests. The meshes in the regions found to have poor

connectivity of elements were refined. Following this, numerical analyses were implemented with the same boundary conditions used for the numerical analysis done before carrying out TO.

The topology-optimized FE HC models were fine-tuned as described in the next subsection using a complementary TO method known as shape optimization (SO) to reduce stresses, and the results were compared to the results of preliminary numerical modelling carried out before TO.

3.5.6 The shape-optimized FE unit cell and HC model

The boundary sensitivity or SO method developed by Hadamard [3] was introduced on the full design space of the FE HC model to fine-tune the shape to reduce stresses. The method is considered an adaptable shape for the change of shape of the topology-optimized FE hexagonal unit cell and HC model while maintaining adequate control over the design fillets. The recommended control over the design fillets is significant because free-shape optimization does not preserve small design features such as the rounding of sharp edges or corners. The iterations of the topologies were implemented with the objective of reducing the maximum stresses to the lowest possible stresses that could be achieved. The application of SO also smoothed the sharp edges and vertices found on the topology-optimized FE hexagonal unit cell and HC model.

3.6. Quasi-static crushing experiments of hierarchical HC structures

3.6.1 Design configurations of hierarchical parts

First and second-order vertex-based hierarchical HCs were built based on a regular HC, using the same dimensions that were used for the regular HC in Section 3.4. In a case where the same design parameters are assigned to the first- and second-order vertex-based hierarchical HC configurations, the parameter t must decrease in value. Figure 3-12 shows the relationship between the parent HC structure and its corresponding self-similar hierarchical configurations using geometrical features [35].

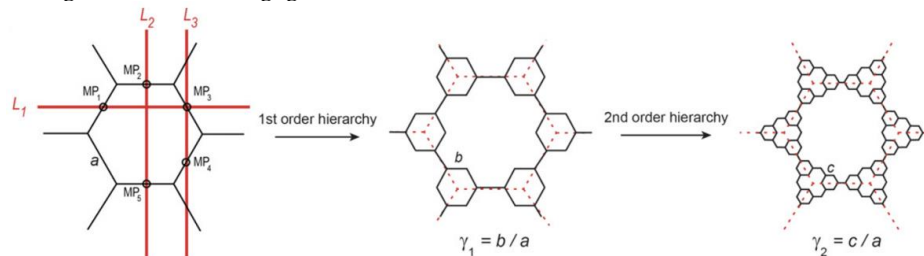


Figure 3-12. The relation derived between the basic HC structure and its corresponding self-similar hierarchical configurations [35]

The ratio of the set hexagonal edge lengths describes the structural configurations of the HC at each level of the hierarchy. In this scenario, the hexagonal edge length for the first-order hierarchical structure is represented by symbol b , and c corresponds to the second-order hierarchical structure, with the original hexagon's edge length being represented by symbol a , shown in Figure 3-12 [35]. The ratios of the edge lengths for the first- and second-order hierarchical HC structures with respect to that of the regular or zero-order hierarchical structure can be written as $\gamma_1 = b/a$ and $\gamma_2 = c/a$, respectively. The first-order hierarchical HC structure is governed by the interval $0 \leq b \leq a/2$, and where the regular structure is described $\gamma_1 = 0$, this interval becomes $0 \leq \gamma_1 \leq 0.5$. For the case of the second-order hierarchical HC structure, either one of the two intervals, namely $0 \leq c \leq b$ or $c \leq a/2 - b$ could be adopted as the geometrical constraint. The ratio parameters can be presented in intervals as well. Given the case where $\gamma_1 \leq 0.25$, this results in an interval of $0 \leq \gamma_1 \leq \gamma_2$, and where it falls in the range $0.25 \leq \gamma_1 \leq 0.5$, the interval becomes $0 \leq \gamma_2 \leq (0.5 - \gamma_1)$ [35].

The dimensionless specific relative density, or the area fraction, could be expressed with regard to the ratio t/a , as shown in Equation 3.13 [62].

$$\rho = 2\sqrt{3} \cdot (1 + 2\gamma_1 + 6\gamma_2) \cdot t/a \quad (3.13)$$

In the design of hierarchical HC parts, the cases of γ_2 and $\gamma_1 = 0$ can be ignored, given that t corresponds to the original wall thickness. For regular and first-order hierarchical HC parts, the relative densities are written as seen in Equations 3.14 and 3.15, respectively [35].

$$\rho_0 = 2\sqrt{3} \cdot 2t/a \quad (3.14)$$

$$\rho_1 = 2\sqrt{3} \cdot (1 + 2\gamma_1) \cdot t/a \quad (3.15)$$

Ajdari et al. [35] highlighted that the relationship deduced from the analytical models they developed for hierarchical HC structures suggests that as γ_1 and γ_2 increase, t/a decreases to maintain a fixed relative density. Figure 3-13 shows CAD, including the regular and its corresponding self-similar hierarchical HC configurations with $\rho = 0.10$ and $a = 20$ mm, which were generated using SolidWorks design software (version 2021 SP5). The regular HC was assigned a value of $t = 1.75$ mm; the first-order hierarchical HC structure was assigned values of $\gamma_1 = 0.3$ and $t = 1$ mm; in addition, the second-order hierarchical structure was assigned values of $\gamma_1 = 0.3$, $\gamma_2 = 0.12$, and $t = 0.75$ mm. These assigned values are often used and considered reliable in the design and manufacturing of structurally stable hierarchical structures [35].

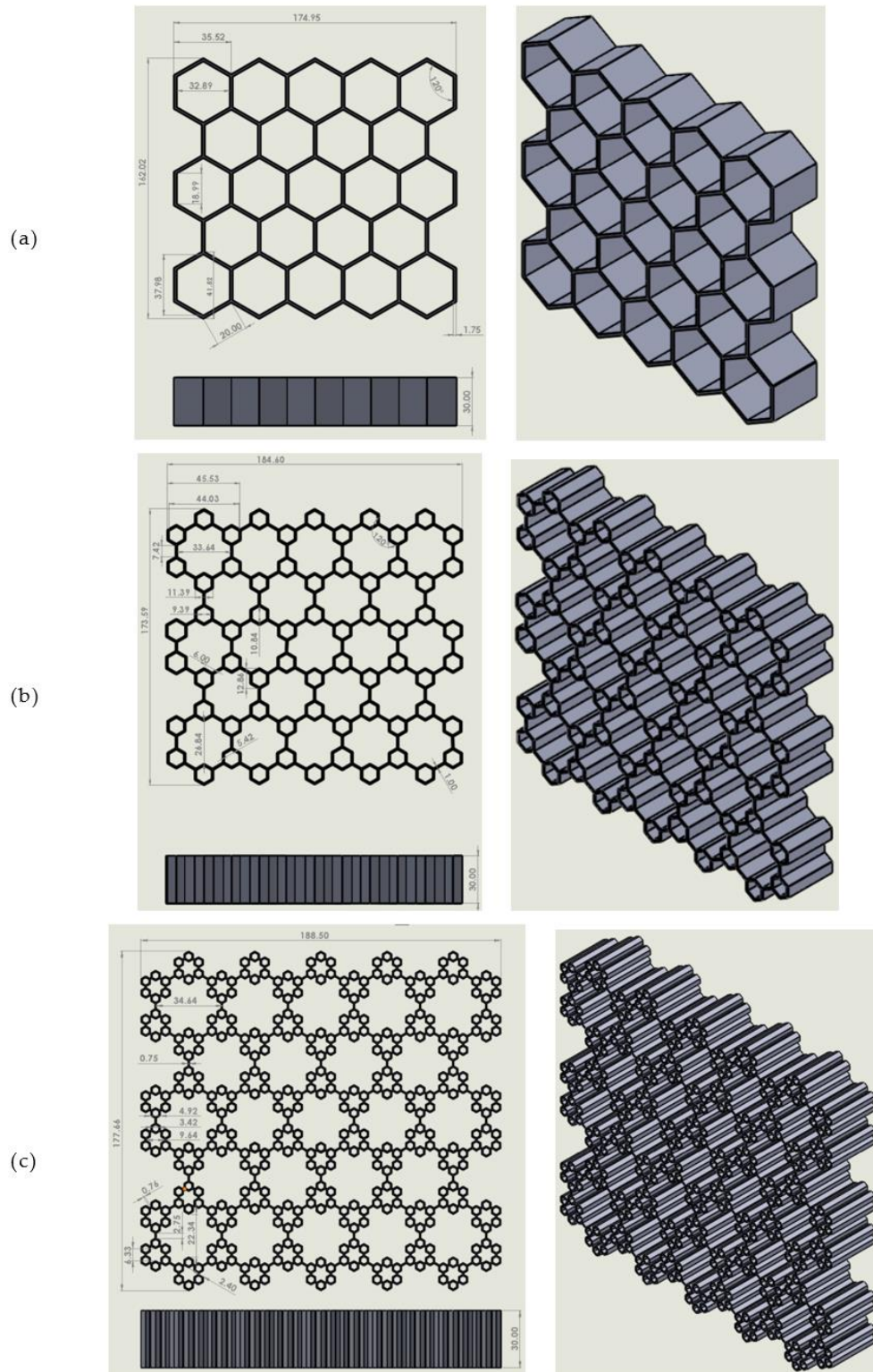


Figure 3-13. Hierarchical CAD designs and dimensions, (a) regular HC, (b) first-order hierarchical HC, and (c) second-order hierarchical HC

In HC designs with hierarchical configurations, the uniform wall thickness of higher orders is reduced progressively to maintain the same relative density. Hierarchical HC parts

produced via AM, as detailed in the following subsection, may struggle to consistently achieve the ideal apparent densities due to factors such as process variability, material inconsistencies, geometry and build orientation, thermal stresses and warping, porosity formation, and post-processing effects []. In addition, the discrete values of γ_1 and γ_2 can prove difficult to obtain as well because of failure to attain the ideal apparent densities. Therefore, a relative density range of 7.5-12.5% was selected in the present work to account for such inconsistencies. This range is typically selected to ensure that the structure performs close to its intended design parameters even with these potential inconsistencies [35].

3.6.2 Additively-produced hierarchical HC parts

An entire set of twelve Ti64Al4V (ELI-extra low interstitial) hierarchical HC parts were printed at the Centre for Rapid Prototyping and Manufacturing of Central University of Technology, Free State, South Africa. These parts were built using a direct metal laser sintering (DMLS) EOSINT M290 400 W machine based on the CAD files used to develop the hierarchical structures shown in Figure 3-13. A titanium base plate was used as a substrate, and argon gas circulated within the build chamber during printing. A minimum wall thickness of 0.75 mm for all the builds was maintained to prevent challenges associated with printability and process control, surface quality and resolution, heat dissipation, and post-processing requirements. After printing, the parts were cooled to temperatures below 60 °C before being removed from the machine. This was done to prevent the builds from warping. Figure 3-14(a) shows four printed regular HC builds before they were cut off the build plate. Three different hierarchical HC builds right after they were cut off from the build platform are also shown in Figure 3-14(b).

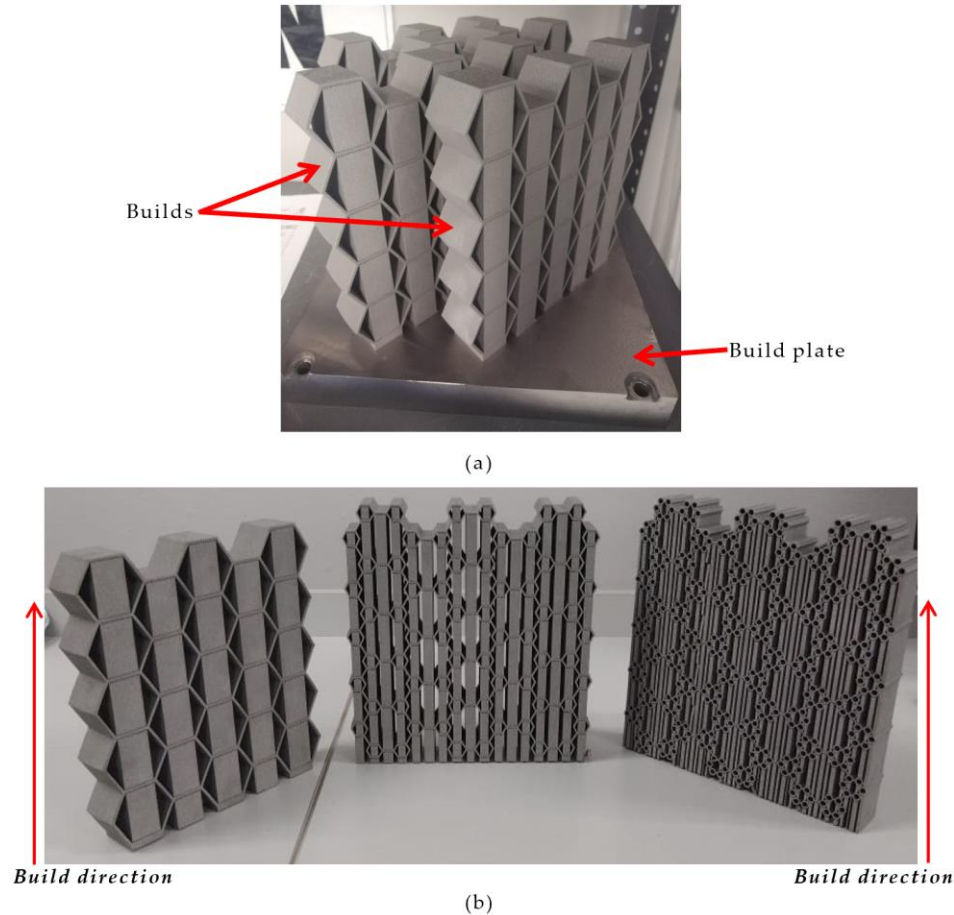


Figure 3-14. Additively-produced parts, (a) regular HC parts before being cut off from the build plate, and (b) from left to right are images of the regular HC, first-order hierarchical HC, and second-order hierarchical HC after being cut off from the build plate, respectively

The structures depicted in Figure 3-14 require both stress relief and high-temperature heat treatment. The temperatures and soaking periods used for both stress relief and high-temperature heat treatment are described in the subsequent section (subsection 3.6.3). Stress relieving addresses the residual stresses that emerge in SLM as a result of the layer-like process and the restraint of current layers by previous layers from contracting. This is done before the removal of built parts from the support base to prevent warping. High-temperature heat treatment, on the other hand, addresses the existence of martensitic needle-like structures formed due to the rapid cooling rates of built parts that are greater than 460 °C/s and the attending brittleness of printed parts [36].

3.6.3 Heat-treatment protocol used on as-built Ti6Al4V hierarchical HC parts

The twelve parts manufactured using DMLS technology, including the as-built regular HC and the first- and second-order hierarchical HC, were first stress-relieved before being separated from the substrate. This stress-relieving regime is recommended by the manufacturers for the Ti6Al4V(ELI) built in the DMLS EOSINT M290 machine. The parts were then heat-treated using a high-temperature two-stage annealing protocol. The two-stage annealing process on the as-built Ti6Al4V parts was carried out to improve their ductility at the cost of reduced strength. This heat treatment protocol is typically used when Ti6Al4V builds with a bimodal microstructure is required [37]. Figure 3-15 shows the graph

that is generated by the input file of the furnace program for two-stage high-temperature annealing.

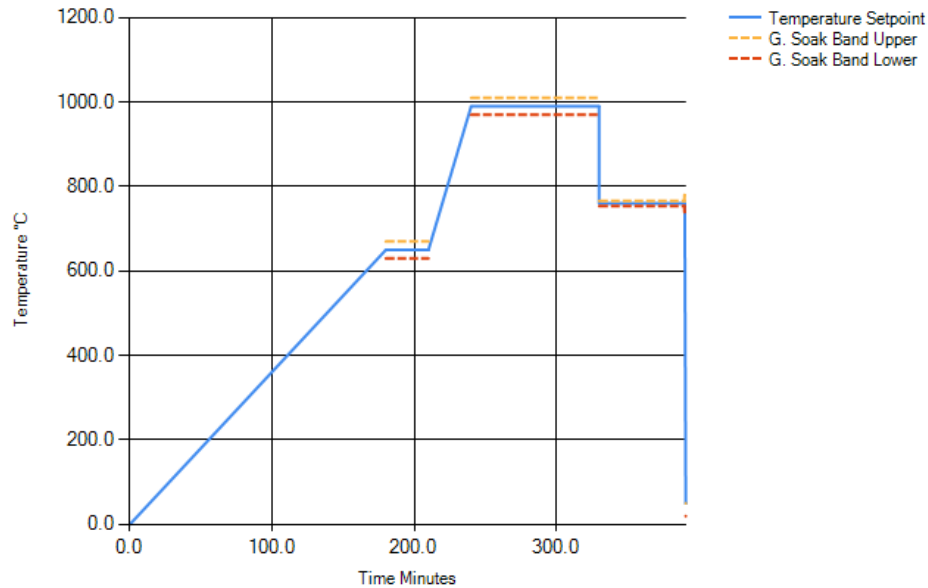


Figure 3-15. A two-stage high-temperature annealing curve for Ti6Al4V(ELI) hollow parts

The Ti6Al4V(ELI) regular and HC hierarchical parts were first stress-relieved in a pre-heated furnace at 650 °C for 180 minutes. This was followed by their heat treatment through two stages of high-temperature annealing. The final temperature in this heat treatment was set to 990 °C. The specimens were soaked at this temperature for 90 minutes. The chosen temperature is slightly higher than Ti6Al4V's beta transus temperature of 980 °C. This is to allow complete decomposition of the martensitic alpha microstructure and stimulate the globularisation of the resulting beta grains. The Ti6Al4V(ELI) parts were then furnace-cooled to 760 °C and soaked at this temperature for 120 minutes. This was done to allow coarsening of the formed alpha grains. In the last stage of this heat treatment, the Ti6Al4V(ELI) parts were slowly cooled to room temperature in the furnace by increasing the flow of argon gas in it.

3.6.4 Removal of supports from the hierarchical HC parts

The supports were printed vertically, along the z-build direction of the Ti6Al4V(ELI) regular and hierarchical HC builds. It must be noted that the DMLS-printed structures in this work are complex in geometry, with an enhanced ductility because of the high-temperature two-stage annealing that was performed. The hydraulic press, tools and parts shown in Figure 3-16 were used to remove the supports from the printed hierarchical HC parts.

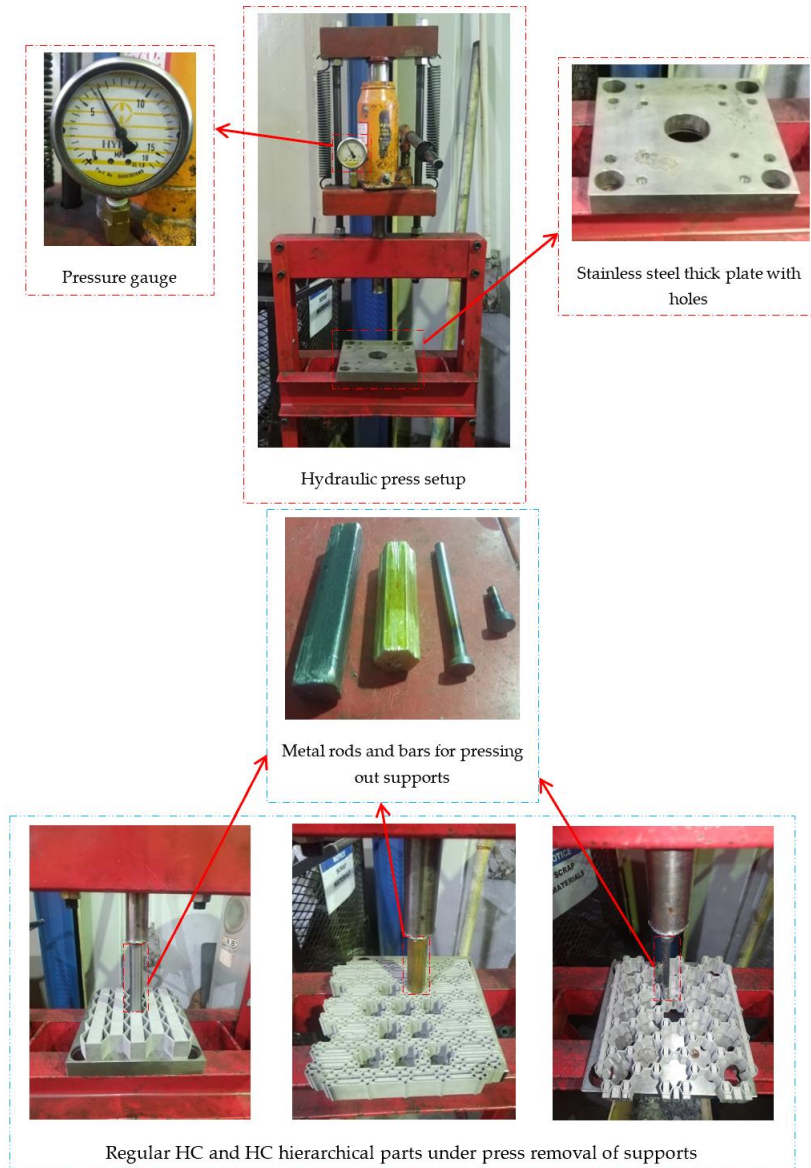


Figure 3-16. The setup used for pressing out supports in hierarchical HC parts

The supports were pressed out, as shown in Figure 3-16, using different shapes and sizes of metal bars and rods. Loads in the range of 4-12 MPa, were used to press out the supports for the smallest to the largest cross-sectional areas of supports, respectively. It is recognized that such loads could result in the deformation of the structures, and better methods should be developed to carry out this exercise. The spread of these loads on the structure was minimized using a thick stainless-steel plate with holes that ensured localization of the applied loads on the supports rather than the hierarchical HCs. The minor support pieces that remained on the Ti6Al4V(ELI) builds, even after using the hydraulic press, were cleared off using a rubber mallet and chisel, which is a further cause for concern about the structural integrity of the final parts. The result of this exercise for the three different Ti6Al4V(ELI) hierarchical HCs is shown in the three images in Figure 3-17.

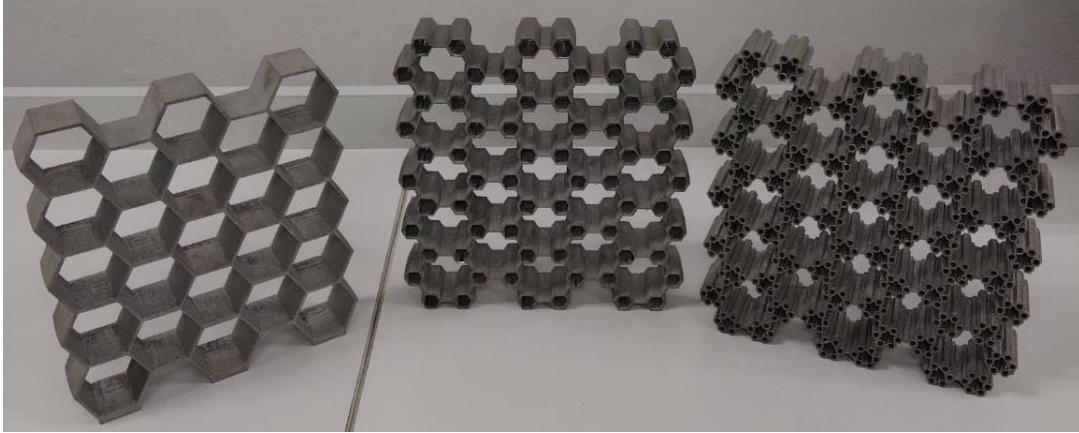


Figure 3-17. The regular HC and its hierarchical parts produced via DMLS technology

The procedure of removing supports in this investigation was time-consuming, tedious, and laborious. Additionally, the total metal scraps accumulated from removing supports were higher in mass compared to all the twelve Ti6Al4V(ELI) hierarchical HC builds. The metal scrap weighed 11.34 kg, whereas all the Ti6Al4V(ELI) parts weighed 5.93 kg. This is a waste-to-use ratio of 1.91:1 and negates the advantage of AM of little or no waste of material. The overall metal scrap that was accumulated from removing supports for all the Ti6Al4V(ELI) parts built is shown in Figure 3-18.



Figure 3-18. Ti6Al4V(ELI) scrap resulting from removing supports of DMLS-produced hierarchical HC parts

3.6.5 Surface roughness testing for hierarchical HC parts

Surface roughness was measured on four Ti6Al4V(ELI) parts that were selected randomly. This consisted of one regular HC, two first- and second-order hierarchical HCs, and a fourth first-order hierarchical HC build that was blast smoothed on three faces of the flat side surfaces for a period of two hours. The three flat surfaces of the smoothed faces were used to determine if the bead blasting strategy had a significant effect in smoothing the surfaces of the Ti6Al4V(ELI) built parts. An automated shot peening strategy, using round stainless-steel beads on the flat surfaces of the build, was adopted. This protocol was conducted following the SAE standard, AMS 2430: 2014.

Surface roughness for each selected face was measured at twelve different points, and the average and standard deviation was calculated. The surface roughness was measured

using a Mitutoyo surface roughness tester (SJ-210). This instrument was connected to a computer running the SurfTest SJ-210 V.1.008 software package. The specimen was first calibrated using the ISO 4287: 1997 standard, as described in the manual for the equipment. During testing, the cutoff length (the length over which the roughness is evaluated) of 2.5 mm was assigned to determine the R_a value. The surface roughness of three top flat faces and three side inclined faces for each of the selected Ti6Al4V(ELI) builds was measured. The R_a measurement indicates the profile's mean arithmetic deviation of the peaks and crests from the mean line, R_z is the average of consecutive highest peaks or crest or the average distance between the highest peak and lowest crest, and R_q is the distance of the highest peak from the mean line (R_p) or the distance of lowest crest from the mean line (R_v). Surfaces with low values of these three roughness indicators are typically regarded as smooth. Roughness in the present work was determined using the R_a value, which corresponds to a component's overall surface roughness. The surface roughness of the bead-blasted Ti6Al4V(ELI) structure was only evaluated for the top flat faces. Inclined surfaces cannot be effectively smoothed because geometries built at any angle other than 90 or 180 degrees are not well exposed to direct blasting of the beads, diminishing overall smoothing effectiveness.

3.6.6 Quasi-static crushing analysis of hierarchical HC builds

An MTS Criterion™, Model 43 universal testing machine was used to perform quasi-static crushing tests on twelve Ti6Al4V(ELI) hierarchical HC parts manufactured via DMLS. Figure 3-19 shows the setup used to carry out these tests.

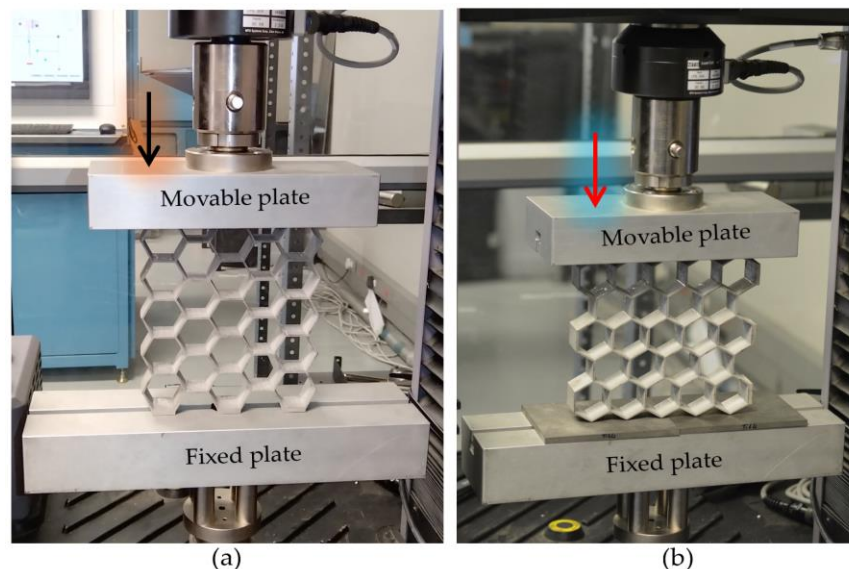


Figure 3-19. Compression experimental setup using MTS Criterion™, Model 43 universal tester for (a) a regular HC loaded in the x-direction, and (b) a regular HC loaded in the y-direction

Two builds of each of the four manufactured Ti6Al4V(ELI) regular HC parts were loaded along the x -axis, with loads applied directly on their flat surfaces, as illustrated in Figure 3-19(a). The remaining two sets of regular HC parts were loaded along the y -direction, which meant that the loads were imposed directly on the apices, as shown in Figure 3-19(b). A testing safety cage made of mild steel sheets with a thickness of 2 mm and length, width, and height dimensions of 380 x 286 x 200 was used to shield operators from objects flying off the structures during crush tests. A digital Nikon camera was also positioned such that

it captured the deformation process of the Ti6Al4V(ELI) parts during the crush tests. Before starting quasi-static compression, the MTS Criterion™, Model 43 universal tester was set to zero load and then a load rate of 5 mm/min set. To facilitate comparison of the crush-tested specimens, the greatest displacement of the Ti6Al4V(ELI) HC parts under the specified crush load rate was fixed at 160 mm, in addition to the machine's limiting load, which was set at 29.5 KN. The foregoing procedure was used to crush first- and second-order hierarchical HC builds as well.

3.7. Summary

This chapter has provided a comprehensive overview of the methodologies employed for all the work contained in this document. A thorough literature review covering key topics such as cellular structures, lattice structures, and hierarchical lattice structures was presented in Chapter 2, with recommendations for further research. Analytical modelling was used to develop new backgrounds for understanding the deformation behaviour of lattice structures, while numerical modelling methods were applied to polygonal and first-order HC structures. A preliminary numerical study predicted the crushing behaviour of HCs, followed by TO and SO of planar HCs, to achieve lightweight, high-strength structures. Lastly, quasi-static crushing experiments were conducted to examine the behaviour of hierarchical lattice HCs.

References

1. Gibson, L. J., and Ashby, M. F. (1997). Cellular solids: Structure and properties, second ed. *Cambridge University Press*, New York.
2. Helou, M., and Kara, S. (2018). Design, analysis, and manufacturing of lattice structures: an overview. *International Journal of Computer Integrated Manufacturing*, 31(3), 243-261.
3. Malek, S., and Gibson, L. (2015). Effective elastic properties of periodic hexagonal honeycombs. *Mechanics of Materials*, 91, 226-240.
4. Gibson, L. J., Ashby, M. F., Schajer, G. S., & Robertson, C.I. (1982). The mechanics of two-dimensional cellular materials. *Proc. Roy. Soc. Lond. A* 382, 25-42.
5. Libonati, F., and Buehler, M. J. (2017). Advanced structural materials by bioinspiration. *Advanced Engineering Materials*, 19(5), 1600787.
6. Chibinyani, M. I., Dzogbewu, T. C., Maringa, M., & Muiruri, A. M. (2022). Reduced order topology optimization of a planar honeycomb defined by a linear elastic Ti6Al4V(ELI) material model. *South African Journal of Industrial Engineering*, 33(3), 299-317.
7. Oftadeh, R., Haghpanah, B., Vella, D., Boudaoud, A., & Vaziri, A. (2014). Optimal fractal-like hierarchical honeycombs. *Physical Review Letters*, 113(10), 104301.
8. Chen, Q., Pugno, N., Zhao, K., & Li, Z. (2014). Mechanical properties of a hollow-cylindrical-joint honeycomb. *Composite Structures*, 109, 68-74.
9. Yadroitsev, I., Krakhmalev, P., Yadroitsava, I., & Du Plessis, A. (2018). Qualification of Ti6Al4V ELI alloy produced by laser powder bed fusion for biomedical applications. *JOM*, 70, 372-377.
10. Zhang, Q., Yang, X., Li, P., Huang, G., Feng, S., Shen, C., & Lu, T. J. (2015). Bioinspired engineering of honeycomb structure—Using nature to inspire human innovation. *Progress in Materials Science*, 74, 332-400.
11. Tao, Y., Duan, S., Wen, W., Pei, Y., & Fang, D. (2017). Enhanced out-of-plane crushing strength and energy absorption of in-plane graded honeycombs. *Composites Part B: Engineering*, 118, 33-40.
12. Fang, J., Sun, G., Qiu, N., Pang, T., Li, S., & Li, Q. (2018). On hierarchical honeycombs under out-of-plane crushing. *International Journal of Solids and Structures*, 135, 1-13.

13. Yin, H., Huang, X., Scarpa, F., Wen, G., Chen, Y., & Zhang, C. (2018). In-plane crashworthiness of bio-inspired hierarchical honeycombs. *Composite Structures*, 192, 516-527.
14. Blakey-Milner, B., Gradl, P., Snedden, G., Brooks, M., Pitot, J., Lopez, E., ... & Du Plessis, A. (2021). Metal additive manufacturing in aerospace: A review. *Materials & Design*, 209, 110008.
15. Najmon, J. C., Raesi, S., & Tovar, A. (2019). Review of additive manufacturing technologies and applications in the aerospace industry. *Additive Manufacturing for the Aerospace Industry*, 7-31.
16. Williams, J. C., and Starke Jr, E. A. (2003). Progress in structural materials for aerospace systems. *Acta Materialia*, 51(19), 5775-5799.
17. Martinez, D. W., Espino, M. T., Cascolan, H. M., Crisostomo, J. L., & Dizon, J. R. C. (2022). A comprehensive review on the application of 3D printing in the aerospace industry. *Key Engineering Materials*, 913, 27-34.
18. Zhang, W., and Xu, J. (2022). Advanced lightweight materials for automobiles: A review. *Materials & Design*, 110994.
19. Czerwinski, F. (2021). Current trends in automotive lightweighting strategies and materials. *Materials*, 14(21), 6631.
20. Chen, Y., & Hu, H. (2020). In-plane elasticity of regular hexagonal honeycombs with three different joints: A comparative study. *Mechanics of Materials*, 148, 103496.
21. Mousanezhad, D., Babaei, S., Ghosh, R., Mahdi, E., Bertoldi, K., & Vaziri, A. (2015). Honeycomb phononic crystals with self-similar hierarchy. *Physical Review B*, 92(10), 104304.
22. Szymczyk, P., Hoppe, V., Ziółkowski, G., Smolnicki, M., & Madeja, M. (2020). The effect of geometry on mechanical properties of Ti6Al4V ELI scaffolds manufactured using additive manufacturing technology. *Archives of Civil and Mechanical Engineering*, 20(1), 1-13.
23. Song, J., Wang, M., Li, D., & Zhang, J. (2024). Deformation and energy absorption performance of functionally graded TPMS structures fabricated by selective laser melting. *Applied Sciences*, 14(5), 2064.
24. Yu, X., Zhou, J., Liang, H., Jiang, Z., & Wu, L. (2018). Mechanical metamaterials associated with stiffness, rigidity, and compressibility: A brief review. *Progress in Materials Science*, 94, 114-173.
25. Zhang, Z., Li, Z., Pan, S., & Chai, X. (2022). Enhanced strength and high-temperature wear resistance of Ti6Al4V alloy fabricated by laser solid forming. *Journal of Manufacturing Science and Engineering*, 144(11), 111011.
26. Zhang, X., Wang, Y., Ding, B., & Li, X. (2020). Design, fabrication, and mechanics of 3D micro-/nanolattices. *Small*, 16(15), 1902842.
27. Da, D., Yvonnet, J., Xia, L., Le, M. V., & Li, G. (2018). Topology optimization of periodic lattice structures taking into account strain gradient. *Computers & Structures*, 210, 28-40.
28. Pan, C., Han, Y., & Lu, J. (2020). Design and optimization of lattice structures: A review. *Applied Sciences*, 10(18), 6374.
29. Zok, F. W., Latture, R. M., & Begley, M. R. (2016). Periodic truss structures. *Journal of the Mechanics and Physics of Solids*, 96, 184-203.
30. Zhang, X., Zhang, H., & Wen, Z. (2014). Experimental and numerical studies on the crush resistance of aluminum honeycombs with various cell configurations. *International Journal of Impact Engineering*, 66, 48-59.
31. Goldmann, T., Huang, W. C., Rzepa, S., Džugan, J., Sedláček, R., & Daniel, M. (2022). Additive manufacturing of honeycomb lattice structure—from theoretical models to polymer and metal products. *Materials*, 15(5), 1838.

32. Du Plessis, A., Broeckhoven, C., Yadroitsava, I., Yadroitsev, I., Hands, C. H., Kunju, R., & Bhate, D. (2019). Beautiful and functional: a review of biomimetic design in additive manufacturing. *Additive Manufacturing*, 27, 408-427.
33. Sarraf, M., Rezvani Ghomi, E., Alipour, S., Ramakrishna, S., & Liana Sukiman, N. (2021). A state-of-the-art review of the fabrication and characteristics of titanium and its alloys for biomedical applications. *Bio-design and Manufacturing*, 1-25.
34. Bührig-Polaczek, A., Fleck, C., Speck, T., Schüler, P., Fischer, S. F., Caliaro, M., & Thielen, M. (2016). Biomimetic cellular metals – using hierarchical structuring for energy absorption. *Bioinspiration & biomimetics*, 11(4), 045002.
35. Ajdari, A., Jahromi, B. H., Papadopoulos, J., Nayeb-Hashemi, H., & Vaziri, A. (2012). Hierarchical honeycombs with tailorable properties. *International Journal of Solids and Structures*, 49(11-12), 1413-1419.
36. Zhang, Q., Yang, X., Li, P., Huang, G., Feng, S., Shen, C., & Lu, T. J. (2015). Bioinspired engineering of honeycomb structure—Using nature to inspire human innovation. *Progress in Materials Science*, 74, 332-400.
37. Wang, S., Liu, L., Huang, Z., Li, Z., Liu, J., & Hao, Y. (2021). Honeycomb structure is promising for the repair of human bone defects. *Materials & Design*, 207, 109832.

CHAPTER FOUR: NUMERICAL MODELLING OF POLYGON STRUCTURES UNDER QUASI-STATIC LOADING

Part of the contents of this chapter has been submitted for publication or has been published in peer-reviewed journals, as follows:

1. **Chibinyani, M. I., Dzogbewu, T. C., Maringa, M., & Muiruri, A. M. (2023).** Numerical modelling of DMLS Ti6Al4V(ELI) polygon structures. *Results in Materials*, 20, 100456. doi.org/10.1016/j.rinma.2023.100456
2. **Chibinyani, M. I., Dzogbewu, T. C., Maringa, M., & Muiruri, A. M. (2024).** Numerical modelling of DMLS Ti6Al4V(ELI) polygon structures. chemical and materials sciences. *Developments and Innovations 4*, 1-53. doi.org/10.9734/bpi/cmsdi/v4/8584E

4.1. Summary

This study covers numerical modelling and ranking the efficiency of four polygon geometries: triangular, square, circular, and hexagonal. A comparative analysis of planar and extruded hexagonal cells is first made. After the ranking for various polygon geometries has been done, the best-performing structure is compared with theoretical predictions and analytical models assessing the effect of thickness (t) on the stiffness of a Ti6Al4V(ELI) structure under compression. Numerical modelling also validates these predictions and examines the impact of t on buckling behaviour. The key insights are pointed out and discussed in comparison with existing literature. The chapter concludes by discussing opportunities for further research.

4.2. Comparative analysis of planar and extruded FE models

The stresses in the planar and extruded hexagonal shell models were both found to be highest at the vertices, as shown in Figure 4-1a and 4-1b, respectively. The planar hexagonal shell model in Figure 4-1a is a plane-strain problem. This is because the load is applied in an xy -plane of the extruded hexagonal shell model, and the thickness of the shell in the out-of-plane axis (z) is comparatively much higher. This implies that the effect of the applied load along the z -axis can be ignored, and the 3D problem is represented by a planar problem [1]. The planar hexagonal shell model was observed to have high stresses on the inner vertices of its inclined members, caused by both direct compressive and bending loads. These stresses give rise to large elastic deformations at the vertices. The Poisson's ratio of the material also leads to the development of small transverse elastic strains in the regions. Similarly, the contour plot for stresses on the extruded hexagonal shell model in Figure 4-1b shows the highest stresses to occur on the vertices of the inclined members. These results are similar to what was observed in references [2-6]. The same distribution of stress was obtained from the analysis of the plane-strain problem.

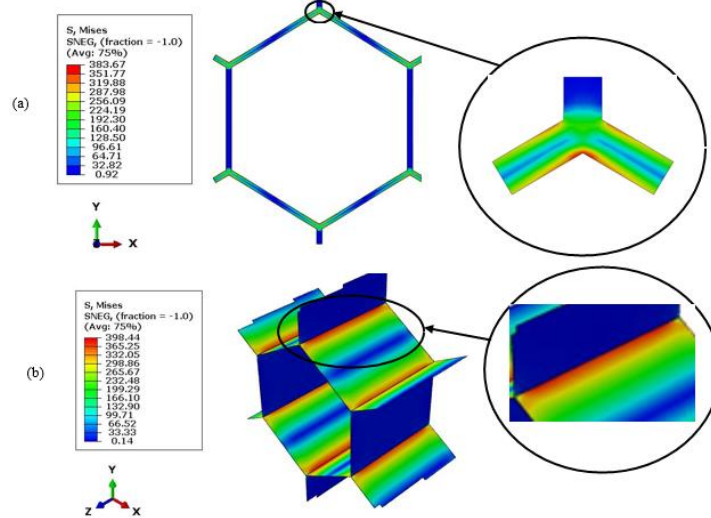


Figure 4-1. Typical contour plot of stress obtained on (a) planar hexagonal and (b) extruded hexagonal shell models

Upon application of a load of 2000 N, the unit hexagon planar and the extruded shell models seen in Figure 4-1 show values of maximum von Mises stresses that are almost the same in magnitude, 383.67 and 398.44 MPa, respectively. This small difference of about 3.71% justifies the use of the planar model instead of the more complex extruded model to save computational time.

When using the extruded HC shell element, a visual problem occurred at the vertices. The visual problem occurred because the faces connecting the vertices of structural members had no congruence. The lack of congruence was observed when the assigned thickness was extruded from the shell, as illustrated in Figure 4-2. The black arrows shown in Figure 4-2 represent the directions of extrusion of the planar shells of the planar geometry.

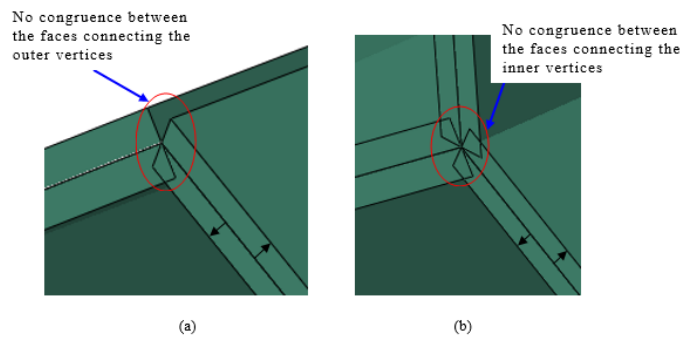


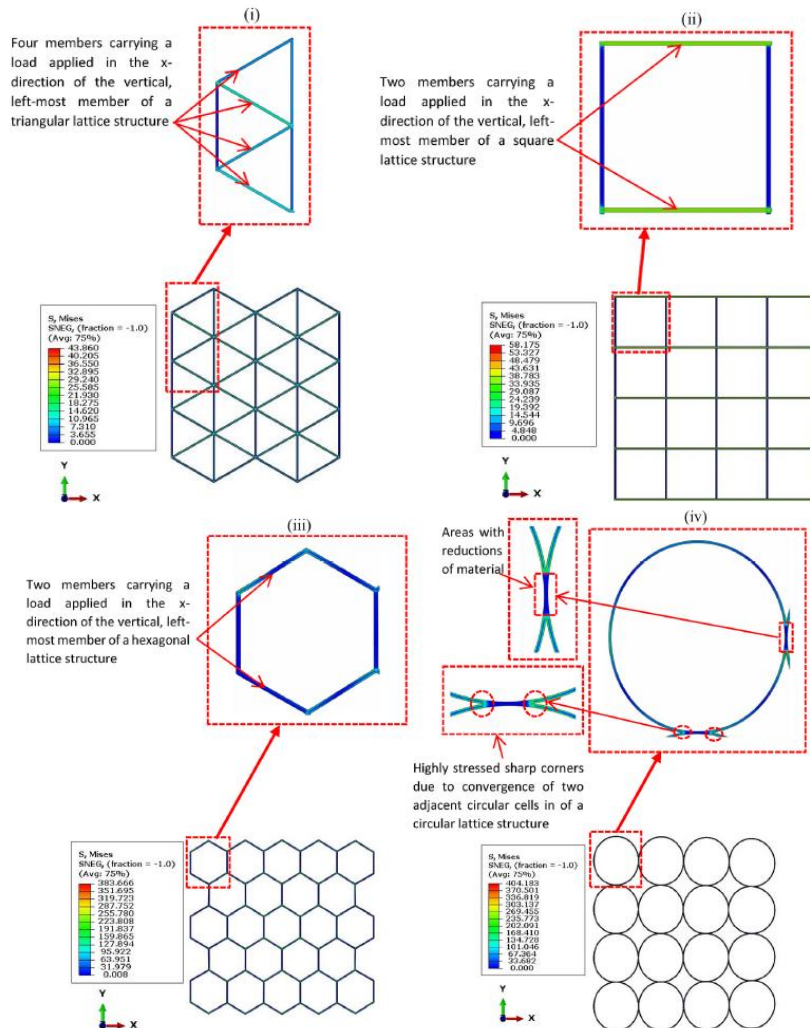
Figure 4-2. Typical visual problem of unshared topology at the (a) outer and (b) inner vertices after extruding a thickness from the extruded shell model

The difference between the images in Figure 4-2 is simply due to the way the wall thickness is depicted in the two cases. Extruding a thickness from an extruded shell takes the surface of a shell and extrudes half a wall thickness in either direction. The discrepancy observed at the vertices will occur for any adjacent surfaces meeting at an angle other than 180 degrees, causing some overlap and some gap. This is, however, only due to the graphical presentation but does not affect the numerical results. The discrepancy referred to at the vertices, however, has limitations when carrying out structural optimizations such as TO and SO. In recent work by the authors [7], a planar honeycomb model was investigated, and it was concluded that the vertices reduced effective iterations in TO and SO. Therefore, using geometries with the discrepancy observed at the vertices of extruded hexagonal shell would result in the generation of topologies with no congruence at the vertices during TO and SO. This would, in turn, create difficulties in the normal

numerical analysis of the topology- and shape-optimized structures and is the subject of further research by the authors.

4.3. Preliminary FE findings for polygon structures

Upon applying an out-of-plane load of 2000 N, separately in the x - and y - directions, numerical results were generated for four different planar polygon models with $t = 1$ mm. These numerical results of stress and deflection are presented in the form of contour plots in Figures. 4-3, 4-4, 4-5 and 4-6, respectively. As seen in Figure 4-3, the order of increasing maximum stress for different planar polygon models is triangular, squared, hexagonal, and circular for a load applied in the x -direction. When the load was applied in the y -direction, as shown in Figure 4-4, it was observed that the order of preference changed to squared, triangular, circular, and hexagonal models. It is noted that while the values of maximum von Mises stresses for the rectangular and circular models remained the same for loads applied in the x - and y -directions separately, they were higher for loads applied in the y -direction for the triangular and hexagonal models. Loading in the y -direction is, therefore, a more critical one for the design of the last two polygons.



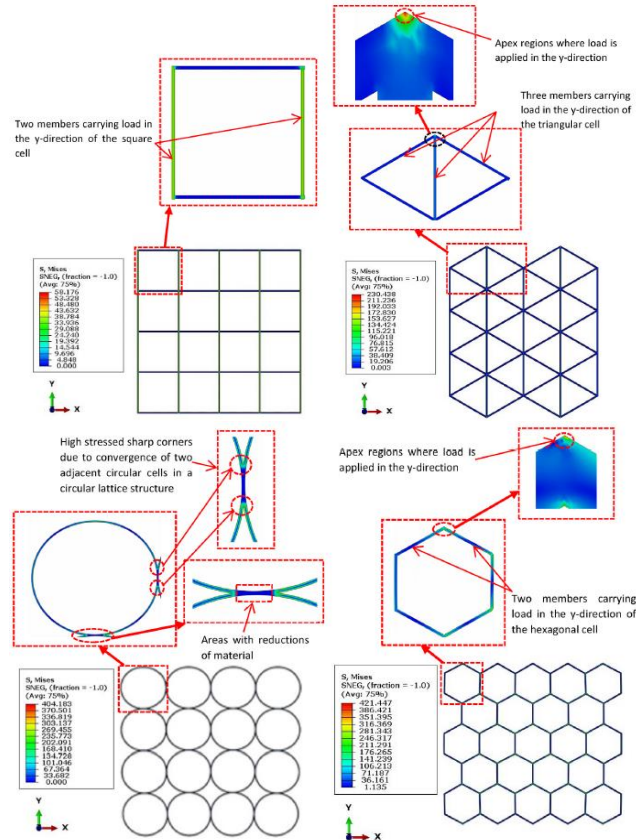


Figure 4-4. The distribution of von Mises stresses in four different models of polygons for an applied load of 2000 N in the y-direction

For loading in the x -direction, it is observed that the triangular and hexagonal models have lower stresses compared to the similar case of loading in the y -direction. This is because the load is applied transversely on the members in the x -direction loading, and at the points of intersection of members in the y -direction loading. The higher stress levels in the second case arise from the fact that loading at the intersection of members occurs in regions of the structure with sharp changes in geometry or apices. Loading at apex regions of a structure is known to cause high-stress concentration in them [1]. The model of triangular polygons recorded the lowest stresses when loaded in the x -direction. This structure can be argued to have a relatively larger effective cross-sectional area for this type of loading because of the four members carrying the load, in contrast to the models of square and hexagonal polygons, with two members each that are perpendicular and inclined to the applied load, respectively, as shown in Figure 4-3 and 4-4. The circular polygon has the highest x -direction stress (404.183 MPa) and the second-highest y -direction stress (404.183 MPa). This is because of the formation of tangential connections between adjacent circular polygons during their tessellation. Furthermore, when moving towards the points of contact or tangential connection, the material that forms the wall thickness of the connected circular polygons decreases, and sharp corners are generated as a result of this type of connection. These points of contact are, therefore, areas of high-stress concentration. For loads applied in the y -direction, the model of square polygons records the lowest stresses compared to other polygons. It achieves first position this time round because the model of triangular polygons is now loaded at the apex areas (designated as highly stressed regions) rather than transversely on its members that are connected to members that are inclined to it for loading in the x -direction. It is deduced from the foregoing discussion that the regions with abrupt changes of geometry, also referred to as peak regions, where the load is applied, and the number of members carrying

the applied load determine the load-bearing capacity and, therefore, stability of polygonal structures. This is consistent with what was reported in reference [4, 8]. Table 4-1 shows a ranking of maximum stresses in the four polygonal structures shown in Figures 4-3 and 4-4.

Table 4-1. Ranking of different polygon structures by stress levels for loading in the x - and y -directions, from the lowest to the highest

Type of polygon structure	Ranking for loading in the x -direction	Ranking for loading in the y -direction
Triangular	First	Second
Square	Second	First
Hexagonal	Third	Fourth
Circular	Fourth	Third

The data in the preceding table shows the model of triangular polygons to have the lowest and second lowest maximum von Mises stress of all four polygon structures for a load of the same magnitude applied in the x -direction and y -direction, respectively. Clearly, the triangular polygon is the best alternative of the four polygons modelled here.

In Figures 4-5 and 4-6, the circular polygon model is observed to have the largest magnitudes of deflection compared to all other polygon models for loading in both directions. This is similar to what was construed in reference [24] and implies that the lattice structures made up of circular polygons are less effective in stiffening structures [9].

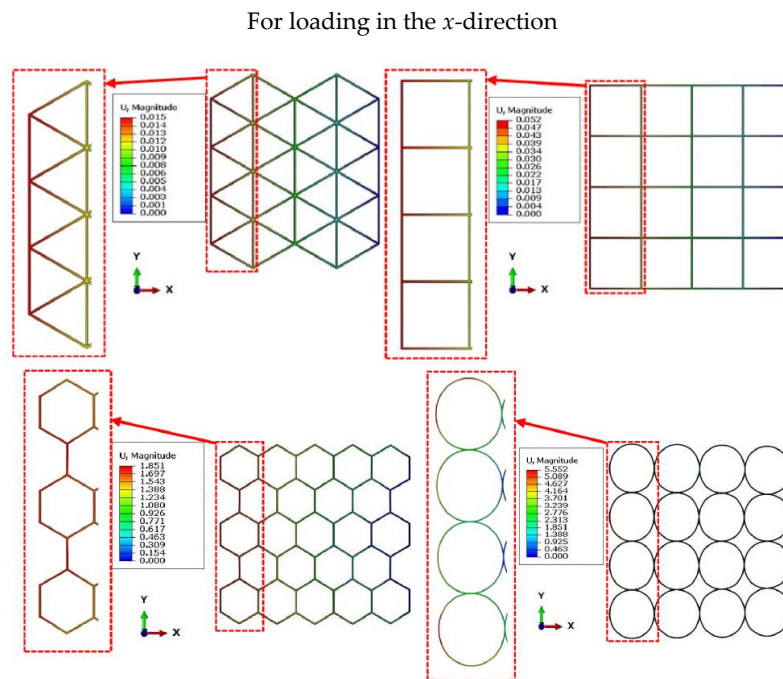


Figure 4-5. Distribution of deflections for the four different models of polygons for an applied load of 2000 N in the x -direction

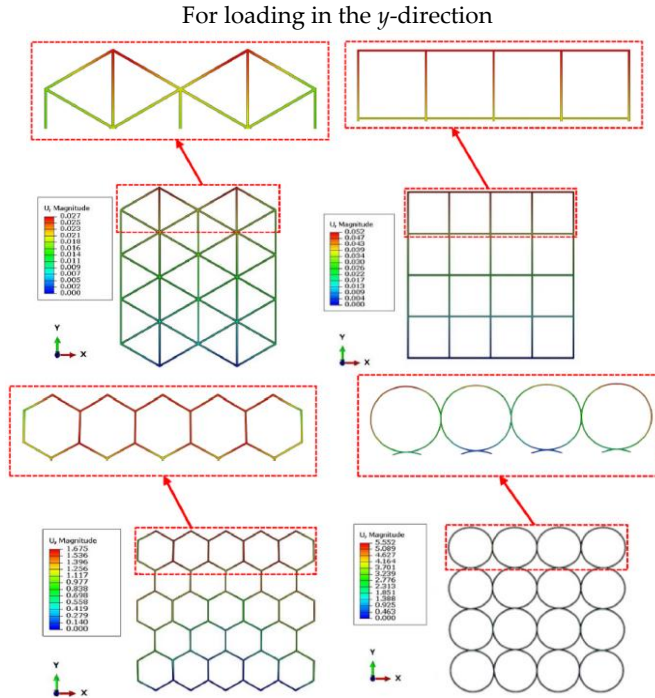


Figure 4-6. Distribution of deflections for the four different models of polygons for an applied load of 2000 N in the y -direction

Table 4-2 shows the ranking of the deflections for the four different types of polygonal structures.

Table 4-2. Ranking of different polygon structures by deflection levels for loading in the x - and y -directions, from the lowest to the highest

Type of polygon structure	Ranking for loading in the x -direction	Ranking for loading in the y -direction
Triangular	First	First
Square	Second	Second
Hexagonal	Third	Third
Circular	Fourth	Fourth

It is evident from the results presented in Figures 4-5 and 4-6 that the models of triangular and square polygons have the lower and second lowest deflections for loading in both x - and y -directions, respectively. This means that the polygon structures made of the two polygons are stiffer compared to those of circular and hexagonal polygons, which recorded the highest and second-highest deflections of all four polygon structures, in both directions, respectively.

From the foregoing work, the triangular polygon records the lowest deflections of all four polygons modelled for a load of the same magnitude and applied in each of the two directions, separately. It also records the lowest maximum von Mises stress for a load of the same magnitude applied in the x -direction and the second lowest maximum von Mises stress for a load of the same magnitude applied in the y -direction. Overall, therefore, the triangular polygon is the best choice of the four polygons modelled here.

Despite the foregoing choice of the best polygon, the hexagonal structure is by far the most widely researched [2, 4, 10-18] and is, therefore, used in the ensuing analysis to compare the results generated in this work and those from the literature.

4.4. Deformation behaviour of HC models

4.4.1 Bending and axial behaviour

Figure 4-7 shows a comparison between the current simulations of HC structures and the ones reported in references [4, 16-18], with regard to their elastic deformation for loading along the x -direction. Identical elastic deformation shapes for both the theoretical [4, 17-18] and current FEA results are observed. The HC model in the current FEA results was obtained using a uniaxial load, whereas the theoretical model in literature is based on a pressure load. Despite this difference in the type of loads applied to both models, there is no significant difference in the results. When the HC structure was exposed to a uniaxial compression load in the x -direction, both elastic bending and axial deformation of cell walls were initiated. The elastic deformation in the members of the structure occurred in the inclined members due to both axial compression and transverse bending induced in them from the applied load acting along the x -axis, as shown in Figure 4-8a. The elastic deformation mechanics of the inclined members shown in Figure 4-8b are similar to what was observed in the theoretical models of references [4, 18].

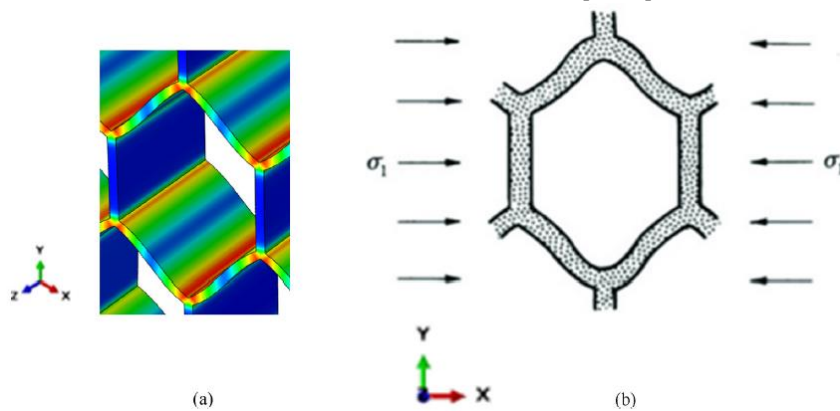


Figure 4-7. Typical elastic deformations of (a) the current numerical model and (b) schematic of a theoretical model in literature [4, 18] for an HC structure loaded along the x -direction

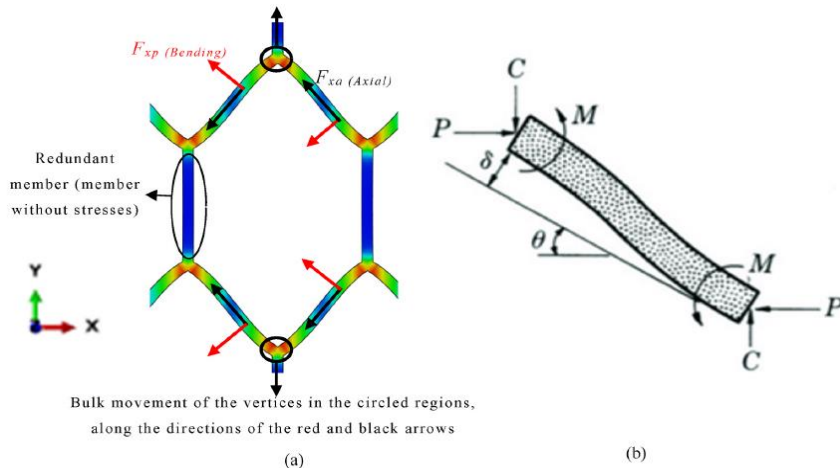


Figure 4-8. The deformation mechanics for the (a) current numerical model and (b) theoretical models [4, 18], for loading in the x -direction

It is garnered from the current FEA results in Figure 4-8a that the elastic deformation shapes resulted from one component stress load acting perpendicular ($F_{xp(Bending)}$) to and the other along ($F_{xa(Axial)}$) the member. This bending deflection and axial deformation of the inclined members contributed to the bulk movement of the upper and lower vertex regions in the y -direction (outwards), as demonstrated by the arrow attached

to the vertical members leading from each one of the two circled regions. This behaviour is similar to the theoretical behaviour reported in references [2, 14-17]. Moreover, the vertices were observed to be highly stressed regions. These vertices of HC structures are, therefore, liable to fail due to the high stresses in these regions. This is similar to what was observed in references [16, 19]. It is, therefore, important to note that such regions are likely to fail first and should be considered carefully when analysing the behaviour of structural frames. It is also evident for all the unit cells that the vertical members have close to zero stresses, as also shown in Figure 4-8a. This is because the direct stresses are only transferred along the axial directions of the members; thus, in the analysis of such structural frames, such members are considered redundant.

A similar numerical result for bending and axial deformation shapes to those discussed in Figure 4-7 was obtained when the extruded HC shell was loaded along the y -direction, as shown in Figure 4-9a. This is also similar to the behaviour of the existing theoretical model in the literature shown in Figure 4-9b [4]. However, the bulk movement of the vertex regions for this loading condition changed in direction. The vertices connecting the two inclined members are compressed into the cell, as shown in Figure 4-10, in contrast to their movement for the previous loading condition along the x -axis, where the vertices regions are pulled away from the centre of the cell. This is similar to what was observed in references [4, 16-19].

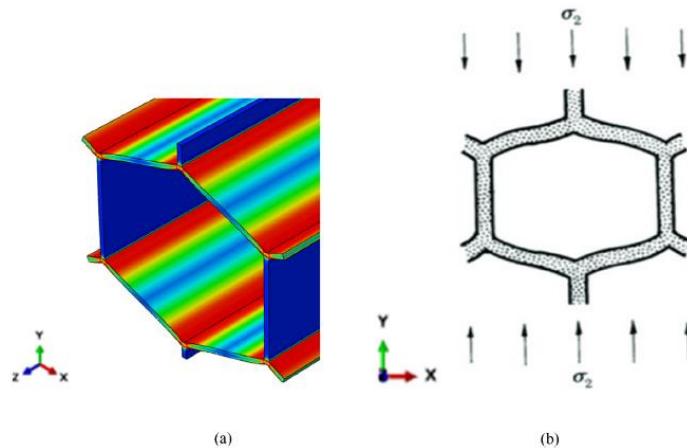


Figure 4-9. Typical elastic deformations of (a) the hexagonal HC numerical model and (b) image of a theoretical model in literature [4, 18] of a HC structure loaded along the y -direction

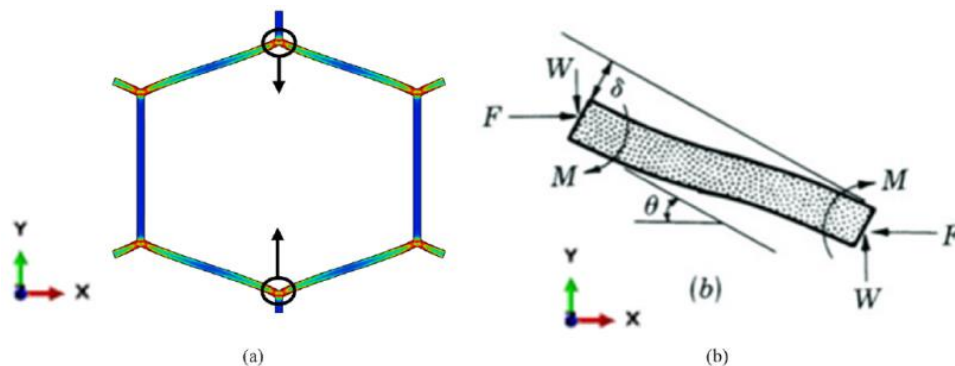


Figure 4-10. The deformation mechanism obtained for the (a) current numerical mode and (b) theoretical models [4, 18] loaded in the y -direction

For efficient design and manufacture of engineering structures with complex behaviour, it is also important to consider the direction of loading. This is evident for the HC structure modelled here, where the contours of deflection for loads applied to it in the x - and y -directions are seen in Figures 4-11 and 4-12,

respectively. The deflections for all thicknesses of members in the two figures were higher for the load applied in the x -direction than in the y -direction.

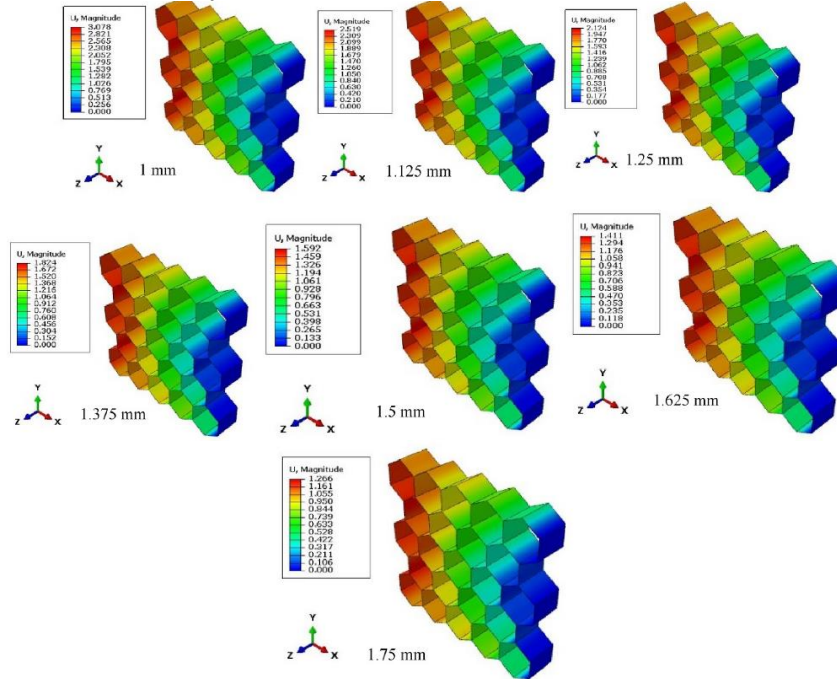
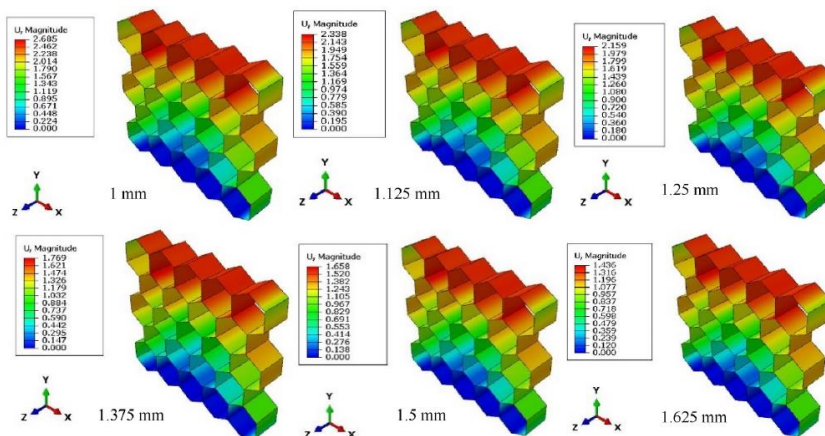


Figure 4-11. Numerical results of deflection for HC structures of different wall thicknesses loaded in the x -direction

In the two figures, the values of deflection for both load cases are seen to reduce with increasing wall thickness. The maximum values of deflection for the HC structure loaded in the x - and y -directions differed from the figures with a structure of 1 mm wall thickness by (18.16, 15.68, 14.12, 12.72, 11.37, and 10.28) per cent and (12.92, 7.66, 18.06, 6.27, 13.39, and 15.81) per cent, respectively. It is clear from these values that the differences in the magnitudes of deflection obtained for different thicknesses of structures loaded in the x - and y -directions are significant, all being greater than 5%. Studies conducted in [4, 20-22] showed that percentage differences of more than 5% are significant.

The maximum values of deflection for the HC structure loaded in x - and y -directions, for different values of maximum elastic loads, are presented in Table 4-3, and the values plotted in Figure 4-13, using polynomial curves fits of order two, to facilitate a search for trends.



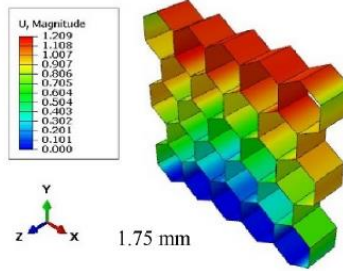
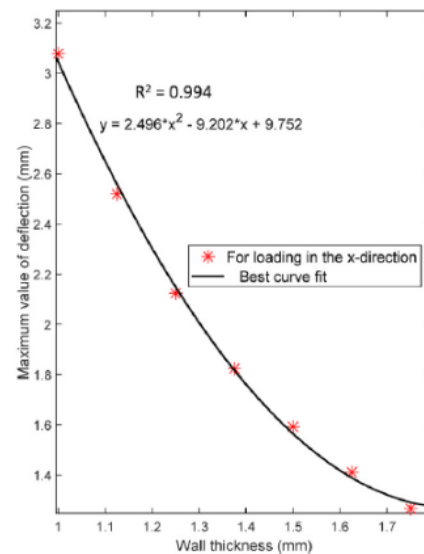
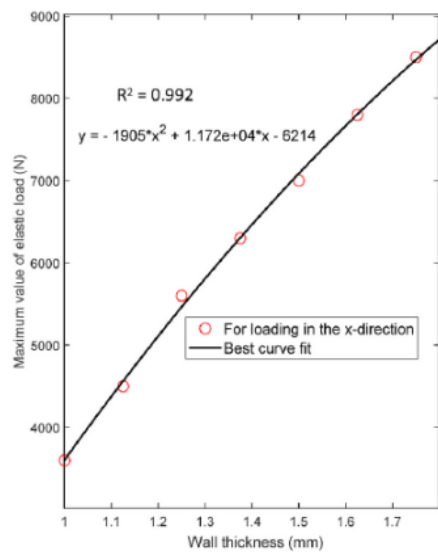


Figure 4-12. Numerical results of deflection for HC structures of different wall thicknesses loaded in the y-direction

Table 4-3. Values of load applied to an HC structure in the x- and y-directions and the corresponding values of deflection

Loading in the x-direction		
Wall thickness (mm)	Maximum value of elastic load (N)	Corresponding value of deflection (mm)
1	3600	3.078
1.125	4500	2.519
1.25	5600	2.124
1.375	6300	1.824
1.5	7000	1.592
1.625	7800	1.411
1.75	8500	1.266

Loading in the y-direction		
Wall thickness (mm)	Maximum value of elastic load (N)	Corresponding value of deflection (mm)
1	3500	2.685
1.125	4350	2.228
1.25	5480	2.159
1.375	6100	1.769
1.5	6880	1.658
1.625	7640	1.436
1.75	8390	1.207



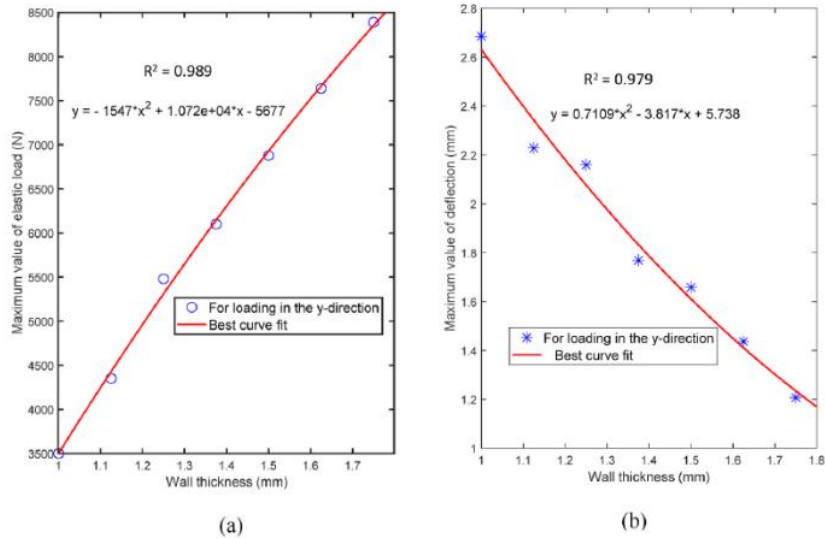


Figure 4-13. Curves with (a) maximum applied loads and (b) maximum deflections experienced in the x - and y -directions of the HC model at different values of thickness (t) of its members

The maximum elastic loads were recorded for a value of stress experienced by the structure that is equal to the yield strength of its material. The curves in Figure 4-13a show that the magnitudes of maximum elastic load applied to the HC model in the x - and y -directions have a directly proportional relationship to the wall thickness. The curves in Figure 4-13b, on the other hand, show that the corresponding values of deflection experienced by the HC model in the x - and y -directions are inversely related to the wall thickness. The correlation coefficients in the four graphs are less than one, showing that the relationship between variables is not coincidental. However, it is indicated in [23-25] that values above 0.95 are considered high correlation coefficients, which is shown for all four graphs.

Curves for the maximum values of elastic load applied against corresponding values of deflection were generated from Figures 4-13(a and b), with the results shown in Figure 4-14.

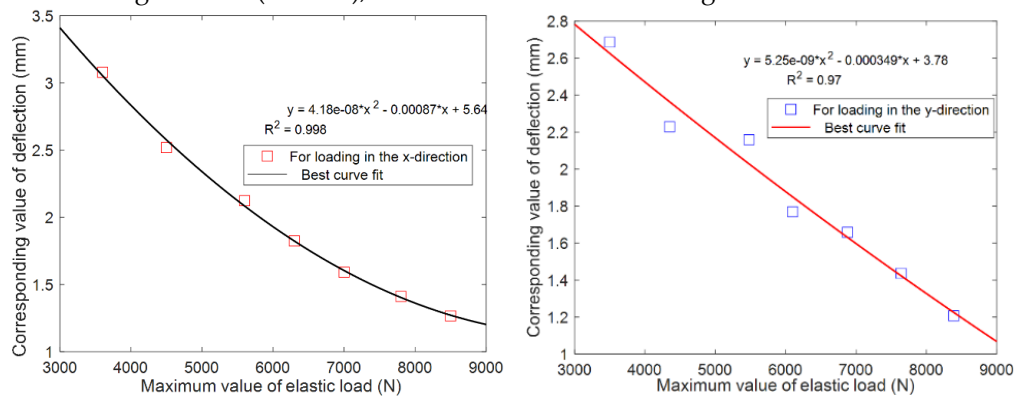


Figure 4-14. Curves of the (a) x - and (b) y -direction maximum applied loads versus maximum corresponding deflections

It is clear from the curves in Figure 4-14 that the maximum values of elastic load applied to the HC model in the x - and y -directions have an inversely proportional relationship to the corresponding values of deflection experienced by the structure. Non-linearities are also observed in the curves depicted in the two figures (Figure 4-13 and Figure 4-14). The non-linearity observed in this figure and the previous one is due to how the applied load and corresponding deflections are dependent on the thickness of the walls of HC structures. The preceding assertion is a fact that is backed up by Equations 3.2 and 3.3 described in Chapter 3, which clearly show that an exponential change to the thickness of the walls of HC structures

relates to the stiffness and corresponding stress for an applied load. The stiffness and corresponding stress that result from a maximum elastic load grow by an exponential increase in the thickness of the walls of HC structures.

4.4.2. Primary buckling behaviour

The extruded HC shell models analysed here, with values of wall thickness of 1, 1.125, 1.25, 1.375, 1.5, 1.625, and 1.75 mm and the same value of length ($L = 20$ mm) had (t/L) values less than 0.1 and are thus, all slender. Therefore, Euler's theory of buckling was adopted in their analysis. The values of critical loads (P_c) and related stresses for each thickness were then calculated using Euler's Equation 4.1 and Equation 4.2, respectively, and are presented in Table 4-4.

$$P_c = \frac{\pi EI}{l_e^2} = \frac{\pi Ebt^3}{12l_e^2} = Bt^3 \quad (4.1)$$

$$\sigma_c = \frac{P_c}{A} = \frac{Bt^3}{bt} = Ct^2 \quad (4.2)$$

where, symbol P_c stands for the critical buckling load, E Young's modulus, I area moment of inertia, b width, l_e equivalent length, A cross-sectional area, b breadth, t thickness, and B and C constants, all the wall plates/shells of the structure.

For uniaxial loading in the z -direction, the calculated values in Table 4-4 show that the HC shell model will fail by elastic buckling ahead of yielding when wall thicknesses (1, 1.125, and 1.25) mm are used. This is because the calculated buckling stresses at these values of wall thickness, for the calculated values of critical loads, are all less than the yield stress of the material for the shell walls of 790 MPa. The von Mises stress contours of the HC shell model are shown in Figure 4-15, and the values of critical loads and their corresponding buckling stresses are presented in Table 4-5.

Table 4-4. Calculated values of critical buckling loads and buckling stresses for the hexagonal extruded shell model with different wall thicknesses

Shell wall thickness t (mm)	Critical buckling load P_c (MN)	Buckling stress σ_c (MPa)
1	0.049	373.533
1.125	0.083	614.815
1.25	0.114	760
1.375	0.151	915.152
1.5	0.197	1094.444
1.625	0.250	1282.051
1.75	0.312	1485.714

Table 4-5. Numerical values of critical buckling loads and the corresponding stresses at these loads for the hexagonal extruded shell model with different wall thicknesses

Shell wall thickness t (mm)	Critical buckling load (MN)	Buckling stress (MPa)
1	1.233	1634.490
1.125	1.748	1832.338
1.25	2.386	2028.081
1.375	3.160	2221.539
1.5	4.079	2412.544
1.625	5.156	2600.933
1.75	6.401	2786.549

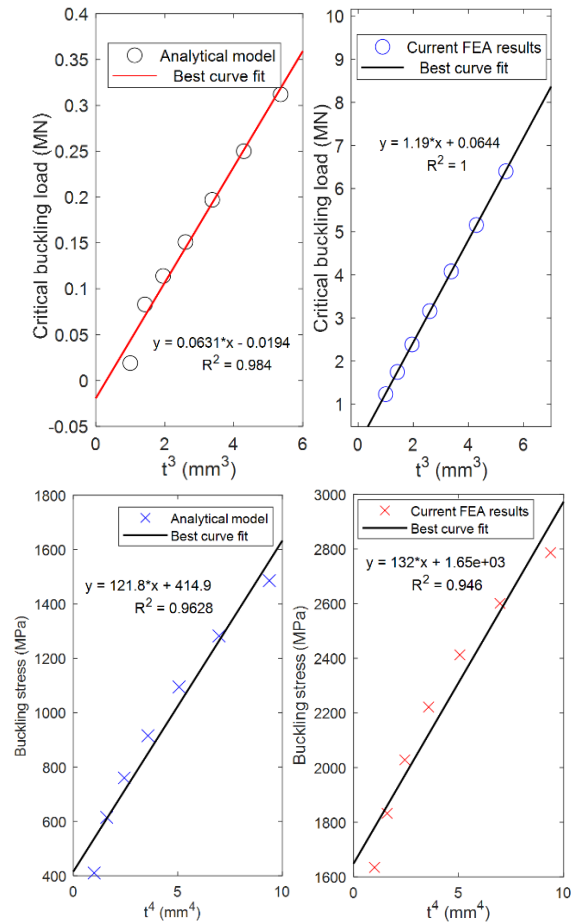


Figure 4-16. Critical buckling loads and stresses versus the wall thickness of the numerical HC model loaded in the z-direction

The curves in these two figures show that the critical load and related stresses are close to directly proportional (with correlation coefficients greater than 0.95 correlation) to the third and fourth power of the thickness of the shells/plates, respectively, for loading in the z-direction. The curves in these two figures are consistent with those reported in reference [4, 18].

The buckled shapes for primary buckling of both the numerical and analytical models are similar, as shown in Figure 4-17.

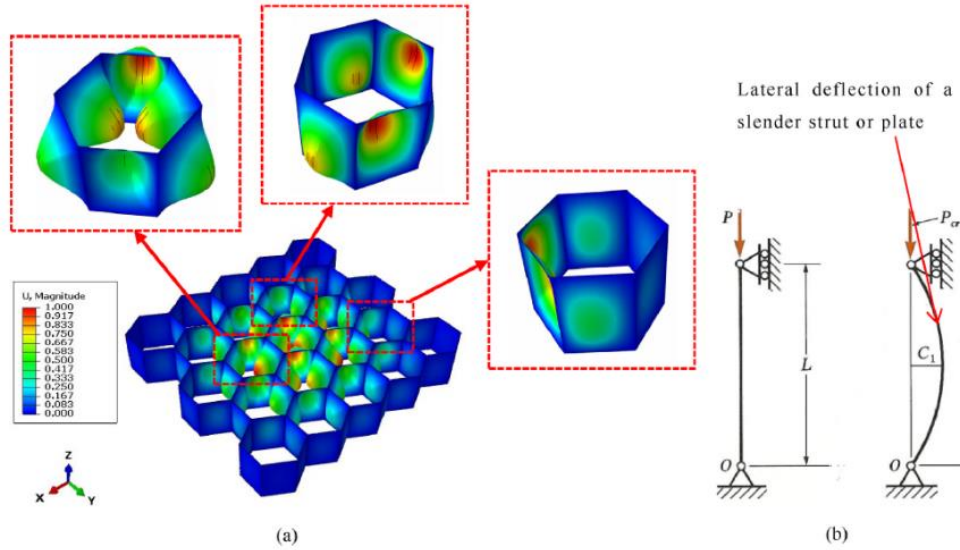
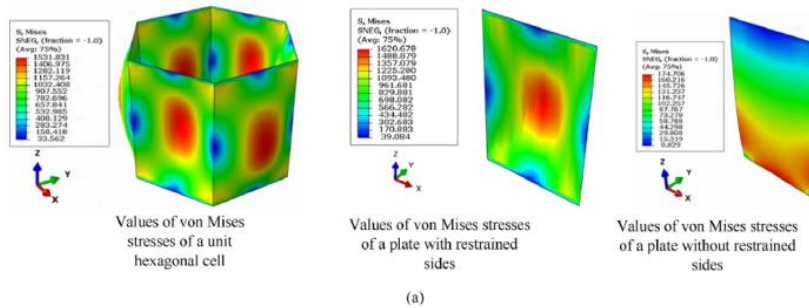


Figure 4-17. Current numerical and existing theoretical elastic buckling first mode shapes on an HC structure with uniaxial loading acting in the z-direction

The values of deflection of the HC shell model in this figure are given relative to a value of 1 for the highest deflection, as is normal for linear buckling, given the fact that its subroutine is set only to detect the presence and absence of buckling. Because linear buckling analysis does not provide absolute values of deflection, it cannot facilitate comparisons of the deflections of models with different thicknesses, which demands the use of an alternative approach. This does not diminish the value of undertaking linear buckling because, in most cases, the primary need is only to determine the presence or absence of buckling. It is clearly shown in Figure 4-17 that the faces adjacent to one another for the HC model buckled in different directions, inwards and outwards. Furthermore, the points of maximum deflection occur at the mid-points of the plates. Figure 4-17 also shows that there is a higher degree of buckling towards the centre than at the peripheries of the plates. This is a function of the intercellular restraint that is higher towards the edges than towards the centre of the plates.

The veracity of the conclusion made regarding the restraining effect of the hexagonal cells against one another for the HC shell model was tested using a unit hexagonal cell, a plate with vertical fixed sides, and another plate without vertical fixed sides, respectively, all pinned at their bottom edges. This was done to determine whether or not the critical buckling loads recorded in the preceding analysis that were above the material's yield stress were attributable to the restraining effect of adjacent shells in the model. Figure 4-18 shows the results in terms of von Mises stress and deflections that were obtained for these models, all of which had plate thickness of 1 mm.



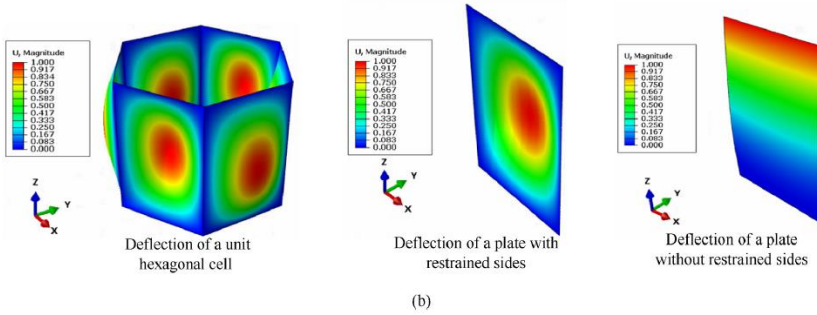


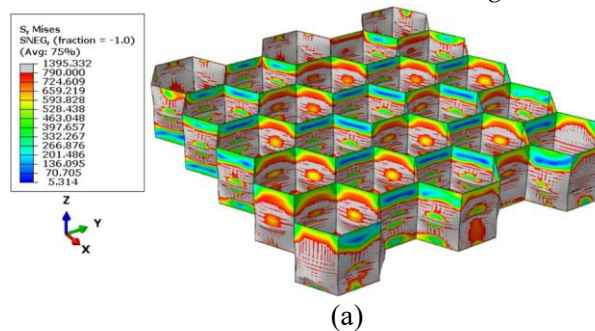
Figure 4-18. A buckled unit hexagonal cell and plates with and without vertical fixed sides from the left to the right, respectively, showing (a) von Mises stress and (b) deflection contours

The three different models shown in this figure required critical loads of (0.141, 0.014, and 0.001) MN for a unit hexagonal cell, a plate with fixed vertical sides, and a plate without fixed sides, respectively, for buckling to occur. The values clearly show that stiffness and, therefore, critical load do increase with increasing restraint of the plates.

It is also observed in Figure 4-18a that the plate without constrained vertical sides buckled below the material's yield stress in contrast to the other two models. Therefore, it can be deduced that the adjacent shells in an HC structure have a stiffening effect on the plates, and therefore, the observed values of stresses of the HC structure at buckling are well above the yield stress of the material for HC models.

The results for linear buckling clearly cannot yield values of deflection, and therefore, there is a need to explore nonlinear buckling analysis. This method employs a nonlinear geometric analysis to model the transition from direct deformation to buckling and to eliminate the observed limitation of linear buckling analysis through other features as well.

In practical buckling, there is no such thing as a perfectly straight structure, perfect constraint, or ideal application of load. There is also no completely homogenous material composition [26]. In practice, all these factors contribute to small eccentricities and changes that attract offset axial stress. This, in turn, causes offset moments, which induce even more eccentricity. Buckling will not occur in a very stable real structure, but eccentricities will build until instability arises in an intermediate typical model of the structure [27]. Figure 4-19 shows a contour plot of the von Mises stress. The von Mises stress contours in this figure clearly show that the HC shell model went plastic before it reached its critical buckling load of 1.46 MN. This image is also accompanied by nonlinear buckling of an extruded single hexagonal cell, as well as plates with and without restrained vertical sides, similar to those shown in Figure 4-18.



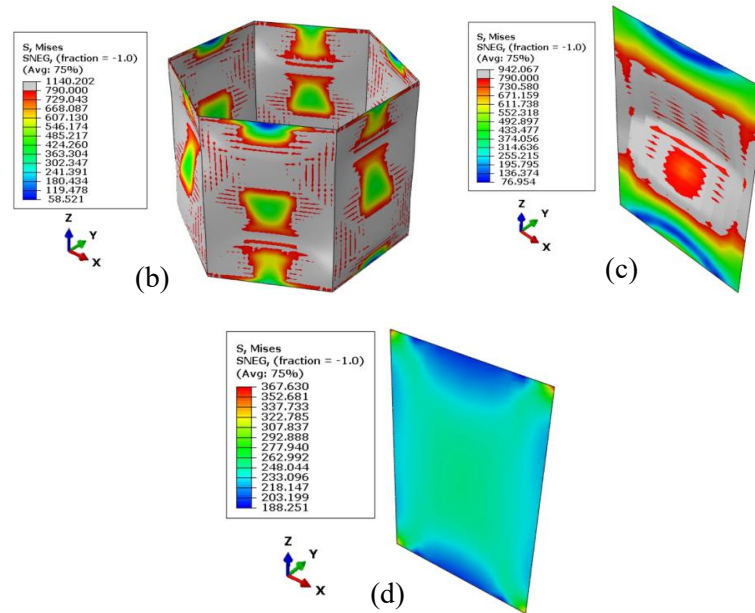


Figure 4-19. von Mises stress contours of shell models of wall thickness 1 mm, including (a) the HC, (b) the unit hexagonal cell, (c) the plate with restrained vertical sides, and (d) the plate without restrained vertical sides

Nonlinear analyses of the chosen shell models of 1 mm thickness show that their use could result in more accurate and detailed behaviour. The results also show that shell models had a large area where stresses higher than the yield stress of the material were experienced (areas with grey contours), except for the plate without restrained vertical sides. This means that a large percentage of the material used to build the structures had deformed plastically before the structure buckled. It is important to note that such HC parts cannot be adopted for normal engineering applications. This is because the structure has far exceeded its design constraints. Therefore, the restraining effect of hexagonal cell walls against one another is also confirmed by the results of nonlinear buckling, and it is evident from Figure 4-19 that the critical buckling load is reduced for decreasing intercellular wall restrains. With reference to the HC model, the load decreased to (0.0930, 0.0145, and 0.0033) MN for the unit hexagonal cell, plates with and without restrained vertical sides, respectively.

One of the advantages of using nonlinear analysis over linear analysis is that it can take into account plastic deformation. The simulation for nonlinear analysis of buckling was run using the Johnson-Cook Model that is built into ABAQUS/CAE. It is common and simple to use the Johnson-Cook (J-C) model to describe the isotropic flow properties of metals and metallic alloys during deformation due to plasticity. Plastic deformation of the Ti6Al4V(ELI) HC structures under nonlinear buckling in this work was investigated using the set of J-C parameters obtained from the literature shown in Table 4-6 [28].

Table 4-6. Set of J-C model parameters [28]

Parameter for J-C model	A (MPa)	B (MPa)	n	C	m
Lee & Lin [28]	782.7	498.4	0.28	0.0028	1

where the symbol A denotes the yield stress, B is the strain hardening factor, C is the dimensionless strain rate hardening coefficient, and n and m are the strain hardening and thermal softening exponents, respectively. Figure 4-20 shows the contours of plastic strain for the same models as in Figure 4-19, except

for the plate model without restrained vertical sides, since it buckled within the elastic phase of deformation.

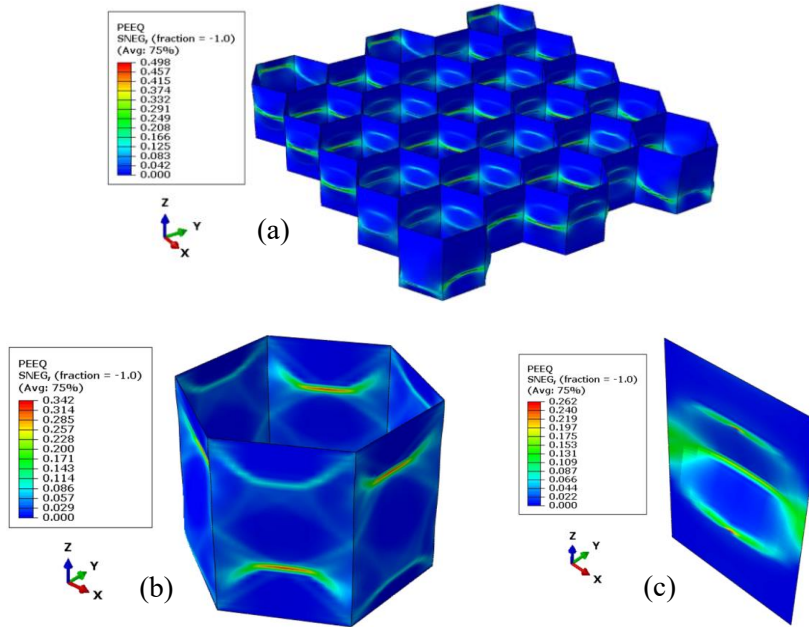


Figure 4-20. Plastic strain contours for the shell models of wall thickness 1 mm, including (a) the HC, (b) the unit hexagonal cell, and (c) the plate with restrained vertical sides

In Figure 4-20, the shell models the highest plastic strains occurred at the mid-span locations of the hexagonal cell. The foregoing results of nonlinear analysis of buckling clearly demonstrate that the structure is more likely to fail first by axial compression than by buckling.

4.5. Effects of the t/L ratio on the effective stiffness of HC structures

For out-of-plane loading of the HC shell model, the corresponding relationships between the yield strain and the ratios t/L and $(t/L)^3$ were plotted in Figure 4-21(a and b), respectively.

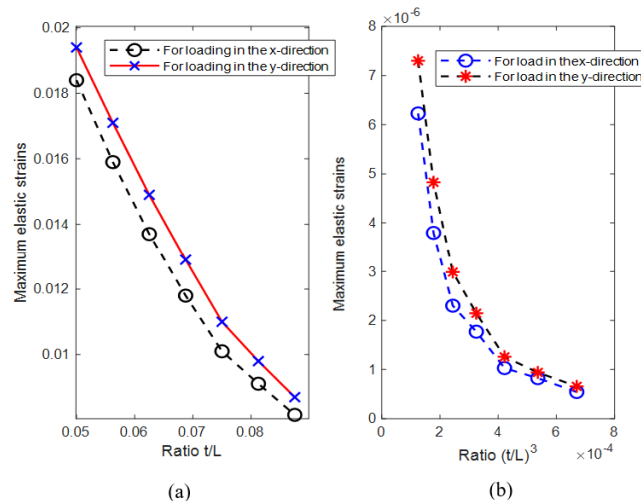


Figure 4-21. Numerical results for elastic strains against the ratio (a) t/L and (b) $(t/L)^3$ for the HC model

The yield strains were obtained for HC structures of different wall thicknesses loaded to maximum elastic stresses close to the yield stress of the selected material of 790 MPa. The curves in the figure are similar to what was observed in reference [29]. The highest strain resulting from each model was evaluated

to determine if the subsequent FEA would be limited to maximum stress values that the HC shell structure could bear before the material surpassed yield stress. To relate strain to Equation 3.2 presented in Chapter 3, the arising strains were plotted against the relevant ratios of t/L and $(t/L)^3$. For Ti6Al4V(ELI), whose values of mechanical properties were used in numerical modelling in this work, a yield strain value of 0.699% is obtained from Hooke's Law based on values of yield stress and stiffness of 790 MPa to 113.8 GPa [30]. With a safety factor of 1.5, this value reduces to 0.446%. These are the strains that should be targeted when using the material as intended for lightweight parts in applications. The FE models, however, recorded elastic strains that were more than the allowable yield strain (0.699%). This likely resulted from the effects of the bulk movement of the structure and, therefore, deflection on top of deformation.

The curves in Figure 4-21, which are generated using numerical models, show that strains decrease nonlinearly as the thickness of the walls of HC structures increases. This is further confirmed by the analytical model in Equations 3.2 and 3.3 presented in Chapter 3. The observation made in Figure 4-21 is because the corresponding strains to either the stiffness or stresses are inversely related to the exponential change in the thickness of HC structure walls. In Figure 4-21a, the nonlinearity in the strains is detected for the last three plotted points, but in Figure 4-21b, the nonlinearity increased to the last five points. This is with the mathematical models, which clearly show that the degree of exponential change in the thickness of the walls of HC structures has a direct influence on how strains decrease with increasing wall thickness. The curves in Figure 4-21 also show that the strains are slightly greater for both ratios when the HC model is loaded in the y -direction as opposed to the x -direction. This is because loading in the x -direction occurs at the face, but loading in the y -direction occurs at the apex regions. When compared to the former, the latter loading case generates slightly higher stressed areas.

The effect of the t/L ratio on the stiffness of HC structures is now discussed, based on Equation 3.2 described in Chapter 3. At first, the thickness of HC cell walls varied from 1 to 1.75 mm, with a corresponding variation of the t/L ratio from 0.05 to 0.0875. Figure 4-22 shows the relation between the moduli ratio and the corresponding t/L ratios from the numerical and analytical results.

It is evident in Figure 4-22 that in the current FE model, the effective stiffness increased nonlinearly as the t/L ratio increased. The mathematical model in Equation 4.2, presented in Chapter 3, confirms this by showing how the stiffness of HC structures increases exponentially with wall thickness. The FE results plotted in this figure agree well with those from the analytical models of Gibson and Ashby [4], with the largest difference being 2.2×10^{-4} and 5.9×10^{-4} for the x - and y -direction loading, respectively. This is because the stiffnesses of structural frames, such as the HCs, are dependent on the t parameter used for constant values of L . By increasing the value of t , the structural frame experiences an increase in structural stiffness. The stiffness of the structure increases as the thickness increases because the material can resist deformation and bending more effectively. The relationship between thickness and stiffness is fundamental to structural mechanics and is described in numerous mathematical models, including the Euler-Bernoulli beam theory and the Timoshenko beam theory [1]. It is noted that the analytical models overestimated the effective stiffness for the two ratios. This could be because the analytical models in reference [6] did not consider the stiffening effects at the fixed nodes/vertices that were demonstrated earlier in Figure 4-15.

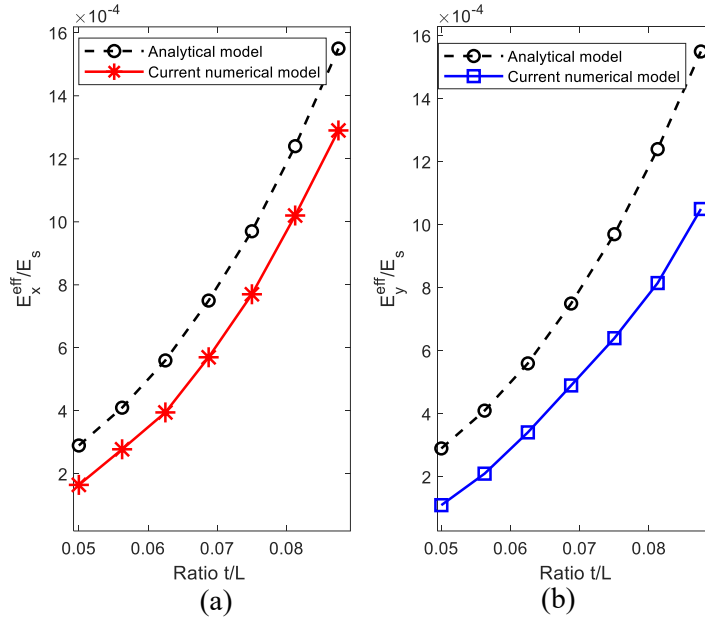


Figure 4-22. The effective stiffness of the regular hexagonal honeycomb, with out-of-plane load: Comparison between current FE predictions and analytical model predictions by Gibson and Ashby [4]

4.6. Comparison of implemented simulation/modelling in the current work and experimental findings in the literature

A comparative analysis of the numerical models implemented in the present work and experimental results on Ti6Al4V hollow structures in the literature can provide useful insights into the accuracy and reliability of predictive approaches in capturing the mechanical behaviour of such complex parts.

The greater part of the documented work in literature for Ti6Al4V hollow structures has been conducted on the strut-based and TPMS-based designs for hollow shapes [31-32]. This is because Ti6Al4V strut-based hollow designs are easy to construct and are used for numerous aerospace applications [32], and Ti6Al4V TPMS-based hollow designs are more amenable to biomedical applications [31]. Experimental results obtained from the literature [15-18, 33] are consistent with those of the numerical models in the present work for various polygon shapes, both concurring that vertices are regions of high stresses for hollow structures. Antolak-Dudka et al. [34] experimented on Ti6Al4V HC parts under static and dynamic compression loads. Their work highlighted the fact that the vertices or nodes typically fail first under compression loading. It must be noted that this pattern of failure is not only applicable to hollow structures built of Ti6Al4V(ELI) but also to those constructed using other alternative materials [4, 15], as the phenomenon is a function geometry and not materials [10-11, 35]. Generated numerical models in the present study also show that the most critical direction of loading hollow shapes is the one in which loads are applied directly at points of sharp changes of geometry, such as apexes where vertices converge. The authors were not able to identify with experimental validation of this last phenomenon, as the literature available on polygon hollow shapes [4, 7, 9, 13, 15-19, 36-37] was on loads applied transversely to the members of these structures. In the present work, it has been shown that numerically modelled triangular hollow structures had the lowest deflection for loading at apexes, as they had more members transferring load than the other polygon structures modelled in this work. In order of ranking, triangular hollow structures were shown in the present work, followed by square, hexagonal, and circular hollow shapes. This is an important finding, as the ranking of various polygon structures with respect to deflection is unavailable in the literature. Experimental confirmation of this ranking forms part of future planned work. In addition, it is noted that of the numerous studies reviewed [5-6, 8, 14-15, 26, 31, 33-34, 36, 38-40], none provides a rationale for the selection of different types of hollow shapes but instead proceed to use the

selected shapes for analysis in engineering applications without considering their rank in terms of their mechanical properties.

According to the numerical models generated in the present work, the predominant deformation behaviour of HC structures is the bending of the walls. This concurs with what has already been analytically and experimentally confirmed in numerous studies [4, 14-19]. Gibson et al. [18] validated HC mechanical models experimentally via compression tests on metal and moulded silicone rubber parts. Their experimental results reproduced the mechanical properties of HC parts consistent with the developed theory [4]. Choy et al. [41] performed compression experiments on Ti6Al4V HC parts built using selective laser sintering (SLM) and confirmed a similar predominant deformation mechanism. The values of deflection resulting from the current numerical models for the HC structure under out-of-plane loads in both the x - and y -directions, separately, diminish with increasing wall thickness. This is consistent with numerous studies that have demonstrated with experimental results that the stiffness of hollow structures is improved by increasing their wall thickness [4, 14, 34, 41]. Hussein et al. [42] modelled the elastic behaviour of laser PBF steel 304L HC parts with different cell wall thicknesses (from a range of 0.2 to 0.5 mm) while retaining a fixed cell size of 3.97 mm. Obadimu and Kourousis [43] then validated the findings of Hussein et al. [42], with results that supported the correlation that exists between geometrical parameters and mechanical properties.

The numerical models implemented in the present work for HC parts that are subjected to in-plane loads generated values of stress exceeding the yield stress of Ti6Al4V, suggesting that failure by axial compression would occur ahead of buckling failure, as highlighted in numerous studies [4-5, 12, 14, 19, 26, 44]. It must be highlighted, however, that the greater part of studies currently available in the literature focuses solely on HC parts made of materials with moduli of elasticity that are lower than the value for Ti6Al4V, such as alloys of aluminium [14, 45-46, 47-50]. Therefore, experiments are clearly required to validate the exact values of deflection and stress obtained in the numerical models of the Ti6Al4V polygon shapes generated in the present work. The numerical results for linear buckling generated in the present work show that the largest stress levels occur at mid-span regions of the plates used to construct the HC shell models. This agrees with the findings in reference [51]. Furthermore, the numerically generated shapes after deflection of the HC plates correlate with those produced in references [51-52]. The numerical analyses for linear and nonlinear buckling carried out in the present work showed that the HC model's adjacent shells exhibit a restraining effect against each other, resulting in the stiffening of the structure. There appears to be a knowledge gap with regard to experimental validation of the aforementioned restraining effect, which calls for future experimentation to solve this shortfall of information. The prediction based on the numerical models for analysing the effect of wall thickness on the effective stiffness of the HC shell in this work correlates well with the results of experiments done in reference [9]. Silva et al. [53] also examined how design and manufacturing parameters affected the compressive behaviour of 3D-printed polymer lattice structures. Their results tie in with those of the present work of increasing density and thus, the mechanical properties of the hollow structures with increasing thickness of the struts.

4.7. Scope and opportunities for future work

4.7.1 Extending the simulation and modelling implemented in this study to other metallics and their various applications

Implementation of the current simulation and modelling procedure to include other alloys could prove useful for developing and optimizing hollow structures with specific applications. This method provides insights into the mechanical properties of hollow shapes and thus improves the basis for developing structures that respond effectively to specific applications. For the purpose of developing innovative and effective designs, the numerical models developed here for Ti6Al4V hollow structures could be tailored and extended to other alloys.

Tungsten alloys are used in shielding radiation applications due to their extremely high density compared to Ti6Al4V, particularly in the medical and nuclear sectors [54]. Tungsten alloy hollow structures could be built to be lightweight while maintaining good shielding. The effects of radiation on materials could be factored into numerical models, and the shielding efficacy of different hollow shapes could be evaluated. Tungsten [55] and nickel-based [56] alloys have good thermal stability and mechanical strength compared to Ti6Al4V. The high thermal conductivity of tungsten and nickel-based alloys allows them to be designed as hollow shapes for efficient heat transfer [57]. Heat conduction and thermal stress distribution within different hollow shapes, as well as their mechanical performance, could be simulated using numerical models. These hollow shapes are often used in aeronautical propulsion systems and defence applications in harsh conditions [57-58]. Additionally, the tungsten alloy's good thermal conductivity results in it being good for heat sinks in electronics [55, 57]. Building hollow structures with such material could assist with heat dissipation. The use of simulations and modelling allows for the evaluation of cooling efficiency for the different hollow shapes and optimization of their design in accordance with specific uses. Tungsten alloys are susceptible to particular corrosive conditions [55], whereas Ti6Al4V is corrosion-resistant [30]. Numerical models could mimic corrosion behaviour and predict how different hollow shapes reduce or further aggravate corrosion effects. The complete densification of tungsten alloys during AM is difficult due to its high melting point and heat conductivity [57]. The potential for porosity and partial densification could be reduced by hollow structure design since there would be less material to solidify. This is because hollow geometry can minimize porosity while improving density by reducing the gradients in temperature and assisting in uniform cooling [57]. Better control over solidification cooling rates could be achieved with hollow structures. Simulation and modelling must, therefore, be extended to examine how different tungsten alloy hollow shapes influence microstructure control regarding minimizing or increasing grain growth, resulting in increased or decreased mechanical properties, respectively.

Copper alloys are popular for their electrical conductivity, which is high compared to Ti6Al4V. Hollow shapes are useful for designing connectors, conductive pathways, and electronics cooling components [59]. Numerical models could assist in the design of different copper alloy hollow shapes to improve the transfer of heat and flow of electrical current. Furthermore, their high thermal conductivity results in copper being a better material for heat exchangers [6]. Hollow structures could further enhance the efficiency of heat transfer. Different hollow shapes could be implemented in simulation and modelling to predict their influence on the distribution of temperature and drop of pressure across a structure. Copper alloys are corrosion-resistant and have been used for decades in applications related to plumbing. Pipes, fittings, and fluid distribution systems are designed as hollow structures [60]. Better structural integrity and flow properties could be predicted by employing numerical models of different hollow shapes built using copper alloys [61]. Integrating copper hollow shapes as fins into current designs of pyramid-shaped solar stills has the prospect of improving heat transfer, evaporation, and condensation rates, ultimately leading to the production of distilled water. To maximize benefits whilst minimizing drawbacks, the design and location of such copper structures could be studied carefully. Incorporating the numerical models developed here in such a design could assist in the optimization of design and understanding of the complex relationship between the copper hollow shapes and the functionality of the solar still [6, 61].

Platinum group metal (PGM) alloys have gained popularity for their good strength-to-weight ratio, corrosion resistance, and stability at high temperatures, resulting in them being ideal for aeronautical applications. The simulation and modelling process in the present work is applicable for optimizing the design of hollow parts that can be coated or built using PGM alloys. These parts include engine parts, exhaust systems, thermal management components, structural components, and aerospace frames to improve performance while reducing weight and the use of materials [62-64]. These alloys are also biocompatible and often used for coating medical devices such as pacemakers, catheters, stents, and dental and prosthetic implants. The simulation and modelling approach described here is adaptable to generating

hollow structures coated with PGM alloys for biomedical applications while optimizing their mechanical properties and performance under physiological conditions. The strategy could enhance the longevity and biocompatibility of PGM alloy-coated implants, resulting in better patient outcomes [64]. PGM alloys are commonly adopted in the chemical processing industries due to their resistance to corrosion, reactions caused by chemicals, and high temperatures. The simulation and modelling strategies used in the current work could prove useful in the design and optimization of hollow parts coated with PGM alloys. These PGM alloy-coated hollow parts can be used in building reactors, heat exchangers, and catalytic converters. As a result, the longevity and efficiency of chemical processing equipment could be improved by accurately predicting the coated PGM alloy's mechanical properties and structural behaviour [62, 64]. These alloys are also used in a variety of energy-related applications, including fuel cells, electrolyzers, and gas turbines, due to their high electrical conductivity and catalytic characteristics. The simulation and modelling procedures used in the current work could assist with the design optimization of PGM alloy-coated hollow structures for catalyst support materials and, thus, an increase in their surface area and reactivity. Accurate prediction of mechanical properties and performance characteristics is anticipated to improve energy conversion efficiency, durability, and operational reliability of the hollow parts [65]. These alloys are additionally used in automobile components such as exhaust systems, sensors, and catalytic converters because of their corrosion resistance and ideal stability at high temperatures. The simulation and modelling strategy adopted in the present work can be used to optimize the design of hollow parts in automotive systems to reduce weight, increase performance, and control gas emissions [66]. PGM alloys tend to be used in electronic and electrical applications, such as contacts, connectors, and sensors, because of their high conductivity and resistance to oxidation. The simulation and modelling process could assist with designing hollow structures for electrical applications by optimizing mechanical strength and contact performance. Engineers can generate more reliable and effective electrical components by customizing numerical models for PGM alloys [67-68]. These precious metals are highly valued for their lustre, durability, and scarcity, which renders them ideal materials for luxury items and jewellery. The simulation and modelling procedures can also be used to improve the design of hollow structures for fleshing-out intricate jewellery designs, ornamental parts, and high-end luxury products, guaranteeing both aesthetic appeal and structural integrity [69].

By systematically comparing the mechanical behaviour of other alloy hollow shapes against Ti6Al4V hollow structures using the implemented numerical models, researchers could arrive at well-versed design decisions that account for performance, cost, and application requirements. Such an approach would, in turn, allow researchers to design hollow structures of each material for their specific applications, optimizing performance while taking material properties and the limits of their mechanical properties into account.

References

1. Case, J., and Chilver, A. H. (2013). *Strength of materials: an introduction to the analysis of stress and strain*. Elsevier.
2. Bührig-Polaczek, A., Fleck, C., Speck, T., Schüler, P., Fischer, S. F., Caliaro, M., & Thielen, M. (2016). Biomimetic cellular metals – using hierarchical structuring for energy absorption. *Bioinspiration & Biomimetics*, 11(4), 045002.
3. Helou, M., and Kara, S. (2018). Design, analysis, and manufacturing of lattice structures: an overview. *International Journal of Computer Integrated Manufacturing*, 31(3), 243-261.
4. Gibson, L. J., and Ashby, M. F. (1997). *Cellular solids: Structure and properties*, second ed. Cambridge University Press, New York.
5. Wadley, H. N., Fleck, N. A., & Evans, A. G. (2003). Fabrication and structural performance of periodic cellular metal sandwich structures. *Composites Science and Technology*, 63(16), 2331-2343.

6. Banhart, J. (2001). Manufacture, characterisation and application of cellular metals and metal foams. *Progress in Materials Science*, 46(6), 559-632.
7. Chibinyani, M. I., Dzogbewu, T. C., Maringa, M., & Muiruri, A. M. (2022). Reduced order topology optimization of a planar honeycomb defined by a linear elastic Ti6Al4V (ELI) material model. *South African Journal of Industrial Engineering*, 33(3), 299-317.
8. Yu, X., Zhou, J., Liang, H., Jiang, Z., & Wu, L. (2018). Mechanical metamaterials associated with stiffness, rigidity, and compressibility: A brief review. *Progress in Materials Science*, 94, 114-173.
9. Chen, Y., and Hu, H. (2020). In-plane elasticity of regular hexagonal honeycombs with three different joints: A comparative study. *Mechanics of Materials*, 148, 103496.
10. Du Plessis, A., Broeckhoven, C., Yadroitsava, I., Yadroitsev, I., Hands, C. H., Kunju, R., & Bhate, D. (2019). Beautiful and functional: a review of biomimetic design in additive manufacturing. *Additive Manufacturing*, 27, 408-427.
11. Benedetti, M., Du Plessis, A., Ritchie, R. O., Dallago, M., Razavi, S. M. J., & Berto, F. (2021). Architected cellular materials: A review on their mechanical properties towards fatigue-tolerant design and fabrication. *Materials Science and Engineering: R: Reports*, 144, 100606.
12. Zhang, X., Wang, Y., Ding, B., & Li, X. (2020). Design, fabrication, and mechanics of 3D micro-/nanolattices. *Small*, 16(15), 1902842.
13. Yang, L., Harrysson, O., West, H., & Cormier, D. (2015). Mechanical properties of 3D re-entrant honeycomb auxetic structures realized via additive manufacturing. *International Journal of Solids and Structures*, 69, 475-490.
14. Zhang, X., Zhang, H., & Wen, Z. (2014). Experimental and numerical studies on the crush resistance of aluminum honeycombs with various cell configurations. *International Journal of Impact Engineering*, 66, 48-59.
15. Goldmann, T., Huang, W. C., Rzepa, S., Džugan, J., Sedláček, R., & Daniel, M. (2022). Additive manufacturing of honeycomb lattice structure—From theoretical models to polymer and metal products. *Materials*, 15(5), 1838.
16. Malek, S., and Gibson, L. (2015). Effective elastic properties of periodic hexagonal honeycombs. *Mechanics of Materials*, 91, 226-240.
17. Gibson, L. J. (1981). *The Elastic and Plastic Behaviour of Cellular Materials*. University of Cambridge.
18. Gibson, L. J., Ashby, M. F., Schajer, G. S., & Robertson, C. I. (1982). The mechanics of two-dimensional cellular materials. *Proc. Roy. Soc. Lond. A* 382, 25-42.
19. Warren, W. E., and Kraynik, A. M. (1987). Foam mechanics: the linear elastic response of two-dimensional spatially periodic cellular materials. *Mechanics of Materials*, 6(1), 27-37.
20. García, D. A., and Rosales, M. B. (2017). Deflections in sawn timber beams with stochastic properties. *European Journal of Wood and Wood Products*, 75, 683-699.
21. Berger, J. B., Wadley, H. N. G., & McMeeking, R. M. (2017). Mechanical metamaterials at the theoretical limit of isotropic elastic stiffness. *Nature*, 543(7646), 533-537.
22. Vrolijk, P. J., Urai, J. L., & Kettermann, M. (2016). Clay smear: Review of mechanisms and applications. *Journal of Structural Geology*, 86, 95-152.
23. Catapano, A., and Montemurro, M. (2014). A multi-scale approach for the optimum design of sandwich plates with honeycomb core. Part I: homogenisation of core properties. *Composite Structures*, 118, 664-676.
24. Akoglu, H. (2018). User's guide to correlation coefficients. *Turkish Journal Of Emergency Medicine*, 18(3), 91-93.

25. Asuero, A. G., Sayago, A., & González, A. G. (2006). The correlation coefficient: An overview. *Critical reviews in analytical chemistry*, 36(1), 41-59.
26. Jiménez, F. L., and Triantafyllidis, N. (2013). Buckling of rectangular and hexagonal honeycomb under combined axial compression and transverse shear. *International Journal of Solids and Structures*, 50(24), 3934-3946.
27. Novoselac, S., Ergić, T., & Baličević, P. (2012). Linear and nonlinear buckling and post buckling analysis of a bar with the influence of imperfections. *Tehnički Vjesnik*, 19(3), 695-701.
28. Lee, W. S., and Lin, M. T. (1997). The effects of strain rate and temperature on the compressive deformation behaviour of Ti-6Al-4V alloy. *Journal of Material Processing and Technology*, 71(2), 235-246.
29. Dos Reis, F., and Ganghoffer, J. F. (2012). Equivalent mechanical properties of auxetic lattices from discrete homogenization. *Computational Materials Science*, 51(1), 314-321.
30. Djavanroodi, F., and Derogar, A. (2010). Experimental and numerical evaluation of forming limit diagram for Ti6Al4V titanium and Al6061-T6 aluminum alloys sheets. *Materials & Design*, 31(10), 4866-4875.
31. Riva, L., Ginestra, P. S., & Ceretti, E. (2021). Mechanical characterization and properties of laser-based powder bed-fused lattice structures: a review. *The International Journal of Advanced Manufacturing Technology*, 113, 649-671.
32. Xiao, L., Feng, G., Li, S., Mu, K., Qin, Q., & Song, W. (2022). Mechanical characterization of additively manufactured metallic lattice structures with hollow struts under static and dynamic loadings. *International Journal of Impact Engineering*, 169, 104333.
33. Yan, L., Chen, Y., & Liou, F. (2020). Additive manufacturing of functionally graded metallic materials using laser metal deposition. *Additive Manufacturing*, 31, 100901.
34. Antolak-Dudka, A., Płatek, P., Durejko, T., Baranowski, P., Małachowski, J., Sarzyński, M., & Czujko, T. (2019). Static and dynamic loading behavior of Ti6Al4V honeycomb structures manufactured by Laser Engineered Net Shaping (LENSTM) technology. *Materials*, 12(8), 1225.
35. Pan, C., Han, Y., and Lu, J. (2020). Design and optimization of lattice structures: A review. *Applied Sciences*, 10(18), 6374.
36. Zok, F. W., Latture, R. M., & Begley, M. R. (2016). Periodic truss structures. *Journal of the Mechanics and Physics of Solids*, 96, 184-203.
37. Gonella, S., and Ruzzene, M. (2008). Homogenization and equivalent in-plane properties of two-dimensional periodic lattices. *International Journal of Solids and Structures*, 45(10), 2897-2915.
38. Noronha, J., Rogers, J., Leary, M., Kyriakou, E., Inverarity, S. B., Das, R., ... & Qian, M. (2023). Ti-6Al-4V hollow-strut lattice materials by laser powder bed fusion. *Additive Manufacturing*, 72, 103637.
39. Da, D., Yvonnet, J., Xia, L., Le, M. V., & Li, G. (2018). Topology optimization of periodic lattice structures taking into account strain gradient. *Computers & Structures*, 210, 28-40.
40. Szymczyk, P., Hoppe, V., Ziólkowski, G., Smolnicki, M., & Madeja, M. (2020). The effect of geometry on mechanical properties of Ti6Al4V ELI scaffolds manufactured using additive manufacturing technology. *Archives of Civil and Mechanical Engineering*, 20(1), 1-13.
41. Choy, S. Y., Sun, C. N., Leong, K. F., & Wei, J. (2017). Compressive properties of Ti-6Al-4V lattice structures fabricated by selective laser melting: Design, orientation, and density. *Additive Manufacturing*, 16, 213-224.

42. Hussein, R., Anandan, S., Spratt, M., Newkirk, J. W., Chandrashekhara, K., Heath, M., & Walker, M. (2020). Effective elastic moduli of metal honeycombs manufactured using selective laser melting. *Rapid Prototyping Journal*, 26(5), 971-980.
43. Obadimu, S. O., and Kourousis, K. I. (2022). Load-rate effects on the in-plane compressive behaviour of additively manufactured steel 316L honeycomb structures. *Engineering Structures*, 273, 115063.
44. Ghatage, P. S., Kar, V. R., & Sudhagar, P. E. (2020). On the numerical modelling and analysis of multi-directional functionally graded composite structures: A review. *Composite Structures*, 236, 111837.
45. Kędzierski, P., Gieleta, R., Morka, A., Niezgoda, T., & Surma, Z. (2016). Experimental study of hybrid soft ballistic structures. *Composite Structures*, 153, 204-211.
46. He, W., Yao, L., Meng, X., Sun, G., Xie, D., & Liu, J. (2019). Effect of structural parameters on low-velocity impact behavior of aluminum honeycomb sandwich structures with CFRP face sheets. *Thin-Walled Structures*, 137, 411-432.
47. Aktay, L., Johnson, A. F., & Kröplin, B. H. (2008). Numerical modelling of honeycomb core crush behaviour. *Engineering Fracture Mechanics*, 75(9), 2616-2630.
48. Chawla, A., Mukherjee, S., Kumar, D., Nakatani, T., & Ueno, M. (2003). Prediction of crushing behaviour of honeycomb structures. *International Journal of Crashworthiness*, 8(3), 229-235.
49. Stanczak, M., Frasz, T., Blanc, L., Pawlowski, P., & Rusinek, A. (2019). Numerical modelling of honeycomb structure subjected to blast loading. *Proceedings of the 12th European LS-DYNA Conf, Koblenz, Germany*, 14-16.
50. Wang, Z., and Liu, J. (2019). Numerical and theoretical analysis of honeycomb structure filled with circular aluminum tubes subjected to axial compression. *Composites Part B: Engineering*, 165, 626-635.
51. Jiménez, F. L., and Triantafyllidis, N. (2013). Buckling of rectangular and hexagonal honeycomb under combined axial compression and transverse shear. *International Journal of Solids and Structures*, 50(24), 3934-3946.
52. Qiu, C., Guan, Z., Guo, X., & Li, Z. (2020). Buckling of honeycomb structures under out-of-plane loads. *Journal of Sandwich Structures & Materials*, 22(3), 797-821.
53. Guerra Silva, R., Salinas Estay, C., Morales Pavez, G., Zahr Viñuela, J., & Torres, M. J. (2021). Influence of geometric and manufacturing parameters on the compressive behavior of 3D printed polymer lattice structures. *Materials*, 14(6), 1462.
54. Liu, Y., Liu, X., Lai, C., Ma, J., Meng, X., Zhang, L., & Chen, S. (2023). Boriding of tungsten by the powder-pack process: Phase formation, growth kinetics and enhanced neutron shielding. *International Journal of Refractory Metals and Hard Materials*, 110, 106049.
55. Pan, S. H., Yao, G. C., Cui, Y. N., Meng, F. S., Luo, C., Zheng, T. Q., & Singh, G. (2023). Additive manufacturing of tungsten, tungsten-based alloys, and tungsten matrix composites. *Tungsten*, 5(1), 1-31.
56. Mostafaei, A., Ghiaasiaan, R., Ho, I. T., Strayer, S., Chang, K. C., Shamsaei, N., ... & To, A. C. (2023). Additive manufacturing of nickel-based superalloys: a state-of-the-art review on process-structure-defect-property relationship. *Progress in Materials Science*, 101108.
57. Yap, C. Y., Chua, C. K., Dong, Z. L., Liu, Z. H., Zhang, D. Q., Loh, L. E., & Sing, S. L. (2015). Review of selective laser melting: Materials and applications. *Applied Physics Reviews*, 2(4).

58. Careri, F., Khan, R. H., Todd, C., & Attallah, M. M. (2023). Additive manufacturing of heat exchangers in aerospace applications: A review. *Applied Thermal Engineering*, 121387.
59. Singer, F., Deisenroth, D. C., Hymas, D. M., & Ohadi, M. M. (2017). Additively manufactured copper components and composite structures for thermal management applications. *16th IEEE Intersociety Conference on Thermal and Thermomechanical Phenomena in Electronic Systems (ITherm)*, 174-183. IEEE.
60. Zhao, Z., Liu, C., Sun, L., Luo, H., Wang, J., & Li, Y. (2021). Experimental and numerical study on the constrained bending-induced collapse of hexagonal honeycomb. *Composite Structures*, 277, 114604.
61. Asadabadi, M. J. R., and Sheikholeslami, M. (2022). Impact of utilizing hollow copper circular fins and glass wool insulation on the performance enhancement of pyramid solar still unit: An experimental approach. *Solar Energy*, 241, 564-575.
62. Boyer, R. R., Cotton, J. D., Mohaghegh, M., & Schafrik, R. E. (2015). Materials considerations for aerospace applications. *Mrs Bulletin* 40(12), 1055-1066.
63. Gialanella, S., and Malandrucolo, A. (2020). *Aerospace alloys*. Cham, Switzerland: Springer. 129-189.
64. Liu, P., and Chen, G. F. (2014). *Porous materials: processing and applications*. Elsevier.
65. Cyril, P. H., and Saravanan, G. (2020). Development of advanced materials for cleaner energy generation through fuel cells. *New Journal of Chemistry*, 44(46), 19977-19995.
66. Hughes, A. E., and Haquem, N. (2021). Northey SA, Giddey S. Platinum group metals: A review of resources, production, and usage with a focus on catalysts. *Resources*. 10(9), 93.
67. Pradhan, D. K., Moore, D. C., Francis, A. M., Kupernik, J., Kennedy, W. J., Glavin, N. R., Olsson, R. H., Jariwala, D. (2024). Materials for high temperature digital electronics. arXiv preprint arXiv:2404.03510.
68. Nitin, S. P., Swarupa, M. L., & Harivardhagini, S. (2023). A review on light-weight materials for electric vehicles. *Second International Conference on Smart Technologies for Smart Nation (SmartTechCon)*. IEEE. 735-743.
69. Sun Y. (2023). Exploring technological application for artistic practices in filigree jewellery design development (Doctoral dissertation, Loughborough University).

CHAPTER FIVE: NUMERICAL MODELLING OF FIRST-ORDER HIERARCHICAL STRUCTURES UNDER QUASI-STATIC LOADING

Part of the contents of this chapter has been submitted for publication or has been published in peer-reviewed journals, as follows:

1. **Chibinyani, M. I., Dzogbewu, T. C., Maringa, M., & Muiruri, A. M. (2024).** Numerical modelling of Ti6Al4V (ELI) hierarchical honeycomb structures of order one at the vertices. *Results in Engineering*, 21, 102024. doi.org/10.1016/j.rineng.2024.102024

5.1. Summary

This chapter presents results on the numerical modelling of hierarchical honeycomb (HC) structures with hexagonal, circular, and triangular polygons at the vertices. It examines the effects of geometry on stress levels, stress concentration, and deflection, followed by a comparison with experimental data from the literature. The chapter also outlines future research opportunities for the study.

5.2. Numerical findings of stress levels and stress concentration

Figures 5-1 and 5-2 show von Mises stress contours generated by applying a 3000 N load to the HCR model, as well as HCH, HCC, and HCT models. These contour plots show the stress levels and contour maps of stress distribution obtained for loading in the x - and y -directions separately. Figures 5-1 and 5-2 show that the hierarchical HC models subjected to loading in the x -direction had the lowest values of maximum von Mises stress. This is because the loading along the x -direction was applied along the lengths of three members (larger contact areas), while along the y -direction, it was applied at five apex points (smaller contact areas).

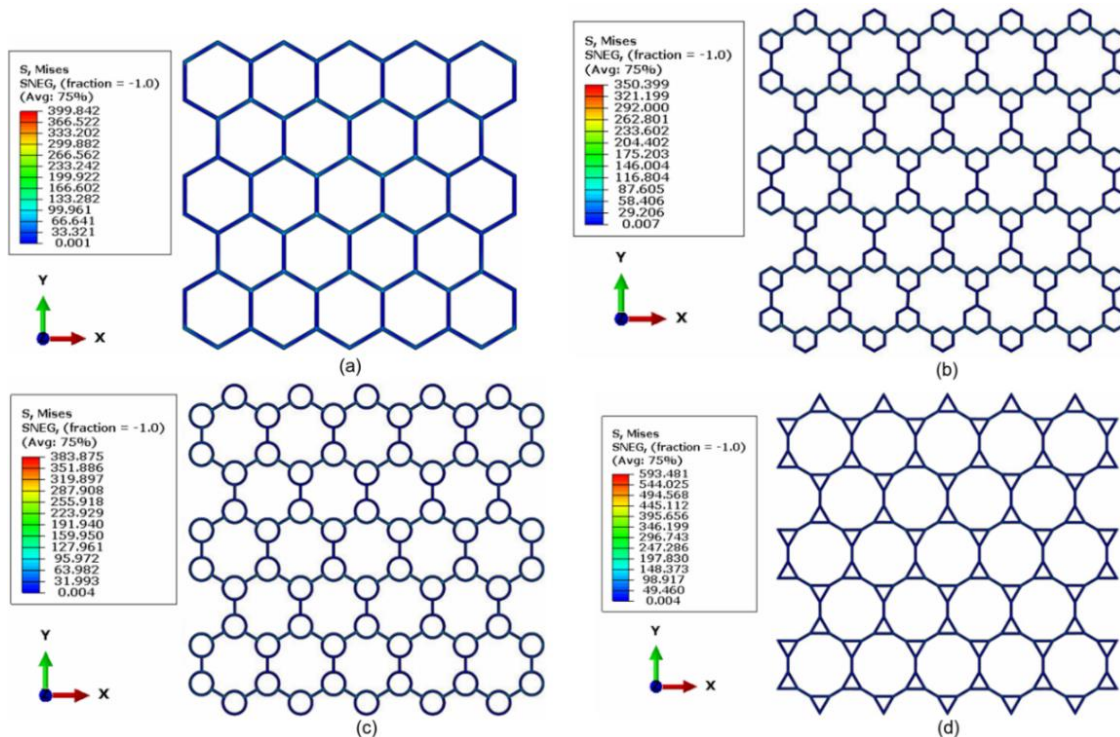


Figure 5-1. The von Mises stress distribution for (a) HCR structure and (b), (c) and (d) HCH, HCC, and HCT structures, respectively, for the case of a load applied in the x -direction

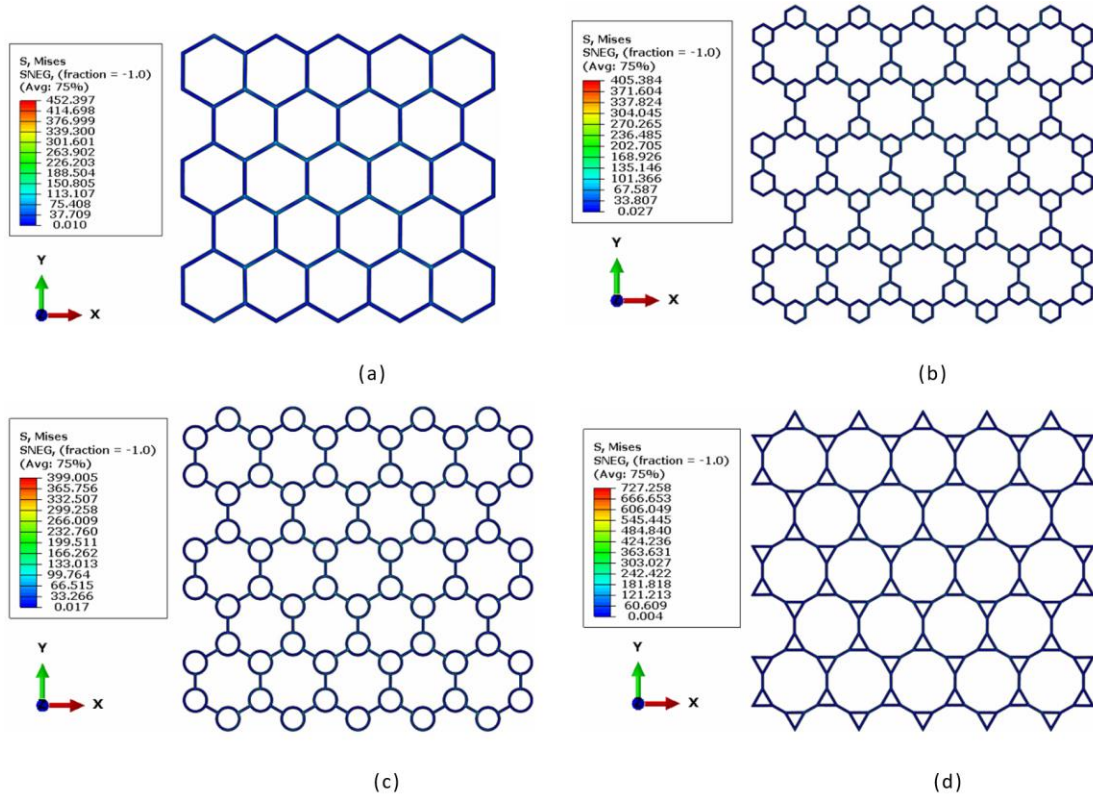


Figure 5-2. The von Mises stress distribution for (a) HCR structure and (b), (c) and (d) HCH, HCC, and HCT structures, respectively, for the case of a load applied in the y-direction

It is garnered from the stress contour keys in Figure 5-1 that when a load is applied in the x-direction, the HCH model has the lowest value of maximum von Mises stress (approximately 12.37% lesser than the value obtained for the HCR model). The HCC model records the second lowest value of maximum von Mises stress (about a 3.99% decrease from that of the HCR model), whereas the HCT model is ranked last. The HCT structure recorded the highest value of maximum von Mises stress because, compared to the other two geometries, it was loaded directly at the apex regions. These are regions with sharply changing geometries. The apex regions are highly stressed regions that are liable to fail even at low applied loads. Instead of the maximum von Mises stress level decreasing for the HCT model, as observed for the other two models, they increased by 48.43% with reference to the HCR model.

Figure 5-2 shows that with the load applied in the y-direction, the HCC model attained the lowest value of maximum von Mises stress (approximately 11.8% lower than the value obtained for the HCR model). For the same loading direction, the HCH model now ranked second in terms of the generated value of maximum von Mises stress (a decrease of about 10.39% with reference to the HCR model). With reference to the value of maximum von Mises stress obtained for the HCR model subjected to y-directional loading, the HCT model showed an increase of 60.76%. The application of von Mises stress to lattice structures provides for an easier and more straightforward assessment of yielding, particularly when dealing with complex stresses arising from the use of intricate geometries. In the present investigations, the analysis was conducted with the aim of ensuring all induced stresses

were solely elastic. Thus, analysis using von Mises stress was useful in easily identifying the loads beyond which the material was expected to yield.

According to the work discussed in the foregoing three paragraphs, the HCH model had the lowest value of maximum von Mises stress when loaded in the x -direction and the second lowest value of maximum von Mises stress when loaded in the y -direction. The percentage changes for the maximum von Mises stress of the HCH model loaded in all directions separately were greater compared to the differences for the HCC model. In comparison with the HCR model, the two models alternated in ranking. For loading in all directions separately, the HCT model ranked last. Clearly, the HCH model was the best alternative of the three hierarchical structures modelled here.

Apart from the contour keys in the preceding two figures, it is not possible to distinguish any distribution of stress in their walls from them. Therefore, sections were extracted and enlarged to study the stress distribution along the very thin-walled cell configurations of the HC structures. It is evident from Figures 5-3 to 5-6 that enlarging the unit cells gives clear details of von Mises stresses in the numerical models. These figures show the presence of von Mises stress concentrations at the vertices.

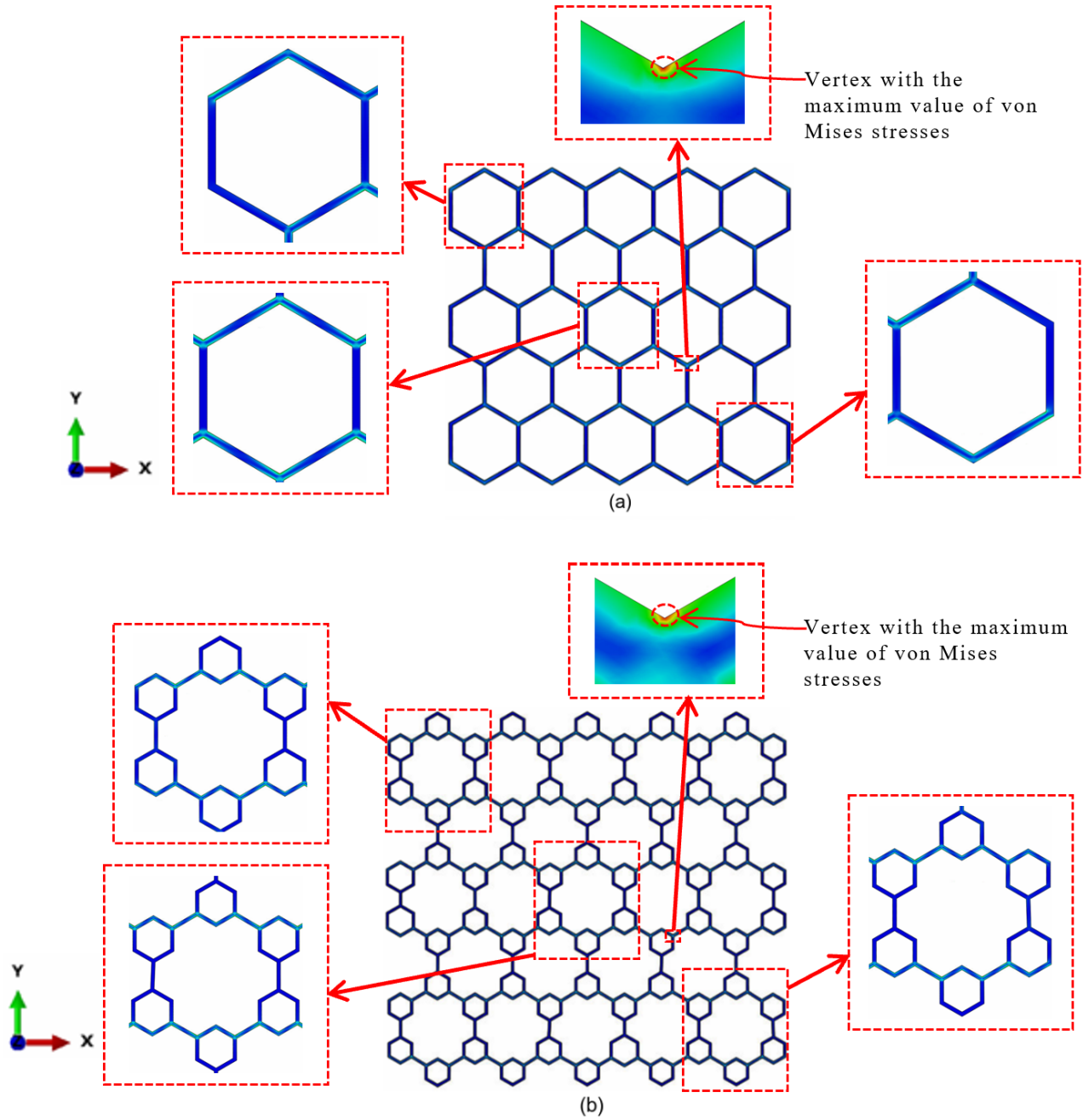


Figure 5-3. Stress distribution in (a) HCR model, and (b) HCH model, when loaded in the x-direction

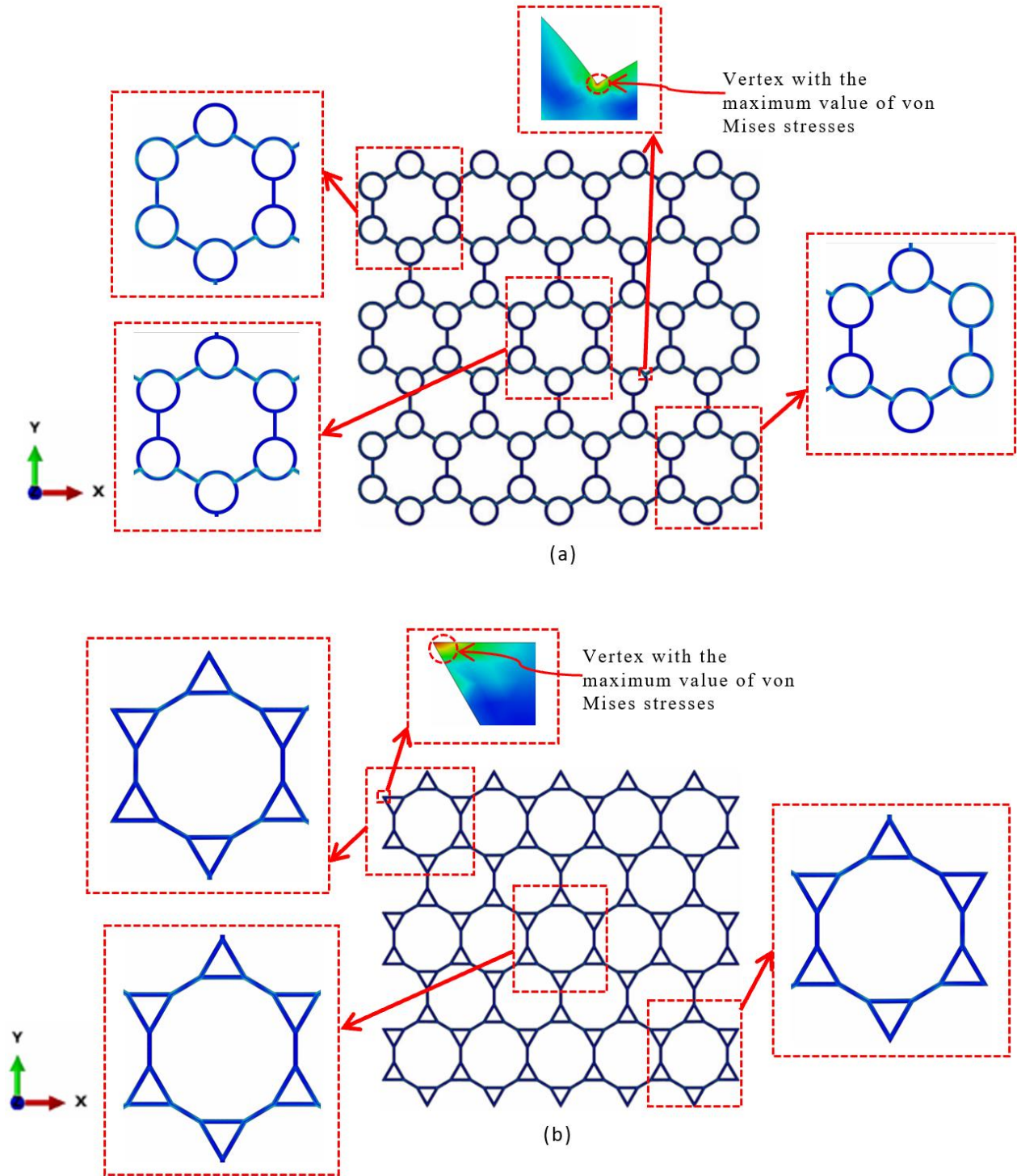


Figure 5-4. Stress distribution in (a) HCC model and (b) HCT model, when loaded in the x-direction

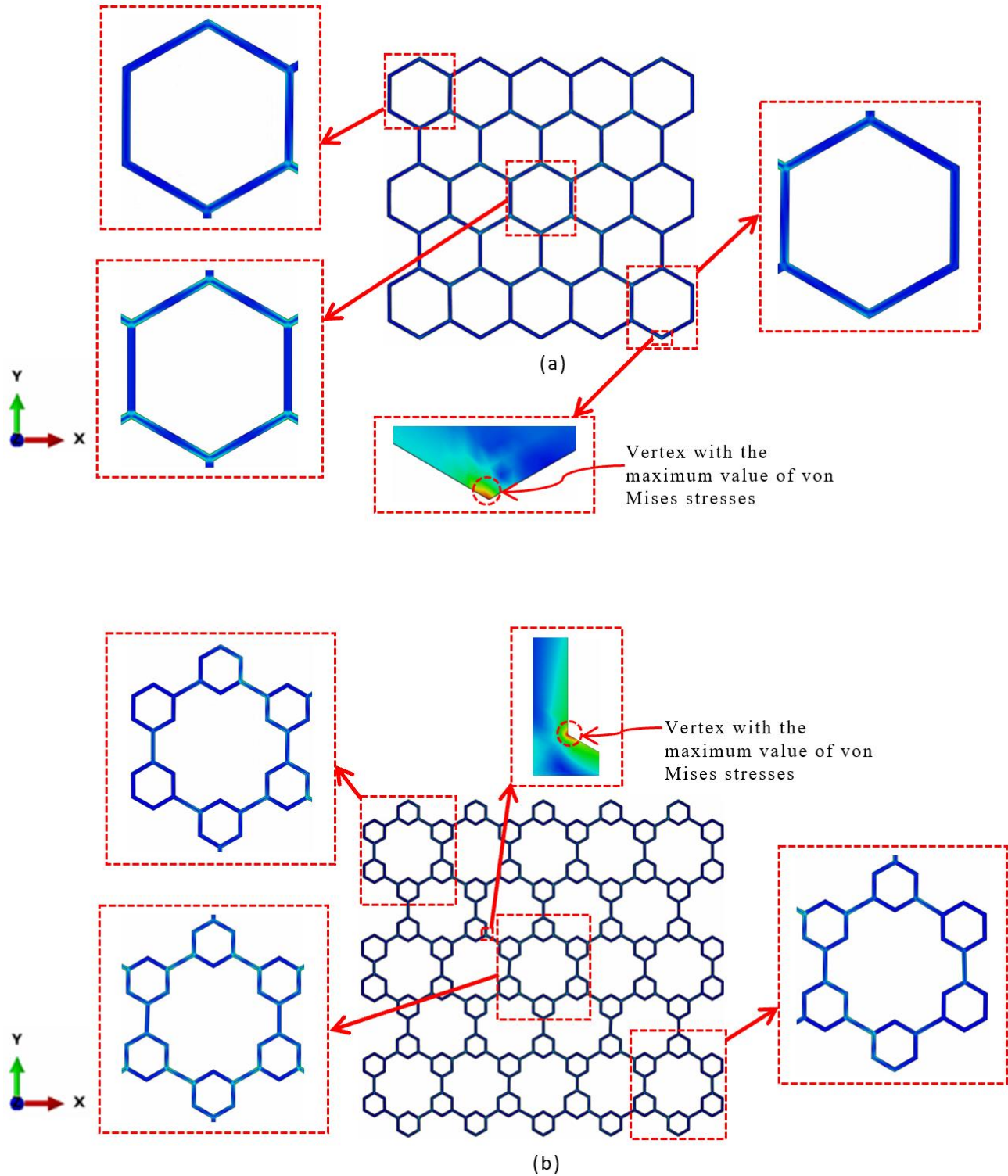


Figure 5-5. Stress distribution in (a) HCR model and (b) HCH model, when loaded in the y-direction

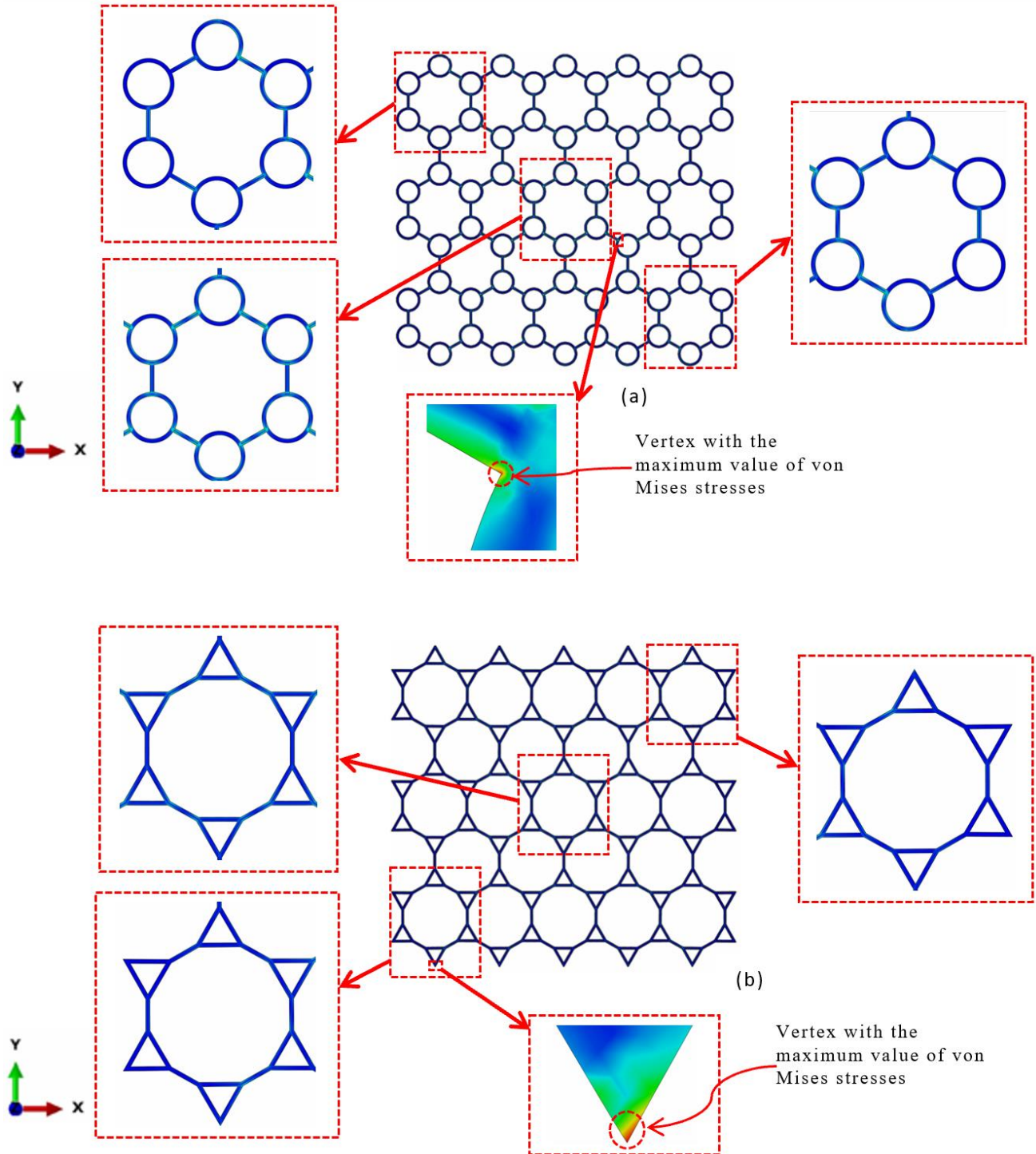


Figure 5-6. Stress distribution in (a) HCC model and (b) HCT model, when loaded in the y -direction

It is evident from Figures 5-3 to 5-6 that the structure with the sharpest geometries at the vertices in contact with the rigid plates used to apply loads on the structures had the greatest value of maximum von Mises stress. Since the loading plates were rigid, the induced stresses were much more likely to be concentrated directly at the corners of structures with sharp angles at which contact with the plates was made. This is observed

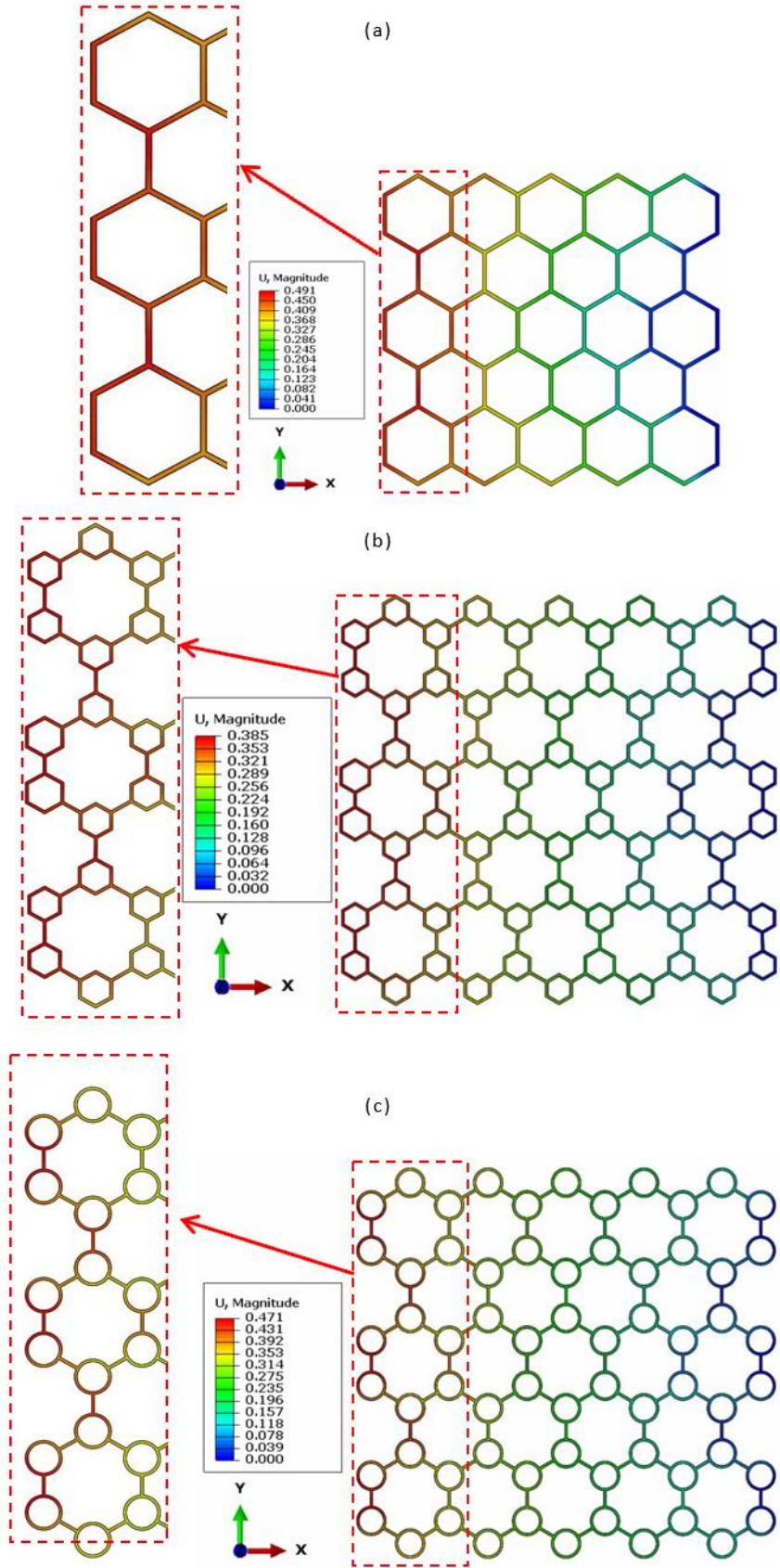
for the HCT model loaded in the x - and y -directions separately, as well as the HCR model loaded in the y -direction. However, as shown in Figures 5-3 to 5-6, the other hierarchical structures experienced maximum values of von Mises stresses at other sharp corners that were not in direct contact with the rigid surfaces. This is likely due to the restraining effect of the cell edges, which becomes greater as one moves closer to the centre of each structure. Work done in [104-106] supports this observation. The HCT model has the sharpest corners (with acute angles of 60 degrees) in contact with the rigid plates on both ends for loading in either one of the two directions. This implies that it is the most stressed and, as a result, is unlikely to withstand the same magnitude of loads as the other hierarchical structures, when loaded along either one of the two planar directions. Therefore, for improved mechanical performance, reducing sharp changes in geometry at vertices in contact with rigid bodies should be prioritized in the design of such engineering structures.

The magnitude of stresses at the vertices of loaded HCR, HCH, HCC, and HCT models are seen from the foregoing discussion to be a function of their geometric configuration. The vertices have been shown to be highly stressed and are prone to failure under lower applied loads in consistency with the observations made in reference [104]. As is known for stress concentration, the sharper the changes of geometry at the structure's vertices, the higher the concentration of stresses in such areas [107], and thus the higher the limitation of such structures to withstand high loads.

From the foregoing discussion, it is deduced that the HCH model attained the lowest maximum von Mises stress when load was applied in the x -direction. This is because the loading plates were resting along the structure's members, distributing the applied load over a larger area compared to other forms of hierarchical HCs modelled. Thus, this type of hierarchical HC structure is expected to withstand the highest loads of all other structures considered here. The HCC model had the lowest maximum von Mises stress for loads applied in the y -direction. This is because it was the only model amongst those studied here that had no sharp change of geometry at regions in contact with loading plates with respect to the y -direction load. Therefore, for loading in the y -direction, this structure is expected to withstand the highest loads among the structures studied here.

5.3. Numerical results of deflection

Figures 5-7 and 5-8 show the deflections of numerically modelled HCR, and HCH, HCC, and HCT structures. When these structures were subjected to load in the x -direction, as shown in Figure 5-7, the HCH model exhibited the lowest value of deflection. Under y -direction loading, as shown in Figure 5-8, the HCC model achieved the lowest value of deflection.



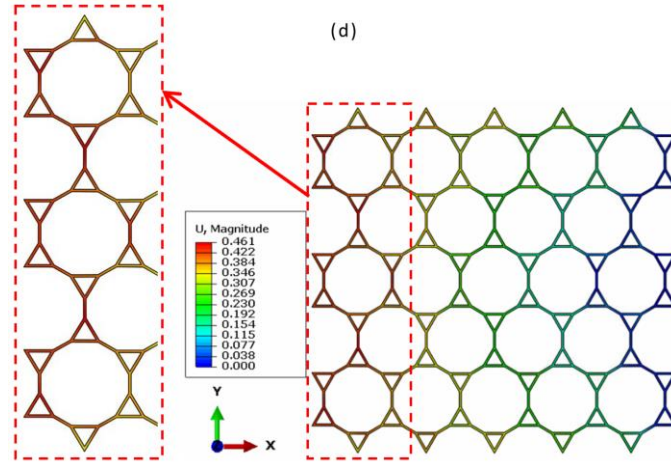


Figure 5-7. Numerical results of deflection of the (a) HCR model, (b), (c) and (d) HCH, HCC and HCT models, respectively, when loaded in the x-direction

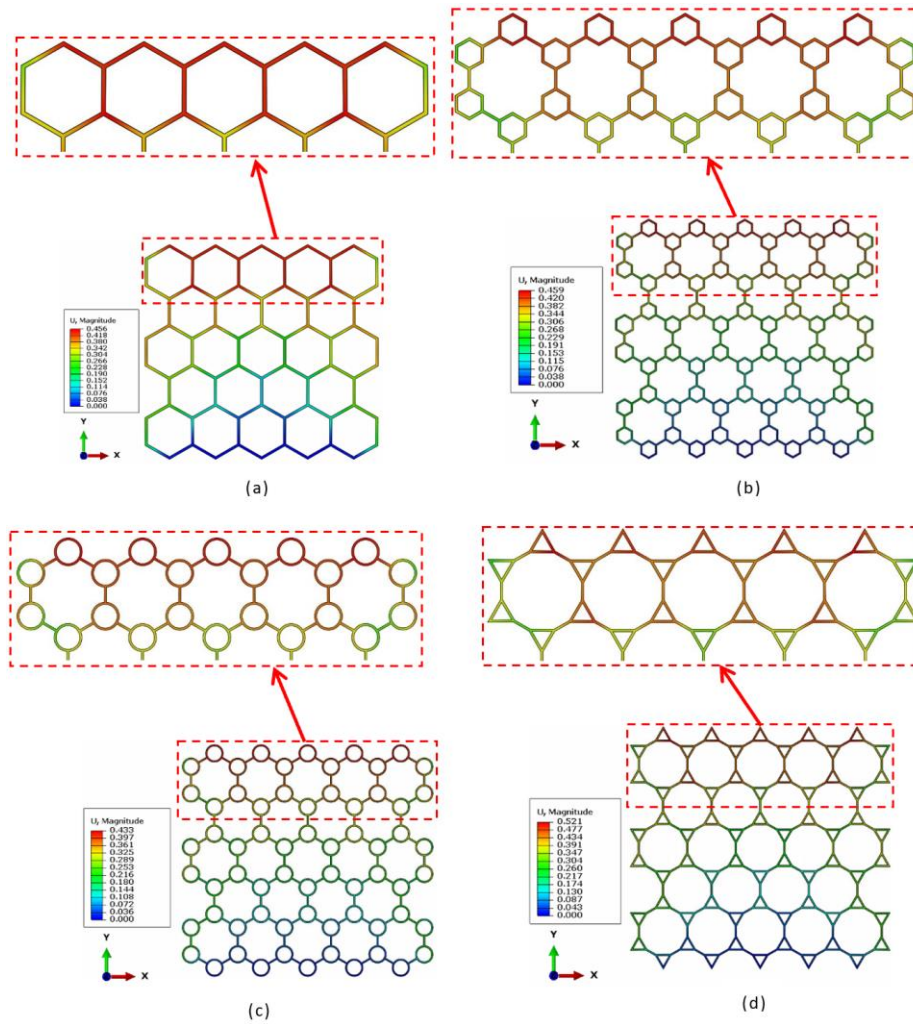


Figure 5-8. Numerical results of deflection of the (a) HCR model, (b), (c) and (d) HCH, HCC, and HCT models, respectively, when loaded in the y-direction

It is seen in Figure 5-7 that for a load applied in the x -direction, the maximum value of deflection in each of the hierarchical HC models is lower than the maximum value of deflection for the HCR model. The HCH, HCT, and HCC models attained 21.59%, 6.11%, and 4.07% reduction of their maximum deflections, respectively, with reference to the maximum deflection of the HCR model. For the case where the load was applied in the y -direction, as shown in Figure 5-8, the HCC model recorded a lower magnitude of maximum deflection than the HCR model by about 5.05%. The HCH and HCC models, on the other hand, recorded an increase in the magnitude of maximum deflection over that of the HCR model by 0.68% and 14.25%, respectively.

The stiffness of a structure is significant in engineering applications as stiffness is inversely related to deflection [85]. According to the results obtained in this study, the HCH model is the stiffest structure under load applied in the x -direction. The HCC model has been shown here to be stiffer in compression for the load applied along the y -direction.

5.4. Comparison of experimental studies in literature and modelling implemented here

Comparative analysis of the numerical models implemented here, as well as experimental results reported in the literature with regard to the behaviour of hierarchical hollow structures, could provide valuable insights into the scientific accuracy and consistency of adopting predictive methods to investigate the behaviour of complex structures.

The numerical models in the current work show that loading hierarchical HC structures in the direction of load transfer with larger areas of contact yields lower values of maximum von Mises stresses than loading in the direction of load transfer at smaller areas of contact, such as the apexes where the vertices converge. Lower values of maximum von Mises stresses suggest that the structure has a higher load-bearing capacity compared to structures with higher values of maximum von Mises stress [106-108]. The authors were, however, not able to validate, with experimental results, the phenomenon mentioned in the sentence before the previous one, as the available literature on hierarchical HC structures of various polygon shapes at the vertices [35, 71-73, 86, 97-100, 109] concentrates only on loads applied transversely to the structural members of these structures. It is observed that all these studies have omitted the outermost sharp vertices formed in the basic designs of the structures in an attempt to generate members that are configured transversely to the loads, as opposed to the regular sharp inclined or arc-shaped members that were adopted in the present work for the HCT and HCC models, respectively. The observation that loading hierarchical hollow structures in the direction of load transfer with larger contact areas results in lower maximum von Mises stresses is consistent with fundamental structural mechanics concepts discussed in [106, 110-111]. The analysis presented in these references highlighted the need to evaluate direction load transfer and optimize contact regions to improve structural performance. The relationship between lower levels of stress and higher load-bearing capacity is crucial for designing lattice structures with optimal strength. Validation of the numerical results with experimental findings is a shortcoming in existing literature. As mentioned earlier in the paragraph, numerous studies [35, 86, 97-100] focusing on loads applied transversely to lattice parts while ignoring the outermost sharp vertices leads to shortcomings in the experimental methodologies used for validation. This underscores the importance of conducting more extensive experimental studies that consider numerous types of loading conditions and geometric configurations to confirm numerical results. The difference between the approach used in the current study (using regular sharp inclined or arc-shaped members) and prior research [35, 86, 97-100, 106, 110-

111] (configuring members transversely oriented to the applied loads) highlights the need to take geometric complexities into account when conducting experimental tests. Numerous studies [93, 96-97, 112-116] have highlighted the fact that the choice and configuration of the structural parts have significant effects on mechanical properties, as was found in the present work. This finding necessitates an overhaul of experimental approaches in lattice structure research to ensure that they capture the intricacies of general engineering applications accurately. Numerical models provide useful insights; however, the absence of accurate experimental confirmatory tests raises concerns with regard to the applicability of the numerical results in general engineering conditions. Engineers and researchers in the field of lattice structures ought to be cautious when using numerical findings alone in general engineering applications without experimental validation. This is particularly important when working with complicated hollow parts and loading conditions. This identified gap in experimental literature, together with the recognition of limitations in prior studies [35, 86, 93, 96-100, 112-124], implies a need for a shift in how experimental investigations are carried out in the field of hierarchical hollow structures. The requirement to replicate the outermost sharp vertices and configurations that correspond to general engineering loading conditions must be met. This is expected to have broad implications for future experimental methods in studies of lattice structures. The relationship observed between lower maximum von Mises stresses and increased load-bearing capacity in the present work suggests the need for contemporary design concepts for lattice structures. Engineers and researchers need to investigate configurations that optimize the direction of load transfer and contact areas in order to improve the structural performance of lattice structures. The foregoing is expected to contribute to the growth of design methods for lattice structures.

Experimental results obtained in literature [77, 86-87] concur with the numerical models implemented in the current work for hierarchical HC structures, that vertices are areas that experience high stresses for complex hollow structures. Alqassim [86] investigated static and dynamic compression-loaded hierarchical HC parts with hexagonal hollow shapes at the vertices. Their research findings suggested that under compression loads, the vertices or nodes tend to fail first. This behaviour of complex hollow shapes has been observed in numerous studies [34-35, 71-79, 85-108] to be purely a function of geometry. The correspondence between the experimental results from Alqassim [107], as well as other literature [93, 96-97, 111-116] and the numerical results obtained in the current research, is consistent with the expectation that vertices are prone to high stresses. This consistency gives credibility to the findings of the present work and improves the understanding of the behaviour of hierarchical hollow structures under compression loads. In addition, the observation made in the present work that the behaviour of complicated hollow structures, particularly the capacity for vertices to fail under compression, is purely a function of geometry and stresses the significance of geometric considerations in the lattice structural design. This finding is consistent with a broader trend in structural engineering [23, 63, 100, 106, 110-111], which highlights the importance of geometric features when determining structural responses. Researchers and engineers working on lattice structures should be aware of the geometric complexities that influence stress distribution and failure mechanisms. The observed sensitivity of vertices to high stresses and failure under compression loads in the present work has direct design implications for lattice structures [106-108]. Engineers, as well as designers, should think about vertex reinforcement strategies or alternative configurations to reduce stress concentrations in these key areas. The foregoing findings offer useful information for optimizing lattice structure designs

to improve total structural performance and durability. Understanding how vertices fail under specific loading conditions is critical for risk assessment and safety considerations in general engineering structures as well. This influences decisions about load-carrying capacities, maintenance routines, and safety factors when using lattice structures in multiple kinds of engineering applications, ranging from architecture to aerospace. The recurrent result on the behaviour observed at the vertices of these hollow structures for numerous studies [63, 101, 106, 111] indicates that more research into the mechanics of vertices in complicated hollow structures is required. Future research ought to investigate more geometric configurations, loading conditions, and materials to acquire a better understanding of the behaviour of lattices around vertices. This could, in turn, lead to novel design concepts and methods of structural optimization.

According to the numerical models generated in the present work, it has been shown that numerically modelled HCH and HCC structures alternate in ranking first with regard to the lowest values of maximum von Mises stress obtained for the two planar loading directions when compared with the HCR structure, respectively. The highest load-bearing capacity in the x -direction was observed for the HCH model and in the y -direction for the HCC model. The HCH model, therefore, has the highest load-bearing capacity in the x -direction, whereas the HCC model has the highest load-bearing capacity in the y -direction of the three hierarchical HC structures modelled here. This is a key finding, as the literature does not give a ranking of such hierarchical structures with various polygon shapes at the vertices with regard to stress levels. Rather, most research [71-79, 88-98] has concentrated on their energy absorption behaviour. The fact that HCH and HCC structures alternatively score first in different loading directions shows a potential for structural optimization based on specific loading conditions. Engineers may be able to tailor lattice structures with HCH configurations for improved performance in one loading direction whilst using HCC configurations in another. The research presented here adds to our understanding of how lattice designs can be tailored to improve performance in a variety of real-world applications. The alternating ranking of HCH and HCC structures highlights the relevance of directional strength in lattice structures. Different arrangements could be particularly good at resisting forces applied along different axes. This understanding is especially important for applications where load directionality is vital, such as architectural design, aerospace engineering, or any field in which lattice structures are used for load-bearing [63, 84, 98, 107]. The numerical modelling results of the present work produce a fresh feature in the literature of ranking HCH and HCC structures based on maximum von Mises stresses. While previous work largely studied the energy absorption behaviour of hierarchical hollow structures [19, 34-35, 98-100, 111-124], this result presents a different approach in which lattice structures are graded in terms of stress levels. This understanding can be used to direct future studies into lattice structures and fine-tune design concepts. The generation of hybrid structures that integrate the advantages of both HCH and HCC designs results in improved performance for different loading conditions. This approach is consistent with the tendency in engineering to tailor designs to specific functional requirements [63, 84]. The results obtained here thus offer the potential for collaboration with material scientists to investigate how material properties could potentially be optimized for specific lattice configurations. Additionally, an interdisciplinary approach could open the path for advances in materials designed particularly for lattice structures [63, 84, 116].

The numerical models implemented in the present work showed an identical ranking based on corresponding values of deflection, as was observed for the maximum von Mises stresses. The results obtained suggest that the HCH structure is stiffest in the x -direction,

while the HCC structure is stiffest in the y -direction. This is also an important finding, given the absence of literature on the ranking of hierarchical HC structures with various polygon hollow shapes at the vertices with respect to deflection. Experimental validation of this ranking forms part of future planned research work. This research sheds light on the stiffness characteristics of hierarchical hollow structures with different polygon hollow shapes at the vertices. Stiffness and this research contribute to our current understanding of directional stiffness in lattice structures [98, 105], noting that stiffness is an important aspect in determining how structures respond to applied loads. The absence of previous literature on the ranking of hierarchical hollow structures in terms of deflection highlights the originality of this study. While numerous investigations in the field of lattice structures have focused on energy absorption [35, 98-100] or strength [93, 96-97, 111-116], this finding broadens our understanding to include the stiffness of lattice hollow structures. The stiffness rankings for HCH and HCC structures in different directions provide information for engineers and designers looking to optimize lattice structures for specific applications that are stiffness-dependent. Thus, depending on the directional loading assumptions in a particular case, designers may tailor their designs to attain the best stiffness. This has ramifications for industries requiring high directional stiffness, such as aerospace [63, 84, 107] and robotics [63, 84]. Future research is planned to undertake experimental validation of the stiffness ranking determined here. Experimental validation is crucial for assuring the reliability and application of the determined values of stiffness and ranking. Therefore, future research to these ends could assist in developing and improving present design methodologies as well.

5.5. Scope and opportunities for future work

5.5.1 Extending the application of the modelling implemented in this study to design for additive manufacturing

Incorporating the numerical modelling implemented in the present work into the AM design process is promising and challenging strategy for optimizing and improving both the design and manufacturing of complicated structures such as hierarchical hollow structures. Numerous key future prospective advantages that must be considered in design for additive manufacturing (DfAM) are as follows:

Numerical modelling allows for tailoring of the design parameters of a structure and/or its manufacturing process. Considering this, the numerical models in the current work could be extended to tailoring their design parameters related to structural integrity, material usage, and manufacturing speed by modelling the behaviour of these structures based on the design limitations in AM technology. Typically, design limitations in AM technology include the maximum size of support structures and the minimum thickness that can be printed for these intricate hollow designs. Additionally, by predicting the behaviour of the numerical models implemented here prior, one could succeed in identifying the most relevant potential challenges or defects in a structural design without the need for manufacturing physical prototypes or parts. Extending the numerical modelling implemented here to the preceding proposed approach reduces prototyping expenses while shortening the manufacturing period. This should be considered a more efficient method to adopt for the design and manufacturing process of complex structures. Numerical modelling is also useful for determining the best material for a given application. In the case of Ti6Al4V(ELI), for instance, the current numerical models could be extended to predict how this material might accurately be used to fabricate geometrical properties such as complex surfaces. This should include extending the current models to model the

response of the material to different mechanical loads based on complex design structures. Alternative numerical modelling packages designed to tackle identical design problems should be implemented to confirm the reliability of the current numerical models. This is performed to verify that design specifications are met before the designs are approved for manufacture. Modelling insights garnered here have the potential to instruct engineers and designers on the key concepts for DfAM and assist in extending comprehension and expertise in the bioinspired engineering field.

However, a number of challenges and factors must be considered as well in incorporating the numerical models implemented here in DfAM. The level of accuracy of the numerical models used in the present work is critical. To confirm that the data that is incorporated in the DfAM process for complex structures is accurate, these numerical models must be confirmed against physical testing. Complex numerical modelling, in particular the one used in the present work, typically necessitates large computational resources and time. Considerations as to whether such numerical models are likely to be completed in a fair amount of time are necessary. Material properties tend to vary in structures, and the numerical models in the current work are likely to fail to account for this variability, resulting in some inaccuracies in the predictions made regarding the behaviour of complex structures. Though AM allows for greater design flexibility, there are still constraints and limitations relating to the effects of build orientation and the use of support structures. It is crucial to strike a balance between design flexibility and these constraints. Managing large amounts of data generated by modelling, as well as tracking and controlling changes to the software code, could also become a challenge.

Integrating numerical modelling into the AM design process, particularly for complicated structures such as hierarchical HC designs, provides several advantages in terms of optimization of design, reduction of cost, and increase of performance. However, careful consideration of the accuracy of models, computational resources, and required knowledge is necessary to guarantee the successful implementation of the models. Collaboration with AM and simulation experts is likely to be useful in this effort.

References

1. Lim, J., You, C., & Dayyani, I. (2020). Multi-objective topology optimization and structural analysis of periodic spaceframe structures. *Materials & Design*, 190, 108552.
2. Chibinyani, M. I., Dzogbewu, T. C., Maringa, M., & Muiruri, A. M. (2023). Numerical modelling of DMLS Ti6Al4V (ELI) polygon structures. *Results in Materials*, 100456.
3. Young, W. C., Budynas, R. G., & Sadegh, A. M. (2012). Roark's formulas for stress and strain. McGraw-Hill Education.
4. Alqassim, G. (2011). *Mechanical properties of hierarchical honeycomb structures* (Doctoral dissertation, Northeastern University).
5. Wang, Y., Naleway, S. E., & Wang, B. (2020). Biological and bioinspired materials: Structure leading to functional and mechanical performance. *Bioactive Materials*, 5(4), 745-757.
6. Combescure, C., and Elliott, R. S. (2017). Hierarchical honeycomb material design and optimization: Beyond linearized behavior. *International Journal of Solids and Structures*, 115, 161-169.
7. Chen, Y., and Hu, H. (2020). In-plane elasticity of regular hexagonal honeycombs with three different joints: A comparative study. *Mechanics of Materials*, 148, 103496.
8. Tao, Y., Duan, S., Wen, W., Pei, Y., & Fang, D. (2017). Enhanced out-of-plane crushing strength and energy absorption of in-plane graded honeycombs. *Composites Part B: Engineering*, 118, 33-40.

9. Fang, J., Sun, G., Qiu, N., Pang, T., Li, S., & Li, Q. (2018). On hierarchical honeycombs under out-of-plane crushing. *International Journal of Solids and Structures*, 135, 1-13.
10. Yin, H., Huang, X., Scarpa, F., Wen, G., Chen, Y., & Zhang, C. (2018). In-plane crashworthiness of bio-inspired hierarchical honeycombs. *Composite Structures*, 192, 516-527.
11. Libonati, F., and Buehler, M. J. (2017). Advanced structural materials by bioinspiration. *Advanced Engineering Materials*, 19(5), 1600787.
12. Oftadeh, R., Haghpanah, B., Vella, D., Boudaoud, A., & Vaziri, A. (2014). Optimal fractal-like hierarchical honeycombs. *Physical Review Letters*, 113(10), 104301.
13. Mousanezhad, D., Babaei, S., Ghosh, R., Mahdi, E., Bertoldi, K., & Vaziri, A. (2015). Honeycomb phononic crystals with self-similar hierarchy. *Physical Review B*, 92(10), 104304.
14. Zhang, D., Fei, Q., Liu, J., Jiang, D., & Li, Y. (2020). Crushing of vertex-based hierarchical honeycombs with triangular substructures. *Thin-Walled Structures*, 146, 106436.
15. Chen, Q., Pugno, N., Zhao, K., & Li, Z. (2014). Mechanical properties of a hollow-cylindrical-joint honeycomb. *Composite Structures*, 109, 68-74.
16. Duysinx, P., and Bendsoe, M. P. (1998). Topology optimization of continuum structures with local stress constraints. *International Journal for Numerical Methods in Engineering*, 43(8), 1453-1478.
17. Chen, Q., Shi, Q., Signetti, S., Sun, F., Li, Z., Zhu, F., & Pugno, N. M. (2016). Plastic collapse of cylindrical shell-plate periodic honeycombs under uniaxial compression: experimental and numerical analyses. *International Journal of Mechanical Sciences*, 111, 125-133.
18. He, Q., Feng, J., & Zhou, H. (2019). A numerical study on the in-plane dynamic crushing of self-similar hierarchical honeycombs. *Mechanics of Materials*, 138, 103151.
19. Tsang, H. H., Tse, K. M., Chan, K. Y., Lu, G., & Lau, A. K. (2019). Energy absorption of muscle-inspired hierarchical structure: Experimental investigation. *Composite Structures*, 226, 111250.
20. Ajdari, A., Jahromi, B. H., Papadopoulos, J., Nayeb-Hashemi, H., & Vaziri, A. (2012). Hierarchical honeycombs with tailorable properties. *International Journal of Solids and Structures*, 49(11-12), 1413-1419.
21. Hu, D., Wang, Y., Song, B., Dang, L., & Zhang, Z. (2019). Energy-absorption characteristics of a bionic honeycomb tubular nested structure inspired by bamboo under axial crushing. *Composites Part B: Engineering*, 162, 21-32.
22. Tao, Y., Li, W., Cheng, T., Wang, Z., Chen, L., Pei, Y., & Fang, D. (2021). Out-of-plane dynamic crushing behavior of joint-based hierarchical honeycombs. *Journal of Sandwich Structures & Materials*, 23(7), 2832-2855.
23. Zhang, Y., Chen, T., Xu, X., & Hu, Z. (2020). Out-of-plane mechanical behaviours of a side hierarchical honeycomb. *Mechanics of Materials*, 140, 103227.
24. Xu, X., Zhang, Y., Wang, J., Jiang, F., & Wang, C. H. (2018). Crashworthiness design of novel hierarchical hexagonal columns. *Composite Structures*, 194, 36-48.
25. Beheshtizadeh, N., Zarei, M., & Azami, M. (2023). Could we use metallic wood for bone tissue engineering applications? *Results in Engineering*, 17, 100845.
26. Khorasani, A. M., Goldberg, M., Doeven, E. H., & Littlefair, G. (2015). Titanium in biomedical applications—properties and fabrication: a review. *Journal of Biomaterials and Tissue Engineering*, 5(8), 593-619.
27. Sandu, A. V., Achitei, D. C., Perju, M. C., & Burduhos-Nergis, D. D. (2024). Perspective Chapter: Titanium—A versatile metal in modern applications. *Titanium-Based Alloys-Characteristics and Applications: Characteristics and Applications*, 3.
28. Cui, C., Hu, B., Zhao, L., & Liu, S. (2011). Titanium alloy production technology, market prospects and industry development. *Materials & Design*, 32(3), 1684-1691.

29. Blanco, D., Rubio, E. M., Lorente-Pedreille, R. M., & Sáenz-Nuño, M. A. (2021). Lightweight structural materials in open access: latest trends. *Materials*, 14(21), 6577.
30. Tepylo, N., Huang, X., & Patnaik, P. C. (2019). Laser-based additive manufacturing technologies for aerospace applications. *Advanced Engineering Materials*, 21(11), 1900617.
31. Song, J., Wang, M., Li, D., & Zhang, J. (2024). Deformation and energy absorption performance of functionally graded TPMS structures fabricated by selective laser melting. *Applied Sciences*, 14(5), 2064.
32. Chibinyani, M. I., Dzogbewu, T. C., Maringa, M., & Muiruri, A. M. (2024). Numerical modelling of Ti6Al4V (ELI) hierarchical honeycomb structures of order one at the vertices. *Results in Engineering*, 21, 102024.
33. Li, Z., Sun, H., Wang, T., Wang, L., & Su, X. (2022). Modularizing honeycombs for enhancement of strength and energy absorption. *Composite Structures*, 279, 114744.
34. Martinez, D. W., Espino, M. T., Cascolan, H. M., Crisostomo, J. L., & Dizon, J. R. C. (2022). A comprehensive review on the application of 3D printing in the aerospace industry. *Key Engineering Materials*, 913, 27-34.
35. Chen, P. Y., McKittrick, J., & Meyers, M. A. (2012). Biological materials: functional adaptations and bioinspired designs. *Progress in Materials Science*, 57(8), 1492-1704.
36. Chibinyani, M. I., Dzogbewu, T. C., Maringa, M., & Muiruri, A. M. (2022). Reduced order topology optimization of a planar honeycomb defined by a linear elastic Ti6Al4V (ELI) material model. *South African Journal of Industrial Engineering*, 33(3), 299-317.
37. Chen, Y., and Hu, H. (2020). In-plane elasticity of regular hexagonal honeycombs with three different joints: A comparative study. *Mechanics of Materials*, 148, 103496.
38. Blakey-Milner, B., Gradl, P., Snedden, G., Brooks, M., Pitot, J., Lopez, E., ... & Du Plessis, A. (2021). Metal additive manufacturing in aerospace: A review. *Materials & Design*, 209, 110008.
39. Najmon, J. C., Raeisi, S., & Tovar, A. (2019). Review of additive manufacturing technologies and applications in the aerospace industry. *Additive Manufacturing for the Aerospace Industry*, 7-31.
40. Williams, J. C., and Starke Jr, E. A. (2003). Progress in structural materials for aerospace systems. *Acta Materialia*, 51(19), 5775-5799.
41. Zhang, W., and Xu, J. (2022). Advanced lightweight materials for automobiles: A review. *Materials & Design*, 110994.
42. Czerwinski, F. (2021). Current trends in automotive lightweighting strategies and materials. *Materials*, 14(21), 6631.
43. Ren, J., Wang, Y., Yao, Y., Wang, Y., Fei, X., Qi, P., ... & Ling, S. (2019). Biological material interfaces as inspiration for mechanical and optical material designs. *Chemical Reviews*, 119(24), 12279-12336.
44. Barthelat, F., Yin, Z., & Buehler, M. J. (2016). Structure and mechanics of interfaces in biological materials. *Nature Reviews Materials*, 1(4), 1-16.
45. Huang, W., Restrepo, D., Jung, J. Y., Su, F. Y., Liu, Z., Ritchie, R. O., ... & Kisailus, D. (2019). Multiscale toughening mechanisms in biological materials and bioinspired designs. *Advanced Materials*, 31(43), 1901561.
46. Tan, H. L., He, Z. C., Li, K. X., Li, E., Cheng, A. G., & Xu, B. (2019). In-plane crashworthiness of re-entrant hierarchical honeycombs with negative Poisson's ratio. *Composite Structures*, 229, 111415.
47. Zhang, Y., Chen, T., Xu, X., & Hu, Z. (2020). Out-of-plane mechanical behaviors of a side hierarchical honeycomb. *Mechanics of Materials*, 140, 103227.
48. Zhu, Y., Zeng, Z., Wang, Z. P., Poh, L. H., & Shao, Y. (2019). Hierarchical hexachiral auxetics for large elasto-plastic deformation. *Materials Research Express*, 6(8), 085701.
49. He, Q., Feng, J., Chen, Y., & Zhou, H. (2020). Mechanical properties of spider-web hierarchical honeycombs subjected to out-of-plane impact loading. *Journal of Sandwich Structures & Materials*, 22(3), 771-796.

50. Yadroitsev, I., Krakhmalev, P., Yadroitsava, I., & Du Plessis, A. (2018). Qualification of Ti6Al4V ELI alloy produced by laser powder bed fusion for biomedical applications. *JOM*, 70, 372-377.
51. Lee, W. S., and Lin, M. T. (1997). The effects of strain rate and temperature on the compressive deformation behaviour of Ti6Al4V alloy. *Journal of Materials Processing Technology*, 71(2), 235-246.
52. Zargarian, A., Esfahanian, M., Kadkhodapour, J., & Ziaei-Rad, S. (2016). Numerical simulation of the fatigue behaviour of additive manufactured titanium porous lattice structures. *Materials Science and Engineering: C*, 60, 339-347.
53. Zhang, Q., Yang, X., Li, P., Huang, G., Feng, S., Shen, C., & Lu, T. J. (2015). Bioinspired engineering of honeycomb structure—Using nature to inspire human innovation. *Progress in Materials Science*, 74, 332-400.
54. Qi, C., Jiang, F., & Yang, S. (2021). Advanced honeycomb designs for improving mechanical properties: A review. *Composites Part B: Engineering*, 227, 109393.

CHAPTER SIX: NUMERICAL CRUSHING OF HIERARCHICAL STRUCTURES UNDER QUASI-STATIC LOADING

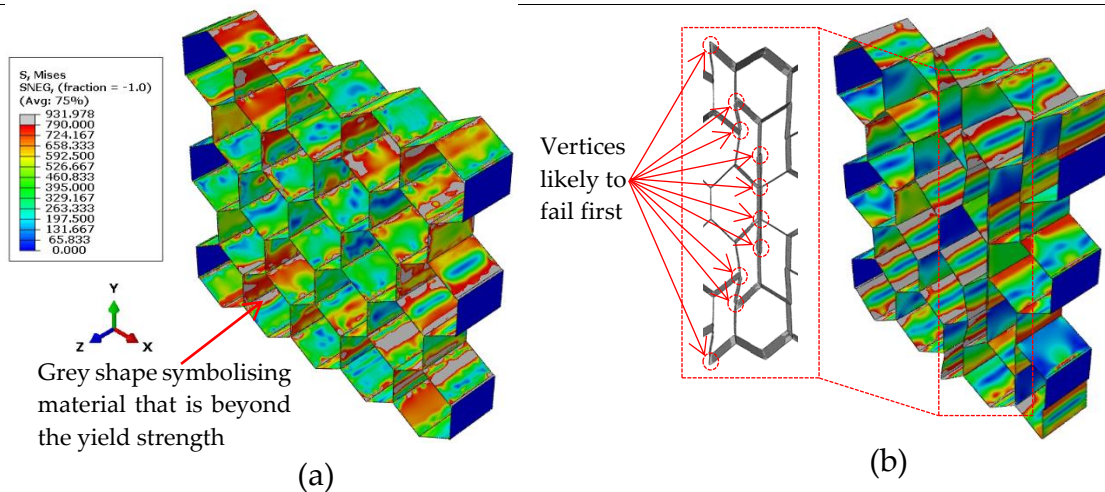
6.1. Summary

This chapter presents preliminary findings on the quasi-static crushing of vertex-based hierarchical honeycombs (HCs). The mechanical behaviour of these structures is analyzed, offering initial insights based on limited time and computational resources.

6.2. Preliminary results on numerical crushing hierarchical HCs

6.2.1. Deformation response modes

The integrity of the material connection under loading is crucial in such structures. Figure 6-1 shows the numerical crushing modes of the regular HC under x -directional load, revealing that such a structure fails first at the vertices. This is underlined by the predominant grey contour, which depicts regions where the load has exceeded the material's yielding strength. This is consistent with what has been reported in references [132-134]. Before failure at the vertices occurs, the analysis shows that the structure deforms primarily by out-of-plane bending of the cell walls [124-128]. Even though the numerical models generated here do not account for the damage behaviour, the numerical findings suggest that the failing vertices do so by fracturing, which are regarded as regions prone to fail at lower applied loads, similar to physical experimental studies performed by [126, 127]. This suggests that the bending of the walls leads to a failure mechanism involving material fracturing at the vertices. The current findings indicate that the material has significantly exceeded its yield strength in the designated regions that are likely to fail first. It is also disclosed that the vertices failed, the cell walls are continually piled, as shown in Figure 6-1b, and the structure is compacted, as shown in Figure 6-1d. Some cell walls additionally exhibit the Poisson's ratio effect [128].



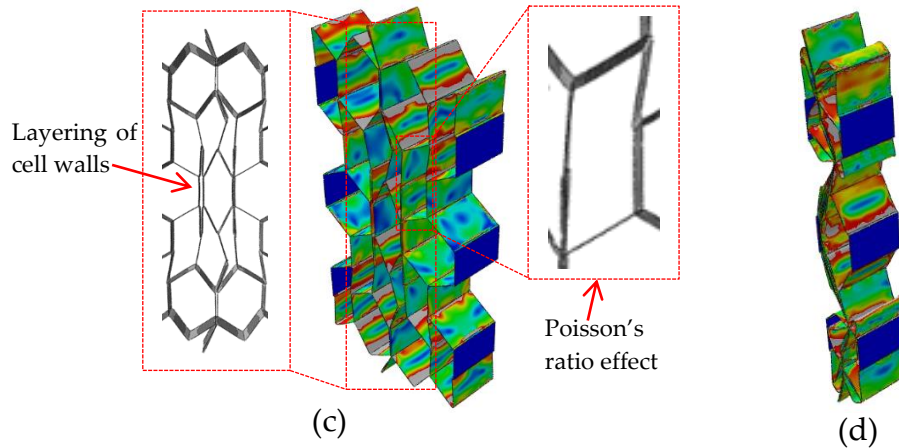
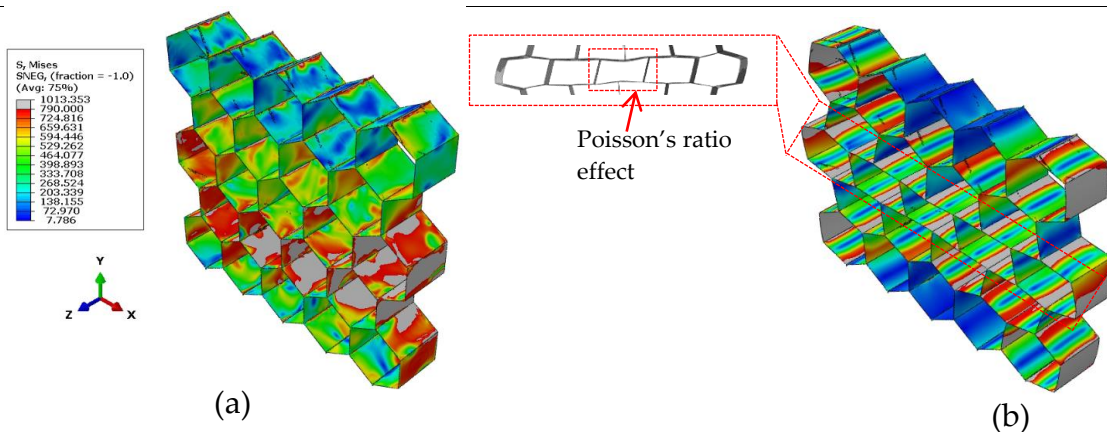


Figure 6-1. Deformation and failure mechanism of regular HC under x -directional load

Under y -directional load, the regular HC deforms predominantly by buckling the vertically positioned struts and bending the inclined walls, as shown in Figure 6-2b. Similarly to what has been revealed for regular HC under an x -directional load, the vertices are regions where the material reaches its yield strength earliest; therefore, they are designated as the regions that are predicted to fail first. During the bending and buckling deformation of the cell walls, some cells reveal the Poisson's ratio effect. Instead of the structure crushing entirely in the prescribed direction for a load rate, it turned out that particular regions of the structure where the material was exposed to loads greater than its yield strength began to twist along the z -axis, as illustrated in Figure 6-2c. Under compressive loads, the thin walls of HC cells are liable to buckling. The buckling could occur asymmetrically, causing the cells to twist and rotate [128]. The onset of plastic deformation reduces structural stiffness, rendering the HC more prone to more buckling and other types of instability. Such instability can lead cells to twist and rotate as they deform. As revealed in Figure 6-2d, the numerical crushing simulation terminated before the structure was fully crushed along the y -axis due to severe twisting of the cell walls. This suggests that torsional loads take precedence over bending and buckling loads under such situations. As a result, when defining the physics problem, one must consider such a displacement response. It is likely that the numerical approach used for integration, particularly here in the explicit method, turned unstable under high torsional loads, causing the simulation to terminate. This can cause convergence issues, in which the solver fails to find a solution within the set constraints.



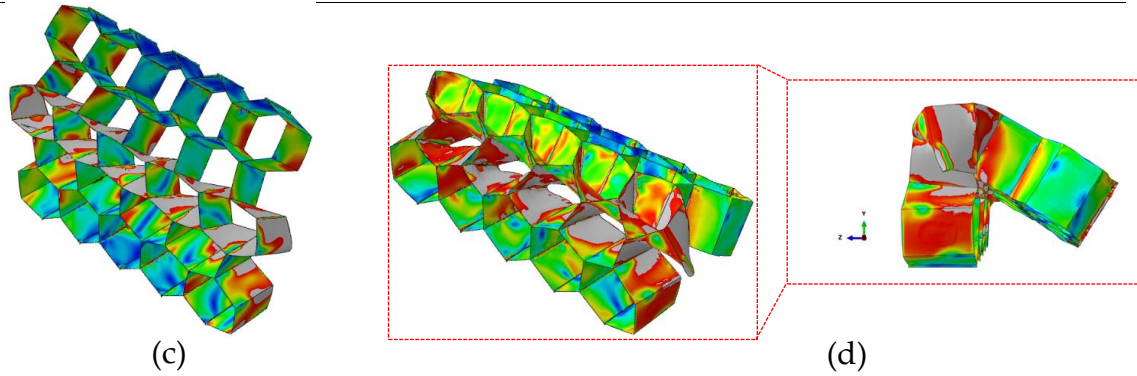


Figure 6-2. Deformation and failure mechanism of regular HC under y -directional load

Given the limitations in computational resources, including time and space, the numerical crushing analysis of the regular HC under y -directional force terminates here. In a similar vein, as illustrated in Figure 6-3, the numerical analysis of the first-order hierarchical HC under x -directional load also failed to be completed because of computational resource constraints.

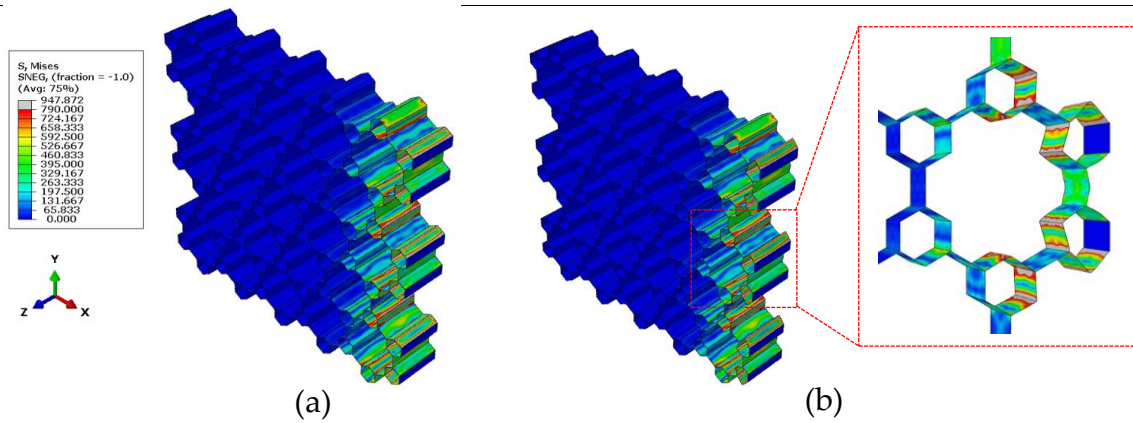


Figure 6-3. Deformation and failure mechanism of first-order hierarchical HC under x -directional load

6.2.2. Energy absorption characteristics

Given that the regular HC under x -directional load was only fully modelled, the current findings for energy absorption response are only available as a load-displacement curve for the associated structure, shown in Figure 6-4. The load-displacement curve has a lower oscillated response, suggesting that static or monotonic loading scenarios significantly influence plastic deformation [122, 125, 128]. This is due to the structure being subjected to quasi-static loads, which in the current work do not account for the damage response such as fracturing; rather, only crushing the structure until its material densifies was considered. The energy that is absorbed by the regular HC under x -directional load can be computed using the area occupied under the load-displacement curve.

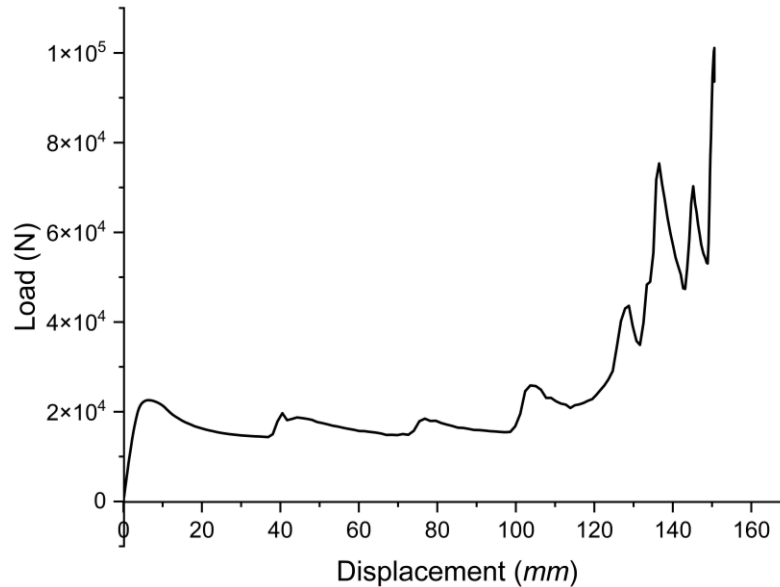


Figure 6-4. Load-displacement curve for a regular HC under x-directional force

References

1. Yap, C. Y., Chua, C. K., Dong, Z. L., Liu, Z. H., Zhang, D. Q., Loh, L. E., & Sing, S. L. (2015). Review of selective laser melting: Materials and applications. *Applied Physics Reviews*, 2(4).
2. Careri, F., Khan, R. H., Todd, C., & Attallah, M. M. (2023). Additive manufacturing of heat exchangers in aerospace applications: A review. *Applied Thermal Engineering*, 121387.
3. Singer, F., Deisenroth, D. C., Hymas, D. M., & Ohadi, M. M. (2017). Additively manufactured copper components and composite structures for thermal management applications. *7 16th IEEE Intersociety Conference on Thermal and Thermomechanical Phenomena in Electronic Systems (ITherm)*, IEEE. 174-183.
4. Li, Z., Sun, H., Wang, T., Wang, L., & Su, X. (2022). Modularizing honeycombs for enhancement of strength and energy absorption. *Composite Structures*, 279, 114744.
5. Hu, L. L., & Yu, T. X. (2013). Mechanical behavior of hexagonal honeycombs under low-velocity impact—theory and simulations. *International Journal of Solids and Structures*, 50(20-21), 3152-3165.
6. Zhao, Z., Liu, C., Sun, L., Luo, H., Wang, J., & Li, Y. (2021). Experimental and numerical study on the constrained bending-induced collapse of hexagonal honeycomb. *Composite Structures*, 277, 114604.
7. Wang, Z., Li, Z., Zhou, W., & Hui, D. (2018). On the influence of structural defects for honeycomb structure. *Composites Part B: Engineering*, 142, 183-192.
8. Thomas, T., & Tiwari, G. (2019). Crushing behavior of honeycomb structure: a review. *International Journal of Crashworthiness*.
9. Song, J., Wang, M., Li, D., & Zhang, J. (2024). Deformation and energy absorption performance of functionally graded TPMS structures fabricated by selective laser melting. *Applied Sciences*, 14(5), 2064.

CHAPTER SEVEN: TOPOLOGY AND SHAPE OPTIMIZATION OF POLYGON STRUCTURES

Part of the contents of this chapter has been submitted for publication or has been published in peer-reviewed journals, as follows:

1. **Chibinyani, M. I., Dzogbewu, T. C., Maringa, M., & Muiruri, A. M. (2022).** Reduced order topology optimization of a planar honeycomb defined by a linear elastic Ti6Al4V (ELI) material model. *South African Journal of Industrial Engineering*, 33(3), 299-317. doi.org/10.7166/33-3-2808

7.1. Summary

This chapter covers details of a new method for creating effective iterations for the HCs. The challenge in TO of HCs being addressed in this study is first pointed out in the introduction section of the chapter. This is followed by analyzing the noteworthy findings and comparing them to existing literature. The chapter ends with a listing of the future scope of the study.

7.2. Introduction

In the application of AM lightweight HC parts, improving the absorption of strain energies in biomedical implants, aircraft, and automobile components is most common [1-4]. These HC parts can be manufactured using titanium alloys, including Ti6Al4V(ELI – extra low interstitial). This alloy is biocompatible, has good mechanical properties, and is corrosion-resistant [5-6]. Incorporating HC models in AM technologies has led to the manufacture of bioinspired HC parts such as the one shown in the image on the right of Figure 7-1 [4]. Direct metal laser sintering (DMLS), a subset of laser powder bed fusion (LPBF), is a layer-wise manufacturing method that has been used for the manufacture of such metallic HC parts [1, 5].

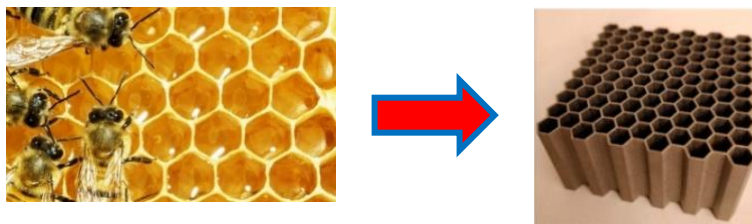


Figure 7-1. An HC part mimicked from a beehive and manufactured by the LPBF method [4]

For the efficient design and manufacture of engineering components, structural optimization is carried out to improve the mechanical properties and reduce the amount of material used [7]. TO is the most common method used for structural optimization. Specific algorithms that are built into TO software packages are used to take advantage of the geometric complexity allowed by AM. These algorithms assist with assigning the amount of material, loading, and setting boundary conditions effectively, particularly in areas of concern such as the vertices and edges [8]. The structural optimization of simple cellular parts with sharp angles in their geometry, such as the HC, which is made of thin connected plates, requires careful analysis. This is because the vertices and edges are regions of high stress that are liable to fail at lower applied loads than other parts of the HC. TO can be useful in improving the structural stability of HC parts [9]. However, the TO method struggles when dealing with 3D HC parts, as they have fewer effective iterations at the vertices and edges. These fewer effective iterations can lead to inaccurate changes of shape for the HC model. This inaccuracy is usually noted when the HC model has lower densities at the vertices and edges than other HC parts after TO [9-11]. TO gives rise to models with changes of shape at their boundaries. The models produced are then exposed to numerical modelling that is followed by shape and size optimization to fine-tune the solution. Shape optimization (SO) affects the boundaries of a

geometry the most. The changes of shape are implemented on the boundary of a structure to reduce stresses in highly stressed regions [12-13].

7.2.1 TO of 3D HC parts

There are two popular techniques for TO: the method of solid isotropic material with penalization (SIMP), which is based on the solution of binary constraints by introducing continuous relaxations to a problem, and the evolutionary structural optimization (ESO) method, which is based on engineering heuristics with proof of optimality [9, 12]. The SIMP method is the more commonly used of the two because the optimization with discrete design variables that are required of ESO can be difficult. Further details of the SIMP and ESO methods can be found in [9, 12-17]. In this work, the SIMP method was adopted since the ESO method has difficulty reaching convergence in TO, as illustrated in Figure 7-2 [17-18].

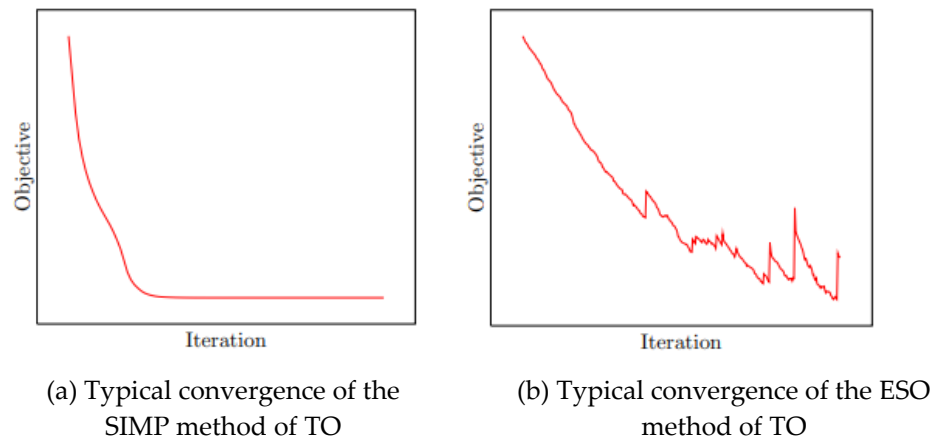


Figure 7-2. Convergence behaviour of the SIMP and ESO methods of TO [17]

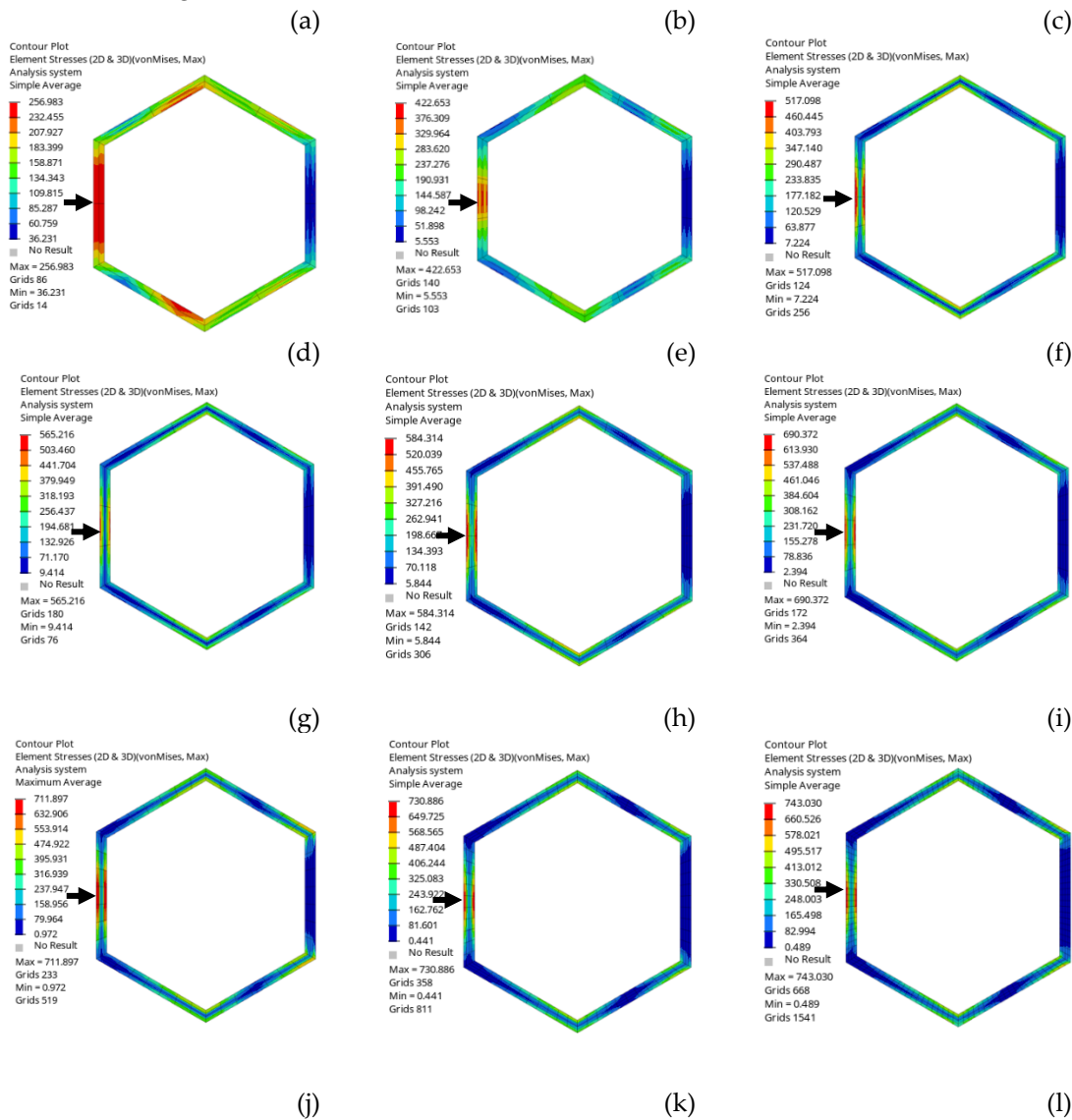
Modelling 3D HC structures is challenging due to their complicated geometries and load distributions. Accurately predicting the behaviour of HC structures under mechanical conditions requires significant computational resources and powerful numerical approaches. The interaction of cells, nonlinear material properties, and localized deformation or buckling further challenge accurate predictions, as does capturing anisotropic behaviour from their cell arrangement. It has been shown that 3D HC parts can be reduced to planar geometries in numerical analyses [11]. This reduction to 2D models provides numerous benefits. It simplifies the computing challenge, rendering it easier to manage and cost-effective. Researchers can zero in on critical factors such as in-plane stresses and deformation with minimal processing effort. Furthermore, it allows for faster simulations and easier parameter optimization, which is useful in early design stages while maintaining the HC's structural characteristics. Modelling anisotropic and orthotropic HC structures is challenging because their mechanical behaviour varies with direction, requiring complicated material models and higher computational effort. These structures exhibit different stiffness, strength, and deformation characteristics along different axes, rendering it difficult to anticipate their response under load. Additionally, anisotropy introduces complications in accurately predicting interactions between cells, leading to increased modelling complexity. By assuming the material forming the ribs of HC structures is isotropic, these complexities are avoided, and their mechanical behaviour becomes more uniform and predictable [7], simplifying analysis and reducing computational demands. The purpose of the study presented in this chapter was to investigate the ability of TO to effectively generate iterations of topologies in areas of concern using planar hexagonal unit cells and HC models.

7.3. Results and discussion

The results of the mesh convergence studies carried out in this study are first presented and discussed. This is followed by the results of the preliminary numerical modelling of a unit hexagonal cell and HC structure to establish the distribution of stresses and deformations. The results of this preliminary work were then fed into the SIMP method for TO, followed by numerical modelling of the topology-optimized FE hexagonal unit cell and HC model, with the results presented and discussed next. Finally, the SO of the topology-optimized FE HC model, followed by the numerical modelling of the shape-optimized FE HC model, was carried out, for which the results are presented.

7.3.1 Mesh convergence analysis

At first, a unit hexagonal cell model was implemented in a numerical integration and meshed with different mesh sizes to predict the optimal mesh size. The twelve different mesh sizes of 9, 8, 7, 6, 5, 4, 3, 2, 1, 0.9, 0.8, and 0.7 mm, when applied to a unit hexagonal cell using Altair-Optistruct software, generated 20, 36, 54, 72, 96, 120, 168, 264, 504, 690, 780, and 900 second-order quadrilateral shell elements, with the results shown in Figure 7-3.



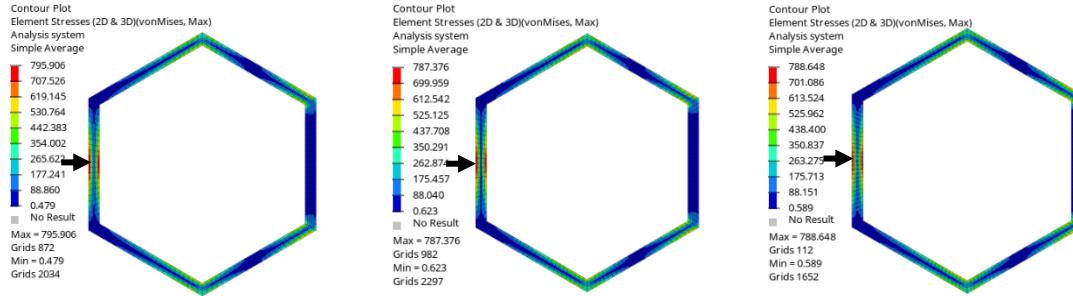


Figure 7-3. Von Mises stress distribution in the members of a planar hexagonal unit cell for different mesh sizes and the same applied load of 3188 N

The percentage changes in the von Mises stress $\Delta\sigma_V$, defined in Equation 7.1, between one mesh size and the next, were obtained as 64.47%, 22.33%, 9.30%, 3.38%, 18.16%, 3.11%, 2.67%, 5.71%, 0.36%, 0.078%, and 0.083%, starting with a mesh size of 9 mm and ending with a mesh size of 0.7 mm. These results were calculated with the following expression:

$$\Delta\sigma_V = \frac{\sigma_f - \sigma_o}{\sigma_o} \times 100\% \quad (7.1)$$

where σ_f and σ_o are the von Mises stresses of the current and previous mesh size, respectively [9]. A curve plot of the von Mises stress (σ_V) obtained at each of these mesh sizes is shown in Figure 7-4. The curve shows a tendency towards a limiting value as the mesh size decreases, with an acceptable low percentage change of $\sigma_V = 0.36\%$ at a mesh size of 0.9 mm.

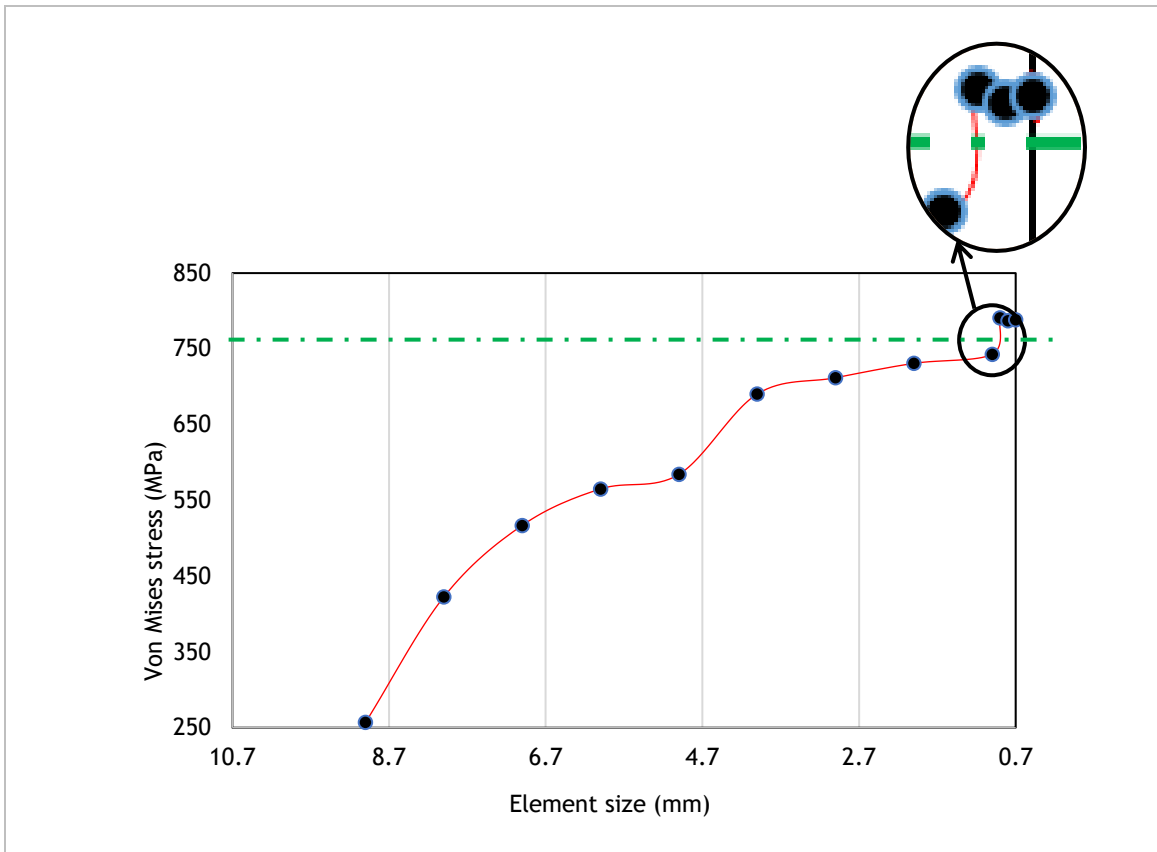


Figure 7-4. Von Mises stress versus mesh size for a planar unit hexagonal cell model

The percentage change of deformation for mesh sizes ranging from 0.7 to 9 mm was found to be 0.041%, 0.072%, 0.11%, 0.27%, 0.20%, 0.29%, 0.11%, 1.93%, 0.93%, 1.25%, and 2.27% respectively, and are plotted in Figure 7-5. These results were obtained from the following equation for the percentage change of axial deformation $\Delta\delta$:

$$\Delta\delta = \frac{\delta_f - \delta_o}{\delta_o} \times 100\% \quad (7.4)$$

where δ_f , and δ_o are the X_1 direction deformation of the current and previously analysed mesh sizes, respectively [9]. The curve of axial deformation against mesh size shown in Figure 7-5 shows a trend to convergence with decreasing mesh size, with an acceptable low percentage change of $\delta = 0.11\%$ at a mesh size of 0.9 mm.

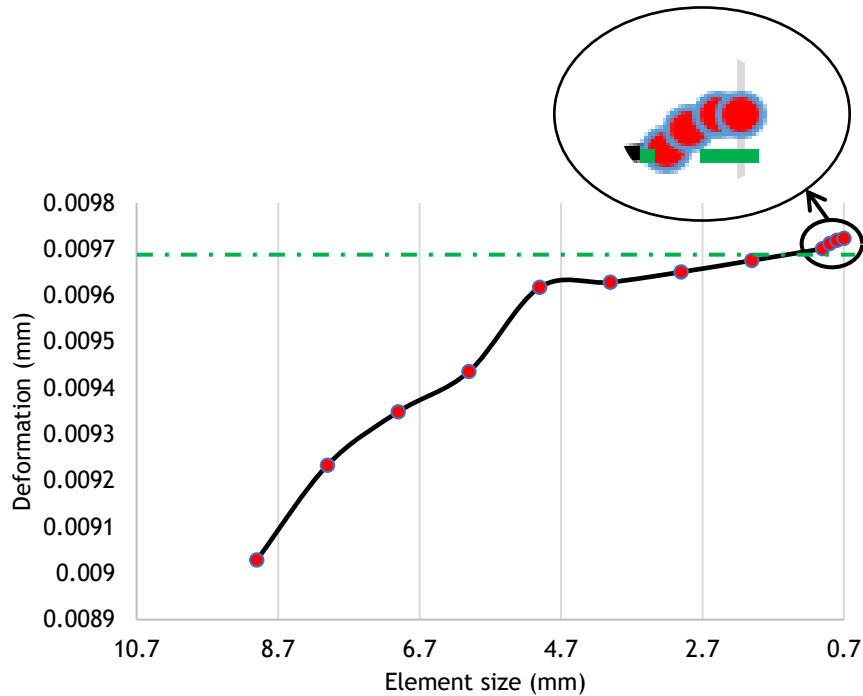


Figure 7-5. Plot of axial deformation versus mesh size for a planar unit hexagonal cell model

The discretisation errors in the two figures for von Mises stress and axial deformation were, therefore, considered insignificant below a mesh size of 0.9 mm, based on the maximum allowed percentage changes of 5% [9] and 1% [12,], respectively. The discretisation errors in a unit hexagonal cell are expected to be higher in the regions with sharp changes in geometry. However, these errors will also diminish with decreasing mesh sizes [9, 10, 12 and 19].

The low percentage changes of von Mises stress and deformation obtained with mesh sizes of 0.9 mm, 0.8 mm, and 0.7 mm in Figures 7-4 and 7-5 create confidence in the use of these mesh sizes in the simulation of the planar unit hexagonal cell and HC model that are the subject of investigation in this work. The smallest of these meshes, that of 0.7 mm, was selected for use in all subsequent modelling.

7.3.2 Preliminary FEA (numerical analysis before TO)

The analysis was done with a limiting axial stress $\sigma_V = \sigma_{ys}$, of 788.089 MPa, which was slightly lower than the known yield stress of 790 MPa for the material of interest, Ti6Al4V(ELI), for a mid-span concentrated load $P = 3188$ N. The load was applied to the vertical cell wall (member) of the unit hexagonal cell shown on the extreme left of Figure 7-6a and to the three vertical cell walls (members) of the HC model indicated on the extreme left of Figure 7-6b. The σ_V contour plots of the two FE models are shown in Figure 7-6. The contour plots in the figure show the highest stresses to occur at the mid-span of the edges of the loaded member and some parts of the inner and outer edges of the inclined members near the vertices.

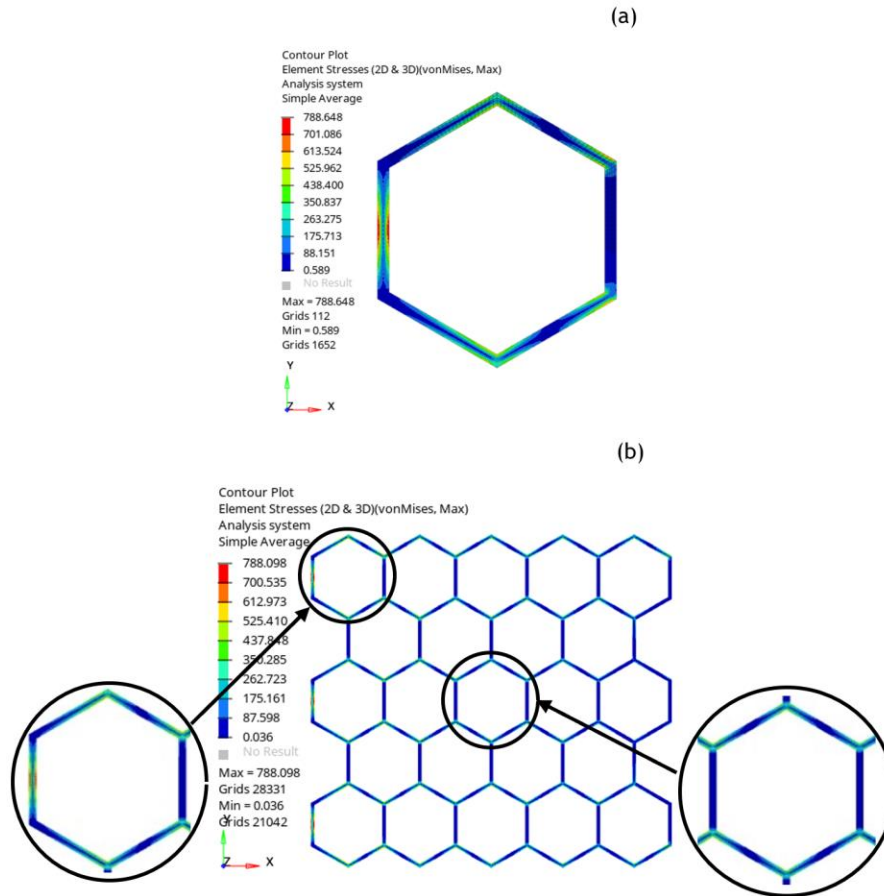


Figure 7-6. The numerical results before TO for (a) a planar unit hexagonal cell model and (b) a planar HC model

It is evident from Figure 7-6 that the outer regions of the cell members were more highly stressed than the central regions, with the exception of some vertices, certain locations on the cell members that are inclined to the vertical, and the vertical members other than those on which load was applied. Similar observations were noted in [4, 8, and 14]. The distribution of von Mises stresses for a unit hexagonal cell model shown in Figure 7-6a was compared with two magnified unit cells placed on the left and right side of an HC model shown in Figure 7-6b. The magnified unit cell on the left side showed a distribution of stresses that was similar to that of Figure 7-6a. The magnified unit cell on the right side had a similar distribution of von Mises stresses except for the loaded vertical member. The vertical members without load had close to zero stresses. This was because the stresses in structural frames are only transferred along the axial directions of the members. It is proposed that the application of multiaxial loads on the unit planar hexagonal and HC structures would ensure the presence of a load applied parallel to these members and, therefore, lead to a different distribution of stress in them. Moreover, the general case of a load inclined in a horizontal direction at an arbitrary angle θ should be useful in exploring the effect of the size of this angle on the stress distribution, deformation, and deflection of members.

Deflection of the members of the frame structures occurred along the x - and y -axes to the magnitudes shown in Figure 7-7. The two diagrams from the left to the right of Figure 7-7a are deflection contour plots for the unit hexagonal cell and the HC model in the x -direction, respectively. The two diagrams on the left and right of Figure 7-7b are similar to the one in Figure 7-7a but show contour plots for deflections in the y -direction. The contour plots in the figures show the largest deflection to occur in the x -direction of the mid-span of the loaded member. In the y -direction, the largest possible deflections are in the top vertices and adjacent members of the three top left-most unit cells.

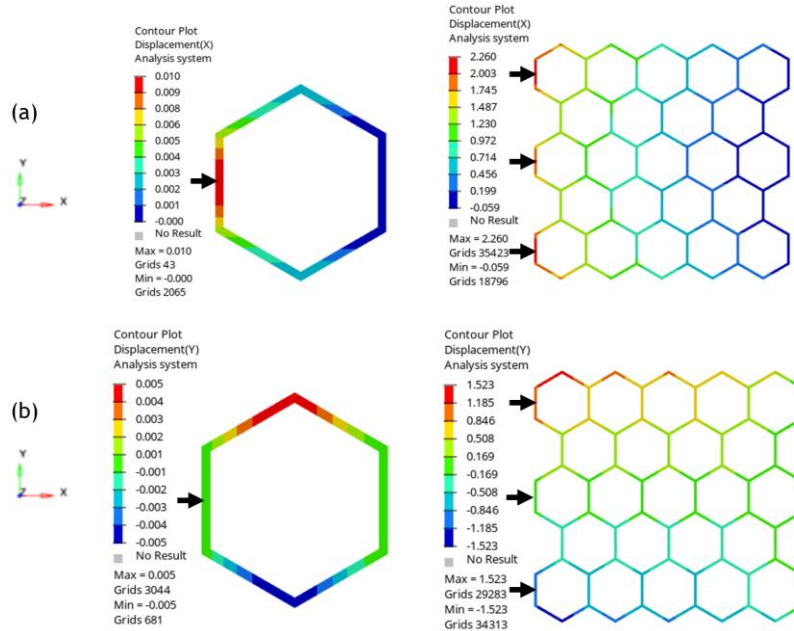


Figure 7-7. FEA showing the deflection of unit hexagon cell (left) and HC (right) along the (a) x -direction and (b) y -direction

It is evident from Figure 7-7 that the largest deflections that occurred in the unit hexagonal cell and the HC structure were caused by bending loads acting on the loaded members. The deflections in the x -direction were higher than those in the y -direction. In addition to the bending deflection of the inclined members, the members also deformed axially, as is expected from the theory of structural frames. The inclined members, therefore, behaved like beam columns that contributed to both their x - and y -directional bulk movement. The vertices and the regions close to these vertices that connect the inclined members exhibited these bulk movements, as shown in Figure 7-8(a, b). Such bulk movements will be dependent on the angle of inclination at the vertices, as both the axial and transverse loads on the members vary with the angle of inclination. This was also observed in [20].

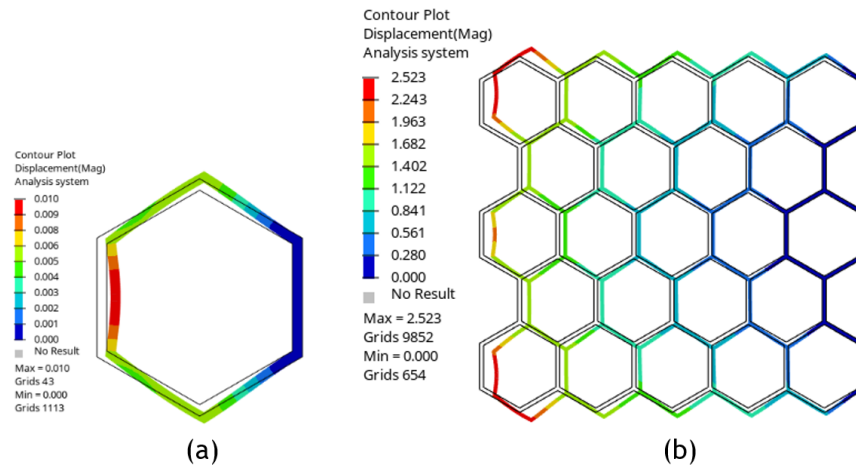
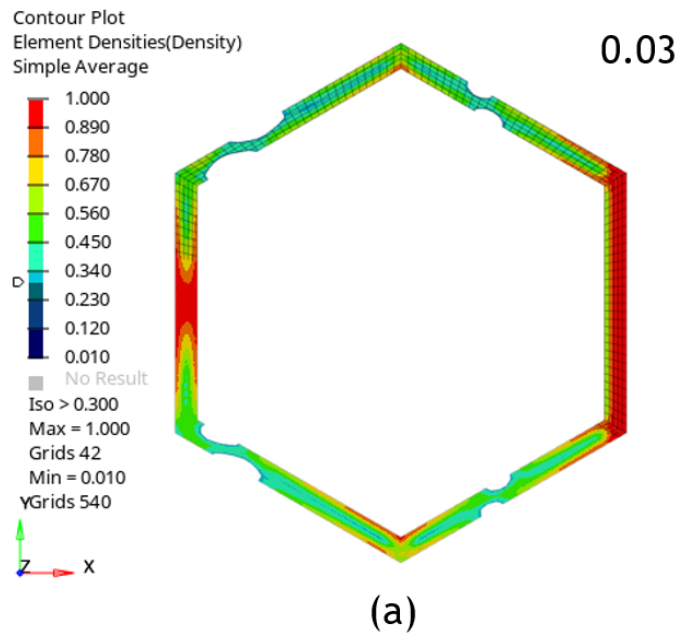


Figure 7-8. FEA results showing deflection contour plots of (a) hexagonal unit cell and (b) HC original geometry superimposed on the deformed geometry

The TO results in the next section were generated using these same geometries, with the advantage of knowledge about the distribution of stress, deformation, and deflection in their members.

7.3.3 TO analysis

TO of the unit hexagonal cell and the HC model generated maximum reductions of the material used of 30% and 8%, respectively, for the maximum respective penalty scores of 0.3 and 0.18 before structural connectivity was lost. The optimized members for these maximum reductions were shown in Figures 7-9a and 7-9b, respectively. The TO solver allowed a minimum penalty score constraint value of 0.106 for the intermediate solid densities of the FE HC model. However, better results for the model shown in Figure 7-9b were obtained using a minimum penalty score value of 0.15, as shown in Figure 7-9d. In contrast, TO unit hexagonal cell models in both Figures 7-9a and 7-9c were obtained without any minimum penalty score constraint. This is because TO results depend on the mesh predicted before TO was carried out. The unit hexagonal cell had a lower total number of sharp angles in its geometry, which meant that there were fewer repetitions of mesh errors in the geometry than in the HC model.



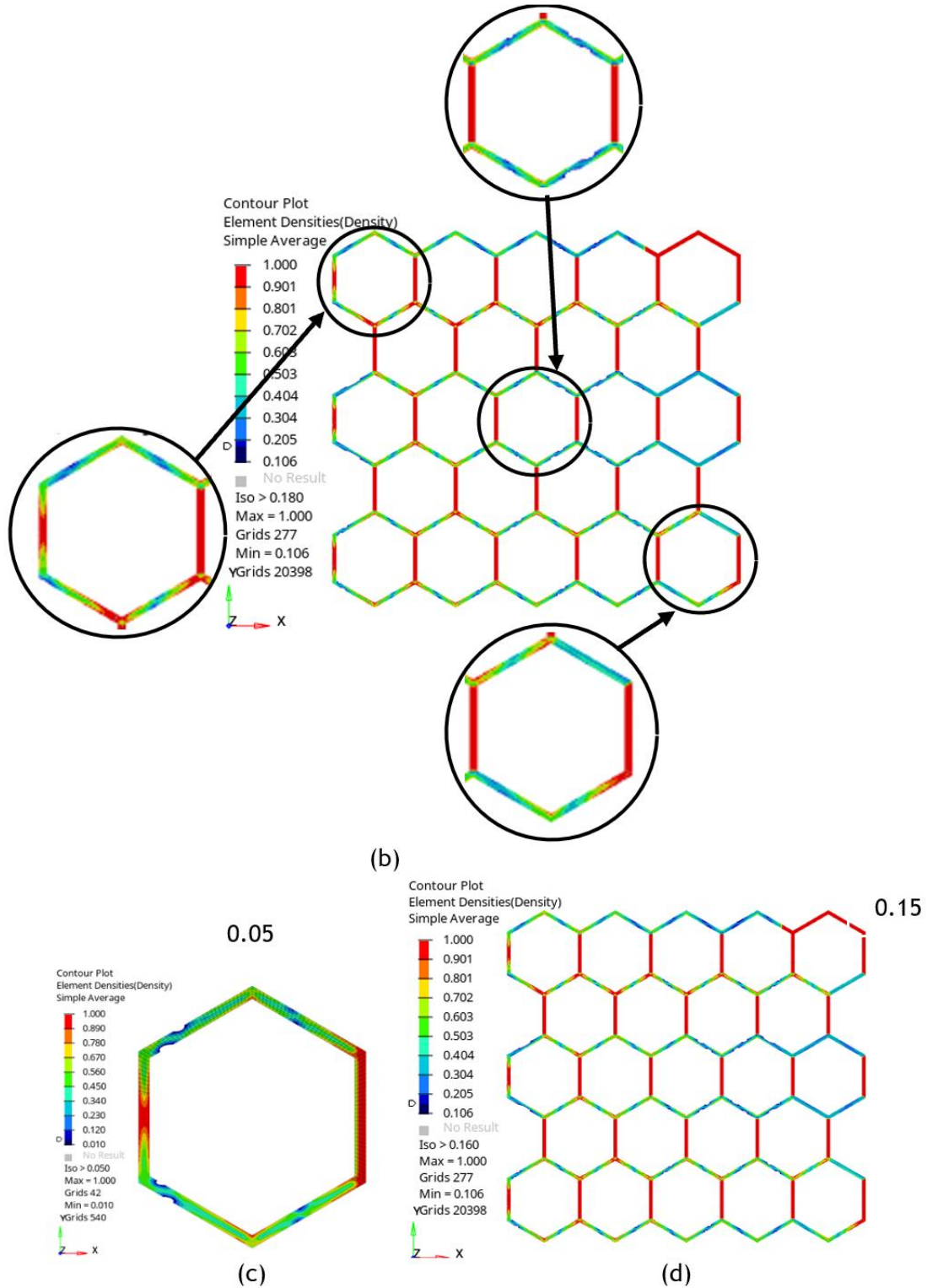


Figure 7-9. FEA results: (a) a unit hexagonal cell model, (b) an HC model after TO yielding maximum reductions of material, (c) the TO unit hexagonal model without a minimum penalty score constraint, and (d) the TO HC model with no minimum penalty score constraint

These new topologies in Figures 7-9a and 7-9c show that the densities of the material in areas that were observed to have high stresses in Figure 7-6a remained largely intact or changed by small amounts. These areas included the vertices and edges of the inclined members, and the mid-span of the member with an applied load and the one with a fixed constraint, as shown in Figure 7-10.

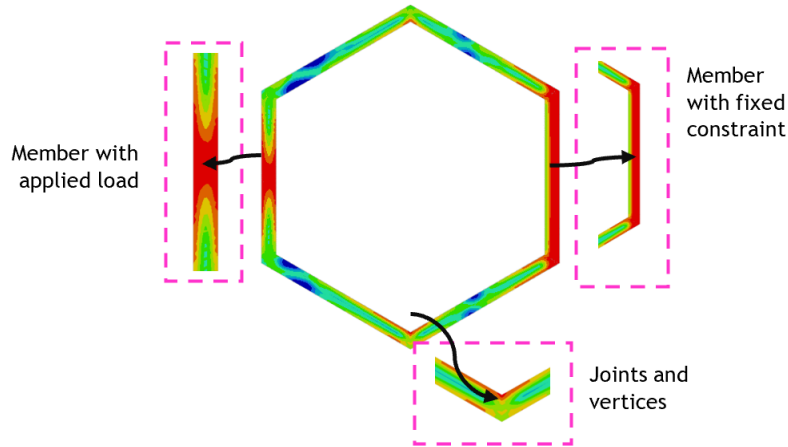


Figure 7-10. Areas on a unit hexagonal cell where the original material densities were preserved or experienced small changes

It is not surprising that the material densities reduced from the original models were small percentage areas of the total area. The honeycombs are classified as delicate structures because of their thin members and the multiple constraints arising from their complex geometry [4, 14]. The densities of the structural members in both models were predominantly preserved in the regions with high stresses shown in Figure 7-6 to preserve the stiffness of the structures, which ties in with the observations made by [9, 12, 14, and 21]. These TO results, however, had rough-edged geometries at this stage and required the implementation of SO to reduce them [9].

The new topologies obtained showed that the fictitious densities were reduced from the edges of the members instead of creating voids in the design space, as expected from the TO theory [12, 22]. To determine the location, to create and shape voids in thin wall sections is very difficult when using the SIMP method for many software packages of TO. This is because such structures have delicate structural connectivity, and by creating voids to optimize the wall sections, further structural discontinuities can easily occur [9-10, 17]. Such voids can also lead to impractical designs because of the limitation of low resolutions required in their manufacture [23]. It is recommended that TO be implemented before and during the design process. The TO done before ensures that the load paths and weaknesses in a structure are identified and considered more effectively when introducing constraints that allow voids to be created in the thin wall sections during TO.

7.3.4 Numerical analysis of TO model

The numerical stress analysis of the TO models obtained in the preceding sections is shown in Figure 7-11. The use of penalty score values of 0.05, 0.10, 0.15, 0.20, 0.25, and 0.30 on the unit hexagonal cell model resulted in values of Von Mises stresses σ_a of 797.7, 810.9, 825.1, 848.4, 856, and 869.7 MPa respectively. This trend was consistent with the linear relation expected between the densities and the material stiffness of a structure. By reducing the densities of a structure, the stresses increase, causing its stability to decrease. The numerical models shown in Figure 7-6 had better stiffnesses than the numerical models of the TO models.

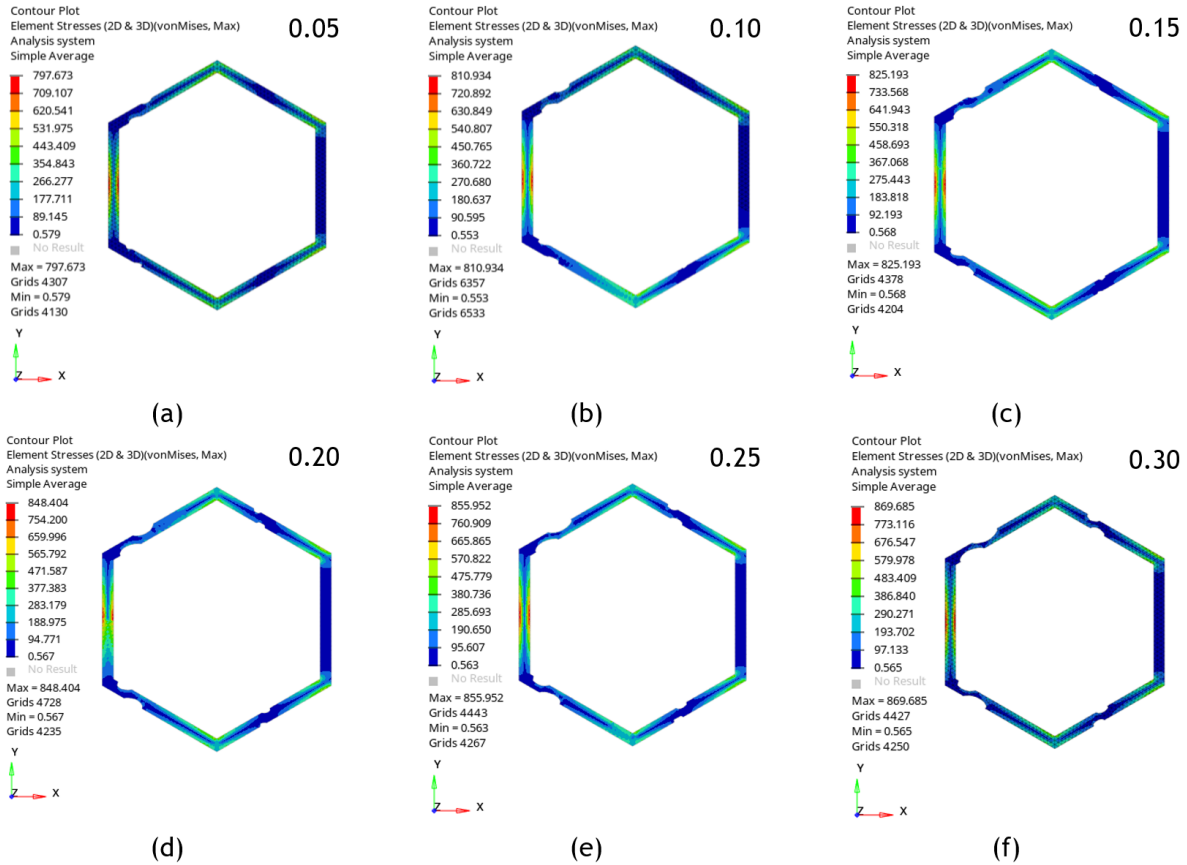


Figure 7-11. The numerical results for a TO unit hexagonal cell model with different penalty scores for the fictitious densities reduced from the solid

It is evident from Figure 7-11 that removing densities causes the stiffness of a frame structure to decrease. Increasing the penalty score values introduced more regions with sharp changes to their geometry, specifically in regions where densities were removed. This caused the stresses in a structure to increase and, in return, the stiffness of the structure decreased.

The numerical results in Figure 7-12 that were obtained for a TO HC model were similar to those of the previous analysis. However, a linear relation between material stiffness and density occurred for the minimum penalty scores, as was the case for the previous model. This relationship was also limited by the multiple constraints arising in the HC model, which were discussed in the TO section. The many sharp angles in the geometry reduced effective iterations in TO.

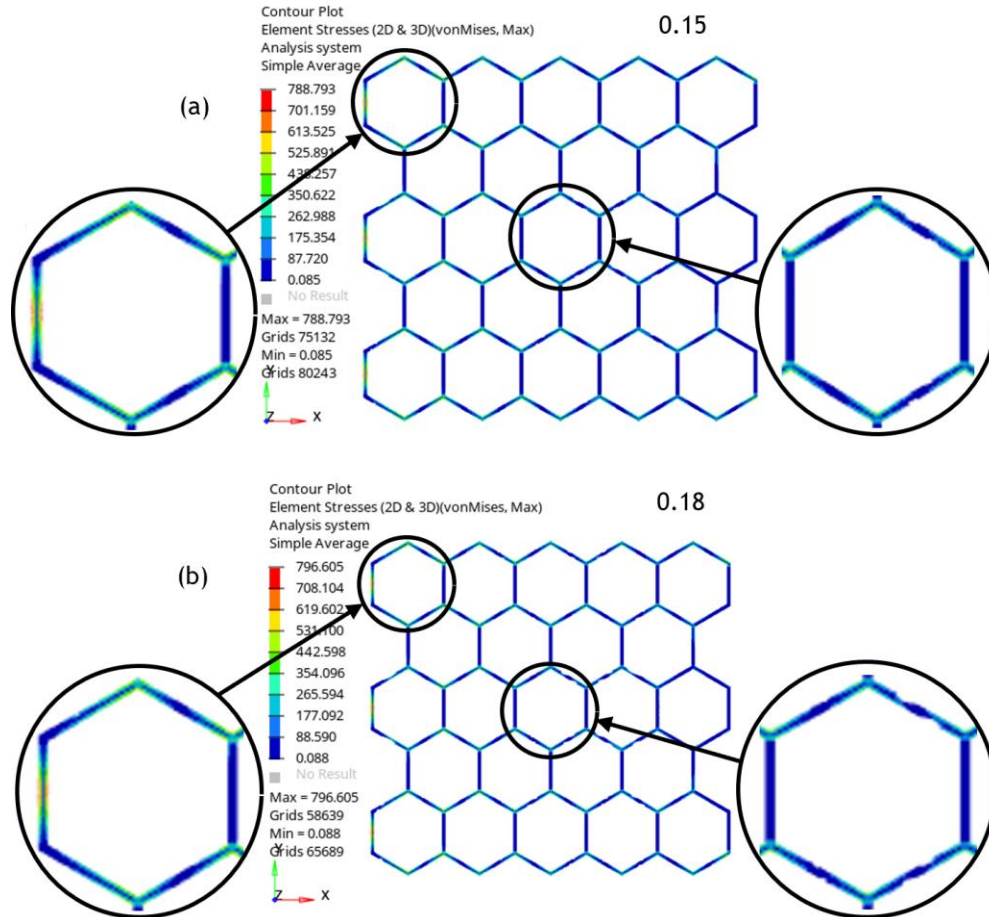


Figure 7-12. The numerical results for a TO HC model with different penalty scores (0.15 and 0.18) for the fictitious densities reduced from the solid

The numerical results of the TO models showed that the stiffnesses were decreased compared to the results observed and discussed in Figure 7-6. This agreed with the findings in [9]. These numerical models were produced before structural connectivity was lost, and the results obtained agreed with what was observed in [20]. The next section shows that the numerical results for TO geometries can be fine-tuned using SO to reduce stresses in areas of concern.

7.3.5 Numerical analysis of SO model

SO was carried out on the numerical models of the TO unit hexagonal cells presented in Figure 7-11, with σ_v values of 797.7 MPa and 869.7 MPa. The maximum stresses obtained decreased from those of non-topologically optimized unit hexagonal cells by 46% and 58%, respectively, as shown in Figure 7-13. For the HC models shown in Figure 7-12, with σ_v values of 788.8 MPa and 796.6 MPa, the percentage stress reductions obtained after SO were 4% and $2.9 \times 10^{-5}\%$ respectively, as shown in Figure 7-14. These last percentage stress reduction results were negligible.

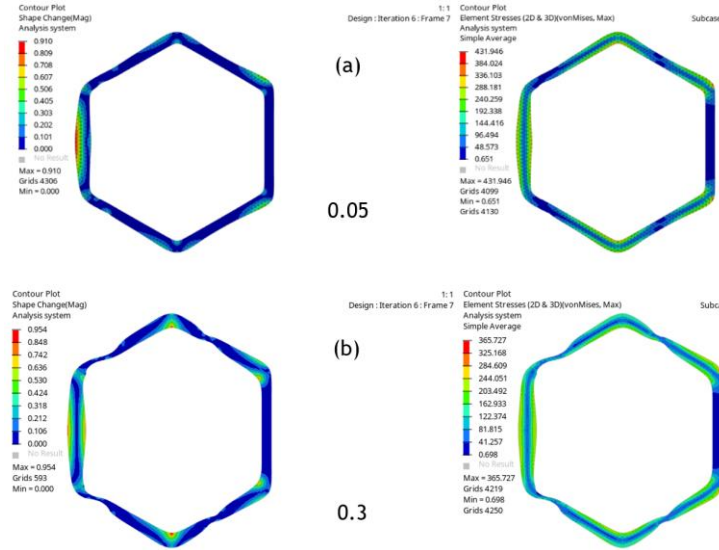


Figure 7-13. The numerical results of SO unit hexagonal cell model with penalty scores for intermediate densities of (a) 0.05 reduced from solid, and (b) 0.3 reduced from solid

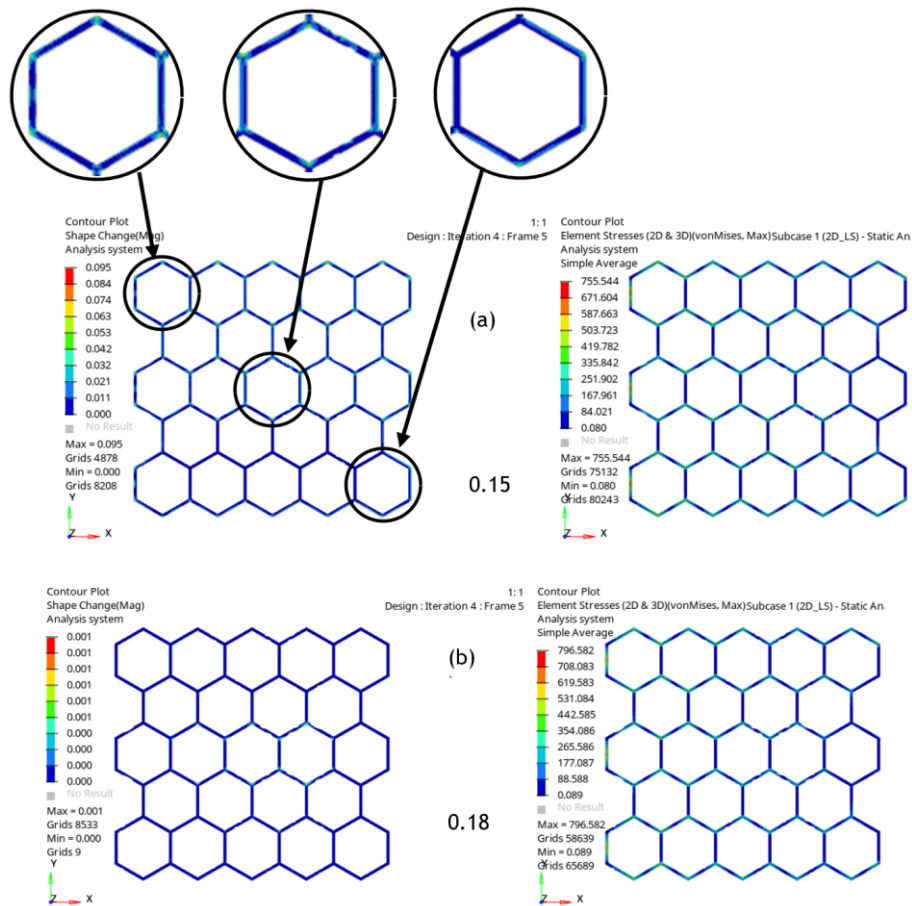


Figure 7-14. The numerical results of the SO HC model with a penalty score of intermediate densities of (a) 0.15 reduced from solid, and (b) 0.18 reduced from solid

The effects of SO on the reduction of maximum stresses for the unit hexagonal cell after TO showed more effective stress reduction than for the HC model. This was consistent with the behaviour observed in [14, 24]. This could be because the unit hexagonal cell had a lower total number of sharp angles in its geometry than the HC. These sharp angles contributed to mesh errors that reduced the effectiveness of iterations in mesh-dependent SO. Having fewer errors occurring ensured that the change of shape during SO was more effective in reducing stresses. The HC model showed lower percentage values of reduction in maximum stresses because of the many constraints and sharp angles at the vertices and edges. This caused mesh errors to increase, and as a result, the effectiveness of iterations in SO was reduced in areas of concern.

7.4. Scope and opportunities for future work

7.4.1 Extending the current topology-optimized low-fidelity HC models to high-fidelity ones

To broaden the scope of this research to high-fidelity models, the following steps are recommended:

Refining geometrical complexity, introducing higher-resolution meshes, and convergence testing: The research effort discusses the adverse effects caused by sharp angles in the geometry of 3D HC systems. High-fidelity modelling calls for greater accuracy in controlling geometric constraints, particularly near the vertices and edges. Advanced meshing techniques or smoothed geometric transitions can capture finer details and improve convergence in the TO step.

Advanced material modelling: High-fidelity models provide more detailed and accurate representations of material behaviour, particularly for complicated materials such as Ti6Al4V(ELI). This includes using more advanced material models that account for nonlinearities such as plasticity, anisotropy, and even fatigue behaviour under cyclic loading. Such features are sometimes overlooked in lower-fidelity models, yet they are critical for accurate predictions.

Full 3D modelling: Though the current research focused on planar HC models, high-fidelity modelling includes a transition towards fully 3D HC structures. This extension should capture out-of-plane phenomena and structural behaviour in a more accurate scenario, resulting in better insights into mechanical performance under current loading events. Additionally, 3D modelling can allow the optimization of complex shapes in fully volumetric conditions.

Multiphysics modelling: Depending on the application, high-fidelity models can feature Multiphysics models that factor in aspects beyond mechanical properties, such as thermal effects, fluid-structure interaction, or electromagnetic interactions. In aeronautical applications, thermal and mechanical loading are necessary for accurately predicting the structure's performance.

Post-topology optimization validation and experimental correlation: After topology optimization, high-fidelity models should be thoroughly validated using experimental data. This should entail not only comparing numerical predictions but also conducting physical tests on the optimized structures. To achieve stability, accurate high-fidelity models should be validated against a variety of experimental scenarios.

SO and TO of 3D HC structures: SO and TO can be applied to 3D HC models. The iterative process of refining geometry, along with increasingly complicated objective functions in optimization, could result in structures that are both lightweight and capable of handling more complex load conditions. Given that more complex geometries and stress concentrations are included in high-fidelity models, optimization accuracy improves.

References

1. Attaran, M. (2017). The rise of 3-D printing: The advantages of additive manufacturing over traditional manufacturing. *Business horizons*, 60(5), 677-688.
2. Gao, W., Zhang, Y., Ramanujan, D., Ramani, K., Chen, Y., Williams, C. B., ... & Zavattieri, P. D. (2015). The status, challenges, and future of additive manufacturing in engineering. *Computer-aided design*, 69, 65-89.

3. Wang, S., Liu, L., Huang, Z., Li, Z., Liu, J., & Hao, Y. (2021). Honeycomb structure is promising for the repair of human bone defects. *Materials & Design*, 207, 109832.
4. Zhang, Q., Yang, X., Li, P., Huang, G., Feng, S., Shen, C., ... & Lu, T. J. (2015). Bioinspired engineering of honeycomb structure—Using nature to inspire human innovation. *Progress in Materials Science*, 74, 332-400.
5. Du Plessis, A., Yadroitsava, I., & Yadroitsev, I. (2018). Ti6Al4V lightweight lattice structures manufactured by laser powder bed fusion for load-bearing applications. *Optics & Laser Technology*, 108, 521-528.
6. Maietta, S., Gloria, A., Improta, G., Richetta, M., De Santis, R., & Martorelli, M. (2019). A further analysis on Ti6Al4V lattice structures manufactured by selective laser melting. *Journal of healthcare engineering*, 2019(1), 3212594.
7. Jihong, Z. H. U., Han, Z. H. O. U., Chuang, W. A. N. G., Lu, Z. H. O. U., Shangqin, Y. U. A. N., & Zhang, W. (2021). A review of topology optimization for additive manufacturing: Status and challenges. *Chinese Journal of Aeronautics*, 34(1), 91-110.
8. Vilardell, A. M., Takezawa, A., Du Plessis, A., Takata, N., Krakhmalev, P., Kobashi, M., ... & Yadroitsev, I. (2019). Topology optimization and characterization of Ti6Al4V ELI cellular lattice structures by laser powder bed fusion for biomedical applications. *Materials Science and Engineering: A*, 766, 138330.
9. Plocher, J., & Panesar, A. (2019). Review on design and structural optimisation in additive manufacturing: Towards next-generation lightweight structures. *Materials & Design*, 183, 108164.
10. Wang, Q., Han, H., Wang, C., & Liu, Z. (2022). Topological control for 2D minimum compliance topology optimization using SIMP method. *Structural and Multidisciplinary Optimization*, 65(1), 38.
11. Maute, K., & Ramm, E. (1995). Adaptive topology optimization. *Structural optimization*, 10, 100-112.
12. Yago, D., Cante, J., Lloberas-Valls, O., & Oliver, J. (2022). Topology optimization methods for 3D structural problems: a comparative study. *Archives of Computational Methods in Engineering*, 29(3), 1525-1567.
13. Bendsoe, M. P. (1989). Optimal shape design as a material distribution problem. *Structural optimization*, 1, 193-202.
14. Edwards, C. S., Kim, H. A., & Budd, C. J. (2007). An evaluative study on ESO and SIMP for optimising a cantilever tie—beam. *Structural and Multidisciplinary Optimization*, 34, 403-414.
15. Bendsoe, M. P., & Sigmund, O. (2013). Topology optimization: theory, methods, and applications. *Springer Sci. Rev*, 1-69.
16. Tanskanen, P. (2002). The evolutionary structural optimization method: theoretical aspects. *Computer methods in applied mechanics and engineering*, 191(47-48), 5485-5498.
17. Browne, P. A. (2013). *Topology optimization of linear elastic structures* (Doctoral dissertation, University of Bath).
18. Rozvany, G. I. (2009). A critical review of established methods of structural topology optimization. *Structural and multidisciplinary optimization*, 37, 217-237.
19. Li, S., Yuan, S., Zhu, J., Zhang, W., Zhang, H., & Li, J. (2021). Multidisciplinary topology optimization incorporating process-structure-property-performance relationship of additive manufacturing. *Structural and Multidisciplinary Optimization*, 63, 2141-2157.
20. Ashby, M. F., & Gibson, L. J. (1997). Cellular solids: structure and properties. *Press Syndicate of the University of Cambridge, Cambridge, UK*, 175-231.
21. Beyer, C. (2014). Strategic implications of current trends in additive manufacturing. *Journal of Manufacturing Science and Engineering*, 136(6), 064701.
22. Thompson, M. K., Moroni, G., Vaneker, T., Fadel, G., Campbell, R. I., Gibson, I., ... & Martina, F. (2016). Design for Additive Manufacturing: Trends, opportunities, considerations, and constraints. *CIRP annals*, 65(2), 737-760.

23. Sigmund, O., & Petersson, J. (1998). Numerical instabilities in topology optimization: a survey on procedures dealing with checkerboards, mesh-dependencies and local minima. *Structural optimization*, 16, 68-75.
24. Hadamard, J. S. C. R. (1911). Mouvement permanent lent d'une sphere liquid et visqueuse dans un liquid visqueux. *CR Hebd. Séances Acad. Sci. Paris*, 152, 1735.

CHAPTER EIGHT: EXPERIMENTATION: QUASI-STATIC CRUSHING OF HIERARCHICAL LATTICE STRUCTURES

8.1. Summary

This chapter contains details on the behaviour of hierarchical HCs of orders zero, one and two under quasi-static crushing. The chapter starts with an introduction followed by experimental results and their analysis. Lastly, the research's most noteworthy results are then highlighted and contrasted with those found in the current literature.

8.2. Introduction

Design for fabricating structures with tailorable, complicated, and smart lattice geometries using the latest manufacturing technologies has significant impacts on their effectiveness as energy-absorbent [1-6] and impact-resistant materials [2, 4, 6-7]. Metal AM technologies, particularly DMLS or SLM, a part of the category of laser powder bed fusion (LPBF) [8-10], give accurate control [8, 10-11] and adaptability in design [9-10, 12] when building hollow or lattice parts with complicated physical features. Such features are typically challenging to attain via traditional manufacturing methods, including casting, forging, machining and moulding [13-15]. Using DMLS technology has numerous advantages [8-15] beyond its capacity for producing complicated shapes and customizing parts minus the requirement for expensive tooling upgrades [14-15]. The addition of materials in DMLS technology reduces generated waste, particularly when compared to subtractive manufacturing methods [15]. The metallic powder that remains after printing parts can be recycled and reused for fabricating structures in other projects as well [11, 15]. The DMLS technology is also compatible with a range of metal alloys, including those of titanium, aluminium, and stainless steel [14-15]. The compatibility of DMLS with various metal alloys creates a broad selection list for engineering applications.

This chapter is focused on the titanium-based alloy, Ti6Al4V, for use in the aerospace, automotive, defence and medical industries, particularly due to its high strength-to-weight ratio [17-20], corrosion resistance [16-17, 21-22], durability at higher temperatures [16-18, 21], enhancement of performance [16-17, 20], reliability [16-17] fracture toughness [17, 21], non-magnetic properties [23-24], ballistic resistance [25-26], biocompatibility [16, 18-19, 21], and adaptability in design [17, 27]. Though DMLS Ti6Al4V parts have numerous benefits, they also bring challenges and constraints that impact their functionality and effectiveness. The significant challenges are broadly classified as material-specific, process-specific, and application-specific challenges for AM [28-30].

Over three decades, significant work has been reported on hollow or lattice geometries, including HCs [31-45]. These hollow-built materials are designed to mimic the hexagonal unit cell configuration seen in organic HCs, with the primary objective of overcoming complex engineering problems [37-38, 46]. The geometric configuration in HCs yields lightweight yet strong and efficient designs, resulting in this type of lattice shape being advantageous for industries such as aerospace, automotive, defence, medical, civil engineering, and packaging [38-39, 46]. As materials science advances, applications and benefits of HCs are anticipated to broaden even further.

For the most part, quasi-static loads are used for analyzing structures, including HCs [47]. A loading rate between 0.01 and 10 mm/min generally must be kept to in quasi-static crushing. Given the gradual application of load in this case, inertial effects are minimized, and the material's inherent mechanical characteristics predominate in the response of loaded structures [48]. For HCs, one of the primary features evaluated in quasi-static crushing is the capacity of the structure to absorb energy. In engineering fields that underline crashworthiness, packaging, and protective gear, extensive use is made of HCs in designing structures corresponding to their particular application [40-46]. The available literature in this field contains numerous reports of experimentation with various materials under quasi-static crushing, comprising aluminium, polycarbonate, and composites, in addition to leveraging polygon hollow shapes built

using hexagonal, rectangular, triangular, and circular unit cells. These studies have repeatedly shown that, regardless of changes in the materials and configuration of the structure, the deformation modes and force versus displacement curve trends stay constant [38-45]. The bulk of work reported in open literature centres around analysing in-plane crushing behaviour, particularly because polygon hollow parts are applied extensively for absorbing energies [40-45]. Mozafari et al. [49] investigated the impact of foam filling in aluminium HCs on their crushing behaviour under in-plane loads. Their findings showed that foam-filled HC can increase specific energy absorption by up to 20-fold and in-plane crushing strength by up to 208-fold. It was also observed that the effect of foam filling diminishes in denser HCs. As a result, increasing the mechanical properties pointed out in the preceding sentence is limited to 6- and 36-fold, respectively. Zhou et al. [50] thoroughly examined the in-plane quasi-static behaviour of a novel re-entrant combined-wall (RCW) HC, which was attained by integrating a hexagonal substructure in each inclined wall of the standard re-entrant (RE) HC. The analysis of the specific absorbed energy (*SEA*) revealed that the RCW HC outperforms the RE HC, with the *SEA* level approximately two-fold that of the latter. Choudhry et al. [51] used parametric modelling and geometric optimization to examine the energy absorption capability of a customized re-entrant HC. It was found in their work that the newly developed HC outperformed a typical re-entrant HC by 36% in terms of *SEA*. The crushing behaviour of HCs is known to be the result of an intricate combination of geometric design, and material characteristics. To optimize these structures for particular applications, it is imperative to carefully analyze and weigh these factors. Comprehending these impacting aspects allows the design of very effective and reliable HCs tailored to a wide range of engineering uses.

Hierarchical structuring in HCs is a powerful strategy reported in numerous studies [38, 52-60], and its implementation has resulted in the fabrication of materials and structures with previously undocumented characteristics and functionalities. This design strategy for materials and structures is typically used to match the stringent requirements of contemporary applications by drawing inspiration from nature, in addition to leveraging advances in materials engineering [53, 56]. This is in part because the hierarchical structuring of structures and materials enhances their mechanical properties and absorption of energies by integrating strength, toughness, fatigue resistance, and effective energy dissipation mechanisms [52, 54, 56-60]. These advantages are attained by mimicking the distinctive physical characteristics and interactions of biological structures at numerous scales, from the atomic to the macroscopic level [52, 54]. In turn, new structures and materials with better mechanical characteristics in general can be produced. As noted previously in this document on Pages 22-23 of Section 2.4 in Chapter 2, there are four preferred strategies for generating hierarchical configurations, namely the vertex-based, cell-wall-based, fractal-based, and spiderweb-based, all of which are inspired by nature, where hierarchical structures are reportedly observed in a range of biological materials [52]. The analysis presented in this chapter is centred around the vertex-based hierarchical HCs.

Recent reported advances in hierarchical lattice designs have impacted their use in defence, aerospace, automotive, medical, and energy industries [52, 57-60]. As reported by Oftadeh et al. [57-58], the in-plane modulus of elasticity of hierarchical HCs improves substantially with increasing levels of hierarchy, resulting in enhanced effectiveness. Their findings showed that the first and second-order hierarchical HCs were 2.0- and 3.5-fold stiffer than traditional HCs and yet retained the same relative density. Zhang et al. [59] investigated SLM-printed AlSi₁₀Mg hierarchical HCs under large deformation in the in-plane axes. Their findings indicated that higher levels of hierarchy substantially enhance the modulus of elasticity of HCs. Conversely, compressive strength improved negligibly. Their findings additionally showed a change in the failure mechanism from cell wall bending to cell wall fracturing when the density ratio and order of hierarchy increased. The findings also showed a direct correlation between failure mechanisms and the thickness of the wall, with a critical value of 0.345 mm, indicating that below this threshold, the structure becomes significantly more prone to premature failure or instability. They concluded that the bending, axial compression, and shear deformation of the original unit cell walls are the primary causes of

in-plane failure in hierarchical HCs. The same authors [60] later conducted plastic crushing failure analysis of corresponding geometries built via SLM using 316L stainless steel and AlSi₁₀Mg materials. Under large deformation, the AlSi₁₀Mg alloy HCs exhibited brittle responses, whereas the 316L steel HCs exhibited ductile responses, with a Poisson's ratio effect and gradient deformation of hierarchical unit cells. The application of unit cell advancements, such as optimized lattice designs, improved control of the inherent porosity of the structure, and refined wall thickness distribution, increased the modulus of elasticity of AlSi₁₀Mg alloy HCs and advanced the densification mechanism of 316L stainless steel HCs by enhancing energy absorption and delaying localized failure.

Based on the studies reported in the open literature that was available to the author [52-60], quasi-static crushing analysis for hierarchical HCs is limited to 316L stainless steel, AlSi₁₀Mg alloy, and polylactides (PLA) materials. There is, thus, a clear need to conduct such tests using other metal alloys, such as Ti6Al4V, which are currently hot topics in DMLS or SLM research, and to examine their influence on the crushing behaviour of hierarchical HCs. The suggested quasi-static crushing testing of hierarchical HCs in this chapter, which is additively built with Ti6Al4V material, is the first of its kind to the best knowledge of the author. The work could provide insights that advance understanding of the comparative benefits of Ti6Al4V in various related engineering applications. Additionally, there are limited details in reported studies describing all the energy absorption mechanisms determined during quasi-static crushing of hierarchical HCs. Comprehending the new findings reported in this chapter, with reference to the progression of deformation and failure mechanisms at various size scales inherently built in these structures, could provide critical value to various applications in engineering as well. Considering these findings before choosing a hierarchical design to adopt in an engineering application grounds the insights of the designer while providing information on the anticipated effectiveness of the structure with reference to its corresponding reported deformation mechanisms. A separate ranking of the crushing behaviour for hierarchical HCs under two in-plane loading directions (the x - and y -axis) has not been reported to date. The ranking now conducted in this work could facilitate a better understanding of the best directional behaviour suited for specific and advanced applications of hierarchical HCs in engineering. Given that there are limited studies [53-60] on the deformation behaviour of hierarchical HCs as well, quasi-static crushing experiments must be repeatable and reproducible. The current experimental study on DMLS-produced hierarchical HCs adds to the bulk of reported material that can be used to ensure consistency of the crushing behaviours of such built structures.

8.3. Results and discussion

8.3.1 Surface roughness

Surface roughness tests were performed to evaluate the quality of HC parts at various hierarchical levels. Figures 8-1, 8-2 and 8-3 feature the results of surface roughness measurements for zero-order, first-order, and second-order hierarchical HCs measured directly on the top flat and side inclined faces, as well as data measured directly on the top flat faces of a bead-blasted first-order hierarchical HC. The figures include average values and standard deviations.

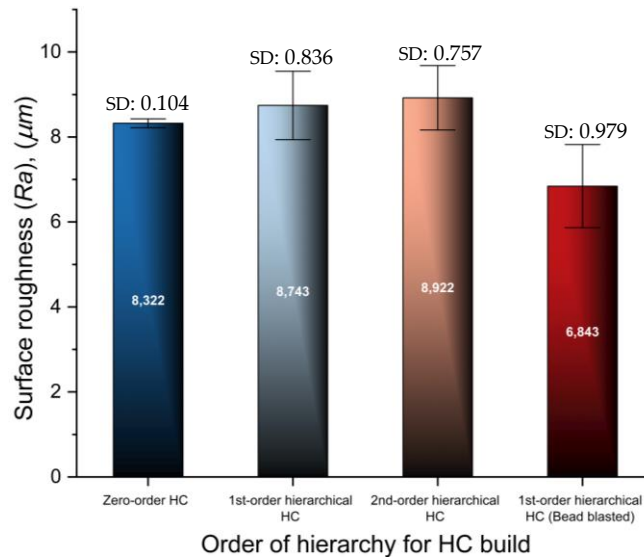


Figure 8-1. The mean surface roughness (R_a) of the surfaces of the top flat faces of the various levels of hierarchy for HCs

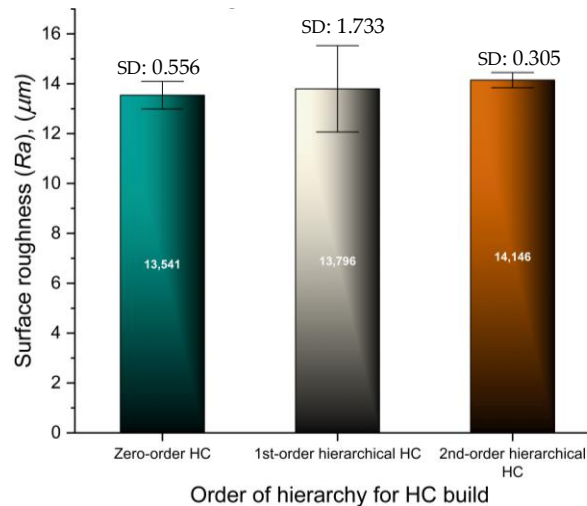


Figure 8-2. The mean surface roughness (R_a) of the surfaces of the side inclined faces of the various levels of hierarchy for HCs

The coefficient of variance (CoV) is calculated for each set of data; the mean and standard deviation are reported in the two figures that preceded to identify if the values of mean have a statistical meaning. This calculated CoV is based on the data set measured for the top flat and side inclined faces of each level of hierarchical HC build separately. The zero-order, first-order, and second-order hierarchical HCs have percentage values of 1.250%, 9.562%, and 8.485%, respectively, for the CoV calculated based on the mean and standard deviation of R_a at the top flat faces. The inclined surfaces of the same hierarchical HCs stated in the previous sentence have percentage values for CoV of 4.106%, 12.562%, and 2.156%, respectively. Typically, values of CoV less than 5% denote clustering and imply that the mean values have a statistical meaning. Large values of CoV imply a large scatter of data away from the mean, which implies the mean has no statistical value [61]. From the perspective of the mechanical properties of metallics in general, constructed Ti6Al4V(ELI) hierarchical HCs with percentage changes in CoVs limited to no more than 5% indicate surface roughness measurements that are more accurate and closer to the true value [61-62].

It is also garnered from Figure 8-1 that there is a gradual increase of the mean surface roughness with increasing order of hierarchy and a sharp drop arising from bead blasting. Smoothing out the top flat faces of the first-order hierarchical HC structure resulted in a $1.479 \mu\text{m}$ drop in Ra value, which is a significant 18% of the value for the unblasted surface. This implies the effect of bead blasting on surface roughness is significant considering that only a two-hour bead blasting period was used in this case. Thus, where surface roughness is critical, the process may be applied to reduce its magnitude. For the side inclined faces, Figure 8-2 reveals a similar trend to the one observed in the previous figure, with Ra values increased with increasing order of hierarchy for the three hierarchical HCs. The result of this analysis shows that the side inclined sides of the second-order hierarchical HC structure have the highest value of the mean surface roughness. The authors identify a knowledge gap on how different hierarchical levels affect surface quality. This forms part of their ongoing investigations on how geometric complexities, such as larger surface areas and variations in texture introduced by higher hierarchy levels, contribute to higher Ra values.

Figure 8-3 depicts the grouped surface roughness findings from the preceding two figures. The bar graphs in this figure clearly show the magnitude of the mean surface roughness to be greater for surfaces on the side inclined faces than on the top flat faces. For the zero-order, first-order, and second-order hierarchical structures, the magnitudes of Ra for the side inclined faces were 62.71%, 57.79%, and 58.55%, times higher than the values for the top flat surfaces, respectively. Therefore, in cases where surface roughness is critical, such as the use of hierarchical structures for transportation of fluids, this big difference demands the use of methods for smoothening surfaces in order to have similar values for all surfaces.

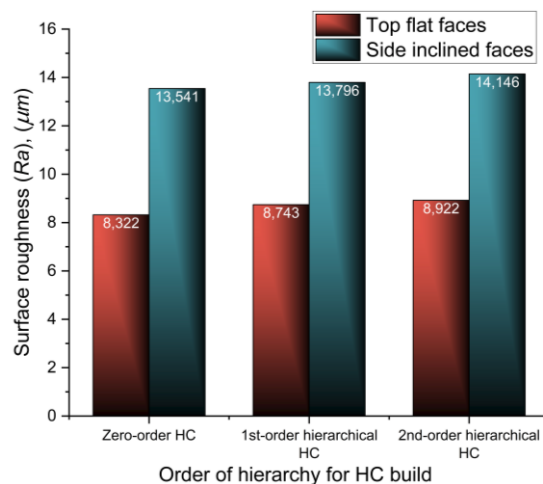


Figure 8-3. Grouped values of mean surface roughness for the top flat and side inclined faces

8.3.2 Mechanical behaviour

The effect of x -direction crushing. Throughout the crushing tests, a video recording examined the evolution of deformation and fracture for each tier of hierarchical HC loaded in the x - and y -directions separately. Camera images for each notable peculiar change in shape and fracture patterns for all the tested structures, for loads applied along the x - and y -directions, are presented in Figures 8-4 and 8-5, respectively.

The evolution of deformation shown in Figure 8-4 (for x -directional loading) reveals that bending loads on the primary walls (walls building the larger unit cells) are predominant and cause out-of-plane deflections of these walls to occur. As the compression load increases, the bending mechanism of the primary walls transitions into fractures in regions closer to the vertices of the primary walls. The regions closer to the vertices where fracture first occurs are highlighted by red circles with dotted lines for each level of hierarchy shown in this figure.

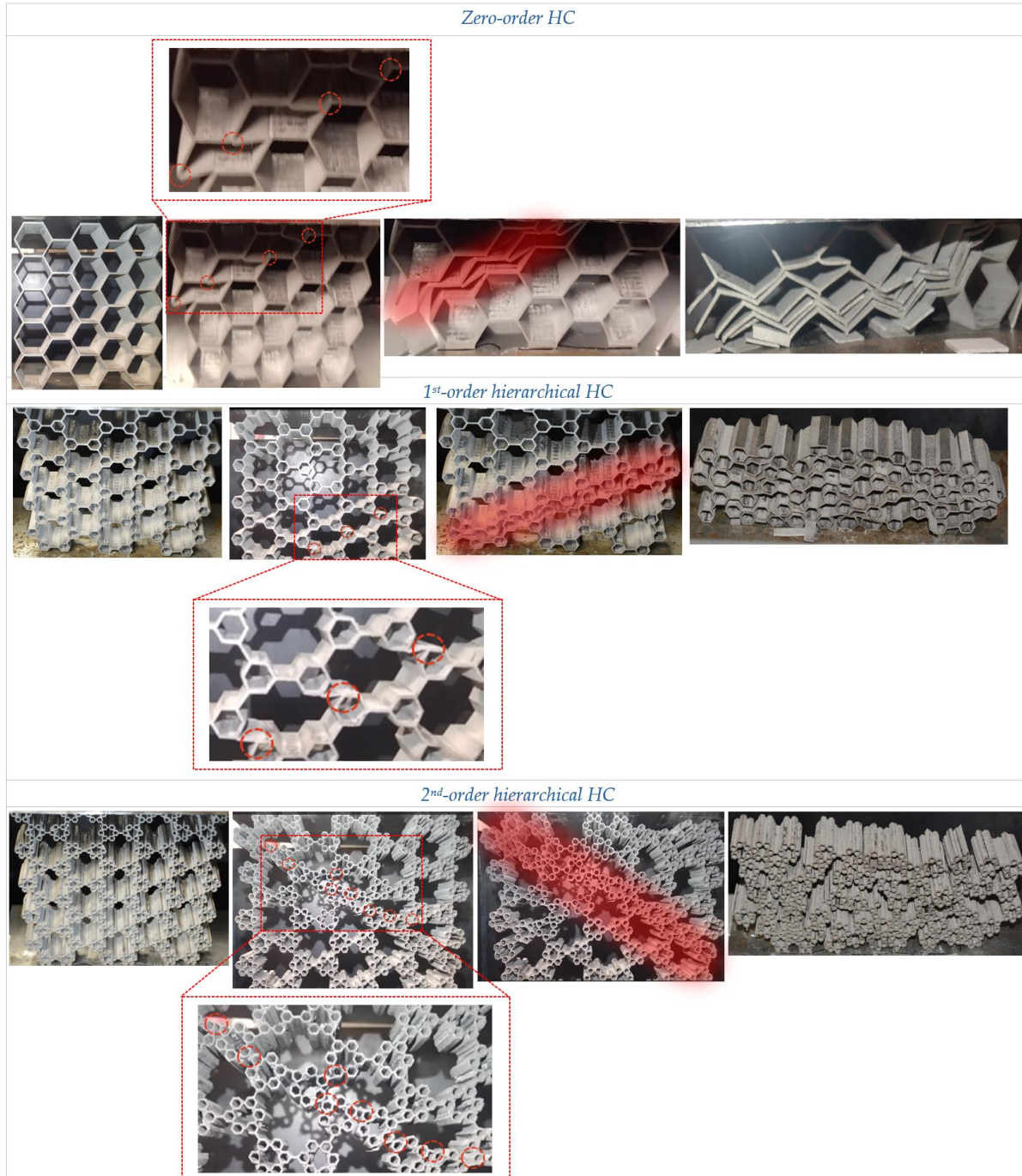


Figure 8-4. Evolution of deformation, fracture and bulk sliding in the three levels of hierarchical HCs under *x*-directional loading

For all the structures presented in this figure, the areas of the first fracture, identified by the red dotted circles, are aligned along an inclined line. During failure, the cell walls were observed to deform through bending and fail by sliding down this inclined line to the point where entire layers of primary unit cells come into contact with one another, as highlighted by the red shading in the third right images in Figure 8-4. During the sliding of primary cell walls along the inclined line, the load continues to drop until the primary cell walls are fully in contact. At this point, a set of primary cell walls for the next higher order of

hierarchy starts to deform and then fracture at the vertices in a similar manner, thus leading to a similar deformation and sliding as occurred for the lower order of hierarchy. Where there is an even higher order of hierarchy, the process repeats itself. This continues until all the primary cell walls are stacked and in full contact with the neighbouring ones, as illustrated in the far-right images of the different orders of hierarchy shown separately in Figure 8-4.

The effect of y -direction crushing. Though bending loads retain their predominance in the deformation of primary walls under the influence of y -directional loading, there are indications of buckling occurring in the vertically configured primary walls of the different levels of hierarchical structures whose camera images are presented in Figure 8-5. In contrast to the case for x -directional loading, the earliest stages of fracture occur at vertices of the primary walls along horizontal lines, which have been identified in Figure 8-5 by dotted red circles.

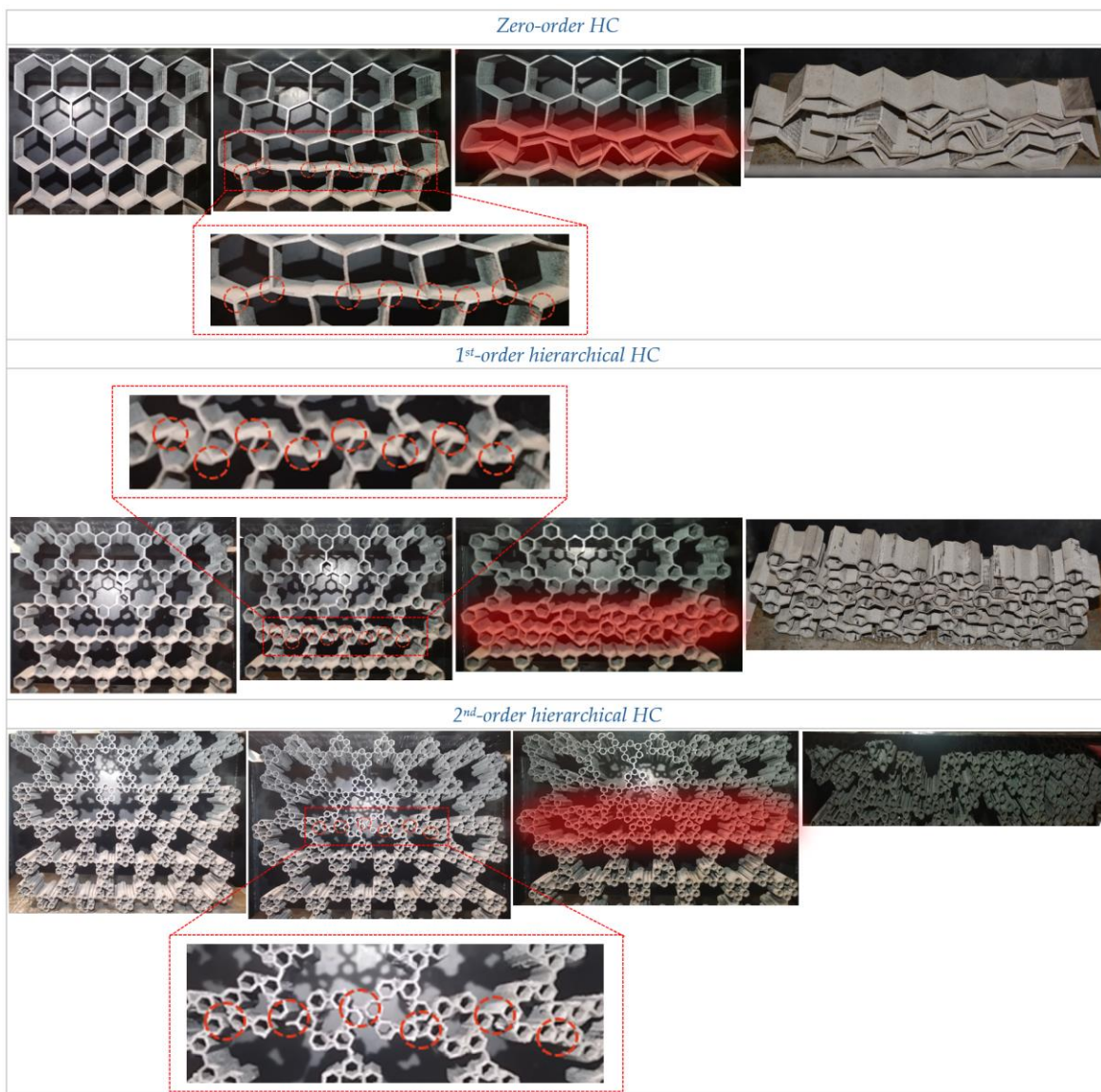


Figure 8-5. Evolution of deformation, fracture and bulk sliding in the three levels of hierarchical HCs under y -directional loading

Gibson and Ashby's foundational research [63], along with later studies [31-45, 52, 63-64], noted that the slender cell walls of HCs are prone to buckling under compressive in-plane loads. When a y -directional load is applied, vertical sections of the cell walls compress, further increasing the risk of buckling.

For loading in the y -direction, the primary cell walls, after the first stages of fracture, resort to sliding horizontally. This continues until adjacent primary cell walls are in full contact, as shown by the red shading of the various levels of hierarchical structures in Figure 8-5. Once full contact is attained, the process repeats itself for the next order of hierarchy and so on until all the primary walls are stacked and in contact with neighbouring ones, as confirmed by the far-right images for each order of hierarchy shown in Figure 8-5.

Deformation of hierarchical HCs was found to be predominantly due to bending loads. This is similar to what has been reported in numerous studies [41-45, 49, 52, 57-60, 65-66]. The observation is acceptable given the fact that the structures were built of thin walls and beams, which typically have low bending stiffnesses. As the applied loads increased, the structures experienced fracture at the vertices of primary walls. This is consistent with observations made in [60]. The vertices where the walls converge are known to be sites of stress concentration and are, therefore, expected to experience higher stress levels than the other areas of the structure, given that the load paths converge at these points. The deformation, fracture and sliding behaviour observed in this work has only been noted for zero-order HC structures [31-45] and is, therefore, novel in its extension to higher orders. Moreover, the different inclinations of sliding for loading along the x - and y -directions separately are peculiar to the present investigations.

Influence of the particular order of hierarchical structure. Further observations regarding the crush loading and the attendant deformation trends of the zero-order HC configuration, independent of the direction of loading (x or y), are made based on the camera images shown in Figure 8-6. The images reveal that, besides bending deflections and buckling deformation of the primary cell walls, some unit cells under crushing loads exhibit the Poisson's ratio effect for loading along both the x - or y -directions. Beyond this, the zero-order HC exhibited deformation and sliding until all the cell walls established full contact with neighbouring ones, at which point densification of the material started.

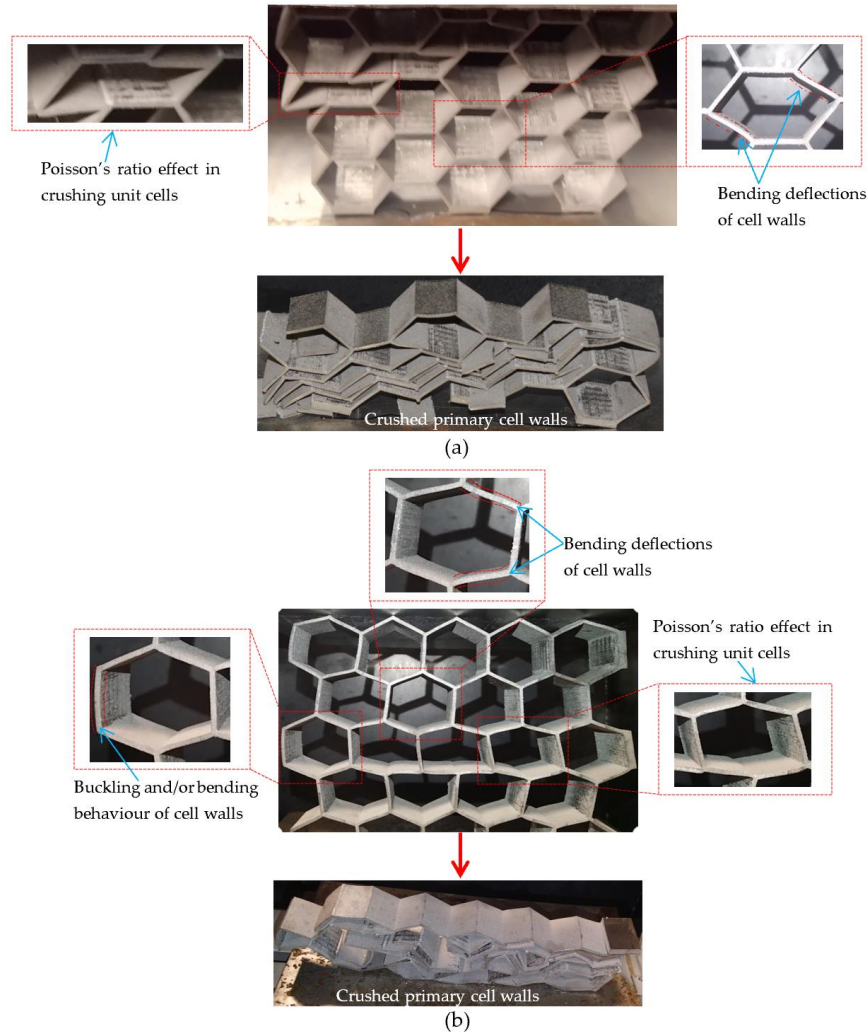


Figure 8-6. The deformation trends and levels of crushing till densification of the material for the zero-order HC loaded in the (a) x -direction and (b) y -direction

Since the lengths of the primary cell walls reduce as the hierarchy level in HCs increases, the magnitude of bending and buckling decreases as well. Moreover, as has been noted in the preceding discussion in this section, each order of hierarchy experiences similar crushing behaviour in a consecutive trend from the lowest to the highest order of hierarchy. Examples of this are shown in Figures 8-7 and 8-8 for the first- and second orders of hierarchy, respectively. This implies that the stiffness of the different hierarchies increases with increasing orders of hierarchy. These two considerations imply that the amount of energy absorbed during crushing will increase with increasing order hierarchy. Furthermore, this implies that the Poisson's ratio effect observed in zero-order HCs reduces with the increasing stiffness of higher hierarchical levels. This experimental finding is consistent with the literature that reports on Poisson's ratio effect on hierarchical HCs from theoretical models [57-60, 65-66]. In zero-order HCs, the load is distributed via a more basic network of cell walls. This implies that the transverse strain response to an axial load for this order is less complicated and simpler to observe. Distribution of load in higher levels of hierarchical HCs gets more complicated as the number of layers and interconnecting networks of cells increases, which could obscure or diminish the Poisson's ratio effect in experimental testing.

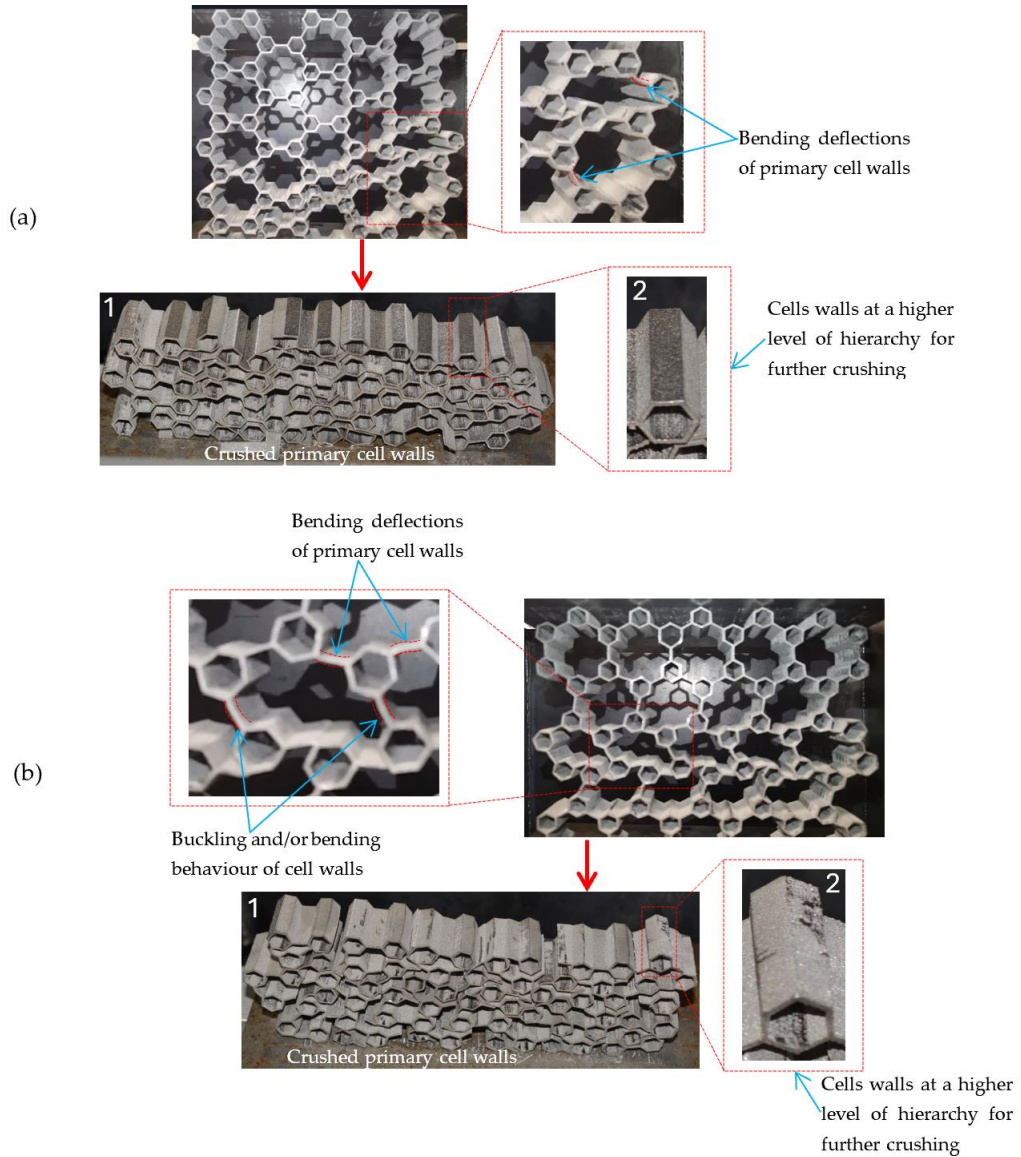


Figure 8-7. The deformation trends and levels of crushing before densification of the material for the first-order hierarchical HC loaded in the (a) x-direction and (b) y-direction

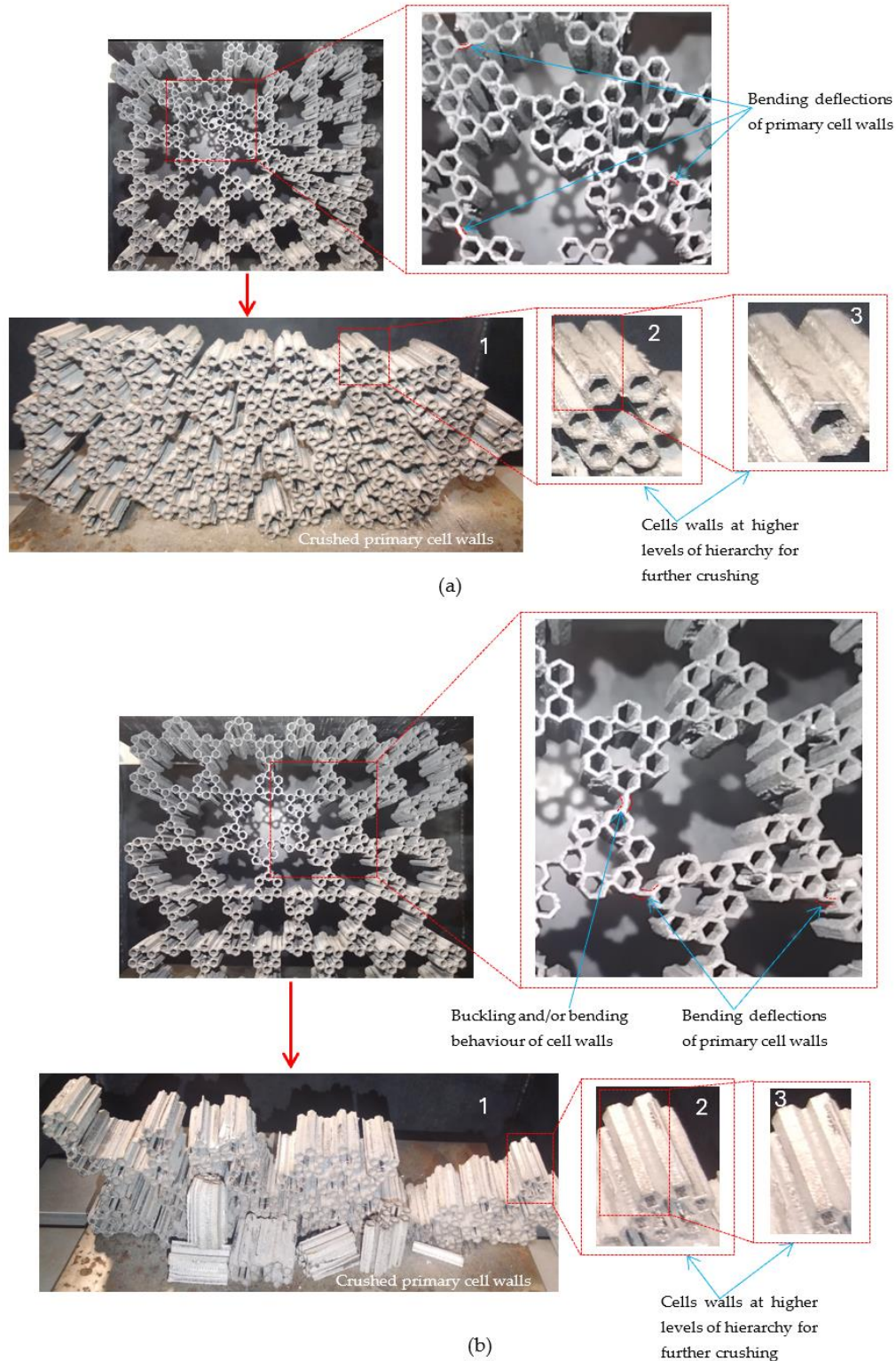


Figure 8-8. The deformation trends and levels of crushing before densification of the material for the second-order hierarchical HC loaded in the (a) x-direction and (b) y-direction

The observed further crushing events for each higher order of hierarchy implies that higher-order hierarchy in HCs is more crashworthy. These crushing events are a function of hierarchy and the attendant

scaling effects. For HC's hierarchical designs, smaller-scale structures were seen in the present work to support larger-scale ones in a progressive process of failure from large-scale to small-scale structures.

From the foregoing discussion, it also stands to reason that even as irreversible failure is experienced at lower levels of hierarchy, elastic recovery of higher levels of hierarchy will still occur after the applied load is removed.

Effects of loading direction on energy absorption in various hierarchical levels. The results in Figure 8-9 are used to rank the mechanical properties of all twelve DMLS-produced Ti6Al4V(ELI) specimens in terms of loading direction and hierarchical order. Since there were four specimens for each hierarchical level examined, numerals 1 and 2 were placed right after the prescribed x - and y -loading directions, which are indicated in brackets in the legend to differentiate their findings. Numerals 1 and 2 represent the first and second specimens in the prescribed direction of loading.

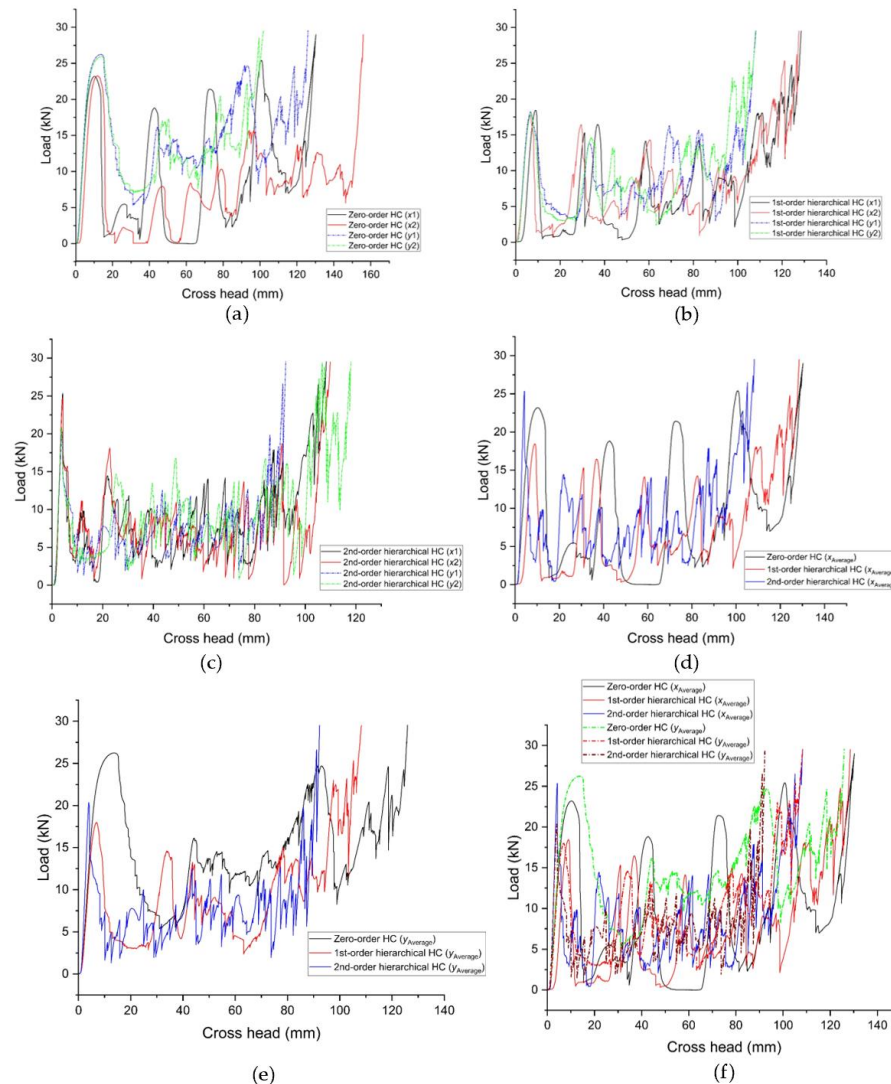


Figure 8-9. Load-displacement curves for crushing three levels of hierarchical HCs along the two x - and y - in-plane directions

The load curves for loading HCs with various hierarchical levels in the x - and y -direction independently (Figure 8-9) show a general trend in the increase in load and subsequent drop due to failure and further increase followed by drops, and so on. The load curve behaviour follows a sequence of

deformation, fracture, and sliding, which were discussed previously in this section and now explains the rise and drop pattern. Initially, the primary cell walls experience bending due to the load, causing out-of-plane deflections. As the load increases, bending transitions into localized fractures near the vertices of the primary walls. After fracturing, the walls begin to slide along an inclined path, resulting in a sudden drop in the load as the primary unit cells move closer together. Once these walls come into full contact, the load starts increasing again as the next level of hierarchy begins to deform, repeating the process. This cycle of bending, fracturing, and sliding continues through each hierarchical level until all walls are stacked in contact, explaining the repeated increases and drops in the load curve.

There is a clear difference between the height of the load drops for zero-order HCs loaded in the x - and y -directions, shown in Figure 8-9(a), where the former drops much lower. This difference in height is seen to diminish for higher hierarchical levels, as seen in Figure 8-9 (b, c). This implies that at lower hierarchical levels, deformation and failure mechanisms are more directionally dependent, with lower resistance in certain orientations. As the hierarchical level increases, the structures' behaviour tends to be more similar in the orthogonal directions in terms of distributing loads more evenly across different directions, leading to more uniform deformation and failure behaviour. This indicates that higher levels of hierarchical structures enhance structural stability [67] and reduce directional sensitivity.

There is also a clear reduction in the height of the load curves following the first peak and then a consistent increase in the peaks for ensuing cycles to a point where the final peaks are higher than the initial one observed for HCs of higher hierarchical levels, as shown in Figure 8-9(d, e). This implies that the deformation and failure mechanisms in HCs of higher hierarchical levels evolve with each cycle. The initial reduction indicates that early deformation and fracture primarily weaken the structure at the beginning, especially as localized fractures occur near the vertices of the primary cell walls [60]. The increasing peaks in later cycles imply that after an initial failure, the structure stabilizes as layers of primary cell walls come into full contact. This stacking effect likely strengthens the HC, allowing it to bear higher loads as the hierarchy continues to deform and fail in a more controlled and uniform manner, ultimately leading to stronger resistance in later stages. This pattern reflects how the hierarchical design enhances load distribution and energy absorption through progressive failure.

Averaging the load curves, as shown in Figure 8-9(d, e, and f), was necessary to account for inconsistencies like misalignments, material imperfections, or manufacturing deviations, which can introduce noise. This process smooths out fluctuations and provides a clearer, more reliable representation of the overall structural behaviour. In contrast, non-averaged curves may reflect irregularities specific to individual tests rather than the inherent material or design behaviour. Averaging highlights consistent trends in load capacity, deformation, and failure mechanisms, offering a more accurate and robust understanding of the structure's performance.

The load-bearing capacity of hierarchical HCs was observed to be ranked from highest to lowest from zero-order, first-order, and second-order hierarchical HCs for loading in the x - and y -directions separately. Such a ranking could occur because as the hierarchy increases, the load paths get more complicated, introducing more possible failure spots and lowering overall load-bearing capacity. Such ranking is not available in the literature, which was all found to be focused on energy absorption instead [31-45, 52-55, 59-60, 67]. Ranking the failure loads of three hierarchical HCs in two in-plane directions reveals significant performance differences among the various hierarchical designs. The zero-order HC ($x_{Average}$) has the lowest failure load and is not able to sustain higher loads before failure. The zero-order HC ($y_{Average}$) performs slightly better but still ranks low compared to HCs of higher hierarchical levels. The first-order hierarchical HCs show a notable increase in failure loads, indicating enhanced structural complexity and better stress distribution. The second-order hierarchical HCs rank the highest, featuring advanced designs that maximize load capacity and energy absorption. For loading in the x - and y -directions, the zero-order hierarchical HCs recorded average peak failure loads of approximately **19.75 kN** and **21.25 kN**, respectively. The first-order hierarchical HCs demonstrated improved performance, with average peak

loads of **23.25 kN** in the x -direction and **25.25 kN** in the y -direction. The second-order hierarchical HCs exhibited the highest average peak failure loads, reaching **25.50 kN** and **27.50 kN** in the x - and y -directions, respectively. This trend underscores the importance of hierarchical design in enhancing mechanical performance, with each level providing increased resilience and strength. In particular, the inclusion of vertex-based features appears to play a critical role in redistributing stress concentrations and delaying the onset of structural collapse. However, as noted previously in this section, the difference in failure loads diminishes with higher hierarchy levels for loading in the two in-plane x - and y -directions independently, preventing a clear ranking of the first- and second-order hierarchical HCs.

It must also be noted that in this study, the first- and second-order hierarchical HCs are only crushed at the first, lowest level of the hierarchy. This implies that if successive crushing events were to occur, higher energy absorption could be achieved due to the increased failure loads at higher hierarchical levels.

Failure as a function of the manufacturing flaws in the cell walls of the structure- The zero-order HC specimens ($x1$ and $x2$), shown in Figure 8-9(a), exhibit clear differences in load peaks after the first peak, with $x2$ showing significantly lower peaks. This difference, simply put, is related to the failure along an inclined line, as observed previously, where the cell wall separation is completed before complete crushing. This might denote the presence of flaws in the cell walls at the points where separation occurred and could denote poor sintering at the points. Figure 8-10 compares the load curves for both HCs in the x -direction, with $x2$ corresponding to the images in the figure.

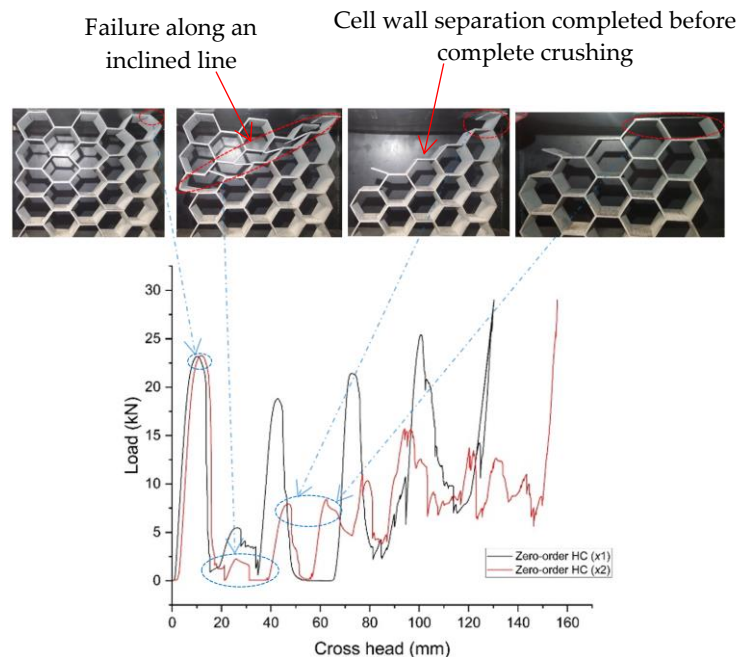


Figure 8-10. Specimen failure as a function of the manufacturing flaws in the cell walls

8.4. Scope and opportunities for future work

8.4.1 Challenges and the way forward in updating design concepts and experimental tests for additively-produced hierarchical lattice parts

Mechanically removing scaffolds is labour-intensive and can result in delamination, surface damage and, therefore, significant inaccuracies, particularly in complex designs such as hierarchical lattice structures [61-62, 68]. In addition, the method of removing scaffolding is laborious and slow and causes delays in production, which is a serious problem, particularly in sectors such as aerospace, where delivery on schedule is crucial [61]. The challenge, thus, is finding faster and more effective removal procedures

without sacrificing the quality or safety of printed complex metallic parts [15, 69]. To address these challenges, robotic systems should be developed equipped with machine learning and vision-based pattern recognition to accurately identify and remove scaffolds from complex lattice structures, reducing labour intensity and improving precision in scaffold removal. Investigation should be carried out to produce scaffolds that are easy to remove, with greater accuracy, and that require minimal human labour. Scaffolds could be developed from materials that dissolve or change phase when triggered by specific stimuli (e.g., heat, solvents, or magnetic fields). This method allows for non-invasive removal, reducing the risk of delamination and surface damage. Material-based design strategies should be explored to reduce the need for scaffolding by optimizing mechanical properties and weight distribution in complex parts during AM. Hierarchical lattices with graded densities can offer inherent support, minimizing dependence on external scaffolds.

The damage models used at present for analysing the crushing behaviour for both regular and hierarchical lattice systems are lacking because their predictions are constrained to the first load drop. Powerful and proven dimensional analysis concepts, including the Buckingham Pi theorem [70], must be applied in the development of upgraded damage models that could add to the core aspect in the study of damage in complicated structures. These upgraded damage models should integrate micromechanical mechanisms for damage to accurately capture progressive failure at various scales within hierarchical structures. The use of continuum damage mechanics strategies that take account of damage accumulation and its effect on the properties of materials should be considered as well. Furthermore, it should interact with cohesive zone models to mimic crack initiation and propagation, thus providing a more accurate representation of post-peak behaviour.

Comparing the current physical experiments on regular hierarchical HCs with numerical models of topology-optimized hierarchical HCs is essential for validating performance improvements from optimization strategies. Regular models offer foundational insights into structural behaviour, while TO enhances effectiveness, reduces weight, and increases robustness by tailoring material distribution to specific loading conditions. This comparison allows researchers to assess the impact of optimization on strength, stiffness, and failure modes, ensuring that theoretical benefits translate into tangible physical advantages, thereby enhancing the entire design process.

References

1. Habib, F. N., Iovenitti, P., Masood, S. H., & Nikzad, M. (2018). Fabrication of polymeric lattice structures for optimum energy absorption using Multi Jet Fusion technology. *Materials & Design*, 155, 86-98.
2. Siddique, S. H., Hazell, P. J., Wang, H., Escobedo, J. P., & Ameri, A. A. (2022). Lessons from nature: 3D printed bio-inspired porous structures for impact energy absorption—A review. *Additive Manufacturing*, 58, 103051.
3. Isaac, C. W., and Duddeck, F. (2022). Current trends in additively manufactured (3D printed) energy absorbing structures for crashworthiness application—a review. *Virtual and Physical Prototyping*, 17(4), 1058-1101.
4. Greco, L., Buccino, F., Xu, Z., Vergani, L., Berto, F., Guagliano, M., ... & Bagherifard, S. (2023). Design and analysis of energy absorbent bioinspired lattice structures. *Journal of Bionic Engineering*, 20(4), 1670-1686.
5. Ramakrishna, D., and Bala Murali, G. (2023). Bio-inspired 3D-printed lattice structures for energy absorption applications: A review. *Proceedings of the Institution of Mechanical Engineers, Part L: Journal of Materials: Design and Applications*, 237(3), 503-542.
6. Mohammadi, H., Ahmad, Z., Petru, M., Mazlan, S. A., Johari, M. A. F., Hatami, H., & Koloor, S. S. R. (2023). An insight from nature: honeycomb pattern in advanced structural design for impact energy absorption. *Journal of Materials Research and Technology*, 22, 2862-2887.

7. Yang, Y., Song, X., Li, X., Chen, Z., Zhou, C., Zhou, Q., & Chen, Y. (2018). Recent progress in biomimetic additive manufacturing technology: from materials to functional structures. *Advanced Materials*, 30(36), 1706539.
8. Dejene, N. D., and Lemu, H. G. (2023). Current status and challenges of powder bed fusion-based metal additive manufacturing: literature review. *Metals*, 13(2), 424.
9. Ahmed, A. A., Nazzal, M. A., Darras, B. M., Eltaggaz, A., & Deiab, I. M. (2024). Comparative sustainability assessment of powder bed fusion and solid-state additive manufacturing processes: The case of direct metal laser sintering versus additive friction stir deposition. *Sustainable Materials and Technologies*, 39, e00858.
10. Jiménez, A., Bidare, P., Hassanin, H., Tarlochan, F., Dimov, S., & Essa, K. (2021). Powder-based laser hybrid additive manufacturing of metals: a review. *The International Journal of Advanced Manufacturing Technology*, 114, 63-96.
11. Zhang, Y., Yang, S., & Zhao, Y. F. (2020). Manufacturability analysis of metal laser-based powder bed fusion additive manufacturing—a survey. *The International Journal of Advanced Manufacturing Technology*, 110, 57-78.
12. Madhavadas, V., Srivastava, D., Chadha, U., Raj, S. A., Sultan, M. T. H., Shahar, F. S., & Shah, A. U. M. (2022). A review on metal additive manufacturing for intricately shaped aerospace components. *CIRP Journal of Manufacturing Science and Technology*, 39, 18-36.
13. Liu, G., Zhang, X., Chen, X., He, Y., Cheng, L., Huo, M., ... & Lu, J. (2021). Additive manufacturing of structural materials. *Materials Science and Engineering: R: Reports*, 145, 100596.
14. Hasanov, S., Alkunte, S., Rajeshirke, M., Gupta, A., Huseynov, O., Fidan, I., ... & Rennie, A. (2021). Review on additive manufacturing of multi-material parts: Progress and challenges. *Journal of Manufacturing and Materials Processing*, 6(1), 4.
15. Ngo, T. D., Kashani, A., Imbalzano, G., Nguyen, K. T., & Hui, D. (2018). Additive manufacturing (3D printing): A review of materials, methods, applications and challenges. *Composites Part B: Engineering*, 143, 172-196.
16. Suresh, G., Ramesh, M. R., & Srinath, M. S. (2022). Surface engineered titanium alloys for biomedical, automotive, and aerospace applications. *Advances in Processing of Lightweight Metal Alloys and Composites: Microstructural Characterization and Property Correlation*, 89-102. Singapore: Springer Nature Singapore.
17. Salihu, S. A., Suleiman, Y. I., & Eyinavi, A. I. (2019). Classification, properties and applications of titanium and its alloys used in automotive industry—A review. *Am. J. Eng. Res*, 4, 92-98.
18. Singh, N., Hameed, P., Ummethala, R., Manivasagam, G., Prashanth, K. G., & Eckert, J. (2020). Selective laser manufacturing of Ti-based alloys and composites: Impact of process parameters, application trends, and future prospects. *Materials Today Advances*, 8, 100097.
19. Avila, J. D., Bose, S., & Bandyopadhyay, A. (2018). Additive manufacturing of titanium and titanium alloys for biomedical applications. *Titanium in Medical and Dental Applications*, 325-343. Woodhead Publishing.
20. Dhinakaran, V., Varsha Shree, M., Jagadeesha, T., & Swapna Sai, M. (2022). Additive manufacturing: technology, materials and applications in aerospace. *Light Weight Materials: Processing and Characterization*, 1-22.
21. Khorasani, A. M., Goldberg, M., Doeven, E. H., & Littlefair, G. (2015). Titanium in biomedical applications—properties and fabrication: a review. *Journal of Biomaterials and Tissue Engineering*, 5(8), 593-619.
22. Tshephe, T. S., Akinwamide, S. O., Olevsky, E., & Olubambi, P. A. (2022). Additive manufacturing of titanium-based alloys - A review of methods, properties, challenges, and prospects. *Heliyon*, 8(3).

23. Salas, D., Ebeperi, D., Elverud, M., Arróyave, R., Malak, R. J., & Karaman, I. (2022). Embedding hidden information in additively manufactured metals via magnetic property grading for traceability. *Additive Manufacturing*, 60, 103261.
24. Hou, N., Wang, M., Wang, B., Zheng, Y., Zhou, S., & Song, C. (2021). Fundamental functions of physical and chemical principles in the polishing of titanium alloys: mechanisms and problems. *The International Journal of Advanced Manufacturing Technology*, 1-19.
25. Colorado, H. A., Cardenas, C. A., Gutierrez-Velazquez, E. I., Escobedo, J. P., & Monteiro, S. N. (2023). Additive manufacturing in armor and military applications: research, materials, processing technologies, perspectives, and challenges. *Journal of Materials Research and Technology*, 27, 3900-3913.
26. Mouzakis, D. E. (2018). Advanced technologies in manufacturing 3D-layered structures for defense and aerospace. *Lamination-theory and application*, 74331.
27. Rouf, S., Malik, A., Singh, N., Raina, A., Naveed, N., Siddiqui, M. I. H., & Haq, M. I. U. (2022). Additive manufacturing technologies: Industrial and medical applications. *Sustainable Operations and Computers*, 3, 258-274.
28. Mani, M., Witherell, P., & Jee, H. (2017). Design rules for additive manufacturing: A categorization. *International Design Engineering Technical Conferences and Computers and Information in Engineering Conference*, 58110, V001T02A035. *American Society of Mechanical Engineers*.
29. Makes, A., and Collaborative, A. A. M. S. (2017). Standardization roadmap for additive manufacturing. (February), *Public Draft*.
30. Russell, R., Wells, D., Waller, J., Poorganji, B., Ott, E., Nakagawa, T., ... & Seifi, M. (2019). Qualification and certification of metal additive manufactured hardware for aerospace applications. *Additive Manufacturing for the Aerospace Industry*, 33-66.
31. Jaiswal, N., Bharti, U., Yadav, A., Srivastava, M., & Rathee, S. (2024). Static structural and thermal analysis of honeycomb structure fabricated by friction stir processing route: A case study. *Friction Stir Welding and Processing: Fundamentals to Advancements*, 283-292.
32. Islam, K. N., Hildenbrand, J., & Hossain, M. M. (2018). Life cycle impacts of three-way ceramic honeycomb catalytic converter in terms of disability adjusted life year. *Journal of Cleaner Production*, 182, 600-615.
33. Tsinoglou, D. N., Eggenschwiler, P. D., Thurnheer, T., & Hofer, P. (2009). A simplified model for natural-gas vehicle catalysts with honeycomb and foam substrates. *Proceedings of the Institution of Mechanical Engineers, Part D: Journal of Automobile Engineering*, 223(6), 819-834.
34. Hu, B., Yao, J., An, N., Mi, H., & Bai, X. (2023). Numerical investigation on the effects of HC geometry on the flow and heat transfer in the disk cavity system at the turbine vane root. *Applied Thermal Engineering*, 230, 120794.
35. Munir, A. (2017). Microwave radar absorbing properties of multiwalled carbon nanotubes polymer composites: a review. *Advances in Polymer Technology*, 36(3), 362-370.
36. Zhang, Y., Yang, L., Tian, Y., Li, L., Li, J., Qiu, T., ... & Ji, X. (2019). Honeycomb hard carbon derived from carbon quantum dots as anode material for K-ion batteries. *Materials Chemistry and Physics*, 229, 303-309.
37. Sajjad, M., and Lu, W. (2022). Honeycomb-based heterostructures: An emerging platform for advanced energy applications: A review on energy systems. *Electrochemical Science Advances*, 2(5), e202100075.
38. Mohammadi, H., Ahmad, Z., Petru, M., Mazlan, S. A., Johari, M. A. F., Hatami, H., & Koloor, S. S. R. (2023). An insight from nature: honeycomb pattern in advanced structural design for impact energy absorption. *Journal of Materials Research and Technology*, 22, 2862-2887.
39. Dai, H., Dai, W., Hu, Z., Zhang, W., Zhang, G., & Guo, R. (2023). Advanced composites inspired by biological structures and functions in nature: architecture design, strengthening mechanisms, and mechanical-functional responses. *Advanced Science*, 10(14), 2207192.

40. Hönig, A., and Stronge, W. J. (2002). In-plane dynamic crushing of honeycomb. Part I: Crush band initiation and wave trapping. *International Journal of Mechanical Sciences*, 44(8), 1665-1696.
41. Papka, S. D., and Kyriakides, S. (1998). Experiments and full-scale numerical simulations of in-plane crushing of a honeycomb. *Acta Materialia*, 46(8), 2765-2776.
42. Hu, L. L., and Yu, T. X. (2010). Dynamic crushing strength of hexagonal honeycombs. *International Journal of Impact Engineering*, 37(5), 467-474.
43. Papka, S. D., and Kyriakides, S. (1998). In-plane crushing of a polycarbonate honeycomb. *International Journal of Solids and Structures*, 35(3-4), 239-267.
44. Galehdari, S. A., Kadhodayan, M., & Hadidi-Moud, S. (2015). Analytical, experimental and numerical study of a graded honeycomb structure under in-plane impact load with low velocity. *International Journal of Crashworthiness*, 20(4), 387-400.
45. Papka, S. D., and Kyriakides, S. (1999). Biaxial crushing of honeycombs: Part 1: Experiments. *International Journal of Solids and Structures*, 36(29), 4367-4396.
46. Zhang, Q., Yang, X., Li, P., Huang, G., Feng, S., Shen, C., ... & Lu, T. J. (2015). Bioinspired engineering of honeycomb structure—Using nature to inspire human innovation. *Progress in Materials Science*, 74, 332-400.
47. Akdag, S., Karakus, M., Nguyen, G. D., & Taheri, A. (2020). Strain burst vulnerability criterion based on energy-release rate. *Engineering Fracture Mechanics*, 237, 107232.
48. Lazarus, B. S., Velasco-Hogan, A., Gómez-del Río, T., Meyers, M. A., & Jasiuk, I. (2020). A review of impact resistant biological and bioinspired materials and structures. *Journal of Materials Research and Technology*, 9(6), 15705-15738.
49. Mozafari, H., Molatefi, H., Crupi, V., Epasto, G., & Guglielmino, E. (2015). In plane compressive response and crushing of foam filled aluminum honeycombs. *Journal of Composite Materials*, 49(26), 3215-3228.
50. Zhou, Y., Pan, Y., Gao, Q., & Sun, B. (2023). In-plane quasi-static crushing behaviors of a novel re-entrant combined-wall honeycomb. *Journal of Applied Mechanics*, 90(5), 051002.
51. Choudhry, N. K., Panda, B., & Kumar, S. (2022). In-plane energy absorption characteristics of a modified re-entrant auxetic structure fabricated via 3D printing. *Composites Part B: Engineering*, 228, 109437.
52. Qi, C., Jiang, F., & Yang, S. (2021). Advanced honeycomb designs for improving mechanical properties: A review. *Composites Part B: Engineering*, 227, 109393.
53. Sajjad, M., and Lu, W. (2022). Honeycomb-based heterostructures: An emerging platform for advanced energy applications: A review on energy systems. *Electrochemical Science Advances*, 2(5), e202100075.
54. Wang, Z. (2019). Recent advances in novel metallic honeycomb structure. *Composites Part B: Engineering*, 166, 731-741.
55. Choi, W. H., and Kim, C. G. (2015). Broadband microwave-absorbing honeycomb structure with novel design concept. *Composites Part B: Engineering*, 83, 14-20.
56. Wei, X., Xiong, J., Wang, J., & Xu, W. (2020). New advances in fiber-reinforced composite honeycomb materials. *Science China Technological Sciences*, 63(8), 1348-1370.
57. Oftadeh, R., Haghpanah, B., Vella, D., Boudaoud, A., & Vaziri, A. (2014). Optimal fractal-like hierarchical honeycombs. *Physical Review Letters*, 113(10), 104301.
58. Oftadeh, R., Haghpanah, B., Papadopoulos, J., Hamouda, A. M. S., Nayeb-Hashemi, H., & Vaziri, A. (2014). Mechanics of anisotropic hierarchical honeycombs. *International Journal of Mechanical Sciences*, 81, 126-136.
59. Zhang, Y., Lin, Y., Li, Y., & Li, X. (2021). 3D printed self-similar AlSi10Mg alloy hierarchical honeycomb architectures under in-plane large deformation. *Thin-Walled Structures*, 164, 107795.
60. Zhang, Y., Lin, Y., & Li, X. (2021). Plastic crushing failure of bio-inspired cellular hierarchical topological sandwich core. *Materials*, 14(17), 5040.

61. Ishfaq, K., Abdullah, M., & Mahmood, M. A. (2021). A state-of-the-art direct metal laser sintering of Ti6Al4V and AlSi10Mg alloys: Surface roughness, tensile strength, fatigue strength and microstructure. *Optics & Laser Technology*, 143, 107366.
62. Fotovvati, B., and Asadi, E. (2019). Size effects on geometrical accuracy for additive manufacturing of Ti-6Al-4V ELI parts. *The International Journal of Advanced Manufacturing Technology*, 104, 2951-2959.
63. Gibson, I. J., & Ashby, M. F. (1982). The mechanics of three-dimensional cellular materials. *Proceedings of the Royal Society of London. A. Mathematical and Physical Sciences*, 382(1782), 43-59.
64. Zhong, H., Song, T., Li, C., Das, R., Gu, J., & Qian, M. (2023). The Gibson-Ashby model for additively manufactured metal lattice materials: Its theoretical basis, limitations and new insights from remedies. *Current Opinion in Solid State and Materials Science*, 27(3), 101081.
65. Chen, Y., and Hu, H. (2020). In-plane elasticity of regular hexagonal honeycombs with three different joints: A comparative study. *Mechanics of Materials*, 148, 103496.
66. Ajdari, A., Jahromi, B. H., Papadopoulos, J., Nayeb-Hashemi, H., & Vaziri, A. (2012). Hierarchical honeycombs with tailorable properties. *International Journal of Solids and Structures*, 49(11-12), 1413-1419.
67. Qiao, J., and Chen, C. (2016). In-plane crushing of a hierarchical honeycomb. *International Journal of Solids and Structures*, 85, 57-66.
68. Narasimharaju, S. R., Liu, W., Zeng, W., See, T. L., Scott, P., Jiang, X., & Lou, S. (2021). Surface texture characterization of metal selective laser melted part with varying surface inclinations. *Journal of Tribology*, 143(5), 051106.
69. Vafadar, A., Guzzomi, F., Rassau, A., & Hayward, K. (2021). Advances in metal additive manufacturing: a review of common processes, industrial applications, and current challenges. *Applied Sciences*, 11(3), 1213.
70. Martínez-Rojas, J. A., and Fernández-Sánchez, J. L. (2023). Combining dimensional analysis with model-based systems engineering. *Systems Engineering*, 26(1), 71-87.

CHAPTER NINE: CONCLUSIONS AND RECOMMENDATIONS

9.1. Introduction

This research study aimed to construct an optimal DMLS Ti6Al4V(ELI) hierarchical honeycomb (HC) lattice design with the highest feasible order of hierarchy using existing literature and discussions on their mechanical properties under quasi-static compression loads. Different polygon types, including triangular, circular, rectangular, and hexagonal unit cells, were examined and graded based on their mechanical properties, including strength, stiffness, toughness, deformation, and stress distribution. Analytical, numerical, and experimental modelling techniques were used to analyze the properties of these polygon types. The study also explored stress distribution in both regular and hierarchical lattice topologies. The restricting order of hierarchy was established for HCs. TO and SO were performed on planar HCs. The same shapes used to generate numerical models were physically tested for mechanical properties to determine the most prevalent failure mechanisms in the modelled hierarchical HCs.

9.2. Conclusions emerging from the various chapters

The four sections now being presented have contents that best summarize the findings drawn from the various chapters of the current work.

9.2.1. Review of cellular and lattice structures (Chapter 2)

Conclusions on cellular structures. Present-day natural cellular structures are sorted into open-based, closed-based, and polygon-based types, with multiscale hierarchical arrangements optimized through evolution. Their diverse morphologies enable various applications, while mechanical properties are influenced by material and geometry. Bioinspired designs are increasingly applied in automotive, aerospace, and medical fields but face limitations in replicating the complexity of natural structures across scales.

Conclusions on lattice structures and hierarchical structures. Present-day lattice structures are categorized into four types: polygon-based, strut-based, skeletal, and sheet TPMS-based. Efficient lattice generation depends on unit cell design and arrangement. Latticing and TO methods are the most effective for optimizing load distribution and improving mechanical properties. Mechanical properties vary with unit cell shape, size, topology, and configuration, enabling tailored designs for specific applications. Material usage and polygon area/volume coverage aid in ranking structures for performance and cost efficiency. While lattice structures mimic natural cellular designs, they are limited by geometric complexity and AM resolution. Biomimetic structures struggle to match natural properties, and quantitative comparisons of diffusion and heat conductivity are lacking. The integration of lattice and biological structures remains challenging, particularly in removing stuck powder and support material in complex designs.

The multiscale design, load transfer mechanisms, anisotropic properties, scale dependency, energy absorption capabilities, and fracture behaviour of hierarchical HCs all affect their deformation behaviour. By thoroughly understanding and characterizing all these factors, it is anticipated that engineers could generate hierarchical HCs with particular mechanical properties for a range of engineering applications, including energy-absorbing structures, lightweight structures, and materials that are capable of withstanding high-impact loads. When determining the possible levels of hierarchy that can be achieved for hierarchical HCs, material properties used in the production of the parts, constraints in using imaging tools for evaluation of parts, generating accurate numerical models to validate experimental data, prematurely developed algorithms for controlling complex hierarchical data sets, heterogeneity observed in biological materials being mimicked, scaling of parts, and manufacturing defects, are all primary challenges in design for AM.

Conclusions on analytical models describing deformation behaviour in cellular and lattice structures. The models built for predicting the behaviour of cellular structures can do so, but their accuracy becomes

limited at particular microscales because of computational constraints or when attempting to predict the behaviour at numerous scales concurrently. Considering this, the existing deformation behaviour models for cellular structures struggle to predict material properties such as non-linearity, anisotropy, or viscoelasticity. The proposed stress-strain curve for cellular designs revealed four stages of deformation: first, buckling and bending of the structure, elastic deformation during densification while buckling and bending continue, full elastic deformation, and lastly, plastic deformation forming a plateau. There are three cases of deformation likely to occur in cellular and lattice structures, namely, buckling deformation, bending deflections, transverse shear and direct deformation. The combined deformation mechanisms prevailing in a loaded lattice structure are best addressed by considering the arising stresses and failure for all of them simultaneously. Thus, the increasing order of direct, bending and buckling failure stresses for the basic model (Figure 2-34) was adopted in Chapter 2. There is an absence of analytical models in the literature describing the application of the Tresca and von Mises failure criteria on lattice structures.

Polygon-based lattice structures are typically designed and manufactured using struts or beams. The mechanical properties of lattice parts are different for varying designs and configurations. The planar in-plane loaded circular hollow structure ranks highest in terms of transverse stiffness compared to those built using hexagonal, triangular, and square cells. Polygon lattice structures are predominantly used in applications requiring a high absorption of strain energy. This is associated with their capability of absorbing high-strain energies for loading in the planar out-of-plane directions. The higher values of stiffness of lattice structures in the planar in-plane directions create possibilities of using them this way for crashworthiness using materials with lower values of stiffness. The analytical models adopted for describing the load-bearing capability of polygon lattice parts loaded in the planar in-plane directions are observed to be limited to general mathematical representations of strain energies. Additionally, the analytical models are lacking in accounting for the effect of unit cell connectivity or the way in which the polygon lattice architecture functions. For loading polygon hollow parts in the planar out-of-plane direction, analytical models in the literature are observed to be limited to the hexagonal shape only. This creates space to develop models based on other types of polygon structures.

9.2.2. Quasi-static numerical modelling of polygon structures (Chapter 4)

- The small difference of about 3.71% in the maximum von Mises stresses of planar and extruded hexagonal models justified using the planar model instead of the more complex extruded model to reduce computing resources.
- The disparities observed at the vertices of the extruded hexagonal shell could result in the development of topologies with no congruence at the vertices in TO and SO and, therefore, constrain further numerical modelling.
- The triangular polygon recorded the lowest deflections for the same magnitude of load applied in each direction separately. It also recorded the lowest maximum von Mises stress in the x -direction and the second lowest maximum von Mises stress in the y -direction for the same magnitude of load applied in both directions, separately. As a result, the triangular polygon is considered the best alternative of the four polygons studied here.
- The FE HC shell model achieved bending deflection and axial deformation shapes that are consistent with the literature for out-of-plane loading.
- The critical buckling loads for HC numerical shell models of different thicknesses generated von Mises stresses that were higher than the material's yield stress. This contrasts with the case for analytical modelling, in which the critical loads generated von Mises stresses for the first three HC shell models of (1, 1.125 and 1.25) mm wall thickness, which was below the yield stress of the material used here. The critical buckling loads were observed to increase as the ratio t/L grew. The HC shell numerical model was significantly stiffened due to the restraining action of hexagonal cells against one another.

- Nonlinear analysis has the advantage of accounting for plastic deformation, which is not possible with linear analysis. The degree of plastic deformation is higher at the mid-points of hexagonal cell plates. Therefore, it may be suggested that the structure fails due to axial compression first and then buckling.
- The numerical and analytical models for the HC shell structure both showed that the effective stiffness increased with the t/L ratio.

9.2.3 Quasi-static numerical modelling of first-order hierarchical structures (Chapter 5)

- The hierarchical HC structure loaded in the x -direction achieved lower values of maximum von Mises stresses than when loaded in the y -direction. This implies that the mechanical properties of hierarchical lattice structures must be tailored for various structural applications in accordance with the load transfer direction.
- The HCH structure showed the lowest value of maximum von Mises stress when load was applied in the x -direction. The structure is thus recommended for higher load-bearing capacity along the x -direction.
- When loaded in the y -direction, the HCC structure achieved the lowest value of maximum von Mises stress. Thus, this structure is recommended for load-bearing capacity along the y -direction. The outcome contributes to our understanding of how lattice designs could be tailored to improve structural performance. The alternating rankings of HCH and HCC structures underline the importance of directional strength in lattice architectures.
- The HCH structure exhibited the lowest deflection for loading in the x -direction, and is, therefore, the stiffest structure for this direction of loading of all the structures analyzed here.
- The HCC structure was determined to be the stiffest for y -direction loading because it had the lowest maximum value of deflection in this direction. The study broadens the existing knowledge base and paves the way for subsequent studies into the deflection behaviour of complex lattice structures. The stiffness rankings for HCH and HCC structures in different orientations are useful for engineers and designers who intend to optimize lattice structures for specific uses. Depending on the directional loading assumptions in a particular case, designers can customize their designs to attain the optimal stiffness.

9.2.4. Quasi-static numerical crushing of hierarchical structures (Chapter 6)

- The numerical quasi-static crushing experiments on hierarchical HCs revealed that bending deformation appears dominant under x -directional load. Conversely, under y -directional load, the deformation response modes showed that they are influenced by bending and buckling loads.
- Most of the material at the vertices of such structures exceeded the value of its yield strength, failing in these regions first for the two loading directions separately.
- Under y -directional load, buckling of the vertically positioned cell walls of a regular HC revealed that this eventually caused instability after some of the cell vertices had von Mises stress values that exceeded the material's yield strength. This caused the structure to rotate along the z -axis instead of being entirely crushed along the y -axis, as expected.
- For crushing the regular HC in both directions separately, some of the deformed cells revealed that they had the Poisson's ratio phenomenon.
- The load-displacement curve generated for loading the regular HC structure in the x -axis revealed a significantly low oscillatory response.

9.2.5 TO and SO for planar HCs (Chapter 7)

- The mesh converged for mesh sizes below 0.9 mm.
- The topology-optimized planar unit hexagonal cell and the HC had maximum material density reductions of 30% and 8%, respectively. The respective fictitious densities gave rise to maximum penalty scores of 0.3 and 0.18 before a lack of continuity in the elements was visible on them. The unit hexagonal cell had high penalty scores compared with the HC model because it had fewer constraints that reduced the effectiveness of TO.
- The reduction of densities occurred on the edges instead of through the creation of voids in the design space. The solver chose this as the most effective solution for controlling the occurrence of element discontinuities, which randomly reduced the stiffness of thin-walled structures.
- The vertices and edges for the inclined members and the mid-span for the loaded and fixed members exhibited higher preservations of density.
- The numerical models of TO with penalty score values of 0.3 and 0.15 with respect to the unit hexagonal cell and the HC model gave rise to maximum stress reductions of 58% and 4%, respectively, SO. The unit hexagonal cell was expected to have higher stress reductions than the HC model because it had fewer constraints that reduced the effectiveness of SO.

9.2.6. Quasi-static crushing experiments of hierarchical structures (Chapter 8)

- The observed surface roughness deviations in DMLS-produced specimens indicate potential inconsistencies in the AM process, which could influence the mechanical performance and reliability of the final parts. Comparisons of three orders of hierarchy of HCs revealed that the average surface roughness (R_a) increased with increasing hierarchy. The R_a for each hierarchical level in HCs also showed lower readings for the top flat surfaces than for side inclined surfaces. Simple bead blasting led to a significant improvement in the average surface roughness.
- The walls of the hierarchical structures were observed to deform primarily through beam bending. Buckling deformation was pronounced for y -direction loading.
- The drop of loads after attaining peaks in an oscillatory manner was thought to be a result of fracture at the vertices of walls, following initial primarily bending and/or buckling as the case was.
- The hierarchical HCs collapsed under compression loads via bending and/or buckling, Poisson's ratio lateral expansion, and finally, sliding along an inclined line and horizontally, for x - and y -direction loading, respectively.
- Crushing was observed to occur sequentially, starting with the lowest order of hierarchy and moving up to the highest order.
- Zero-order HCs had the lowest average failure load (19.75 kN and 21.25 kN for loading in the x - and y -directions, respectively). While first-order HCs showed an increase to 23.25 kN and 25.25 kN for loading in the x - and y -directions, respectively. Second-order HCs exhibited the highest average failure loads (25.50 kN and 27.50 kN for loading in the x - and y -directions, respectively). Variations in failure loads decreased with higher hierarchy levels, making it challenging to rank first- and second-order HCs in the two loading directions.
- The zero-order HC specimens (x_1 and x_2) had notable load peak differences after the first one, with x_2 having substantially lower peaks, most likely due to failure along an inclined line, implying flaws or poor sintering at separation points of the cell walls.

9.3. Recommendations for further research

Experimentation should be performed for all the differing polygon structures computationally modelled in Chapter 4 to confirm the results obtained. Moreover, to reduce stress concentrations and

increase stiffness, TO and SO at the vertices and size optimization of the polygon structures should be investigated, respectively.

The production of AM hierarchical HC parts with geometries similar to those studied in Chapter 5 should be done to validate the results obtained in the present work experimentally. Moreover, future studies should investigate the possibility of improving the load-bearing capacity of the hierarchical HC structures studied here through TO and SO of the highly stressed regions identified in this study.

Future studies should also aim to develop AM HC parts to validate the optimized FE models experimentally in Chapter 7. Numerical simulation of optimized FE models under harsh load conditions, such as dynamic loading, should also be carried out to test the load-bearing capacity of HC parts under such conditions. Additionally, SO and TO can be effectively applied to 3D hierarchical cellular (HC) models. Through an iterative process that refines geometry and incorporates increasingly complex objective functions, this approach can produce structures that are both lightweight and capable of withstanding more intricate load conditions. As these high-fidelity models account for more complex geometries and stress concentrations, the accuracy of the optimization process is expected to improve.

Furthermore, future research should focus on comparing physical experiments of regular HC models in Chapter 8 with numerical models of topology-optimized hierarchical HCs. This is essential for validating performance improvements achieved through optimization strategies. Regular hierarchical models offer foundational insights into structural behaviour, while TO enhances the design by enabling more efficient, lightweight, and robust configurations through the adaptive distribution of material tailored to specific loading conditions and constraints. This comparison allows researchers to assess how optimization influences key characteristics like strength, stiffness, and failure modes in practical applications, ensuring that theoretical improvements lead to tangible benefits and enhance the overall design process.